Response and design of high strength steel structures employing square and rectangular hollow sections

By

Michaela Gkantou

A thesis submitted to the University of Birmingham
for the degree of Doctor of Philosophy

Department of Civil Engineering, School of Engineering
University of Birmingham
Edgbaston B15 2TT, Birmingham, UK

14 February 2017

List of Publications

The present PhD study has led to a list of journal papers, conference papers and technical reports, as follows:

Journal papers

- Wang, J., Afshan, S., **Gkantou, M.**, Theofanous, M., Baniotopoulos, C. and Gardner, L. (2016) Flexural behaviour of hot-finished high strength steel square and rectangular hollow sections. Journal of Constructional Steel Research, 121: 97–109.

- **Gkantou, M.**, Theofanous, M., Antoniou, N. and Baniotopoulos, C. (accepted1) Compressive behaviour of high strength steel cross-sections. Proceedings of the Institution of Civil Engineers.

- **Gkantou, M.**, Theofanous, M., Wang, J., Baniotopoulos, C. and Gardner, L. (accepted2) Behaviour and design of high strength steel cross-sections under combined loading. Proceedings of the Institution of Civil Engineers.

- Wang, J., Afshan, S., **Gkantou, M.**, Theofanous, M., Baniotopoulos, C. and Gardner, L. (in preparation) Behaviour and design of high strength steel prestressed trusses.

Conference papers

- **Gkantou, M.**, Baniotopoulos, C., Theofanous, M. and Hemida, H. (2014) Numerical study of the structural response of S460 & S690 Beams. Proceedings of the 5th Annual BEAR Conference. University of Birmingham, Birmingham, UK. 15 December 2014.

- **Gkantou, M.** and Baniotopoulos, C. (2014) Post-tensioned trusses of High Strength Steel for long span applications. Poster Conference, University of Birmingham, Birmingham, UK. 10 June 2014.

- **Gkantou, M.**, Theofanous, M. and Baniotopoulos, C. (2015) Optimisation of high strength steel prestressed structures. In the 8th GRACM International Congress on Computational Mechanics. Volos, Greece. 12-15 July 2015.

- **Gkantou, M.**, Theofanous, M. and Baniotopoulos, C. (2016) On the structural response of high strength steel prestressed trusses. A numerical approach. In the 11th HSTAM International Congress on Mechanics. Athens, Greece. 27-30 May 2016.

- **Gkantou, M.**, Theofanous, M. and Baniotopoulos, C. (2017) Finite element modelling of compressive and tensile prestressed tubular members. In the CESARE'17 International Conference Coordinating Engineering for Sustainability and Resilience. Dead Sea, Jordan. 3-8 May 2017 (accepted).

- **Gkantou, M.**, Theofanous, M. and Baniotopoulos, C. (2017) Structural response of square and rectangular high strength steel hollow sections under combined biaxial bending and compression. In the EUROSTEEL. Copenhagen, Denmark. 13-15 September 2017 (accepted).

- **Gkantou, M.** (2017) Response and design of high strength steel structures employing square and rectangular hollow sections. In the Istructe Young Researchers' Conference. London, UK. 5 April 2017 (selected for oral presentation).

- **Gkantou, M.**, Theofanous, M. and Baniotopoulos, C. (2017) Studies on the response of high strength steel structures employing square and rectangular hot-finished hollow sections. In the 9th National Conference in Steel Structures. Larissa, Greece. 5-7 October 2017 (accepted).

Technical reports

- **Gkantou, M.**, Antoniou, N., Theofanous, M. and Baniotopoulos, C. (2014) HILONG RFCS Project - Deliverable D2.2. Report on numerical analysis of S460 and S690 members.

- **Gkantou, M.**, Theofanous, M. and Baniotopoulos, C. (2016) HILONG RFCS Project - Deliverable D4.2.2. Report on numerical analysis of post-tensioned trusses and vibration considerations.

- **Gkantou, M.**, Theofanous M., Baniotopoulos C., Gardner L., Afshan S., Wang J. and Wadee A. (2016) HILONG RFCS Project - Deliverable D4.3b. Report on design guidance - Prestressed truss.

Abstract

Structural steels with yield strengths over 460 N/mm^2, widely known as high strength steels (HSS), can potentially lead to lighter structures. The reduced deadweight of HSS structures allows for lower construction costs and transportation workloads, which in turn lead -both directly in less material usage and indirectly in lower transportation costs- to lower carbon emissions and energy use. The latter, combined with potential time and cost savings, comprise sustainability gains that can emerge from the use of HSS as a structural material.

The benefits associated with the use of HSS have attracted growing attention from structural engineers. Most international structural design codes have been developed on the basis of ordinary structural steels and cover the design of HSS with some restrictions, due to the inferior ductility and strain-hardening characteristics compared to ordinary structural steel. Given that HSS design provisions are largely based on test data for mild steel and the recommended rules and methods for HSS are identical to those for carbon steel, further investigation on the applicability of such design specifications to HSS is required.

A comprehensive literature review on the structural response of HSS has identified a gap in knowledge on the structural performance of hot-finished hollow sections. To this end, a series of studies are carried out to investigate the ultimate behaviour of HSS hot-finished square and rectangular hollow sections. In addition to the studies on the ultimate capacity, focus is placed upon the mitigation of excessive deflections that could prevent full exploitation of the enhanced material strength in high strength steel long span structures, where serviceability limit state is most likely the governing design consideration. In line with past research and based on recent applications of carbon steel structures, the possibility of applying prestress is examined. Complementing the existing knowledge, the present study aims to boost the structural application of HSS.

Finite element modelling is applied for the investigation of the behaviour of S460 and S690 structures. The numerical models are meticulously validated against test results and subsequently utilised for the execution of parametric studies that allows the evaluation of key parameters' effect on the structural performance. The same methodology is applied to study the response of individual components and trusses.

In particular, the performance of HSS stub columns, beams, stub columns subjected to combined uniaxial bending and compression and stub columns under combined biaxial bending and compression, is studied in depth. The influence of the cross-section slenderness, the cross-section aspect ratios, the moment gradient and the loading eccentricities on the ultimate cross-sectional capacity is examined. The applicability of design specifications, with particular emphasis on current European standards, to HSS is assessed. Design recommendations, in line with observed response, are proposed.

An extensive study on a number of commonly employed prestressed truss configurations is performed, revealing that the application of prestress can act as a means of increasing both the strength and the stiffness of a structure. Based on the gained knowledge, a set of simplified verifications for prestressed steel truss design is provided. It is concluded that combining prestress with high strength structural steel could reduce the material consumption and maximise the overall structural performance, thereby further stretching the limits of what is attainable in modern engineering design practice.

Acknowledgements

The work presented here has been carried out under the supervision of Prof. Charalampos Baniotopoulos, Dr. Marios Theofanous and Dr. Hassan Hemida, to whom I would like to express my special appreciation and my sincere gratitude for their constant and motivational support, their exceptional technical and mentoring guidance and their valuable advice.

I would like to gratefully acknowledge the fund received from the European Community Research Fund for Coal and Steel (RFCS) under grant agreement [RFSR CT 2012-00028] that financially supported this research. I could not omit to express my gratitude for the partial funds received from the School of Engineering of the University of Birmingham that allowed me to attend three international conferences, thus gaining the experience of presenting my work on widely recognised audience.

Thanks to all staff members of the University of Birmingham who have supported me when I needed. Additionally, I would like to thank the academic and research staff of Imperial College London, particularly Prof. Gardner and Jie, for their inspiring guidance into their labs and an efficient and productive collaboration.

I would like to thank my friends in Birmingham, Nick, Danial, Steffie, Giulio, Fred, Panos, Lena, Alkistis, Chrysa, Vicky, to name a few, as well my friends in Greece, Ioanna, Rania and Zoe, for giving me strength to keep on with my hard work. The quiet environment of my office provided by Mike and Ali has allowed the timely completion of my thesis.

Last but not least, I would like to express my sincere thanks to my parents, Ioanna and Drosos, my brother, Giannis, my sister-in-law, Athina, my lovely niece, Ioanna and my aunt Adelais for their continuous and unconditional love and support during my PhD study and my deepest thanks to my fiancé Alexandros for his endurance, love and serenity in every possible manner all along the way.

Table of Contents

List of Figures

List of Tables

Nomenclature

Latin characters

A	Cross-sectional area
A_c	Cross-sectional area of the cable
A_{eff}	Effective cross-sectional area
A_t	Cross-sectional area of the tube
b	Section width
b_{eff}	Effective width
BC	Boundary conditions
$c/t\varepsilon$	Cross-section slenderness
CHS	Circular hollow section
COV	Coefficient of variation
CSM	Continuous strength method
$e_{0,n}$	Nominal initial loading eccentricity
e_0	Actual initial loading eccentricity
${e_u}'$	Eccentricity at ultimate load generated due to 2nd-order effect
e'	Eccentricity generated due to 2nd-order effect

E	Young’s modulus
E_{sh}	Young’s modulus of the strain-hardening region
EC3	Eurocode 3
f_{cr}	Elastic critical buckling stress
f_{csm}	CSM ultimate stress
f_u	Ultimate strength
f_y	Yield strength
FE	Finite element
FEM	Finite element method
FEA	Finite element analysis
F_{SLS}	Load at δ_{SLS}
h	Section depth
h/b	Aspect ratio (depth-to-width)
HSS	High Strength Steel
I	Second moment of area
k_{initial}	Initial stiffness
k	Buckling coefficient
L	Length

LVDT	Linear variable displacement transducer
M_{Ed}	Design bending moment
M_{el}	Elastic moment
$M_{el,Rd}$	Elastic moment resistance
M_{pl}	Plastic moment
$M_{pl,Rd}$	Plastic moment resistance
$M_{u,Exp}$	Experimentally obtained ultimate moment
$M_{u,FE}$	Numerically obtained ultimate moment
M_u	Ultimate moment
n	Number of tests or FE simulations
N_{Ed}	Design axial load
$N_{b,Rd}$	Design buckling resistance
$N_{pl,Rd}$	Design plastic resistance
$N_{u,Exp}$	Experimentally obtained ultimate load
$N_{u,FE}$	Numerically obtained ultimate load
N_u	Ultimate load
P_{nom}	Nominal prestress force

P_{opt}	Optimal prestress force
q_{Ed}	Uniform loading
r_i	Internal corner radius
R_{Exp}/R_{Pred}	Utilisation ratio of experimental to predicted capacity
R_{FE}/R_{Pred}	Utilisation ratio of FE to predicted capacity
R	Rotation capacity
RHS	Rectangular hollow section
RP	Reference point
SHS	Square hollow section
SLS	Serviceability Limit State
t	Thickness
ULS	Ultimate Limit State
W_{eff}	Effective section modulus
W_{el}	Elastic section modulus
W_{pl}	Plastic section modulus

Greek characters

γ_{Mo}	Partial factor for resistance of cross-sections
γ_{M1}	Partial factor for resistance of members to instability
δ_{SLS}	Deflection limit for SLS
δ_L	Average vertical displacement
δ_M	Vertical displacement at mid-span
$\varepsilon_{concave}$	Strain on concave side of cross-section
ε_{convex}	Strain on convex side of cross-section
ε_{csm}	Strain at f_{csm}
ε_{eng}	Engineering strain
ε_f	Strain at fracture
ε_{ln}^{pl}	Logarithmic plastic strain
ε_u	Strain at ultimate load
ε_y	Strain at yield load
θ_{pl}	Elastic rotation
θ_u	Rotation at ultimate load
κ_{pl}	Elastic curvature

κ_u	Curvature at ultimate load
$\bar{\lambda}_{\mathrm{cs}}$	Cross-section slenderness
$\bar{\lambda}_{\mathrm{p}}$	Plate slenderness
ρ_{cs}	Reduction factor for the cross-section
ρ_f	Reduction factor for the flange
ρ_w	Reduction factor for the web
σ_{cr}	Elastic critical buckling stress
σ_{eng}	Engineering stress
σ_{true}	True stress
φ_u	Mean end-rotation at ultimate load
χ	Buckling reduction factor
ψ	Stress ratio across section depth
ω_0	Measured initial local geometric imperfection
ω_{DW}	Initial geometric imperfection according to Dawson and Walker (1972)

CHAPTER 1: INTRODUCTION

1.1. Background

It was back in the 19th century when structural steel made its first appearance. Its potential as a structural material due to its high strength, reliable material properties, rapid and high quality construction, was quickly recognised (Russell and Dowell, 1933). Structural steel grades had a specified minimum yield stress of 220 N/mm^2 for bridges and 240 N/mm^2 for buildings (Bjorhovde, 2004). Growing market demands together with the technological advances in material science, brought structural steels with higher strength into the construction industry. Over the past decades, the steel industry has developed structural steels with yield strength higher than 460 N/mm^2, widely regarded as high strength steels (HSS).

The most important benefit arising from the use of HSS is the weight reduction which is achieved due to its high yield strength. A lighter structure requires smaller foundations, shorter transportation and construction times, which in turn lead -both directly in less material usage and indirectly in lower transportation costs- to lower carbon emissions and energy use. This brings apparent advantages for high strength steel as a sustainable and economical construction material, given the importance of sustainable development in modern society. In addition to this, light structures lead to better space utilisation, freedom in design and aesthetically more elegant solutions. On the other hand, slender sections make HSS structures less stiff and hence more susceptible to buckling and excessive deflections, thus potentially limiting the extent to which the advantage of their high yield strength can be taken.

Even though HSS has been broadly applied in automobile, crane and offshore engineering, restricted market availability and structural behaviour considerations (i.e. reduced ductility and weldability), have limited its use in the construction sector. Additionally, structural design specifications for HSS are largely based on a limited number of test data and assumed analogies with mild strength steel. Hence, their applicability to HSS needs to be assessed. Upon identifying a gap in literature on the structural performance of hot-finished square and rectangular hollow sections and with the aim to complement the existing knowledge on high strength steel's response, the current research study presents a series of comprehensive studies on the structural performance of HSS members and structures.

1.2. Aim

The main aim of the current study is to investigate the performance of high strength steel structures, extending the pool of HSS structural performance data. The obtained results, the comments and conclusions upon data analysis and the design proposals can be used by designers and researchers interested in the structural performance of HSS employing square and rectangular hollow sections. The generated results together with the subsequent design recommendations and proposals aim to allow for more safe, accurate but also economical design guidelines in line with the observed response and to potentially contribute to the development of future revisions of HSS design specifications. Further to this, as the research on HSS is expanded and the comprehension of the structural performance of HSS deepens, a more widespread application of HSS in the construction industry can be expected, thereby leading to material and cost savings and potentially to sustainability gains and more elegant structures.

1.3. Objectives

In order to achieve the aforementioned research aim, the objectives set are as follows:

- Investigate the behaviour of S460 and S690 members in compression, for varying cross-section slendernesses and aspect ratios.
- Study the structural response of 3-point and 4-point S460 and S690 beams, for varying cross-section slendernesses, aspect ratios and moment gradients.
- Examine the cross-sectional response of S460 and S690 short columns under eccentric loading, for varying cross-section slenderness and load eccentricities, considering the case of combined uniaxial bending and compression and the case of combined biaxial bending and compression.
- Investigate in detail the structural behaviour of HSS trusses and study the possibility of applying prestress to control the deflections and enhance the overall performance.
- Assess current design specifications and provide design recommendations in line with the observed structural response.

1.4. Outline of thesis

In this chapter an introduction on high strength steel structures is given, whilst the project's research aim and objectives are provided. The outline of the thesis is presented hereafter.

In Chapter 2, a comprehensive literature review regarding high strength steel and the structural response of HSS members and structures is carried out. Fundamentals on the compressive response are provided. A literature review on prestressed steel structures is also included.

The methodology followed to investigate the structural performance of HSS members and structures is described in Chapter 3. Note that some general assumptions applicable to the numerical modelling performed throughout the whole study are also incorporated in this chapter.

The compressive behaviour of S460 and S690 square and rectangular hollow sections for varying cross-section slendernesses and aspect ratios is thoroughly studied in Chapter 4. The applicability of relevant design specifications is assessed and suitable design recommendations are made.

Chapter 5 focuses on the response of beams under 3-point and 4-point bending. Once the flexural response is studied, the suitability of current Eurocode specifications is assessed.

Having examined the compressive and flexural response, Chapter 6 studies the cross-sectional behaviour of S460 and S690 stub columns under combined loading, investigating the case of uniaxial bending and compression and the case of biaxial bending and compression. The results facilitate the development of interaction failure surfaces, allowing the assessment of relevant design provisions.

Moving from the behaviour of individual members to the performance of more complex structures, the response of HSS trusses is the main focus of Chapter 7. Aiming to control vertical deflections and improve the overall performance, the possibility of applying prestress is rigorously examined. A set of required verifications for the design of prestressed trusses is also provided.

A summary of the research outcomes accompanied with some recommendations for future research is given in Chapter 8.

It is worth noting that Chapters 3-7 have adopted the same structure in terms of subsections, thus making following and comprehending the whole research study easier.

CHAPTER 2: LITERATURE REVIEW

2.1. Introduction

The principal objective of this chapter is to determine the understanding of the structural response of high strength steel. The definition of high strength steel together with the benefits arising from its use, the production processes, the market availability, examples of applications to date and available international structural design standards are provided in Section 2.2. In Section 2.3, a review of the fundamental principles underpinning the structural behaviour of steel members is conducted, whereas the design methods relevant to the current research project are also provided. Research studies carried out to evaluate the structural performance of HSS members and structures are collated in Section 2.4. Section 2.5 is dedicated to prestressed steel structures which will be the subject of study in Chapter 7. The emerging knowledge gap is stated in Section 2.6.

2.2. High Strength Steel

2.2.1. Definition and benefits

Steel is an alloy of iron and other elements, primarily carbon. It possesses high strength, stiffness, weldability and ductility. Structural steels with yield capacity up to 355 N/mm^2 have been broadly applied in projects across the world. Advancements in steel materials and production methods enabled higher steel grades for use as construction materials. Considerable attraction has been drawn from structural designers and researchers, owing to the potential weight reductions emerging from the use of HSS. In structural engineering, HSS can be defined as the steel with nominal yield strength equal to or higher than 460 N/mm^2. Additional definitions for different application sectors are shown in Table 2.1.

Table 2.1: Definition of HSS in different sectors [adapted from Steel Construction Institute (2014)].

High Strength Steels Definition	Product Form	Specified Minimum Yield Strength (N/mm^2)											
Sector		235	275	300	355	400	420	450/460	500	550	690	890	1100+
Buildings	Profiles	L	L	M	M	H	H	H					
Foundations, quay walls	Sheet piles, piles	L	L	M	M	H	H	H					
Bridges: road (small and medium spans)	Fabricated girders/ profiles	L	L	M	M	H	H	H					
Bridges: road	Fabricated girders				L	L	M	M	H	H	H		
Bridges: rail	Fabricated girders/ profiles	L	M	M	H								
Pipelines-Onshore Pipelines-Offshore trunk lines	Seam welded pipe				L	L	M	M	H	H	H		
Pipelines- flow lines/risers	Seamless pipe				L	L	M	M	M	H	H		
Pipelines- tubing/casing	Seamless pipe				L	L	M	M	M	M	M	H	H
Pressure vessels	Welded plate		L	L	M	M	M	H	H				
Storage tanks	Welded plate	L	M	M	H	H	H	H					
Fixed offshore rigs	Welded plate				M	M	M	M	M	H	H		
Mobile offshore rigs	Welded plate				L	L	M	M	M	H	H	H	
Bulk container ships	Welded plate	L	M	M	M	H	H						
Military ships, fast Ferries	Welded plate			L	M	M	H	H					
Wind towers	Welded plate / profiles		L	L	M	M	H	H	H	H			
Mobile cranes	Welded tubulars / profiles						L	L	M	M	H	H	H
Quarrying & mining	Wear plates					L	L	M	H	H	H		
Yellow goods	Welded plate		L	L	M	M	M	H	H	H	H		

L=Low M=Medium H=High

The reduced deadweight arising from the application of HSS leads to lighter structures with smaller foundations, less material consumption and welding needs, lower manufacturing, transportation and assembly costs and thus a more economic design. Potential benefits associated with the economic efficiency of HSS can be seen in Figure 2.1(a), where the relative price per tonne and the relative material cost is shown for increasing yield strength, taking as reference value S235 steel grade. Under the assumption that the material strength is fully utilised, the relative material cost -disregarding the fabrication and erection costs- decreases for higher steel grades, reflecting the gains that can emerge from HSS's usage. Similarly, in Figure 2.1(b), it is shown that the mass reduction due to HSS's usage could compensate for the increased material price (Stroetmann, 2011).

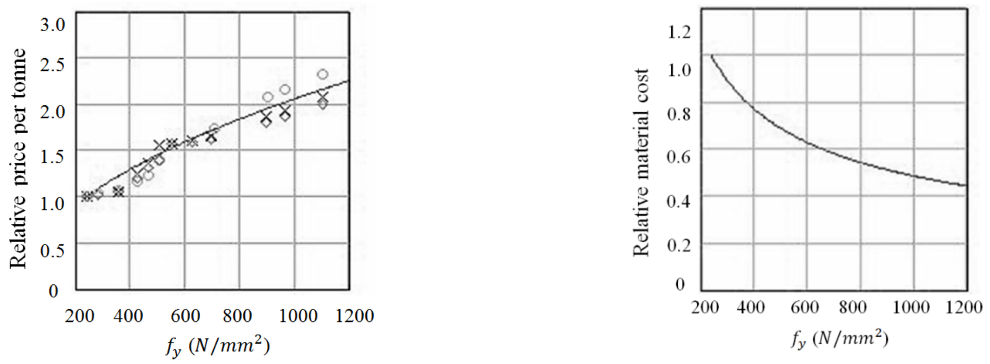

a) Approximate price per tonne and material cost of hot rolled steel (Collin and Johansson, 2006)

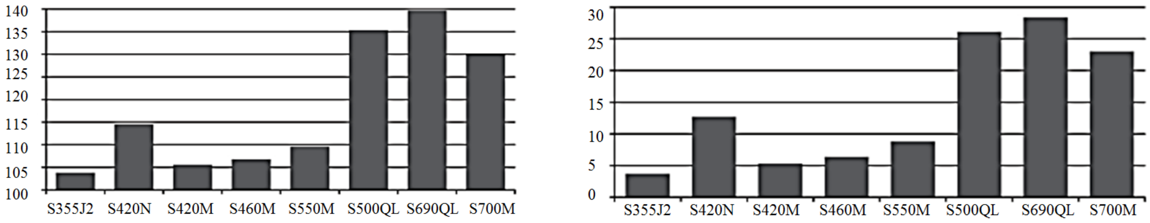

Steel prices referring to S235 in %

Required mass reduction referring to S235 in %

b) Economic efficiency of HSS (Stroetmann, 2011)

Figure 2.1: Material and cost savings.

Similar conclusions were drawn from studies by Dubina (2008), who evaluated the decrease in the weight of steel columns through the use of S460 grade, finding reductions equal to 24% and 17% for the Mapfre Tower in Barcelona and for the 77 Hudson, Colgate Center in Jersey City, respectively.

Further to the economic efficiency of HSS, a lighter structure leads to reduced amount of raw material and thus of required energy use. Moreover, it allows for shorter construction times and lower transportation workloads, reducing further the carbon emissions and securing profound sustainability gains. Steel is the most recyclable material in the world with more than 500 Mtonnes being recycled every year (World Steel Association (WSA), 2017). Further to steel's favorable sustainability properties, the application of HSS can potentially decrease the amount of material to be fabricated and eventually to be recycled. For instance, the use of high strength steel in Friends Arena Stadium in Sweden, reduced the weight of the roof structure from 4584 tonnes to 4000 tonnes, resulting in a reduction in greenhouse gas emissions from steel production, transportation and recycling equal to 900 tonnes CO^2 (Jernkontoret, 2017).

Given the growing environmental awareness and the demand for a green economy and specifically for sustainability in construction, there is one more strong reason to encourage the use of HSS. Complementing the aforementioned benefits, the smaller sizes of HSS structural elements can give more freedom in design and allow for more elegant structures.

2.2.2. Production processes and chemical composition

Recent advances in material and production technology have allowed steels not only with higher strength, but also with better toughness, higher weldability, improved cold formability and corrosion resistance, thereby rendering HSS an attractive material for structural applications. These steels are known as High Performance Steels (HPS). Examples of HPSs include the high strength steel low alloys (HSLA) that contain low percentage of microalloying elements and provide better mechanical properties and corrosion resistance, the high strength weathering steels that offer great corrosion resistance against salts and the high toughness steels, in which brittle failure is avoided even in cold regions (Miki et al., 2002). Note that an improvement in one of HPS's properties occurs usually at the expense of others. The choice of the most appropriate HPS depends on material and design requirements.

The strength of steel is controlled by the formation of its microstructure, which is mainly determined by its thermal history. Heat treatment techniques can therefore be implemented in order to meet HPS requirements. During the heating processes austenite, martensite, bainite, pearlite and ferrite are formed, depending on the carbon content.

The following heat treatments are applied for the development of high strength steels: normalising (N), quenching and tempering (QT) and thermomechanical controlled rolling process (TMCP). N produces rolled sections of moderate strength up to 460 N/mm^2, QT results in very high strength steel plates up to 1100 N/mm^2, whilst TMCP sections can have a yield strength up to 690 N/mm^2 (Hanus et al., 2005). Normalising process is a heat treatment that occurs after hot rolling, during which steel has been heated above the austenite recrystallisation temperature (Ac3). Reheating steel slightly above Ac3 followed by slow air cooling results in a homogeneous grain microstructure of ferrite and pearlite. This process can also be found as normalised rolling with the only difference that the heat treatment is included in the rolling process. Quenching and tempering process consists of two stages. Rolling, heating above Ac3 and rapid water cooling which gives a strong martensitic or bainite grain structure at first stage and tempering below the temperature that austenite starts to form in order to improve toughness properties at second stage. QT steel plates are commonly known as ultra or very high strength steel plates. They possess very high yield strength but low ductility. Thermomechanical control process implies controlled rolling at a temperature below the recrystallisation temperature or sometimes in the temperature range where austenite and ferrite/pearlite coexist. After rolling, accelerated cooling or tempering (for very thick plates or higher grades) gives fine-grained microstructure. The rolling procedure should be continuously controlled and adapted to the final plate thickness in order to achieve high quality TMCP plates (Hanus et al., 2005). TMCP generally produces rolled steel with high toughness properties and better weldability than ordinary steel (Samuelsson and Schröter, 2005).

The historical evolution of the production processes is shown in Figure 2.2(a), whereas a schematic description of the different types of heat treatments and rolling processes in relation with the temperature is given in Figure 2.2(b). The microstructures of N, Q+T, TM (air) and TM (acc) steels are depicted in Figure 2.2(c), with the black areas corresponding to higher carbon contents.

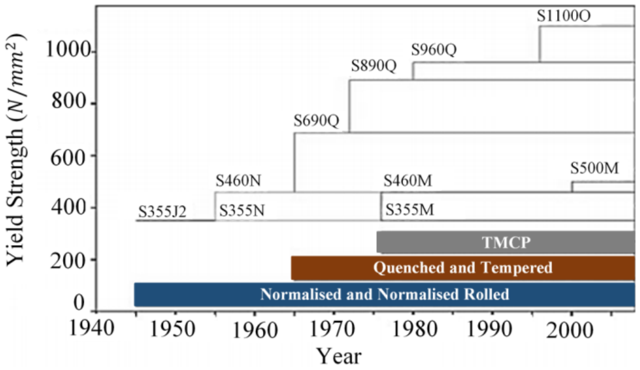

a) Historical development of grades and production processes [adapted from Samuelsson and Schröter (2005)]

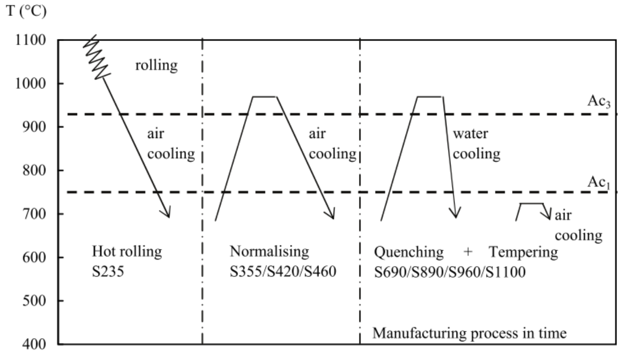

b) Temperature/time dependence diagram (Pijpers, 2011)

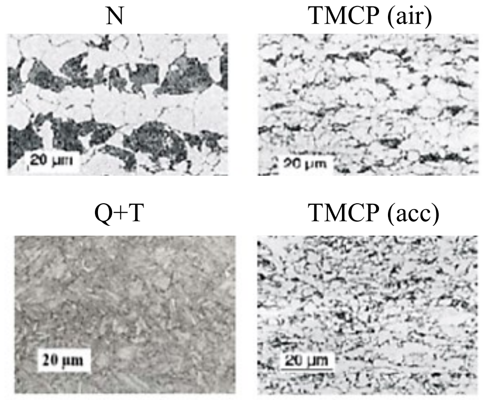

c) Grain microstructure comparison (Hanus et al., 2005)

Figure 2.2: Heat treatments applied in high strength steels.

Apart from the thermal history of steel, the chemical composition also affects the formation of its microstructure and hence its mechanical properties. Strength is primarily controlled by the amount of carbon. The actual amount of carbon in HSS is lower than 0.20%, whilst increased amount of carbon reduces weldability and toughness. Decreased grain size achieved by microalloying with Nb (niobium), V (vanadium) or Al (aluminium) increases strength and toughness. Increased strength is also achieved by Mn (manganese) and Mb (molybdenum) and increased fracture toughness by Ni (nickel) (Samuelsson and Schröter, 2005). Finally note that besides the steel grade, the alloying content vary also with the thickness range.

2.2.3. Stress-strain curves and design standards

The chemical composition and heat treatment of steels as well as the production and fabrication process of cross-sections may result in different stress-strain response. Examples of stress-strain curves of steels with increasing strength are shown in Figure 2.3(a) and Figure 2.3(b). Even though the values may be prone to variation, it can generally be observed that, contrary to the carbon steel's material response that is characterised by a sharp yield point, a well-defined yield plateau and significant strain-hardening and high ductility, the stress-strain curves of higher steel grades exhibit a more rounded response with inferior strain-hardening and ductility characteristics. Note that for steels demonstrating rounded response, an offset yield point at 0.2% plastic strain (known as proof strength) is considered for the estimation of the yield strength. Figure 2.3(c) displays a relation between the tensile-to-yield strength ratio and the yield or proof strength, showing a monotonic decrease for increasing steel grade.

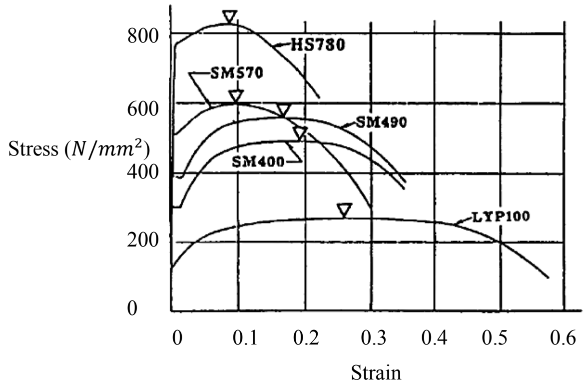

a) Stress-strain curves for various steel grades (Ricles et al., 1998)

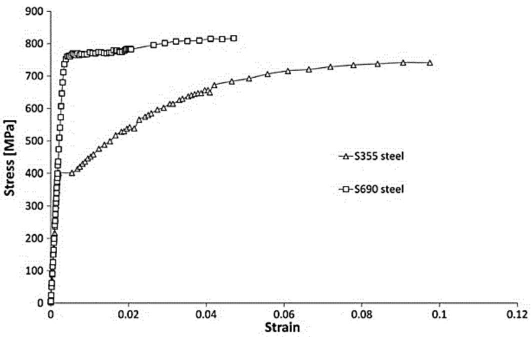

b) Typical stress strain curves for S355 and S690 curves (de Jesus et al., 2012)

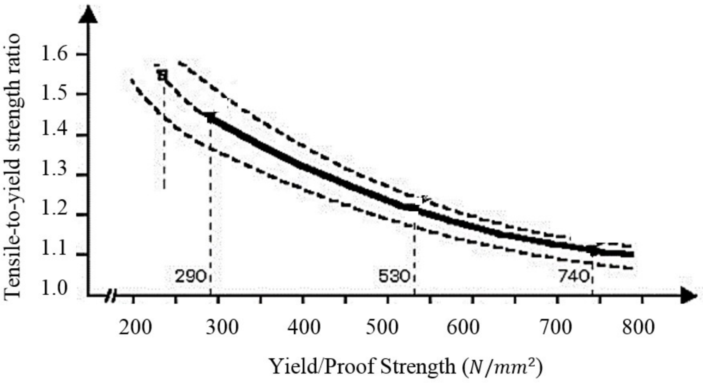

c) Tensile-to-yield strength ratio vs yield/proof strength (Dahl et al., 1983)

Figure 2.3: Material response of steels.

Based on steel's production processes as well as the chemical and mechanical properties, material standards provide requirements for the most commonly applied structural steel grades. One such standard is the EN 10025 (2004) which refers to normalised, thermomechanical rolled and quenched and tempered steels in Parts 3, 4 and 6 respectively. The aforementioned standard defines quality limits for structural steels, including minimum values for the yield and tensile strength, maximum contents for alloying and minimum energy values for impact tests.

Given the variations in the stress-strain response between normal and high strength steels, the structural design of HSS necessitates careful treatment by international code specifications. In order to consider the effect of lower material ductility and strain-hardening characteristics on the structural performance, specifications for HSS are currently available in most international structural design codes. The Chinese code for the design of steel structures provides guidance for steels with nominal yield strength up to Q420 steel (yield strength 420 N/mm^2) (GB 50017-2003, 2006). The American specification for structural steel buildings allows the use of HSS up to A514 steel (yield strength ≈690 N/mm^2) (ANSI/AISC 360-10, 2010). The Australian steel structures code allows for steels with yield strength up to 690 N/mm^2 (AS-4100-A1, 2012). In Europe, Part 1-12 of Eurocode 3 extends the rules for design of steel structures up to steel grades S700 for cold or hot rolled flat products and S690 for cold or hot rolled structural steel (EN 1993-1-12, 2007).

With regard to the material characteristics, more relaxed requirements are imposed for HSS material in most of structural design codes, accompanied by restrictions in applicable design methods. For example, EN 1993-1-12 (2007) provides new relaxed material requirements with respect to ultimate-to-yield strength ratio f_u/f_y, strain at fracture ε_f and strain at ultimate stress ε_u ($f_u/f_y \geq 1.05$; elongation at failure ε_f not less than 10%; $\varepsilon_u \geq 15 f_y/E$) compared to the equivalent mild steel ones ($f_u/f_y \geq 1.10$; elongation at failure not less than 15%; $\varepsilon_u \geq 15\varepsilon_y$).

Indicative attained values of f_u/f_y, ε_f and ε_u of high strength steels are found at Wang et al. (2017). Additionally, owing to the restricted plastic deformation capacity and thus the insufficiency to form a collapse mechanism, EN 1993-1-12 (2007) allows only elastic analysis for HSS, despite the provisions of Class 1 slenderness limit, whilst it recommends undermatched electrodes for welded HSS connections to make them more ductile (Johansson and Collin, 2005).

Similar recommendations are made in other structural codes. However, due to limited available HSS test data when the specifications for HSS were published, an extensive reference to the design rules and methods for carbon steel is apparent. Given the uncertainties concerning the applicability of the design methods for ordinary carbon steel to HSS, as well as the existing limitations and gaps in knowledge, further research is needed to fully verify and further develop the design rules for HSS.

2.2.4. Market availability and applications

HSS is greatly advantageous for an economic and sustainable design. In structures where self-weight consists a significant part of the total load, such as long-span applications, HSS is particularly cost-effective. Despite its benefits, HSS's usage in the construction sector has been relatively low compared to other sectors, due to a series of reasons including lack of long-term experience, design restrictions and market restraints, such as limited suppliers, long lead-in times and increased material price. A list of some prominent HSS manufacturers, together with the nominal yield strength of their products, followed fabrication process and the type of sections available, are presented in Table 2.2.

Table 2.2: HSS manufacturers (based on product brochures).

Manufacturer	Name	Nominal Yield Strength (N/mm^2)	Fabrication process	Type
Tenaris	TS590, TS690, TS770, TS890	590, 690, 770, 890	QT	CHS
Vallourec-Mannesmann (V&M)	MSH S460NH	460	N	SHS, RHS, CHS
	Forterior 450, 470, 500, 650	450, 470, 500, 650	N/QT	SHS, RHS, CHS
	FineXcell 550, 690, 770, 890	550, 690, 770, 890	QT	SHS, RHS, CHS
	Spirafort 450, 470, 590	450, 470, 590	N/QT	CHS
	Avadur 552, 758, 862	552, 758, 862	QT	CHS
ArcelorMittal	HISTAR 460, 460 L	460	TMCP	IPE, HE, HL, HD, HP
	HISTAR A913, Grade 65, 70	450, 485	QT	“W”, “S”, “MC”, “L”, “C” shapes
Ruukki Construction (Part of SSAB)	Optim MC 500, 550, 600, 650, 700, 750	500, 550, 600, 650, 700, 750	TMCP	plate material
	Optim 700 QL	700	QT	plate material
	S690 QL	690	QT	plate material
Tata Steel	Ympress S460MC, S500MC, S550MC, S650MC, S690TM, S700MC	460, 500, 550, 650, 690 700	TMCP/QT	plate material
	RQT 501, 601,701, 901	470÷830	QT	plate material
Dillinger Hütte	DI-MC 460	460	TMCP	plate material
	DILLIMAX 500ML	500	TMCP	plate material
	DILLIMAX 500, 550, 690, 890, 965, 1100	500, 550, 690, 890, 965, 1100	QT	plate material
JFE Steel Corporation	HITEN 590, 690, 780, 980	450÷960	TMCP/QT	plate material
ThyssenKrupp	PERFORM 460, 500, 550, 600, 650, 700	460, 500, 550, 600, 650, 700	TMCP	plate material
	XABO 460, 460 T, 500, 500 T	460, 460	TMCP	plate material
	N-A-XTRA (M) 550, 620, 700	550, 620, 700	QT	plate material
	XABO 890, 960, 1100, 1300	890, 960, 1100, 1300	QT	plate material

As the list of HSS manufacturers is expanded, steel designers are encouraged to apply HSS in the construction. As of now, HSS applications have already been reported across the world.

In Sweden, a bridge with a hybrid girder (i.e. mixed steel grades within the cross-section), employing S690 (Weldox 700) for the bottom flange and S460 for the web and the upper flange was proved to be the most economical solution (Johansson and Collin, 2005). The use of S1100 cold-formed plates was selected as the most efficient structural solution in a long span military bridge (Johansson and Collin, 2005). For the complex roof truss structure of

Friends Arena Stadium in Stockholm, S460 and S690 grades have been employed for the hollow section top chords, the U-shaped bottom chords and the end diagonals (Jernkontoret, 2017).

In order to meet the architectural demands for slender sections even in regions of peak stresses, S690 was applied at the hollow section lattice structure of a long composite bridge in Stuttgart, Germany (Johansson and Collin, 2005). The use of S460 was required for the erection of a new cable-stayed bridge in the north of Düsseldorf, where the pylons were restricted in height due to a landing zone nearby and therefore were highly loaded (Schröter, 2006). A suspended roof structure, making use of S460 and S690 steel grades to keep the dimensions of the structural elements small, was erected at the Sony Centre in Berlin in order to protect the facade of an old masonry hotel by carrying the lower apartment of the integrated building (Johansson and Collin, 2005). An airbus-hangar in Frankfurt Airport was designed with S460 grade for the girders, thus attaining the required long span, whilst respecting the codified stress limitations for increasing plate thickness (Willms, 2009).

Application of S460 grade has been reported for the highly stressed regions of the girders in the Remoulins road bridge in France (Schröter, 2006). In Millau Viaduct multi-cable-stayed bridge, the tallest bridge of the world to date with one of its masts summiting to 343 m, S460 was used for the construction of the pylons and the box girders (Schröter, 2006). The roof transformation of London Olympic Stadium has been designed with S460 for the girders and some circular hollow section bracing elements (Buro Happold Engineering, 2014).

HSS applications are also found out of Europe. In Japan, HSS has been employed in bridge engineering since 50s, leading to the erection of Akashi Kaikyo Bridge, the longest suspension bridge in the world to date. In particular, rolled S800 TMCP steel was applied for the stiffening truss of the bridge, allowing dead load reduction, whilst ensuring high weldability (Miki et al., 2002). The National Stadium in China, widely known as Beijing Bird's Nest and the CCTV Headquarters tower in Beijing made use of S460 steels (Shi et al., 2014a), whilst the Shanghai World Financial Centre (SWFC), the ninth tallest structure in the world to date, used S460 for the erection of its braced truss belts that connect the mega columns with the concrete core (Willms, 2009). The recently completed highest skyscraper in the Western hemisphere, Freedom Tower, NYC, on the site of the former World Trade Centre, also exploited the enhanced strength of S460 (ArcelorMittal, 2017).

Other projects where various HSS grades have been applied include the Reliant Stadium in Houston, Texas (Griffis et al., 2003), the ponta della musica bridge in Rome, the Stratford town center link in London, the Khan Shatyr entertainment Centre in Kazakhstan, the M8 Harthill footbridge in Scotland, the Emirates Stadium in London, the National Convention Centre in Qatar (Buro Happold Engineering, 2012).

A list of collated HSS structures together with the applied steel grade and the project’s completion year is given in Table 2.3, whilst examples of HSS structures are illustrated in Figure 2.4.

Table 2.3: HSS structures across the world.

Structure	Country	HSS	Year of completion
Hybrid bridge in Mittadalen	Sweden	S460, S690	1995
Fast bridge 48 military bridge	Sweden	S690, S1100	2008
Friends Arena	Sweden	S460, S690	2012
Composite bridge Nesenbachtalbrücke	Germany	S690	2000
Rhine-bridge in the north of Dusseldorf	Germany	S460	2002
Sony centre (roof truss)	Germany	S460, S690	2000
Airbus Hangar, Frankfurt Airport	Germany	S460	2007
Remoulins bridge	France	S460	1995
Millau Viaduct bridge	France	S460	2004
London Olympic Stadium Transformation	UK	S460	2016
Akashi Kaikyo bridge	Japan	S800	1992
Shanghai world financial Center (WFC)	China	S460	2008
CCTV Headquarters tower in Beijing	China	S460	2012
National Stadium (Bird's Nest)	China	S460	2008
NRG Stadium (Reliant Stadium)	USA	S690	2002
One World Trade Centre	USA	S460	2014

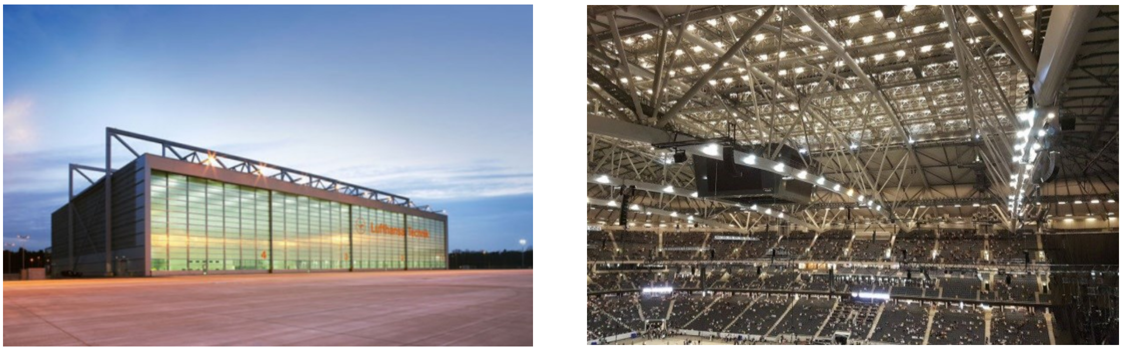

a) Airbus Hangar, Frankfurt, Germany
(Willms, 2009)

b) Friends Arena, Stockholm, Sweden
(Biliouri, 2016)

c) Akashi Kaikyo bridge, Japan
(Wikipedia, 2017)

d) Millau Viaduct bridge, France
(Aslam, 2017)

Figure 2.4: HSS structures.

2.3. Cross-section and member response

Before presenting literature on the structural performance of high strength steel, the current section describes the fundamental principles underpinning steel's performance as well as its codified treatment at cross-sectional and member level. In particular, the basic principles governing the compressive behaviour of steel are provided in Subsection 2.3.1. The cross-sectional response including the codified slenderness limits, the effective width equations applicable to slender sections, the design interaction surfaces relevant to cross-sections subjected to combined loading and the continuous strength method proposed for the treatment of local buckling are given in Subsection 2.3.2. Eurocode specifications for member response are provided in Subsection 2.3.3. Note that the design methods presented herein are assessed in Chapters 4-7.

2.3.1. Fundamentals of the compressive response

The conditions under which a structural system ceases to be stable are determined by the stability theory. The physical meaning of the three possible equilibriums i.e. stable, neutral (or critical) and unstable are illustrated in Figure 2.5(a). In all structural members or systems, instability can occur under the existence of compressive stresses. Buckling can be described as the behaviour of a structure or a structural element, which suddenly deforms in a direction orthogonal to the direction of loading. The simplest type of buckling is that of an initially straight strut compressed by an axial force P. The system is stable if P is small enough and becomes unstable for load values exceeding the critical value P_{cr}, known as the bifurcation point.

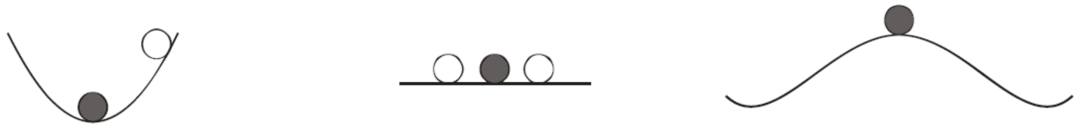

Stable equilibrium Neutral or Critical equilibrium Unstable equilibrium

Figure 2.5: Definition of stability [adapted from Full (2002)].

Assuming that there is a bifurcation point, up to which the elemental stresses change proportionally (i.e. linear behaviour) until they intersect in primary and secondary loading paths, the buckling response of a structural system can be evaluated according to Equation (2.1).

$$[K]\,x = \lambda\,[K_g]\,x \tag{2.1}$$

where λ the buckling load factor with a corresponding mode factor x for a global stiffness matrix $[K]$ and $[K_g]$ the geometric stiffness matrix, reflecting the effect of geometric change on the element force vector from a known stress state. Within this linearised treatment of buckling, the critical loads and corresponding buckling modes can be obtained.

Within the following chapters the buckling of columns and plates is studied. Hence focus is set on these two cases hereafter.

The first three elastic instability modes of a simply-supported column and the linear buckling mode of a plate which is dependent on its aspect ratio (a/b) are shown in Figure 2.6. The elastic buckling modes are usually a good estimator of the collapse mode.

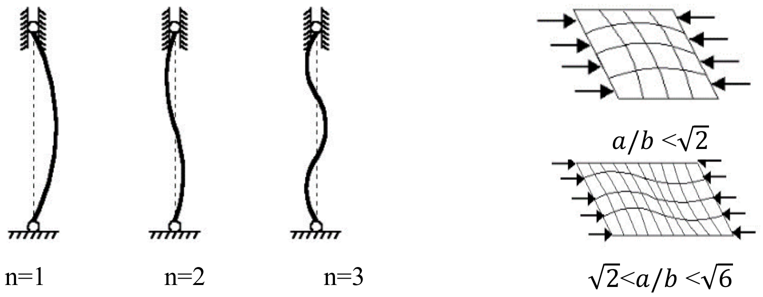

a) Column buckling b) Plate buckling

Figure 2.6: Elastic instability modes (Timoshenko and Gere, 1961).

The elastic critical buckling load of a column, free from any mode of imperfections, can be derived from Equation (2.2).

$$P_{cr} = \pi^2 EI/(kL)^2 \tag{2.2}$$

where P_{cr} is the Euler's (the name owes to the mathematician Leonhard Euler that firstly derived the formula) critical buckling load, E is the Young's modulus of the column's material, I is the minimum moment of inertia of the cross-section of the column, L is the unsupported length of the column and k the effective length factor, depending on the column ends' boundary conditions. The theoretical values of k for fixed-fixed, simply-supported-simply-supported and fixed-free ends are 0.5, 1.0 and 2.0 respectively (Timoshenko and Gere, 1961).

The elastic critical buckling stress of a plate is evaluated from Equation (2.3).

$$f_{cr} = k \frac{\pi^2 E}{12\,(1 - v^2)} (\frac{t}{b})^2 \tag{2.3}$$

where E is the Young's modulus, v the Poisson's ratio, b and t the depth and the thickness of the plate respectively and k the plate buckling coefficient. The theoretical values of k for fixed-fixed, simply-supported-simply-supported and fixed-free unloaded edges are 6.97, 4.00 and 1.27 respectively (Timoshenko and Gere, 1961). For long plates, more than one buckled mode is possible, with one half-wave transversely and m half-waves longitudinally. The relationship between the aspect ratio a/b for various m values is shown in Figure 2.7. In a long plate (large aspect ratio), the greatest initial inhibition to buckling is the transverse flexural stiffness of the plate between unloaded edges, tending towards the situation a/m=b for very long plates, which can be accurately simulated by considering a simply-supported, square panel.

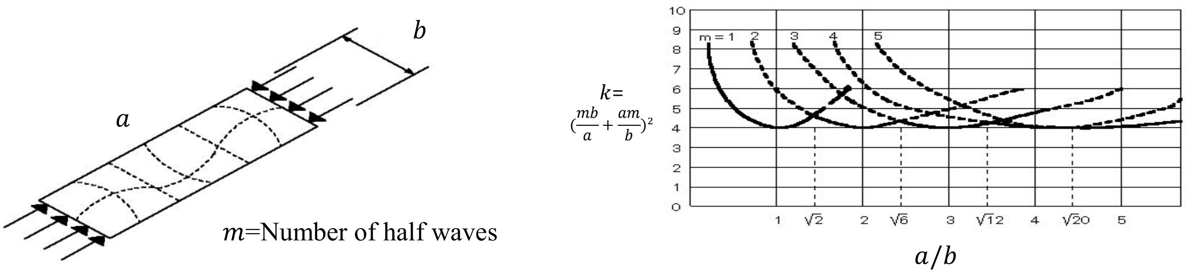

Number of half-waves   Variations in buckled mode with a/b

Figure 2.7: Plate buckling (Timoshenko and Gere, 1961).

For behaviour in the elastic range, the fundamental differences in the ideal post-buckling load-deformation response of columns and plates are shown in Figure 2.8, showing a stable post-buckling response for plates. In particular, the buckled plate causes an increase in length of the transverse plate strips, as the longitudinal edges are restrained against free shortening of the plate in the transverse direction. This causes tensile membrane forces in the transverse strips, exerting a stabilising effect on the longitudinal strips and thus providing post-buckling stiffness and strength.

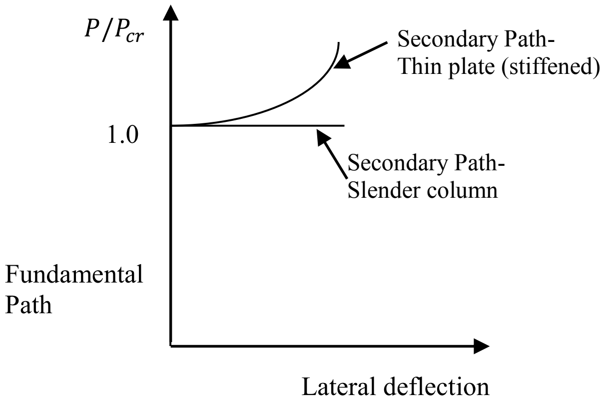

Figure 2.8: Ideal post-buckling response (Galambos, 1998).

However, real structural members do not behave exactly as elastic bifurcation theory predicts and hence the actual response is different from the ideal one. The material is not infinitely elastic and it is possible that inelastic buckling occurs. Additionally, real members contain imperfections (mostly of geometric nature) which may considerably affect the behaviour, while the applied load might be deviated from the idealised position due to imperfect connections, erection tolerances or lack of verticality of the member. Moreover, for increasing deformations, second order effects can emerge that combined with material inelasticity convert the problem to overall nonlinear.

The ultimate nonlinear behaviour of a simply-supported column and a simply-supported plate are illustrated in Figure 2.9. In both graphs, continuous lines correspond to the ideal elastic behaviour whilst the dots represent the actual behaviour, as determined from tests. The vertical axis corresponds to the ultimate capacity σ_u normalised by the yield strength f_y, whilst the horizontal axis corresponds to a quantity, commonly known as non-dimensional slenderness $\bar{\lambda}$, defined as $\sqrt{\frac{f_y}{f_{cr}}}$, where f_{cr} the elastic critical buckling stress, corresponding to the lowest buckling mode shape.

Manufacturing and fabrication processes result in unavoidable geometric imperfections and residual stresses that affect the buckling performance of columns. For low slendernesses, it is possible to find some results above the yield stress line due to strain-hardening, occurring in stocky columns. For slender columns, inelastic buckling occurs. In both cases, the ideal elastic response defines an upper bound limit of the actual response.

For plates of low slendernesses, the behaviour is mainly affected by material plasticity and yielding might precede plate buckling. At the point of buckling of slender plates, the purely compressive state switches into a combined bending/compression but the plate continues to carry additional load with a reduced stiffness, exhibiting considerable post-buckling strength. In plates of intermediate slenderness, the influence of the initial geometric imperfections is expected to be more significant and the results of the ultimate performance appear more scattered.

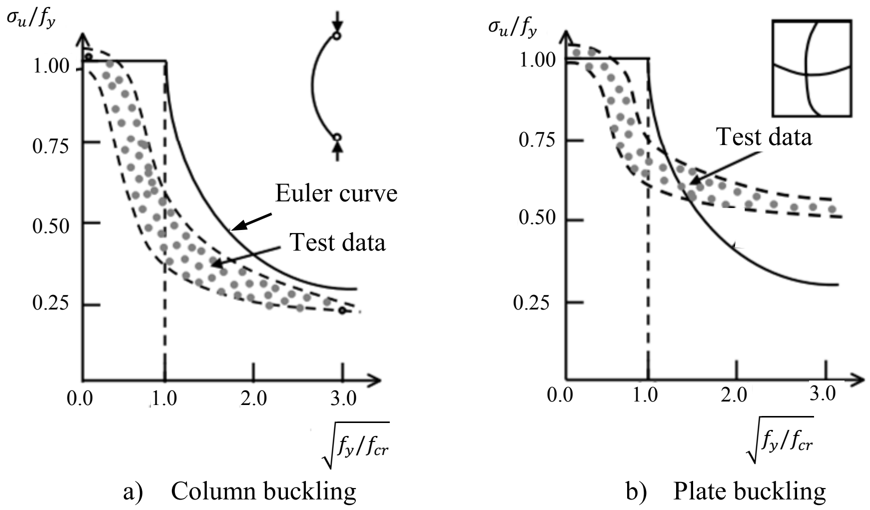

a) Column buckling b) Plate buckling

Figure 2.9: Relationship between strength and slenderness (Institute of Steel Development and Growth, 2017).

2.3.2. Codified treatment of local buckling

The buckling mode which occurs at cross-section level (i.e. buckling occurring over a length smaller than the largest cross-section dimension) is known as local buckling and its occurrence could limit the exploitation of the material's yield strength. Illustrations of local buckling failure modes are shown in Figure 2.10.

Figure 2.10: Local buckling failure mode (Theofanous and Gardner, 2010; Shi et al., 2014b).

In order to treat local buckling, all modern structural design codes make use of the cross-section classification procedure. In Eurocode (BS EN 1993-1-1, 2014), the resistance of the cross-sections is covered in Part 6.2. Based on the comparison of the width-to-thickness ratio (c/t) to codified slenderness limits, the constituent plate elements comprising a cross-section can be classified in four classes, with the cross-sectional response being related to the class of the most slender plate element. The slenderness limits depend on the applied stress gradient, the element's boundary conditions, the element's yield strength and the manufacturing process.

Class 4 (or slender sections) cannot reach their yield stress due to local buckling. Class 3 sections (or semi-compact) can develop their elastic moment capacity ($W_{el}f_y$) but fail before the achievement of their plastic capacity. Class 2 sections can exceed their plastic resistance ($W_{pl}f_y$) but with limited rotation capacity (R). Class 1 sections are able to form a plastic hinge without a reduction of their capacity below their plastic moment resistance.

Class 3 limit (also termed yield slenderness limit) defines the transition from a fully effective section (Class 1-3) that can attain its yield load capacity (Af_y) under pure compression to a slender section (Class 4) that fails by local buckling before its squash load is reached. The four cross-section classes together with Eurocode assumption for elastic-perfectly plastic material response are shown in Figure 2.11.

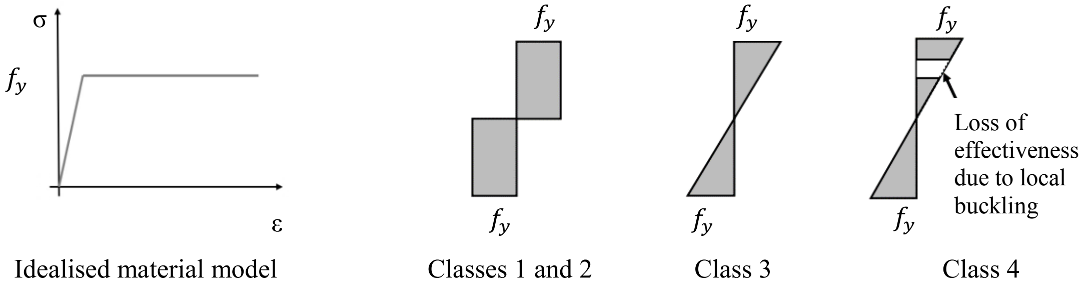

Figure 2.11: Cross-section classification (BS EN 1993-1-1, 2014).

The Eurocode slenderness limits for internal elements are given by Table 5.2 of BS EN 1993-1-1 (2014) and provided for reference in Figure 2.12. The slenderness limits have been based on a series of stub column and bending tests. Note that stub column refers to a short compression test specimen, short enough so that no column buckling would occur, but long enough to provide a valid representation of the imperfections and residual stresses over the cross-section (Galambos, 1998). Local buckling is expected to occur in the more slender constituent elements of short columns or in the more slender compressive regions of beams.

Owing partly to the limited HSS test data during the development of EN 1993-1-12 (2007), the cross-section classification limits for mild steel are also adopted for HSS sections. These limits are of particular interest for HSS sections, which are exploited in the presence of high stresses and hence the compactness of the sections is important for an economical design. The applicability of current Eurocode slenderness limits to HSS will be assessed in the following chapters.

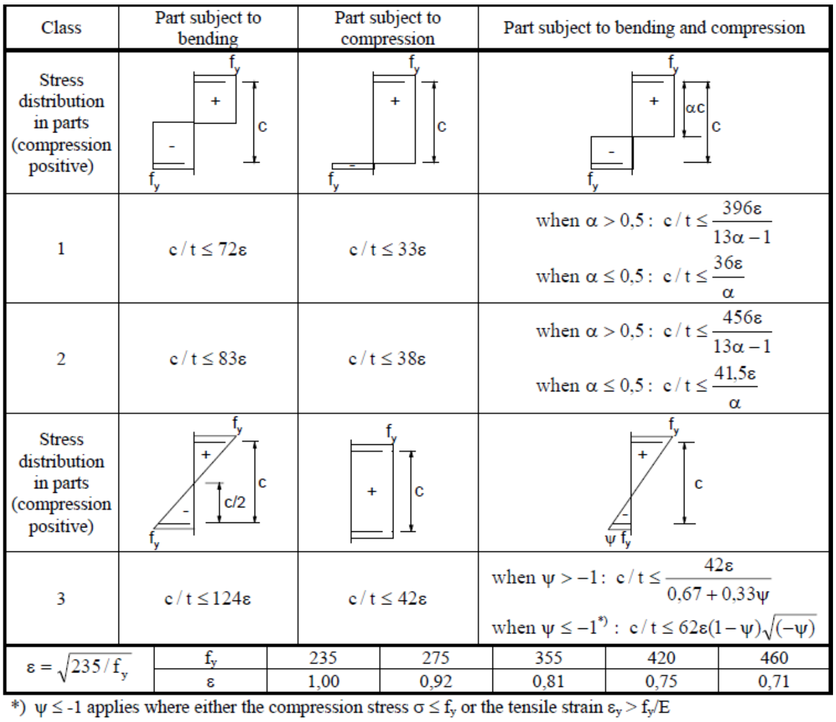

Class	Part subject to bending	Part subject to compression	Part subject to bending and compression
Stress distribution in parts (compression positive)			
1	$c/t \leq 72\varepsilon$	$c/t \leq 33\varepsilon$	when $\alpha > 0{,}5$: $c/t \leq \frac{396\varepsilon}{13\alpha - 1}$ when $\alpha \leq 0{,}5$: $c/t \leq \frac{36\varepsilon}{\alpha}$
2	$c/t \leq 83\varepsilon$	$c/t \leq 38\varepsilon$	when $\alpha > 0{,}5$: $c/t \leq \frac{456\varepsilon}{13\alpha - 1}$ when $\alpha \leq 0{,}5$: $c/t \leq \frac{41{,}5\varepsilon}{\alpha}$
Stress distribution in parts (compression positive)			
3	$c/t \leq 124\varepsilon$	$c/t \leq 42\varepsilon$	when $\psi > -1$: $c/t \leq \frac{42\varepsilon}{0{,}67 + 0{,}33\psi}$ when $\psi \leq -1^{*)}$: $c/t \leq 62\varepsilon(1-\psi)\sqrt{(-\psi)}$

$\varepsilon = \sqrt{235/f_y}$	f_y	235	275	355	420	460
	ε	1,00	0,92	0,81	0,75	0,71

*) $\psi \leq -1$ applies where either the compression stress $\sigma \leq f_y$ or the tensile strain $\varepsilon_y > f_y/E$

Figure 2.12: Current slenderness limits for internal elements (BS EN 1993-1-1, 2014).

The rotation capacity (R) relevant to Class 1 sections can be viewed as the exploitation level of the inelastic range of the material stress-strain curve under monotonic static loading and is thus closely related to the material ductility. This is particularly important in plastic and seismic design, where the structural system should carry severe loads that induce inelastic deformation and the structure should have sufficient plastic deformation capacity in order to form a collapse mechanism. According to Eurocode, the rotation capacity of a 3-point beam can be estimated by Equation (2.4).

$$R = \frac{\theta_u}{\theta_{pl}} - 1 \tag{2.4}$$

where θ_{pl} is defined as the elastic part of the total rotation at mid-span when M_{pl} is attained on the ascending branch, whilst θ_u is the total rotation at mid-span when the moment-rotation curve falls back below M_{pl}. The definition of R is also illustrated in Figure 2.13. The horizontal axis should be substituted with the respective curvature values (κ) in case of a 4-point beam. Minimum rotation capacity equal to 3 is required by Sedlacek and Feldmann (1995) for the use of Class 1 sections in plastic design (see Appendix A). As previously mentioned, no specific guidelines for the use of HSS in plastic design are currently provided by EN 1993-1-12 (2007), despite the existence of Class 1 limit.

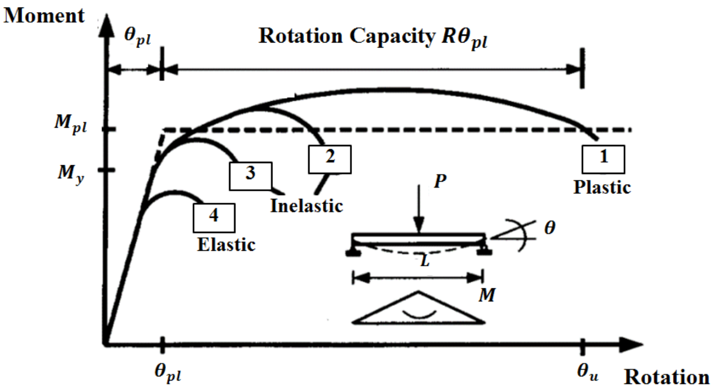

Figure 2.13: General flexural behaviour of a beam [adapted from Ricles et al. (1998)].

In order to account for the loss of effectiveness due to local buckling occurring in Class 4 sections, the traditional method of effective width equations is recommended by BS EN 1993-1-1 (2014). This method is adopted by most structural design codes. In the post-buckling range of a plate element, the stresses are non-uniformly distributed, as illustrated in Figure 2.14(a). To account for this phenomenon, the effective width method considers an equivalent uniform stress distribution on an “effective width” of the plate, as shown in Figure 2.14(b). In Figure 2.14(c), the Winter curve (Winter, 1947), adopted by Eurocode for the evaluation of the reduction ρ of the plate width as a function of the plate slenderness $\bar{\lambda}_p$, is depicted. It should be noted that only the local buckling of internal elements is discussed herein, as the thesis focuses on the response of square and rectangular hollow sections.

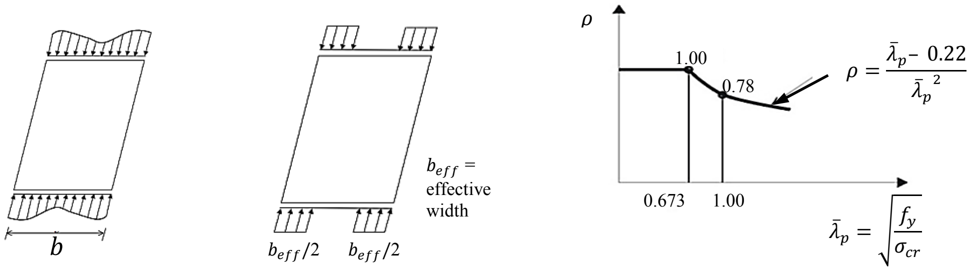

a) actual stress distribution

b) assumed stress distribution

c) Winter curve

Figure 2.14: Plate buckling - Winter curve (EN 1993-1-5, 2006).

Equation (2.5) is used for the estimation of the effective width (b_{eff}) of internal elements in compression with cross-section slenderness $c/t\varepsilon$>42, where ε is equal to $\sqrt{\frac{235}{f_y}}$. The reduction factor ρ is based on the Winter curve and is given by Equations (2.6)-(2.7), where $\bar{\lambda}_p$ the plate slenderness, calculated from Equation (2.8) (EN 1993-1-5, 2006). The applied stress ratio (ψ) of the axial load to the bending moment can belong to one of the three cases of Figure 2.15 for internal elements.

$$b_{eff} = \rho\, b \tag{2.5}$$

$$\rho = 1.00\ for\ \bar{\lambda}_p \leq 0.673 \tag{2.6}$$

$$\rho = \frac{\bar{\lambda}_p - 0.055(3+\psi)}{\bar{\lambda}_p^{\ 2}}\ for\ \bar{\lambda}_p > 0.673 \tag{2.7}$$

$$\bar{\lambda}_p = \frac{c}{28.4\sqrt{k_c}t\varepsilon} \tag{2.8}$$

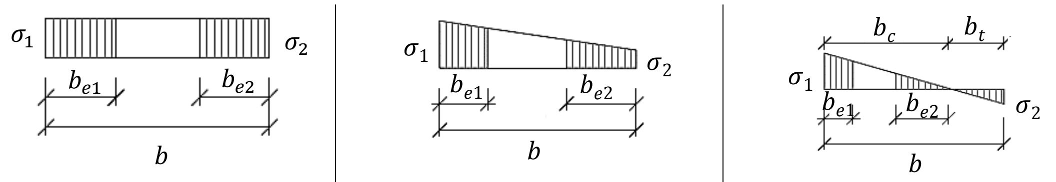

ψ= 1 (pure compression) b_{e1}=b_{e2}=0.5b_{eff}

1>ψ≥0 (combined loading) b_{e1}=$\frac{2}{5-\psi}b_{eff}$ b_{e2}=b_{eff}-b_{e1}

ψ<0 (combined loading) b_{e1}=0.4b_{eff} b_{e2}=0.6b_{eff}

Figure 2.15: Effective width for internal elements (EN 1993-1-5, 2006).

The buckling coefficient k_c in Equation (2.8) depends on the plate's support conditions and the applied stress ratio. It is worth noting that Eurocode suggests a value equal to 4 for the buckling coefficient k_c for internal elements in compression, assuming simply-supported edges for the plates of both square and rectangular hollow sections. Even though this would be true for a uniformly compressed square hollow section, for increasing cross-section aspect ratio, the slender webs are more effectively restrained against local buckling by the shorter (hence stockier) flanges. The disregard of the interaction effects emerging among the constituent plate elements of a cross-section is a significant drawback of the traditional method of the effective width equations and it will be further discussed in Chapter 4.

Having evaluated the effective width of each constituent element of a cross-section, the effective cross-sectional area (A_{eff}) and the effective modulus (W_{eff}) can be determined.

For cross-sections subjected to compression, it should be checked that the compressive resistance (Af_y/γ_{M0} for Classes 1, 2 and 3 sections and $A_{eff}f_y/\gamma_{M0}$ for Class 4 sections) is greater than or equal to the design axial compressive load N_{Ed}. Similarly, for cross-sections subjected to bending, it should be verified that the bending resistance ($W_{pl,y/z,Rd} f_y/\gamma_{M0}$ for Classes 1 and 2 sections, $W_{el,y/z,Rd} f_y/\gamma_{M0}$ for Class 3 sections and $W_{eff,y/z,Rd} f_y/\gamma_{M0}$ for Class 4 sections) is greater than or equal to the design bending load $M_{y/z,Ed}$. The subscripts y and z denote the major and minor axis, respectively. Eurocode recommended value for the partial safety factor for cross-sections (γ_{M0}) is 1.0.

For cross-sections subjected to combined bending and compression, Clause 6.2.9.1(5) in BS EN 1993-1-1 (2014) is applicable. For Classes 1 and 2 cross-sections, the resistance of square and rectangular hollow sections is determined from Equations (2.9)-(2.10) for major axis and minor axis bending respectively.

$$M_{N,y,Rd} = M_{pl,y,Rd}(1-n)/(1-0.5a_w) \text{ but } M_{N,y,Rd} \leq M_{pl,y,Rd} \tag{2.9}$$

$$M_{N,z,Rd} = M_{pl,z,Rd}(1-n)/(1-0.5a_f) \text{ but } M_{N,z,Rd} \leq M_{pl,z,Rd} \tag{2.10}$$

where $n = N_{Ed}/N_{pl,Rd}$, N_{Ed} is the design axial compressive load, $N_{pl,Rd}$ is the cross-section yield load (Af_y), $M_{N,Rd}$ is the reduced cross-section moment resistance to allow for the presence of axial load, $M_{pl,Rd}$ is the cross-section plastic moment capacity ($W_{pl} f_y$), $a_w = (A-2bt_w)/A$ but $a_w \leq 0.5$ and $a_f = (A-2bt_f)/A$ but $a_f \leq 0.5$.

For Class 3 cross-sections, a linear N-M interaction expression is specified in BS EN 1993-1-1 (2014), as given in Equation (2.11).

$$\frac{N_{Ed}}{N_{Rd}/\gamma_{M0}} + \frac{M_{y,Ed}}{M_{el,y,Rd}/\gamma_{M0}} + \frac{M_{z,Ed}}{M_{el,z,Rd}/\gamma_{M0}} \leq 1 \tag{2.11}$$

where $M_{el,Rd}$ is the elastic moment capacity ($W_{el} f_y$) of the cross-section and γ_{M0} partial factor for the resistance of cross-sections.

For Class 4 cross-sections under combined axial load and bending, BS EN 1993-1-1 (2014) provides again a linear N-M interaction, as given in Equation (2.12).

$$\frac{N_{Ed}}{A_{eff}f_y/\gamma_{M0}}+\frac{M_{y,Ed}+N_{Ed}e_{Ny}}{W_{eff,y,min}f_y/\gamma_{M0}}+\frac{M_{z,Ed}+N_{Ed}e_{Nz}}{W_{eff,z,min}f_y/\gamma_{M0}}\leq 1 \tag{2.12}$$

where A_{eff} the effective area of the cross-section when subjected to uniform compression, $W_{eff,min}$ is the effective section modulus when subjected only to bending about the relevant axis, and e_N is the shift in the relevant neutral axis of the effective cross-section under pure compression (which is zero for doubly symmetric sections, as the ones studied).

Having described the Eurocode specifications for the design of steel cross-sections, another design method for the treatment of local buckling, namely the continuous strength method (CSM), the applicability of which to HSS is assessed in the following chapters, is also briefly presented hereafter. As already mentioned, Eurocode assumes elastic-perfectly plastic material response for the cross-section classification. Aiming to effectively and rationally account for the pronounced strain-hardening properties of stainless steel sections, CSM was developed by Gardner (2002). Later the method was also extended to cover carbon steel and aluminium alloys (Gardner and Ashraf, 2006; Su et al., 2014; Foster et al., 2015).

CSM is based on an empirical relationship between the cross-section slenderness $\bar{\lambda}_{cs}$ and the strain at failure due to local buckling ε_{csm}, defining the so-called base curve. The method assumes an elastic-linear hardening material response with strain-hardening modulus E_{sh}, thus allowing stresses in excess of the yield stress f_y to be taken into account, when designing very stocky cross-sections. It is only applicable to sections with cross-section slenderness $\bar{\lambda}_{cs}\leq 0.68$, which can reach stresses beyond their yield stress.

The cross-section slenderness $\bar{\lambda}_{cs}$ is defined from Equation (2.13).

$$\bar{\lambda}_{cs}=\sqrt{f_y/f_{cr}} \tag{2.13}$$

where f_{cr} is the elastic critical buckling stress of the cross-section and f_y the yield stress.

On the basis of the observed response, different relationships have been proposed for the base curve, the latest one defined by Equation (2.14). The base curve and the assumed material response for the CSM are shown in Figure 2.16.

$$\frac{\varepsilon_{csm}}{\varepsilon_y} = \frac{0.25}{\bar{\lambda}_{cs}^{\,3.6}} \; but \; \frac{\varepsilon_{csm}}{\varepsilon_y} < 15 \tag{2.14}$$

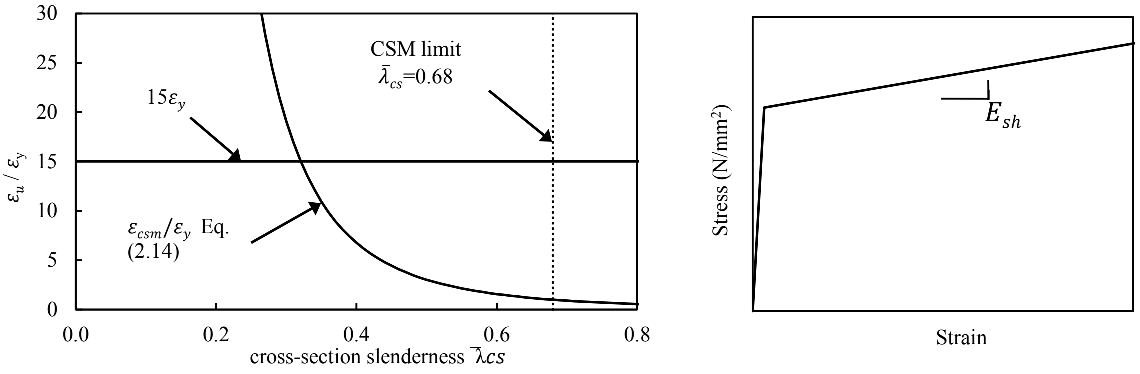

a) CSM base curve b) CSM material response

Figure 2.16: The continuous strength method.

Once ε_{csm} is computed and a value for the material hardening modulus E_{sh} is assumed, then the cross-section compression resistance N_{csm} can be evaluated from Equation (2.15).

$$N_{csm} = Af_{csm} = A(f_y + E_{sh}\left(\varepsilon_{csm} - \varepsilon_y\right)) \tag{2.15}$$

where A the cross-sectional area and f_{csm} the CSM failure stress. In addition to the compression resistance, relationships to evaluate the bending and combined loading cross-sectional resistance have also been proposed (Liew and Gardner, 2015). The method does not limit the maximum attainable stress of a cross-section to the yield stress, but allows for the strain-hardening exhibited by stocky sections, which fail at high inelastic strains. In order to obtain accurate strength predictions over the full slenderness range, a rational exploitation of the strain-hardening, exhibited for sections in the stocky slenderness region is deemed necessary and the applicability of the CSM is assessed on Chapter 4.

Finally, it should be noted that throughout this thesis the elastic critical buckling stress f_{cr} of the cross-section, as opposed to the critical stress of a single element, is utilised both within the CSM framework and in other novel design approaches. This was obtained from the expressions developed by Seif and Schafer (2010). After executing finite strip analysis on a large number of sections, Seif and Schafer (2010) proposed Equations (2.16)-(2.18) for the elastic critical buckling stress of rectangular hollow sections, which provide a good fit to the finite strip analysis results.

$$f_{cr,axial\ compression} = k_b \frac{\pi^2 E}{12\,(1-v^2)} (\frac{t}{b})^2, \ k_b = 4/(h/b)^{1.7} \tag{2.16}$$

$$f_{cr,major\ axis} = k_h \frac{\pi^2 E}{12\,(1-v^2)} (\frac{t}{h})^2, \quad 1/k_h = \frac{0.19}{(h/b)^{1.7} + 0.03} \tag{2.17}$$

$$f_{cr,minor\ axis} = k_b \frac{\pi^2 E}{12\,(1-v^2)} (\frac{t}{b})^2, \quad k_b = 5.5/(h/b)^2 \tag{2.18}$$

where E is the Young's modulus, v the Poisson's ratio, h and b the centreline depth and width of the section, t the thickness of the plate material and k_b and k_h the local buckling coefficients accounting for both boundary and loading conditions and including plate element interaction effects.

2.3.3. Codified treatment of member buckling

Moving from cross-sections to members and from local to member buckling, Part 6.3 of BS EN 1993-1-1 (2014) provides recommendations for the estimation of steel members' capacity, in order to prevent from the buckling mode, illustrating in Figure 2.17.

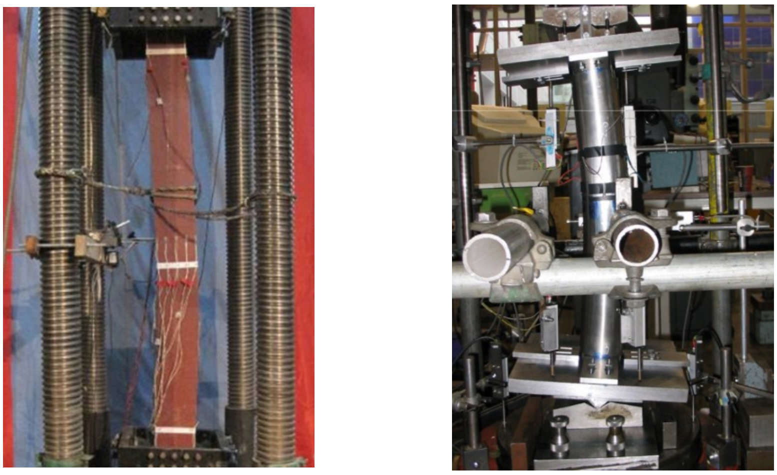

Figure 2.17: Member buckling (Ban et al., 2012; Theofanous et al., 2009).

As in most structural design codes, the strength of compression members is determined as the product of the section capacity and a buckling reduction factor, accounting for the decrease in strength related to the overall stability. According to Eurocode, the buckling resistance of members under uniform compression is given by Equations (2.19)-(2.20) for Class 1-3 and Class 4 sections respectively.

$$N_{b,Rd} = \chi\, A\, f_y / \gamma_{M1} \tag{2.19}$$

$$N_{b,Rd} = \chi\, A_{eff}\, f_y / \gamma_{M1} \tag{2.20}$$

where χ the reduction factor for the relevant buckling mode, computed from Equations (2.21)-(2.24) and γ_{M1} the partial factor for the resistance of members, equal to 1.

$$\chi = \frac{1}{\Phi + \sqrt{\Phi^2 - \bar{\lambda}^2}} \tag{2.21}$$

$$\Phi = 0.5\,\left(1 + a\left(\bar{\lambda} - 0.2\right) + \bar{\lambda}^2\right) \tag{2.22}$$

$$\bar{\lambda} = \sqrt{\frac{A\, f_y}{N_{cr}}} \quad \text{for Class 1-3} \tag{2.23}$$

$$\bar{\lambda} = \sqrt{\frac{A_{eff}\, f_y}{N_{cr}}} \quad \text{for Class 4} \tag{2.24}$$

N_{cr} is the elastic critical force for the relevant buckling mode depending on the buckling length in the considered buckling plane and α is an imperfection factor allowing for the effects of the geometric imperfections and residual stresses which vary for cross-sections of different shapes, material properties and manufacturing process. The imperfection factors result in the five Eurocode buckling curves of Figure 2.18. For high strength steel hot-finished hollow sections, the buckling curve a_0 (a_0=0.13) is recommended (EN 1993-1-12, 2007). As will be explained in Section 2.4, this choice is related with the less detrimental influence of the residual stresses on the strength of HSS columns.

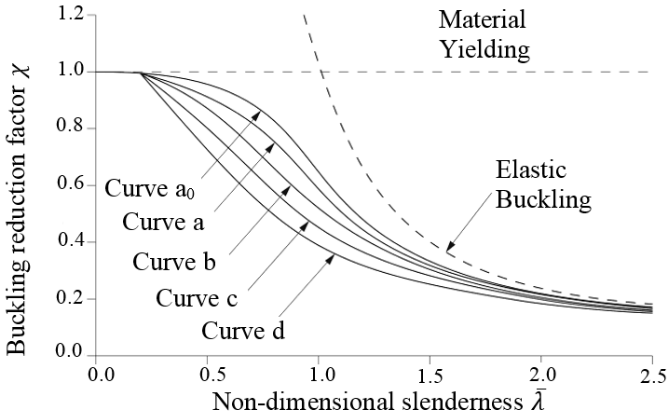

Figure 2.18: Eurocode buckling curves (BS EN 1993-1-1, 2014).

Note that the design codes also provide guidance for the buckling resistance of members under bending, combined loading and lateral torsional buckling but these are beyond the scope of the present thesis.

2.4. Research on the structural performance of HSS

Numerous experimental and numerical programmes have been carried out in order to evaluate the structural response of HSS cross-sections, individual members and structures and estimate the suitability of design specifications to HSS. Subsection 2.4.1 critically presents and summarises literature on the compressive response of HSS. Subsection 2.4.2 places focus upon flexural behaviour, whilst Subsection 2.4.3 covers other structural issues.

2.4.1. High strength steel members in compression

A series of stub column tests have been carried out in order to investigate the cross-sectional response of HSS. The reported work is summarised in Table 2.4, where the number of the experiments performed together with the software applied for FE analysis and the parameters investigated numerically, are shown.

Table 2.4: HSS in compression - short columns.

Name	Authors	Year	Section	Number of experiments	Software for FEA (parameters studied)	Nominal Strength
Experimental investigation of the buckling of plates with residual stresses	F. Nishino, Y. Ueda and L. Tall	1966	Welded box	4	N/A	f_y=690 N/mm^2 (ASTM A514)
Local and overall buckling of welded box columns	T. Usami and Y. Fukumoto	1982	Welded box and cruciform	24	N/A	f_y=690 N/mm^2
Plate slenderness limits for high strength steel sections	K.J.R. Rasmussen and G.J. Hancock	1992	Welded box, cruciform and I-section	6+6+6	N/A	f_y=690 N/mm^2 (BISALLOY 80)
Tests of high strength steel columns	K.J.R. Rasmussen and G.J. Hancock	1995	Welded box and I-section	6+5	N/A	f_y=690 N/mm^2 (BISALLOY 80)
Local buckling of high strength steel W-shaped sections	B. Yuan	1997	Welded H-section	6	N/A	f_y= 480 N/mm^2 f_y= 700 N/mm^2
Local buckling in the stub columns fabricated with HSA800 of high performance steel	J.H. Yoo , J.W. Kim, J.G. Yang, J.W. Kang and M.J. Lee	2013	Welded box and I-section	5+10	Ansys (width-to-thickness ratios)	f_u=800 N/mm^2 (HSA800)
Experimental and numerical investigations of high strength steel welded H-section columns	F. Zhou, L. Tong, and Y. Chen	2013	Welded H-section	2	Abaqus (cross-section geometry)	f_y=460 N/mm^2
Local buckling of 460 MPa high strength steel welded section stub columns under axial compression	G. Shi, W. Zhou, Y. Bai and C. Lin	2014	Welded box and I-section	4+9	Ansys (width-to-thickness ratios)	f_y=460 N/mm^2 (Q460)
Strength and residual stress evaluation of stub columns fabricated from 800 MPa high-strength steel	D.K. Kim , C.H. Lee, K.H. Han, J.H. Kim, S.E. Lee and H.B. Sim	2014	Welded box, cruciform and I-section	1+3+3	N/A	f_u=800 N/mm^2 (HSA800)
Local buckling behavior of welded stub columns with normal and high strength steels	G. Shi, K. Xu, H. Ban and C. Lin	2016	Welded box and I-section	N/A	Ansys (width-to-thickness ratios)	f_y=460 N/mm^2 f_y=690 N/mm^2 f_y=960 N/mm^2

Early HSS stub column tests were conducted by Nishino et al. (1966) who examined the buckling behaviour of welded sections comprising ASTM A514 plates and found considerable post-buckling strength for the plates buckled in the elastic range. Two decades later, the local buckling behaviour of HSS cross-sections with large width-to-thickness ratios was studied by Usami and Fukomoto (1982).

Following, the applicability of design specifications to HSS sections was studied by Rasmussen and Hancock (1992, 1995), who tested I-sections, box and cruciform BISALLOY 80 cross-sections to failure, concluding that the yield slenderness limits for mild steel should generally apply to HSS. During these studies, it was also found that stocky HSS plates with lower strain-hardening properties display lower compressive capacity than their ordinary steel counterparts, given that the plate has achieved strains within the strain-hardening range at its ultimate load. For plates of intermediate slenderness, the attained load appeared dependent to the interaction between the inelastic local buckling and the effect of the geometric imperfections and residual stresses. In addition, it was found that for internal elements (i.e. plates simply supported along both longitudinal edges, e.g. the flanges of square and rectangular hollow sections), HSS and ordinary steels displayed comparable local buckling resistance, whilst slender HSS outstand elements (i.e. plate elements with one longitudinal edge simply supported and the other free, e.g. the flanges of I-sections) exhibited superior local buckling performance to those of ordinary carbon steels. The underpinning reason of this is the fact that the residual stresses are independent of the yield stress level and the residual stress over yield strength ratio is more critical than the magnitude of the compressive stresses themselves, thus resulting in higher non-dimensional strength for HSS plates than their mild steel counterparts. This conclusion has been reconfirmed in more recent HSS studies (Wang et al., 2012a, 2012b).

Yuan (1997) examined the local buckling behaviour of HSS wide flange beam sections and assessed the applicability of codified limits to HSS, finding them inappropriate for 700Q steel. The local buckling response of welded H-sections and square hollow sections built up from high performance steel HSA800 was experimentally and numerically investigated by Yoo et al. (2013), whilst a total of 10 additional concentric stub column tests on cross-sections made of the same material were executed by Kim et al. (2014) in order to assess the applicability of local (i.e. Korean) stability criteria.

Two more experimental and numerical programmes on stub columns with nominal yield strength 460 N/mm^2 were executed in order to evaluate the applicability of various international design codes to HSS (Zhou et al., 2013b; Shi et al., 2014b). The design provisions of European, American and Chinese specifications on yield slenderness limits were found too conservative for HSS welded H-sections (Zhou et al., 2013b), whereas the design methods underestimated the ultimate strength of the flanges of I-sections, particularly for cases with relatively high width-to-thickness ratios. Complementing their previous studies, Shi et al. (2016) recently performed an extensive numerical study to examine the ultimate behaviour of normal and high strength steel welded sections, confirming the need for modification of the design methods for HSS.

Research carried out to evaluate the strength of long columns is summarised in Table 2.5.

Table 2.5: HSS in compression - long columns.

Name	Authors	Year	Cross-sections	Number of experiments	Software for FEA (parameters studied)	Nominal Strength
Local and overall buckling of welded box columns	T. Usami and Y. Fukumoto	1982	Welded box and cruciform	24	N/A	f_y=690 N/mm^2
Tests of high strength steel columns	K.J.R. Rasmussen and G.J. Hancock	1995	Welded box and I-section	6 + 5	N/A	f_y=690 N/mm^2 (BISALLOY 80)
Experimental and numerical study on the behavior of axially strength steel columns with H-section	Y.B. Wang, G.Q. Li, S.W. Chen and F.F. Sun	2012	Welded H-section	6	Ansys (initial geometric imperfections, residual stresses)	f_y=460 N/mm^2 (Q460)
Tests and numerical study of ultra-high strength steel columns with end restraints	G. Shi, H. Ban and F.S.K. Bijlaard	2012	Welded I-section	8	Ansys (validation of the FE models)	f_y=690 N/mm^2 f_y=960 N/mm^2
Overall buckling behavior of 460MPa high strength steel columns: Experimental investigation and design method	H. Ban, G. Shi, Y. Shi and Y. Wang	2012	Welded box and I-section	5+6	Ansys (cross-section sizes, column slenderness)	f_y=460 N/mm^2
Experimental and numerical investigations of high strength steel welded H-section columns	F. Zhou, L. Tong and Y. Chen	2013	Welded H-section	6	Ansys (column slenderness)	f_y=460 N/mm^2
Experimental investigation of the overall buckling behaviour of 960MPa high strength steel columns	H. Ban, G. Shi, Y. Shi and M.A. Bradford	2013	Welded box and I-section	3+3	Ansys (cross-section sizes, column slenderness)	f_y=960 N/mm^2
Experimental and numerical study on the behavior of axially compressed high strength steel box-columns	Y.B. Wang, G.Q. Li, S.W. Chen and F.F. Sun	2014	Welded box section	6	Ansys (initial geometric imperfections, residual stresses)	f_y=460 N/mm^2 (Q460)

Early long column tests on high strength steel were executed by Usami and Fukomoto (1982). Rasmussen and Hancock (1995) performed tests on pin-ended long columns employing welded box and I- HSS sections in order to assess the design column curves. It was found that HSS columns have higher strength than their normal strength steel counterparts when compared on a non-dimensional basis. This owes to the less detrimental influence of residual stresses on the strength of HSS columns and is expected to result in higher buckling reduction factors χ for the design of HSS columns compared to that of mild steel, of similar non-dimensional slenderness; hence the use of a higher buckling curve for HSS columns is warranted.

The sensitivity of Q460 columns to geometric imperfections was examined by Wang et al. (2012c, 2014) who executed tests and numerical studies on H-section and box section columns. It was found that the currently adopted design curves underestimate the ultimate bearing capacity of HSS welded box columns and I-sections with buckling about the weak axis. In order to take into account the improved non-dimensional buckling strength of high strength steel columns, a new design column curve was proposed by Ban et al. (2012). The suitability of column curves specified in various international codes was also evaluated by Zhou et al. (2013b), finding that best design predictions were provided by Eurocode.

Research on ultra-high strength steel columns fabricated from S690 and S960 resulted in no significant difference between the buckling strengths of the two studied steel grades (Shi et al., 2012). It was concluded that the buckling behavior of S690 columns is similar to that of columns fabricated from ultra-high strength steels. Going a step forward, a year later Ban et al. (2013) proposed a new higher column curve, more adequate for S960 columns.

Further to the research studies presented in Table 2.4-Table 2.5 it is worth pointing out that extensive experimental and numerical work has focused on the performance of high strength steel cold-formed cross-sections and members. An Australian research project entitled “Compression Stability of High Strength Steel Sections with Low Strain-Hardening” investigated thoroughly the compressive response of cold-formed structures employing various G550 thin-walled sections (Yang and Hancock, 2004; Yang et al., 2002). Recently, the behaviour of S650 circular and polygonal cold-formed cross-sections and the influence of key parameters on the ultimate response was experimentally and numerically evaluated by Tran et al. (2016a, 2016b).

2.4.2. High strength steel members in bending

A summary of the collated research work on the flexural response of HSS is provided in Table 2.6.

Table 2.6: HSS in bending.

Name	Authors	Year	Cross-sections	Number of experiments	Software for FEA (parameters studied)	Nominal Strength
Plastic bending of A514 Beams	J.F. McDermott	1969	Welded I-section	7	N/A	f_y=690 N/mm^2 (ASTM A514)
Role of strain-hardening in structural performance	B. Kato	1990	H-section	N/A	N/A	f_y=690 N/mm^2 (ASTM A514)
Slenderness limit of class 3 I cross-sections made of high strength steel	D. Beg and L. Hladnik	1996	Welded I-section	10	Finas (flange slenderness)	f_y=700 N/mm^2 (NIONICRAL 70)
High-strength steel: implications of material and geometric characteristics on inelastic flexural behavior	J.M. Ricles, R. Sause and P.S. Green	1998	Welded H-section	12	Abaqus (flange and web slenderness)	f_y=552 N/mm^2 (HSLA-80)
Strength and ductility of HPS flexural members	P.S. Green, R. Sause and J.M. Ricles	2002	Welded I-section	12	Abaqus (calibration of the FE model)	f_y=552 N/mm^2 (HSLA-80)
Strength and ductility of HPS 100W I-Girders in negative flexure	R. Sause and L.A. Fahnestock	2001	Welded I-section	2	N/A	f_y=690 N/mm^2 (HPS-100W)
Flexural strength and rotation capacity of I-shaped beams fabricated from 800-MPa steel	C. Lee, K. Han, C. Uang, D. Kim, C. Park and J. Kim	2013	Welded I-section	21	N/A	f_u=800 N/mm^2 (HSB800, HSA800)
The rotational capacity of beams made of high-strength steel	N. Schillo and M. Feldmann	2016	Welded I-section	12	Abaqus (cross-section slenderness)	f_y=690, 700 N/mm^2 (S690, S700)

Early research exploring the inelastic performance of A514 I-section beams under both uniform moment and moment gradient was reported by McDermott (1969). For cross-sections with small flange slenderness, the delay in the onset of local buckling offered by the stocky flanges allowed for large rotation capacity values. Note that similar observations regarding the effect of flange and web interaction on the local buckling response were extensively made for carbon steel cross-sections (Kemp, 1986; Kato, 1989; Kuhlmann, 1989). The rotation capacity of a HSS flexural member and the influence of material's strain-hardening has also been meticulously examined by Kato (1990), who recommended evaluating the deformation capacity in terms of the complementary energy of the base material. Recently, the inherent difficulty of I-shaped HSS sections to achieve high rotation capacity values was demonstrated by Lee et al. (2012).

To better comprehend HSS's flexural performance, Ricles et al. (1998) summarised the key characteristics affecting the flexural response of HSLA-80 members, concluding that the moment gradient and monotonic loading allow for larger rotation capacity values to be achieved compared to uniform moment and cyclic loading. Findings regarding the effect of the material properties, the loading type and the local slenderness on the rotation capacity were also reported in subsequent publications (Green et al., 2002).

The results of flexural tests/FE analysis on HSS members facilitate the estimation of the applicability of design methods to HSS. On this basis, Beg and Hladnik (1996) derived a new slenderness limit between slender and semi-compact I-sections, taking into account the interaction between flange and web local buckling, which is usually ignored in most design codes. In the same direction, Sause and Fahnestock (2001) examined I-section girders made from HPS-100W and found that the flange and web slenderness limits of the American bridge design specifications for mild steel are applicable to HSS. Based on the experimental and numerical results of S690 and S700 beams, Eurocode specifications for higher steel grades were assessed by Schillo and Feldmann (2016).

Overall, a careful observation of Subsection 2.4.1 and 2.4.2 shows that past experimental and numerical studies on the compressive and flexural response of HSS structures primarily focused on welded and cold-formed sections, with strong emphasis on I-sections, leaving the structural behaviour of hot-finished square and rectangular hollow sections relatively unverified. The fact that focus has been placed on cold-formed and welded HSS sections is mainly related to the residual stresses that could be significant in those cases, affecting the ultimate performance. However, as mentioned earlier and has been demonstrated in past studies (Rasmussen and Hancock, 1995; Wang et al., 2012a, 2012b), the ultimate structural performance is related to the ratio of the residual stresses to the yield strength and not the magnitude of the residual stresses themselves, which appear similar for mild and high strength steels. Therefore, the influence of the residual stresses is expected to decrease for increasing steel grades, while the effect of the reduced strain-hardening and ductility of higher steel grades remains. The latter means that the effect of the material response of HSS needs to be considered also for hot-finished sections, where the final processing is performed using high temperature thermal treatment, resulting in lower residual stresses. Hence, the investigation of the structural performance of HSS hot-finished hollow sections is warranted.

2.4.3. Other research on the structural performance of HSS

In addition to the compressive and flexural behaviour of HSS, the fields of seismic performance, fatigue life and serviceability of HSS structures have attracted the attention of researchers and are discussed herein.

The first field regards the seismic performance of HSS structures. Due to inferior material ductility, design codes do not provide guidance for the use of HSS in seismic design. Early tests of HSS beams subjected to cyclic loading have demonstrated that increasing yield-to-tensile ratio decreases the energy dissipation (Kato and Kuwamura, 1989). In order to employ HSS members in seismic areas, Dubina et al. (2014) suggested an optimised solution for seismic frames employing mild steel for dissipative members and HSS for members designed to remain in the elastic range. Recent tests on frames comprising tubular HSS columns confirmed the possibility to design HSS structures under earthquake loading, provided that high strength steel is employed for non-dissipative elements (Ferrario et al., 2016).

Another topic stimulating the research interest concerns the fatigue life of HSS structures. Given that high stress variations appear in cyclically loaded high strength steel structures, enhanced fabrication quality and post-weld treatments are required in order to avoid large stress concentrations. Miki et al. (2002) investigated the relationship between the steel grade and fatigue strength of three joints and proposed a newly developed weld material to improve the fatigue crack performance of HSS, whereas Pijpers (2010) examined the strength of HSS welded connections of truss girders under static and fatigue loading, stating that the optimal use of high strength steels in fatigue loaded joints necessitates high fabrication quality and avoiding large stress concentrations in connections.

The third research topic is related to the slender nature of HSS structures and its effect on the instability phenomena and serviceability limit state requirements. Even though the yield stress increases together with the steel grade, the Young's modulus remains unchanged, rendering buckling phenomena and second order effects critical for HSS's structural design. On this basis, a research project examining the economic efficiency of HSS found that it is more beneficial to apply higher steel grades to stocky columns or other members with small load eccentricities and to non-sway frames, where strength and not stiffness governs the design (Long et al., 2011). Going a step forward, techniques to mitigate the aforementioned barriers could be applied in order to maximise the economic efficiency of HSS and expand its application even in structures where stiffness is the principal design concern. Inducing forces opposite in nature from those caused at a structural member by external loading, could be used to control serviceability limits. This can be achieved with the application of prestress and has already been successfully implemented in carbon steel structures (S-Squared, 2017). The possibility of applying prestress in HSS structures is investigated in Chapter 7, whilst relevant literature is provided in the following section.

2.5. Prestressed steel structures

The present section sheds light to the application of prestress in steel structures which will be extensively studied in Chapter 7. Subsection 2.5.1 gives an overview of prestressed structures, whereas their structural performance and the applications to date are presented in Subsection 2.5.2 and Subsection 2.5.3 respectively.

2.5.1. Prestressed structures

The idea of prestressing was introduced many years ago in the construction of ships, wooden barrels and chariot wheels in form of heating steel strips prior to application in order to keep parts together on cooling. Later, prestress was applied in several structures and especially in concrete buildings in order to reduce the deadweight, improve the structural performance, limit deflections and cracking and potentially allow for cost savings. The same principle applies to steel structures, where cables of very high strength are prestressed, so that under service loads, the prestress balances the induced stresses.

2.5.2. Research on the structural performance of prestressed steel structures

In order to better understand the structural behaviour of prestressed steel structures, the response of prestressed flexural members, trusses, arched frames and cable-stayed columns has been investigated. The enhanced performance of prestressed structures is commonly studied together with the potential economies owing to prestess.

The weight and cost savings emerging from the application of prestress on truss girders were firstly reported by Magnel (1950). Following, a report on prestressed flexural members was published (Subcommittee 3 on Prestressed Steel of Joint ASCE-AASHO Committee on Steel Flexural, 1968). Belenya (1977) developed a book on the load-bearing capacity of prestressed metal structures, whereas Troitsky (1990) focused on the design of prestressed steel bridges. General principles, analytical design models and applications of long-span post-tensioned structures, from individual members to complex systems, were described by Ellen et al. (2012).

The structural performance of prestressed beams was studied by Bradford (1991), who examined the buckling strength of I-shaped prestressed girders, as well as by Nunziata (2003), who conducted experimental tests and presented simple calculation methods for the design of prestressed beams. Belletti and Gasperi (2010) investigated the flexural response of medium span prestressed girders, focusing on the effect of the prestress level on the overall response.

Research on cable-stayed columns primarily focused on the critical buckling load, the post-buckling response and the interactive buckling behaviour (Saito and Wadee, 2009; Osofero et al., 2012). A design procedure for a cable-stayed column for varying geometry, prestress level and global imperfection was later presented (Wadee et al., 2013). The prestressed stayed column system with a single horizontal cross-arm to restrain column buckling displacement, studied in the aforementioned papers, can be seen in Figure 2.19.

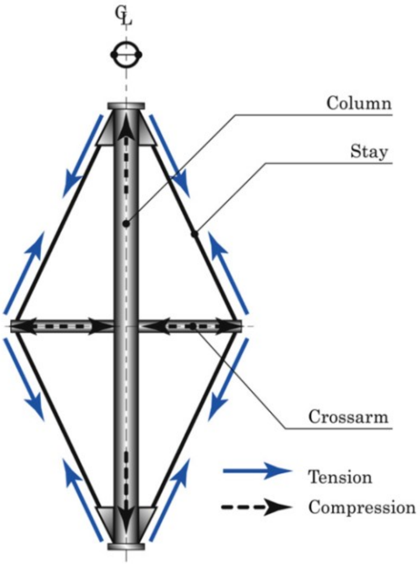

Figure 2.19: Prestressed stayed column system with a single cross-arm (Saito and Wadee, 2009).

The tensile and compressive behaviour of tubular elements, where the prestressed cables are inside the cross-sections (known as cable-in-tube systems), have been thoroughly experimentally, numerically and analytically studied for different prestress levels, including an optimal prestress level (P_{opt}), at which both the cable and the tensile tube yield simultaneously (Gosaye et al., 2014, 2016). For tensile systems prestressed at P_{opt} level, the initial stiffness is maintained until the ultimate load is attained, when both the tube and the cable yield simultaneously, thus minimising the displacements required to achieve the ultimate load. The possibility of adding grouting has also been examined, showing that the combination of steel's high ductility and tensile strength with concrete's compressive resistance can lead to enhanced overall performance. A typical prestressing configuration of the cable-in-tube systems of the previous studies is shown in Figure 2.20.

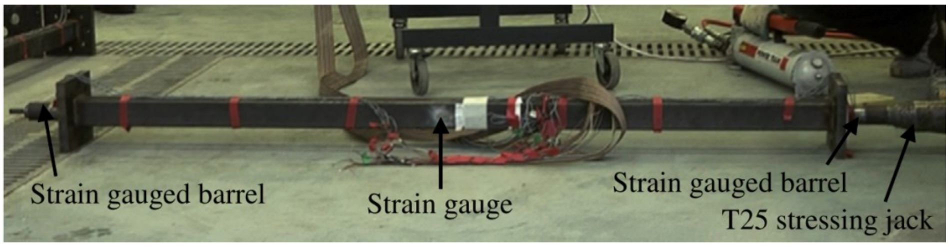

Figure 2.20: The prestressing configuration (Gosaye et al., 2016).

Early research on prestressed trusses focused on the reliability of prestressing technique as a method to strengthen deficient truss bridges (Ayyub and Ibrahim, 1990). The effects of the applied tendon profile, the truss type and the prestress level were investigated through rigorous parametric studies that revealed the efficiency of the post-tensioning method, as a means to enhance the performance of existing truss bridges (Han and Park, 2005). The rehabilitation of angular and tubular truss bridges by post-tensioning method was also studied for Mansard and Pratt trusses (Sawant and Vijapur, 2013).

Further to the enhanced structural performance, the post-tensioning process can also be utilised for the erection of a steel structure, excluding the need of traditional building techniques for cranes and scaffoldings. Arched trusses and frames, domes and space hypar trusses, initially assembled at the ground floor, can reach their final shape formation by the use of prestress. The methodology for assembling arched post-tensioned frames was patented by Ellen (1987).

Research on the structural performance of trusses assembled with the use of prestress dates back to 80s, when a series of arched trusses erected with the tensioning of a cable on their bottom chord were tested at the University of Sydney. The aforementioned pretensioning allows the predetermined gaps on the bottom chord to close, creating the upward curvature of the top chord. The tensioning forces of the cable induce compressive forces at the bottom chord, which is subsequently subjected to tensile stresses after the application of the external vertical loading. The top chord is subjected to negative bending during the uplift of the truss. For very highly curved configurations, the top chord might be deformed in the plastic range and its compressive capacity should be large enough in order to satisfy the axial equilibrium with the tendon force on the bottom chord. A simplified illustration of the erection method is shown in Figure 2.21.

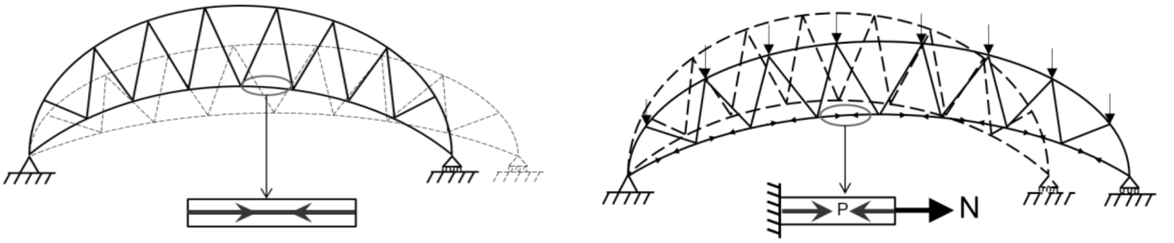

a) Application of prestress

b) Application of external downwards vertical loading

Figure 2.21: Erecting an arched truss with prestress.

The effect of the upward curvature of the top chord formed by prestressing was studied by Hancock et al. (1988), who experimentally and numerically tested two different trusses employing cold-formed square and circular hollow sections, finding a 35% decrease on the compressive strength of the top chord occurring during the erection process. A series of tests on subassemblies of stressed-arch frames under vertical loading and finite element analyses considering geometric nonlinearity and material plasticity were performed to determine the strength of the top chord (Clarke and Hancock, 1991, 1995). A simplified design procedure for the calculation of the top-chord of stressed-arch frames has also been presented (Clarke and Hancock, 1994). In addition, studies on steel domes erected by the post-tensioning method, placing special focus on the strength of the top chord and the joints that should be effectively controlled at the erection process, were also conducted (Schmidt and Li, 1998).

2.5.3. Applications of prestressed steel structures

Both economical and structural benefits can be achieved via the application of prestress for the construction of new steel structures or the consolidation of existing ones.

Examples of prestressed steel applications include the Pierre Mauroy Stadium in Lilly, France where prestress has been applied in its two mean truss girders. This allowed for decreased self-weight and thus a smaller height of the truss, improving the overall visibility of the spectators in the stadium (Muzeau, 2014). In both the Berlin Main Station and the Waterloo Train Station, arched prestrseed trusses were applied as a means of mitigating exceeding deflections. Tensioned cables, capable of controlling premature buckling phenomena, have been used in the cable-stayed structures of Algarve Football Stadium in Portugal and of Manchester City Stadium in UK. Radially arranged prestressed stringer steel cables have been applied in Millenium Dome, an entertainment and recreation building in London (da Silva et al., 2014).

Numerous long span applications like stadia, warehouses and aircraft hangars, where prestress techniques can offer lightweight and efficient structural solutions, have been designed and constructed by S-Squared (2017) company. In these structures, cables are inserted in tubular cross-sections and prestressed prior to the application of the live loads. Two examples, namely a temporary steel structure in Hyde Park in London and the Sydney Olympic Stadium reconfiguration, are illustrated in Figure 2.22. It should be noted that the lightweight, post-tensioned truss in Sydney Olympic Stadium was assembled outside and lifted into position with cranes, allowing the Stadium to remain fully operational during construction. In this case, the S-squared solution of prestressed trusses delivered a high level of sustainability with steel weight reductions of 40%, compared to the conventional solution (S-Squared, 2017).

a) Arched trusses in Hyde Park b) Sydney Olympic Stadium reconfiguration

Figure 2.22: Application of prestressed steel trusses (S-Squared, 2017).

In long span steel structures made from higher steel grades, where serviceability rather than strength could be more critical for the design, prestress could act as an effective way to control deflections, thus maximising the exploitation level of HSS. This will be the focus of Chapter 7.

2.6. Knowledge gap

High strength in steels can be achieved by appropriate heat treatments that improve its material and mechanical properties. HSS applications have demonstrated the potential benefits emerging from the use of HSS in building and bridge applications. In order to maximise these benefits and increase the usage of HSS in the construction industry, appropriate design guidance in line with the observed structural response needs to be available.

After describing the structural response of steel and the codified specifications for local and member buckling, results of experimental and numerical investigations on the compressive and flexural behaviour of HSS to date have been summarised. It was found that strong emphasis has been placed on the response of welded and cold-formed sections.

Aiming to complement the existing literature and provide design recommendations based on the observed response, this thesis reports a series of comprehensive studies on the structural performance of HSS hot-finished square and rectangular hollow sections that were left unexplored from past research.

In addition, in order to overcome potential issues with excessive deflections in long span high strength steel structures, the idea of utilising prestress in HSS applications, both promising and novel, is also investigated. The present research work will hopefully contribute to increasing the use of HSS in design practice.

CHAPTER 3: METHODOLOGY

3.1. Introduction

In order to investigate the structural response of HSS members and structures, the following steps were followed:

- Brief description of the test programme.
- Development of the finite element models.
- Validation of the finite element models.
- Parametric studies.
- Analysis of the results and design recommendations.

The same methodology was adopted for HSS members in compression (Chapter 4), in bending (Chapter 5), in combined bending and compression (Chapter 6), as well as for HSS trusses (Chapter 7).

The current chapter presents in detail the adopted methodology with special focus on the development of the finite element models. Numerical modelling assumptions, including selected element types, material properties and incorporation of initial geometric imperfections, relevant to the analyses of the whole study, are also included in this chapter.

3.2. Brief description of the test programme

A series of static tests performed at the Structures Lab of Imperial College London were used for the validation of the finite elements models developed within the present research study. The tests were part of the HILONG research project with principal aim to investigate the structural behaviour of HSS (HILONG, 2016). The test specimens employed square and rectangular hollow sections in S460 and S690 steel grades. In order to capture the structural performance and obtain the required information during testing, the following instrumentation was applied:

- Strain gauges were attached by a suitable adhesive to specified locations of each specimen in order to measure strain. The strain gauges comprise a metallic foil pattern supported on an insulating flexible backing. When the specimen is deformed, the foil is deformed as well, leading to a change in its electrical resistance that can be measured and subsequently related to the strain through a quantity known as the gauge factor.
- Inclinometers were employed to measure the angles of tilt (i.e. the rotation) of the specimens.
- Linear variable displacement transducers (LVDTs) were used to measure displacements.
- String potentiometers were applied in order to monitor and record vertical deflections.
- Load cells, transducers creating an electrical signal directly proportional to the force, were placed to monitor the applied force during testing.

Hydraulic jacks of various lifting capacities ($2000\ kN \div 3500\ kN$) were used for the application of the load, which was assigned as prescribed incremental displacements or loads. Slow rates were operated in order ensure static tests. A data acquisition system was employed in order to record the required information during each test. Additional equipment including wooden blocks, steel plates and cables needed to be applied in certain cases, as will be explained in the following chapters.

3.3. Development of the finite element models

The finite element (FE) method was used in order to firstly replicate the experimental behaviour and subsequently investigate further the structural performance of HSS through the execution of parametric studies. The current section provides information on the finite element analysis performed within the whole study.

3.3.1. Finite element method

In finite element method (FEM), a model body is divided in smaller pieces which are interconnected at common points (i.e. nodal points), in which adjacent elements share the same degree of freedom. The name of the method originates from the concept of subdividing a continuum which is infinitely divisible, to smaller, simpler finite parts (i.e. finite elements), thus converting a set of differential equations that is valid in continuum mechanics to a set of algebraic equations relevant to the discretised domain of the continuous problem. The finite element method is the numerical procedure that finds approximate solutions to the emerging boundary value problem, and is commonly used in engineering and mathematical physics.

One significant advantage of the finite element method is that it can readily handle complex geometry, loading, materials and boundary conditions for a wide variety of engineering problems from solid mechanics to dynamics and to heat problems, fluids and electrostatic problems. On the other hand, the finite element method provides only approximate solutions and contains inherent errors, which are accumulated during numerical computation, whereas, more importantly, incorrect modelling might lead to significant errors. The errors may relate to: discretisation, solution of finite element equations by iteration, round-off etc. (Bathe, 1982).

Most commercial FEM software packages originated in the 70s (Abaqus, Adina, Ansys, etc.) and have been extensively upgraded and used ever since. In all cases, the finite element analysis (FEA) consists of the three following steps: i) pre-processing, ii) solution and iii) post-processing. In pre-processing, the finite element model is built. The elements and the nodes together form a mesh, which comprise the main data structure. The geometric domain, the element types to be used, the material and geometric properties, the element connectivity and the physical constraints (boundary conditions and loads) need to be defined. In the solution step, the numerical analysis is conducted at a computer. The unknown values of the primary field variable(s) (within the context of this research the nodal displacements and rotations) are evaluated and subsequently used for the computation of additional derived variables (i.e. stresses and strains). In post-processing, the results are extracted and visualised.

The most common FE approach is based on the so-called displacement or stiffness method, in which the nodal displacement are the unknowns of the analyses. In the solution step, the equations are formed on the basis of energy methods and in particular on the principle of virtual work, which states that the stresses, the body forces and the tractions are in equilibrium if and only if the internal virtual work equals the external virtual work for every virtual displacement field, where the term virtual refers to infinitesimal change of the system coordinates. Based on the aforementioned principle, the FEM constructs an equilibrium for a subset of virtual displacements relevant to the discretised body, hence providing an approximate solution to the actual displacement field. In case of elastic engineering problems, the principal algebraic equation $k = uF$, where k stands for the stiffness (property), u for the displacement (behaviour) and F for the force (action) is applied. In order to understand FEM's concept, the simplest problem is a single spring of k stiffness, where the displacement

u induced by a force F can be found through the equation $k = uF$. To solve more complex geometries, the following steps are followed (Bathe, 1982):

- The body is divided into elements and the basic variables (i.e. the displacement vectors $[q]$ and the nodal displacements $[u]$) are defined.
- Given that displacements $[u]$ are only defined in the nodes, an interpolation function $[N]$, known as displacement or shape function, is used in order to interpolate the displacement fields within the elements, leading to $[u] = [N][q]$.
- In order to relate the strains $[\varepsilon]$ with the displacements $[u]$, the strain-displacement matrix $[B]$ is formed in accordance with element kinematics, so that $[\varepsilon] = [B][u]$.
- The relationship between the stresses $[\sigma]$ and the strains $[\varepsilon]$ depends on the respective material model or constitutive law and is given through the stress-strain matrix $[D]$ from the relationship $[\sigma] = [D][\varepsilon]$.
- The stiffness matrix of each element $[K]$ is formed by $\int [B^T][D][B] \; d(vol)$. The global stiffness matrix can be formed, using transformation matrices in order to relate local coordinates with general coordinate systems.
- Applying the principle of virtual displacements, a set of algebraic equations is now created for the nodal displacements, and can be solved via algebraic procedures, such as Gauss elimination or iterative methods.
- Once the nodal displacements are evaluated, stresses and strains can be calculated.

For the execution of the finite element analyses for the nonlinear problems presented herein, the general purpose FE package Abaqus has been used (Hibbitt et al., 2012). Abaqus can determine the solution of a nonlinear problem either by iterating with the implicit method (by Abaqus/Standard), or without iterating by explicitly progressing the kinematic state from the previous increment with the explicit method (by Abaqus/Explicit). The implicit method is commonly applied for static stress analyses, where inertia effects can be neglected. In explicit analysis, a dynamic equilibrium state is solved at the start of each time increment, which should be small enough for the solution to be stable. Explicit method is preferred in dynamic problems, particularly where the response is sought over a small period of time, whilst it can also be applied in highly nonlinear static problems, under the condition that the kinetic energy is only a small proportion of the total energy (i.e. quasi-static problems). The implicit method was adequate and suitable for the scope of the current study and was therefore implemented. A detailed explanation of the applied analysis technique is given in Subsection 3.3.9.

3.3.2. Elements

In finite element modelling, there are a number of different element types that can be used for the development of the models. Each element is characterised by its family from a structural point of view (solid or continuum, shell, beam, truss etc.), the number of nodes (linear or first-order, quadratic or second-order, cubic or third-order), the degrees of freedom, the formulation and the integration scheme (full, reduced).

The most commonly applied element types are illustrated in Figure 3.1. Continuum or solid elements simply model small blocks of material in a component. Shell elements approximate a three-dimensional continuum with a surface model and are used to model structures in which the one dimension (the thickness) is significantly smaller than the other dimensions and the stresses in the thickness direction are negligible. In beam elements, one dimension (the length) is significantly greater than the other two dimensions and the longitudinal stress is most important. Truss elements are rods that can carry only tensile or compressive loads and have no resistance to bending.

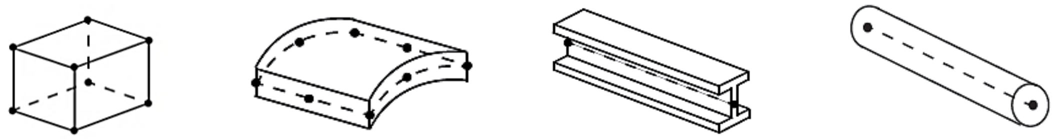

Continuous or solid elements

Shell elements

Beam elements

Truss elements

Figure 3.1: Most commonly applied element types (Hibbitt et al., 2012).

The number of nodes refers to how the nodal degrees of freedom are interpolated over the element domain. The mathematical theory used to define the element’s behaviour corresponds to the element’s formulation. Examples of different element formulations include the plane stress and plane strain formulations for solid elements, applicable for structures of small and large thickness, respectively, the Euler-Bernoulli and Timoshenko beams formulation for slender and shear flexible beams, respectively, the Kirchoff and Mindlin–Reissner formulations for thin and thick shells, respectively etc.

The stiffness of an element is calculated numerically at specific points within the element, which are called integration points. Full and reduced integration schemes correspond to the case that the integration order is the minimum required for exact integration of the strain energy for an undistorted element with linear material properties or an order less than the full integration rule, respectively. Typical cases of full and reduced integration for first-order and second-order interpolation elements are shown in Figure 3.2 (Hibbitt et al., 2012).

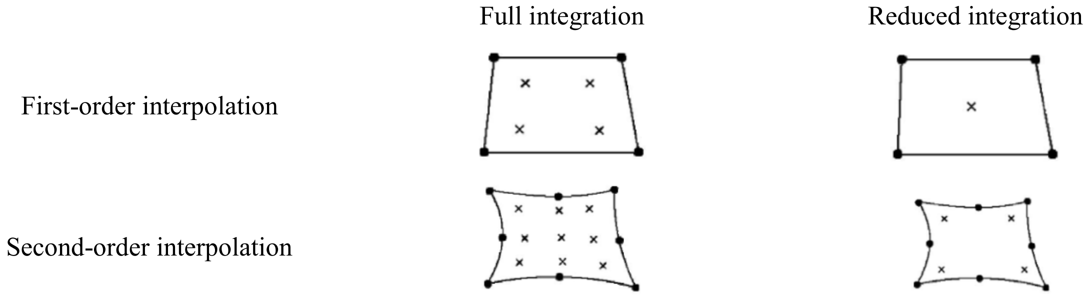

Figure 3.2: Full and reduced integration for first and second order interpolation elements (Hibbitt et al., 2012).

Two problems often encountered in pure bending applications of finite element simulations with first-order elements and which should be carefully considered when modelling with FE, are the so-called shear locking and hourglassing phenomena. The first one concerns elements with full integration and the second one with reduced integration scheme. Modelling bending using linear fully integrated elements allows generating shear instead of bending deformation, as shown in in Figure 3.3(a). In order for the element edges to remain straight, the angle between the deformed edges becomes non-90°, allowing shear strain detection and thus resulting in overly stiff behaviour (called shear locking). In general, mesh refinement, i.e. using more elements to discretise the domain, reduces the shear locking. Modelling bending using linear reduced integrated elements could eliminate shear locking phenomenon; however, a single element through the thickness is not able to detect strain in bending and could lead to zero energy mode (deformation but zero strain, as there is no change in the length), as illustrated in Figure 3.3(b). To overcome this, a minimum of three elements, where each element captures either compressive or tensile axial strains, should be used through the thickness of a structure, if first-order, reduced integration solid elements are used to model bending.

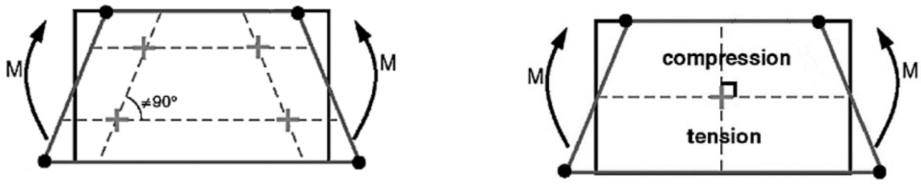

a) Shear locking b) Hourglassing

Figure 3.3: Phenomena on linear elements under pure bending (Hibbitt et al., 2012).

Abaqus offers a wide range of elements. The elements primarily applied within the present research study are the following (Hibbitt et al., 2012):

- S4R: General purpose four-noded shells with reduced integration and finite membrane strains, therefore suitable also for large-strain analysis. To allow for a change in the shell thickness as a function of the membrane strain in large strain analysis, Poisson's ratio should be defined. S4R allow transverse shear deformation, by using either thick shell or Kirchhoff theory, depending on the shell thickness. In cases where transverse shear flexibility is important, second-order interpolation thick shell theory is implemented, whilst Kirchhoff thin shell theory is applied in cases where transverse shear flexibility is negligible and the Kirchhoff constraint must be satisfied accurately i.e. the shell normal remains orthogonal to the shell reference surface. S4R have six degrees of freedom at each node (three translations and three rotations).
- C3D8R: Eight-noded general purpose first-order solid elements with one integration point and hourglass control in order to prevent from uncontrolled mesh distortion. Solid elements have only translational degrees of freedom at each node.
- B31: First-order interpolation 3D beam elements, following Timoshenko (shear flexible) beam theory.
- T3D2: Two-noded, first-order displacement truss elements.

It is should be born in mind that solid elements could be computationally expensive for 3D problems and, where appropriate, should be substituted by structural elements (shells and beams) for a more economical solution. Based on this concept and in line with previous studies (Zhou et al., 2013a, 2013b; Tran et al., 2016b) and with recommendations for FE on metal structures (Ellobody et al., 2013), shell elements have been chosen for the modelling of many of the structural steel components presented herein. In order to evaluate the capability of these structural elements to accurately predict the compressive and flexural performance, the same structural components have been discretised with solid and shell elements, as shown in Table 3.1.

Aiming to assess the influence of the element type, a typical case of a stub column (detailed description in Chapter 4) and a beam (detailed description in Chapter 5) have been studied and the relevant load-deformation path is shown in Figure 3.4(a) and Figure 3.4(b), respectively. To exclude the influence of the material model, only elastic material properties (Young's modulus and Poisson's ratio) have been introduced in the models. Almost identical response was observed for all of the studied element types. Note that the analyses have been continued up to very large strains, well beyond the nominal yield point for an assumed S460 steel grade. Considering average element size equal to the section's thickness (see Subsection 3.3.3), Figure 3.4 also reports the number of elements and the required computation time (CPU) in percentage comparison bars, indicating that the S4R element type allows significant computational time savings. Note that the quadratic solid element led to excessive computational times and was therefore not included in the comparison bars.

Table 3.1: Elements considered in the element type study.

Name	Order	Type	Other
Brick-8 (C3D8)	1st (linear)	8-noded brick	Full integration, 3 displacement dofs/node
Brick-8 (C3D8R)	1st (linear)	8-noded brick	Reduced integration, 3 displacement dofs/node
Brick-8I (C3D8I)	1st (linear)	8-noded brick	3 displacement + 13 incompatible modes dofs
Brick-20 (C3D20R)	2nd (quadratic)	20-noded brick	Reduced integration, 3 displacement dofs/node
Thickshell-4 (S4R)	1st (linear)	4-noded doubly-curved rectangle	Finite strain, reduced integration, hourglass control, dofs/node
Thickshell-8 (S8R)	2nd (quadratic)	8-noded doubly-curved rectangle	Small strain, finite rotation, reduced integration, 6 dofs/node
Thinshell-8 (S8R5)	2nd (quadratic)	9-noded doubly-curved rectangle	Small strain, finite rotation, reduced integration, 5 dofs/node

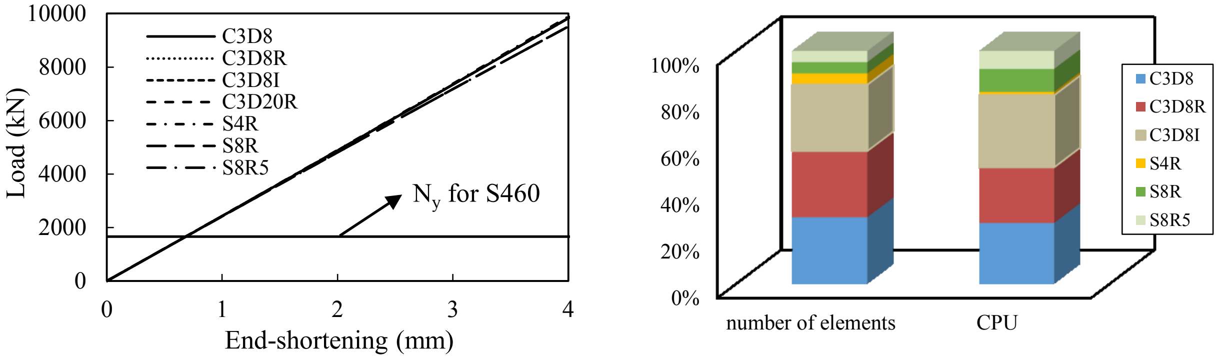

a) Stub column model (corresponding to Chapter 4)

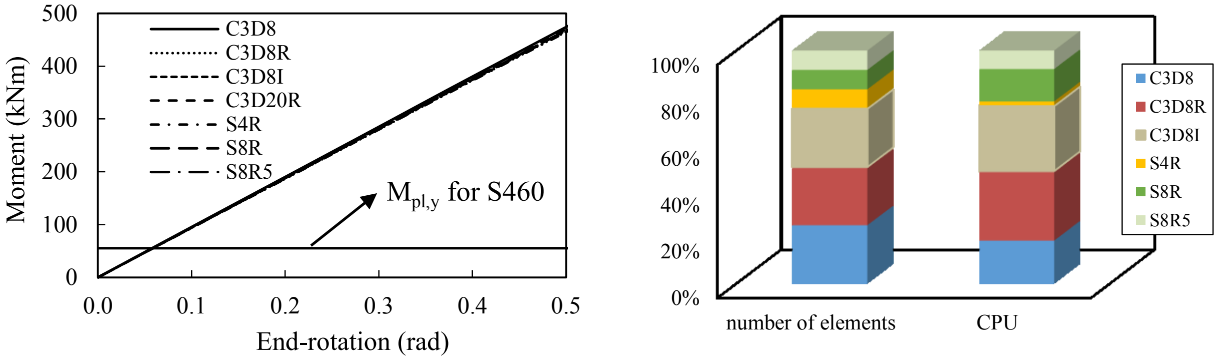

b) Beam model (corresponding to Chapter 5)

Figure 3.4: Element type study.

3.3.3. Mesh

A sufficiently refined mesh able to provide accurate solutions is particularly important in finite element modelling. Coarser meshes might yield inadequate solutions, whilst decreasing the mesh size is expected to lead to more precise modelling. When further refinement brings only negligible change in the accuracy of the solution, the mesh is said to be converged. However, the possible level of refinement is usually limited by the available computational resources. In these cases, further mesh refinement should be primarily implemented in highly stressed locations, where a fine mesh is required to capture sharp stress verifications.

Abaqus provides different techniques for mesh generation, including free, swept and structured meshing. The latter one has been applied within the current study. Additionally, options for quadrilateral, quadrilateral-dominated and triangular elements and hexahedral,

hexahedral-dominated, tetrahedral and wedge elements are provided for meshing of 2D and 3D structures respectively. For the majority of the models presented hereafter, quadrilateral and hexahedral elements have been chosen. Attention was paid to the aspect ratios of the mesh elements, trying to avoid significantly smaller or larger than one values. This was further monitored from mesh controls and verifications provided by the software.

In order to select the most appropriate mesh configuration that would provide accurate results whilst keeping computational time to a minimum, an initial convergence study from coarser to finer mesh was performed for the developed models. In all cases, the mesh was sought to be uniform on the faces of the hollow section. An example of a mesh convergence study corresponding to the finite element models developed in Chapter 4 is given in Figure 3.5. A detailed explanation of the models is given in the respective chapter, whilst focus here is only set on the influence of the mesh size on the overall performance. As anticipated, the accuracy of the results decreased for an increasing mesh size; this is more evident in the post-buckling regime, whilst the ultimate capacity appeared less sensitive to the mesh variations. Similar conclusions were drawn for most of the FEM models presented hereafter. A mesh with an average element size equal to the section’s thickness and with at least three elements for the curved regions of the sections (i.e. 12 elements per full circle), was found to provide a good balance between accuracy and computational time and was therefore applied.

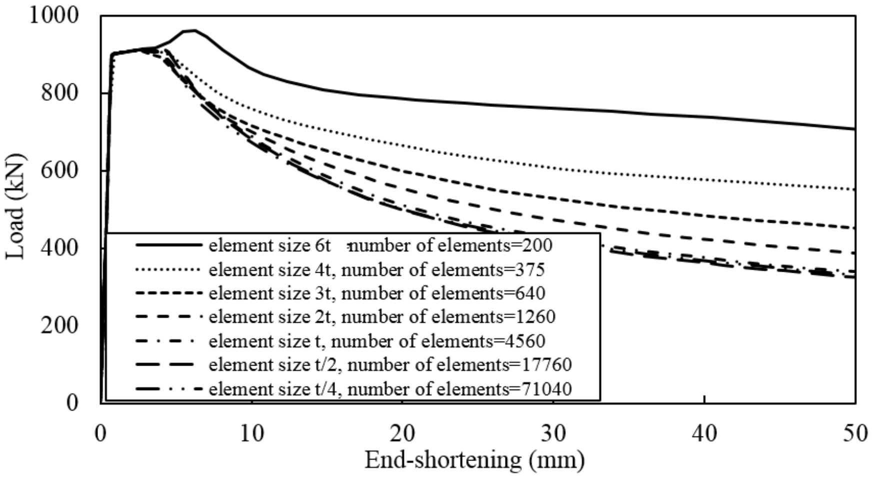

a) Load-deformation response

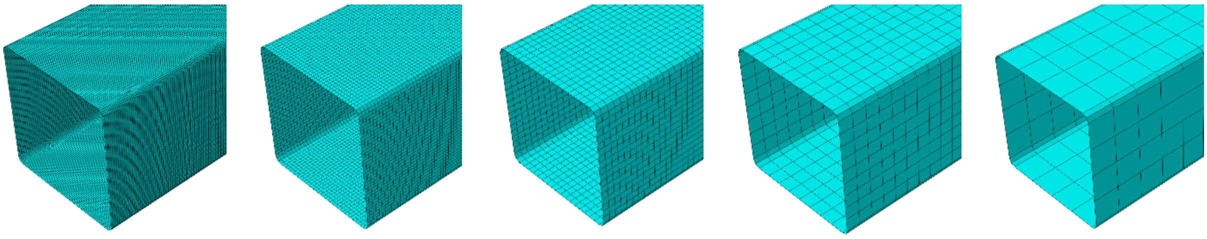

b) Typical considered meshes from finer (left) to coarser (right)

Figure 3.5: A typical example of mesh convergence study.

3.3.4. Material properties

In order to simulate plastic deformation and work hardening in 3D steel structures, the data from simple coupon tests can be used. The S460 and S690 material properties incorporated in the finite element models were based on a series of coupon tests executed at the Structures Lab of Imperial College London (HILONG, 2016). In particular, a comprehensive coupon testing programme covering tensile flat, tensile corner and compressive flat coupons has been carried out as part of HILONG project. For each cross-section, four flat and one corner coupon tests were conducted. The locations of the coupon specimens and the extracted material properties for typical S460 and S690 specimens are given in Figure 3.6(a)-Figure 3.6(c).

It is worth noting that the sections were hot-rolled, seamlessly fabricated from continuously cast round ingots and hollowed out in a piercing mill to their final section shape. The high strength in S460 sections was achieved with the normalising process (N), whilst in S690 with the quenching and tempering process (QT).

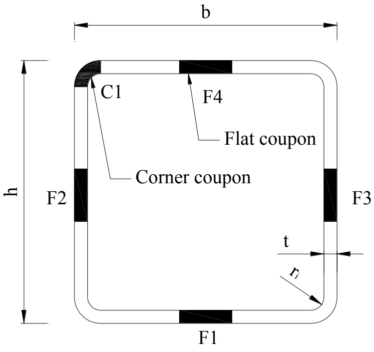

a) Locations of flat and corner coupons

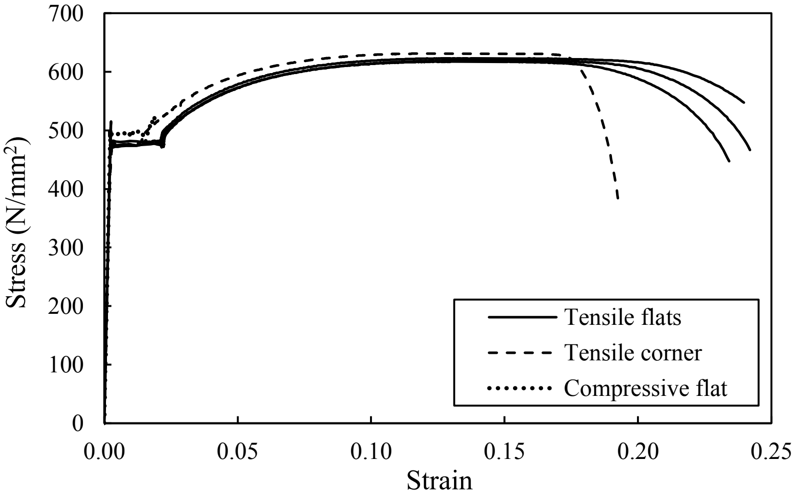

b) S460 coupon tests

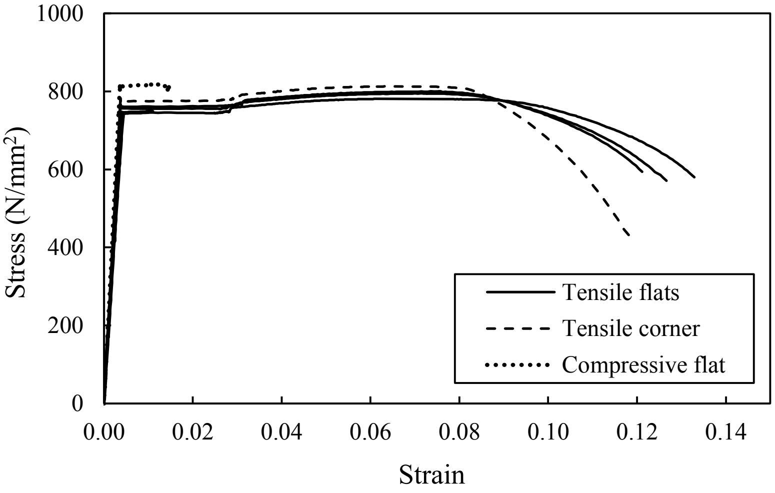

c) S690 coupon tests

Figure 3.6: Tensile flat, tensile corner, compression flat coupon tests.

As can be observed, in all cases the stress-strain curves start with a linear response up to the yielding point, followed by a well-defined plateau and a strain-hardening part after it, which is more prominent in the case of S460 than S690. The corner coupons are observed to behave very similarly to their flat counterparts, both in terms of the shape of the stress-strain curve and the key material parameters. The fact that the material behaviour of the corners is similar to that of the flat coupon tests is related to their hot-rolled production process, during which the corner regions do not experience work-hardening, as occurs in cold-formed sections. It is therefore deemed sufficient to use the results from the tensile flat coupon tests only in the numerical modelling and data analysis hereafter.

The material properties for each of the studied sections, as shown in Figure 3.7, are used for the validation of the finite element models, whereas the average values, as depicted in Figure 3.8, are employed in the parametric studies of the present research work. The material properties as obtained from the mill certificates and from the tensile flat coupon tests together with statistical quantities are also given for reference in Table 3.2 and Table 3.3 respectively. For steel grade S460, the average obtained values for yield strength f_y and ultimate tensile stress f_u were 506 N/mm^2 and 643 N/mm^2 respectively, whilst the respective average values for steel grade S690 were 778 N/mm^2 and 802 N/mm^2. Note that besides the strength, the main differences between the two studied grades and the conventional S355 grade is that the latter has higher strain-hardening and ductility properties. As can be seen in Table 3.3, f_u/f_y has been found equal to 1.27 and 1.03 for S460 and S690 respectively, while for typical S355 the same ratio is approximately equal to 1.50 (see Figure 2.3(b)).

Additionally, it is mentioned for reference that the main chemical components and their respective proportions on average, as stated in the mill certificates, are the following: carbon (C) 0.16% for S460 and 0.15% for S690, silicon (Si) 0.36% for S460 and 0.33% for S690 and manganese (Mn) 1.54% for S460 and 1.51% for S690.

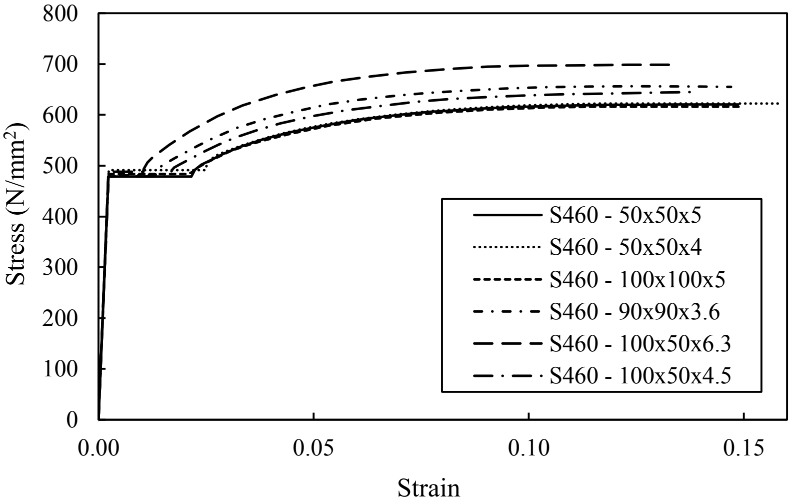

a) S460, tensile flat coupon tests

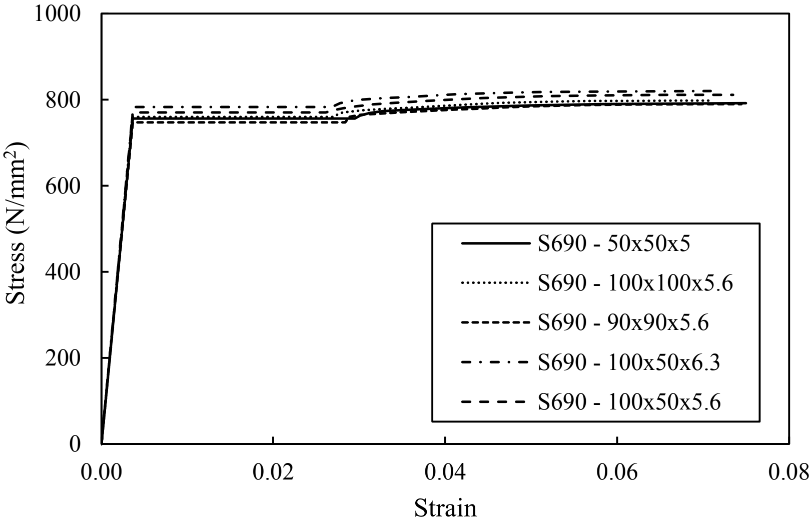

b) S690, tensile flat coupon tests

Figure 3.7: Measured stress-strain curves used in the validation of the finite element models.

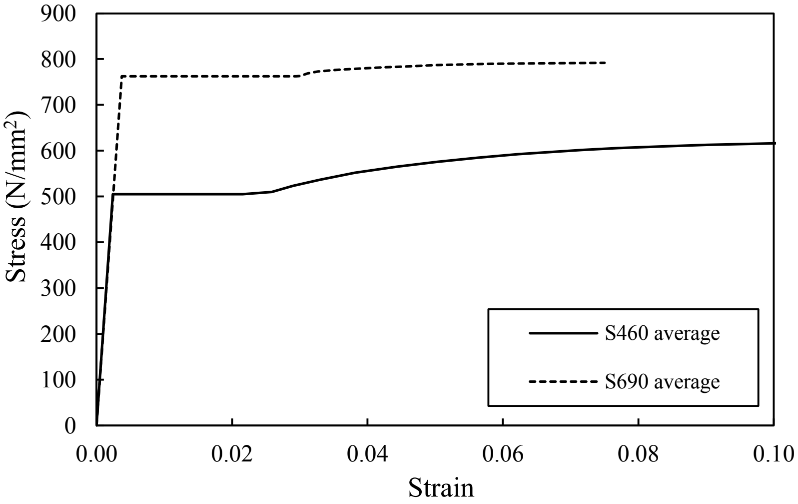

Figure 3.8: Average material properties applied in parametric studies.

Table 3.2: Mechanical properties in mill certificates (Wang et al., 2016).

Cross-section	$f_{y,mill}$ (N/mm^2)	$f_{u,mill}$ (N/mm^2)	ε_f (%)
S460 SHS 50×50×5	473	615	26.5
S460 SHS 50×50×4	524	639	33.0
S460 SHS 100×100×5	492	619	29.0
S460 SHS 90×90×3.6	463	656	25.5
S460 RHS 100×50×6.3	495	668	23.5
S460 RHS 100×50×4.5	505	642	27.5
MEAN (S460)	492	640	28.0
COV (S460)	0.04	0.03	0.12
S690 SHS 50×50×5	797	838	22.4
S690 SHS 100×100×5.6	821	829	20.1
S690 SHS 90×90×5.6	789	825	16.6
S690 RHS 100×50×6.3	792	834	20.9
S690 RHS 100×50×5.6	778	822	19.0
MEAN (S690)	795	830	20.0
COV (S690)	0.02	0.01	0.11

Table 3.3: Average tensile flat material properties (Wang et al., 2016).

Cross-section	E (N/mm^2)	f_y (upper) (N/mm^2)	f_u (N/mm^2)	ε_f (%)	f_u/f_y
S460 SHS 50×50×5	211100	505	620	31.0	1.23
S460 SHS 50×50×4	210700	523	623	28.5	1.19
S460 SHS 100×100×5	211300	511	616	29.2	1.21
S460 SHS 90×90×3.6	206200	500	655	27.9	1.31
S460 RHS 100×50×6.3	212200	498	699	26.3	1.40
S460 RHS 100×50×4.5	210200	498	645	28.3	1.30
MEAN (S460)	210283	506	643	28.5	1.27
COV (S460)	0.01	0.02	0.05	0.05	0.06
S690 SHS 50×50×5	204200	759	790	21.7	1.04
S690 SHS 100×100×5.6	210300	782	798	19.2	1.02
S690 SHS 90×90×5.6	205700	774	790	20.1	1.02
S690 RHS 100×50×6.3	212500	799	820	19.0	1.03
S690 RHS 100×50×5.6	209800	777	811	18.8	1.04
MEAN (S690)	208500	778	802	19.8	1.03
COV (S690)	0.02	0.02	0.02	0.06	0.01

In addition to the studies on S460 and S690 square and rectangular hollow sections, Chapter 7 contains numerical modelling of a cable with nominal tensile strength 1860 N/mm^2, designated as Y1860S7 according to prEN 10138-3 (2000). A comprehensive description of the aforementioned modelling is provided in the relevant chapter, whereas focus is currently set on the adopted material properties.

Similarly to the high strength steel hollow sections, material tests were also executed for the cables of different lengths. Significant variations in the stress-strain response, particularly in the apparent Young's modulus, were noticed among the executed tests. The extracted stress-strain curves are shown in Figure 3.9, where Ec90, Ec130 and Ec215 stands for a cable with apparent Young's modulus 90000 N/mm^2, 130000 N/mm^2 and 215000 N/mm^2 respectively. A rounded response with an average 0.2% proof strength of 1700 N/mm^2 was observed. In order to describe the material's response, a 2-stage Ramberg-Osgood model (Gardner and Nethercot, 2004a) according to Equations (3.1)-(3.2) has been employed.

$$\varepsilon = \frac{\sigma}{E_0} + 0.002\left(\frac{\sigma}{\sigma_{0.2}}\right)^n \quad for\ \sigma \leq \sigma_{0.2} \tag{3.1}$$

$$\varepsilon = \frac{\sigma - \sigma_{0.2}}{E_{0.2}} + (\varepsilon_{tu} - \varepsilon_{t0.2} - \frac{\sigma_u - \sigma_{0.2}}{E_{0.2}})(\frac{\sigma - \sigma_{0.2}}{\sigma_u - \sigma_{0.2}})^{n'_{0.2,u}} + \varepsilon_{t0.2} \quad for\ \sigma_{0.2} \leq \sigma \leq \sigma_u \tag{3.2}$$

where E_0 and $E_{0.2}$ the Young's modulus and the tangent modulus at 0.2% offset stain, $\sigma_{0.2}$ the proof strength at 0.2% offset strain, $\varepsilon_{t0.2}$ and ε_{tu} the total strains at $\sigma_{0.2}$ and σ_u respectively and n and $n'_{0.2,u}$ strain hardening exponents, determined from tests.

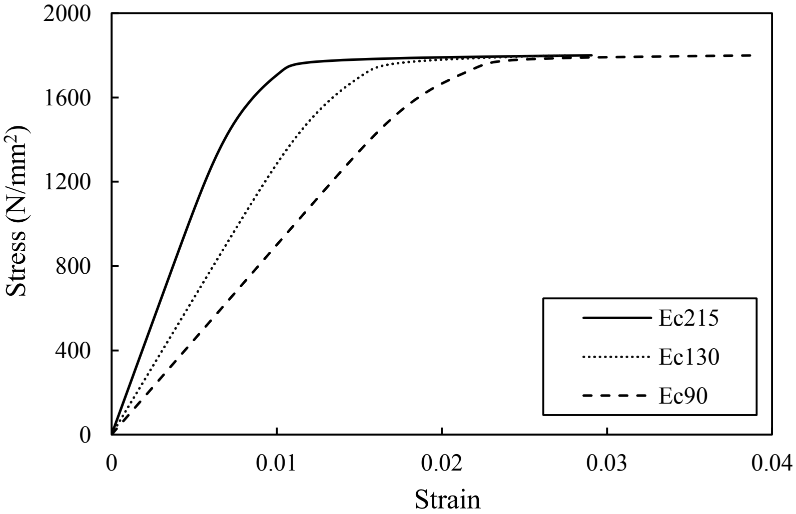

Figure 3.9: Measured stress-strain curves for cable coupons.

Having established the material response under uniaxial tension, a yield/failure criterion needs to be defined. For ductile materials like steel, yielding is independent from the hydrostatic stress component of the stress tensor and plasticity can be satisfactorily modeled by the von Mises yield criterion, according to which yielding occurs when the second deviatoric stress invariant reaches a critical value, whilst the response is assumed to be elastic until that point. This theory is expressed in Equation (3.3) for multiaxial stress state (von Mises, 1913).

$$\sigma_y = \sqrt{½[\,(\sigma_1-\sigma_2)^2+(\sigma_2-\sigma_3)^2+(\sigma_3-\sigma_1)^2} \tag{3.3}$$

where $\sigma_1,\ \sigma_2, \sigma_3$ are the principal stresses. Von Mises expression leads to a cylindrical yield surface with radius $\sqrt{2/3}\,\sigma_y$ around the hydrostatic axis ($\sigma_1=\sigma_2=\sigma_3$), as depicted in Figure 3.10.

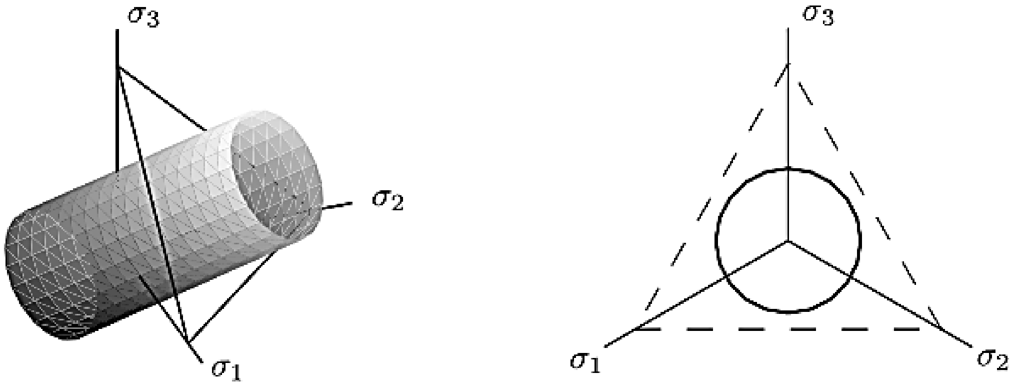

Figure 3.10: Von Mises yield criterion [adapted from von Mises (1913)].

Furthermore, for steels, isotropic hardening, which means that the yield surface remains the same shape but expands with increasing stress, according to Equation (3.4), is considered to be a good approximation of the plasticity flow for material response under monotonic loading.

$$f(\sigma_{ij}) - K = 0 \tag{3.4}$$

where $f(\sigma_{ij})$ and K the yield function and the hardening parameter respectively.

Hence, the von Mises yield criterion with isotropic hardening was applied for the steel structures within the current study. In line with Abaqus requirements, before the input of the piecewise linear approximation of the actual continuous engineering stress-strain curves of Figure 3.7-Figure 3.9 into the software, the engineering stress-strain curves were converted to true stresses and logarithmic plastic strains through Equations (3.5)-(3.6).

$$\sigma_{true} = \sigma_{eng}\left(1 + \varepsilon_{eng}\right) \tag{3.5}$$

$$\varepsilon_{ln}^{pl} = \ln\left(1 + \varepsilon_{eng}\right) - \frac{\sigma_{true}}{E} \tag{3.6}$$

where σ_{eng}, ε_{eng} are the engineering stress and strain respectively, E is the Young's modulus and σ_{true} and ε_{ln}^{pl} are the true stress and logarithmic plastic strain respectively. This conversion is necessary because Abaqus formulations have been set not on the basis of the engineering stresses (i.e. based on loads divided by the initial cross-sectional area) but of the true ones (i.e. based on loads divided by the cross-area at that instant; e.g. in a uniaxial tensile test, the length increases and the width and thickness shrink, when pulling, and the instantaneous cross-sectional area is different form the initial one).

3.3.5. Geometric imperfections

Real structural members contain geometric imperfections both in the way the load is applied (eccentricity with respect to the centroid of the section) and as deviations from the ideal geometry. For structures prone to buckling, the presence of these unavoidable imperfections can have a significant effect on their structural performance. For this reason, geometric imperfections should be accounted for in the numerical simulations.

In line with previous studies (Gardner and Nethercot, 2004b; Zhou et al., 2013a, 2013b; Schafer et al., 2010), geometric imperfections were incorporated in the numerical models in form of the lowest elastic buckling mode shapes of the relevant buckling mode. The critical deformed shapes can be estimated by Linear Buckling Analysis (LBA) and are usually a good estimator of the collapse failure mode.

For the structures of Chapters 4-6 that are sensitive to local buckling, the imperfections can be introduced as a function of the section's thickness. The following values of local imperfection magnitudes were examined: 1%, 2%, 10% of the section wall thickness.

Additionally, ω_{DW}, an imperfection value evaluated from the predictive model of Dawson and Walker (Dawson and Walker, 1972), as modified by Gardner and Nethercot (Gardner and Nethercot, 2004b) according to Equation (3.7), was considered.

$$\omega_{DW} = \beta \cdot \left(\frac{\sigma_y}{\sigma_{cr}}\right)^{0.5} t \tag{3.7}$$

where σ_y is the material yield strength, σ_{cr} is the elastic critical buckling stress of the most slender constituent plate element in the section and t is the plate thickness. Due to limited amount of local imperfection data for high strength steels, a value of 0.028, which was recommended for ordinary carbon steel hot-rolled rectangular hollow sections (Gardner et al., 2010), was adopted for the β parameter.

Furthermore, in order to enable accurate numerical modelling, the maximum imperfections ω_0, as measured at the Structures Lab of Imperial College London for the tests of Chapters 4-6, were also studied. A displacement transducer mounted on the head of a milling machine was moved along the length of each of specimen. A total of three runs, one in the middle and two close to the edges of each of the faces of the sections, were performed for each cross-section. Based on the measured results, the maximum deviations ω_0 from a flat datum for the four faces of each cross-section were determined.

For the structures of Chapter 7, where global buckling of a truss member was the observed failure mode, the geometric imperfections were given as a fraction of the length of the relevant buckled member, whilst both out-of-plane and in-plane buckling modes were considered. The selected mode shapes were based on the observed failure modes and will be discussed in detail in the relevant chapter.

3.3.6. Residual stresses

Residual stresses are a self-equilibrating set of stresses within a member in the absence of external loads (Withers and Bhadeshia, 2001). They exist in most structural steel members and are induced during the production or manufacturing processes like welding, flame cutting, non-uniform cooling or cold-forming. Uneven cooling of the sections results in compressive and tensile residual stresses for the parts that cool quicker and slower, respectively. The residual stresses can either remain uniform through the thickness of the cross-sections (membrane residual stresses, typical for hot-rolled sections) or vary linearly (bending residual stresses, typical for cold-formed sections (Schafer and Peköz, 1998)). Residual stresses can affect the stiffness, the stability and the fatigue life of a structure and thus should be carefully examined. For structural components, the influence of residual stresses on their structural performance depends on their imperfection sensitivity and their slenderness (Galambos, 1998).

Among others, common techniques to measure residual stresses are the hole-drilling (a semi-destructive method) and the sectioning technique (a destructive method). In the hole-drilling method, a small hole into the material causes a relief of the residual stresses which is accompanied by associated deformations that are measured with the use of strain gauges. Sectioning method is more appropriate for structural steel members and measures the released strains on sectioned strips. The sectioning method has been applied in order to measure the residual stress pattern of the currently studied HSS cross-sections. The measurements were executed at the Structures Lab of Imperial College London and the results for a S690 SHS 90×90×5 section are shown in Figure 3.11. The specimen was divided into strips and the strains in the outer and inner surfaces of the material strips were measured prior and after sectioning, through the use of a Whittemore gauge. It was found that the measured residual stresses were associated only with axial membrane and not with any bending residual stresses, as no curving of the strips was observed. The maximum measured longitudinal membrane residual stresses were found to be $0.055f_y$ in tension and $0.031f_y$ in compression (Wang et al., 2016). The low magnitudes can be attributed to the seamless fabrication procedure. These magnitudes, especially the ones corresponding to bending residual stresses, are expected to be larger in cold-formed cross-sections, where the manufacturing process influences greatly the residual stress patterns. For instance, Ma et al. (2015) have conducted residual stress measurements on cold-formed HSS hollow sections, finding maximum stresses as high as $0.2f_{0.2}$ and $0.8f_{0.2}$ for the longitudinal and bending stresses, respectively, where $f_{0.2}$ the material's proof strength. Further to this, it is worth noting that Rasmussen and Hancock (1995) and Wang *et al*. (2012b) that have studied the residual stress pattern for HSS welded box sections, have concluded that the ratio of the residual stress over the yield strength for HSS sections is lower than the corresponding one of their mild steel counterparts.

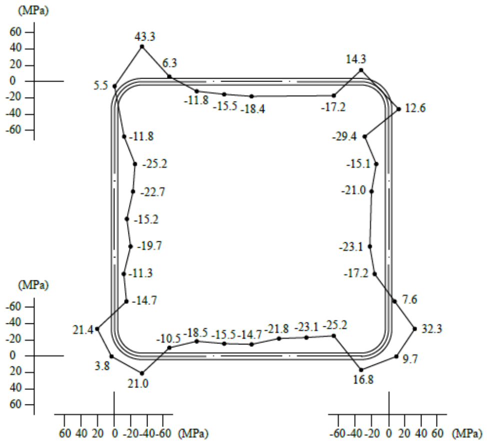

Figure 3.11: Typical residual stress distribution for a S690 specimen (Wang et al., 2016).

Owing to the very low magnitudes of the residual stresses for the currently studied sections, it was decided not to explicitly model them in the finite element modelling herein. Nevertheless, as will be shown in the following chapters, the introduction of initial geometric imperfections was able to trigger buckling and the structural response was successfully captured. It should be born in mind though that the residual stresses should be explicitly incorporated in the numerical models when their magnitude is significant, like in steel columns of lower yield strength where the residual stresses comprise a considerable proportion of the yield strength.

3.3.7. Boundary conditions and constraints

The effect of the supports and the applied loading in the test rig was modelled through appropriate boundary conditions and constraints. In order to capture the exact test conditions, the translational and rotational degrees of freedom were appropriately restrained, whilst suitable constraints were used. Examples of applied constraints are the following: rigid body which allows constraining the motion of regions of an assembly to the motion of a reference point, kinematic coupling which provides a constraint between a reference node and the nodes on a surface (the coupling nodes) and tie constraint which provides a simple way to bond surfaces together permanently, using a master-slave formulation. In case of symmetry of the test configuration with respect to geometry, boundary conditions, loading and the observed failure mode, only part of the cross-section/structure was modelled and suitable symmetry boundary conditions were employed along the assumed symmetry axis. Boundary conditions and constraints are further discussed in Chapters 4-7, where a full description of the applied boundary conditions and constraints for each model is given.

3.3.8. Analysis techniques

Within the current study, two analyses techniques have been primarily used: Linear buckling analysis and Riks analysis.

Linear buckling analysis (LBA) is a linear perturbation procedure that evaluates the elastic critical buckling loads of structures. The analysis searches for loads that make the model stiffness matrix become singular for nontrivial displacement solutions by solving Equation (3.8).

$$({K_0}^{NM} + \lambda_i {K_\Delta}^{NM}){u_i}^M = 0 \tag{3.8}$$

where ${K_0}^{NM}$ is the stiffness matrix corresponding to the base state, ${K_\Delta}^{NM}$ is the differential initial stress and load stiffness matrix due to incremental loading pattern, λ_i and u_i the eigenvalues and the eigenvectors (i.e. the buckling mode shapes) of the ith buckling mode respectively, M and N the degrees of freedom of the whole model. To solve Equation (3.8), the subspace extraction method, a robust and efficient iteration algorithm, firstly introduced by Bathe (Bathe and Wilson, 1973) and widely applied in finite element codes ever since, is used. The extracted mode shapes can be subsequently used as a representative geometric imperfection pattern, scaled to an appropriate magnitude, as discussed in Subsection 3.3.5, whilst also provide an estimate of the collapse failure mode. In case a negative eigenvalue is derived, this means that the structure would buckle if the load was applied in the opposite direction.

The Riks method is used to carry out geometrically (large displacement and large rotation) and materially (nonlinear stress-strain relationship) nonlinear analysis with imperfections included, the so-called GMNIA. The Riks analysis uses the Newton-Raphson method in order to find successively better approximations to the roots of a function and thus to solve the nonlinear equilibrium problems.

In the Newton-Raphson method, the first and the second iterations of the nonlinear load-displacement path analysis are shown in Figure 3.12, where K_0, u_0 and K_a, u_a the structure's stiffness and the displacement at the initial state and at the first iteration respectively and ΔP a small load increment. Once the updated stiffness and displacement are formed at the first iteration, an updated configuration I_a, which is used for the calculation of a force residual $R_a\ (= P - I_a)$, and a displacement correction factor c_a are calculated. R_a and c_a are compared with previously defined tolerance values and if they are smaller, the problem is said to be converged; otherwise a second iteration utilising R_a and c_a and resulting in updated residuals and correction factors is attempted. The procedure iterates until the equilibrium is satisfied and continues to the next increment. The solver can automatically adjust the size of the load increments (automatic time incrementation) to find a converged solution. Note that iterations conducted within an increment could be either regular equilibrium iterations (smooth variation in the solution) or severe discontinuity iterations (abrupt variation in stiffness). In problems involving severe contact and material nonlinearities, convergence is not guaranteed and hence other techniques should be adopted (Hibbitt et al., 2012).

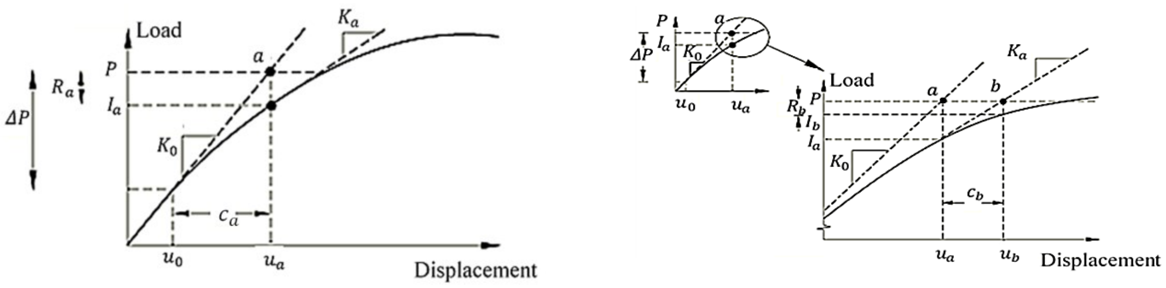

a) First iteration

b) Second iteration

Figure 3.12: Nonlinear analysis (Hibbitt et al., 2012).

The Riks method solves simultaneously for loads and displacements, using another quantity, called arc length, to measure the progress of the solution along the load-displacement equilibrium path. During Riks analysis, the loading is always proportional by a load proportionality factor λ. The initial load proportionality factor is calculated based on the user-specified total arc length scale factor, whilst further increments are based on the convergence rate. Instead of the conventional load-displacement path, the solution follows the load magnitude-displacement path, scaled so that the dimensions of each axis are approximately the same size. The Riks method can be applied to obtain convergence of unstable, geometrically nonlinear collapse of structures. The analysis is terminated when either the specified maximum number of increments or the specified maximum displacement value has been reached. Contrary to the ordinary Newton-Raphson method which fails to converge when the tangent stiffness matrix becomes singular, the arc-length method, is able to obtain converged solutions and trace the ultimate load response of a structure.

3.3.9. Output

Once the boundary value problem was solved and the analysis was completed, output data including stresses, strains and displacements (both translational and rotational) and forces in locations of interest were extracted and visualised.

3.4. Validation of the finite element models

Upon meticulous development of the finite element models, the numerically generated response was compared with the experimental one. The measured geometric and material properties obtained from the experimental investigation were incorporated into the finite element models. In order to verify that the numerical models are able to precisely capture the structural performance of the test specimens, the validation in all cases was based on the comparison of the experimentally and numerically obtained:

- Initial stiffness of the structural system (i.e. the initial linear part of the load-deformation behaviour obtained from the experiments was compared with the numerical one).
- Ultimate capacity (i.e. the maximum load achieved during testing was compared with the numerically obtained ultimate load - the latter is defined separately in each chapter).
- Failure mode (i.e. the shape of the experimentally failed structure was compared with the one captured numerically).
- Overall load-deformation response (i.e. the overall experimental load-deformation response from the beginning of loading up to strains beyond the failure load was compared with the numerical one).

As explained in Subsection 3.3.5, the finite element models were calibrated, considering different magnitudes for the initial geometric imperfections, against the test results. The calibration was based on the satisfaction of the aforementioned four criteria. The imperfection sensitivity analysis performed during the validation of the FE models is shown in tabulated form in Figure 3.13 and comprised six and ten cases for the models of Chapters 4-6 and Chapter 7 respectively. The results of the sensitivity analysis together with typical graphs of the load-deformation response and representative failure modes are presented in the following chapters, where the comparison ratios of ultimate loads together with statistical quantities are also detailed, thus allowing the selection of the imperfection magnitude that successfully captured the test performance.

Cross-sectional response (Chapters 4-6)

Stub columns	Members in 3-point and 4-point bending	Eccentrically loaded short columns

1) no imperfection
2) 1% of the section wall thickness t (i.e. $t/100$)
3) 2% of the section wall thickness t (i.e. $t/50$)
4) 10% of the section wall thickness t (i.e. $t/10$)
5) the maximum measured imperfections ω_0
6) ω_{DW}, an imperfection value evaluated from the predictive model of Dawson and Walker (Dawson and Walker, 1972)

Trusses (Chapter 7)

	Out-of-plane	In-plane
1)	L / 1000	L / 1000
2)	L / 2000	L / 1000
3)	L / 1000	L / 2000
4)	L / 1500	L / 750
5)	L / 750	L / 1500
6)	L / 1000	0
7)	0	L / 1000
8)	L / 2000	L / 2000
9)	L / 750	L / 750
10)	L / 1500	L / 1500

L length of buckled member

Figure 3.13: Imperfection sensitivity analysis.

3.5. Parametric studies

Upon establishing a successful validation, the numerical models were used to investigate further the considered structural response and evaluate the influence of key parameters on the structural response.

For the HSS components of Chapters 4-6, the influence of the cross-section slenderness $c/t\varepsilon$, where c is the compressed flat width, t is the plate thickness and $\varepsilon = \sqrt{235/f_y}$ with f_y being the material yield strength, on the ultimate response was examined for both S460 and S690 steel grades. Additionally, rectangular hollow sections with varying aspect ratios h/b, where h and b the section depth and width respectively, were studied. Note that for the considered aspect ratios, the outer dimensions were maintained, while the cross-section thickness was appropriately changed and the internal radius was set equal to half of the plate's thickness t. In addition to the aforementioned parameters, it was deemed necessary to assess the effect of the moment gradient on the response of HSS beams in Chapter 5 and to study the influence of various loading eccentricities for HSS stub columns in Chapter 6. It is worth noting that the selection of the parameters examined in Chapters 4-6 was largely based on past studies focusing on key parameters affecting the cross-sectional performance of hollow sections, as given in Section 2.4.

For HSS prestressed trusses of Chapter 7, the parametric studies emphasised on the effect of various influential parameters such as the applied load level, the truss configuration and the employed steel grade on the overall performance. The aforementioned parameters were mainly based on a preliminary study that examined the benefits due to the prestress application and their sensitivity to different variables.

The matrix of parametric studies is shown in Figure 3.14, whilst additional information is provided in the following chapters. Nonlinear static analysis with the Riks method was applied for the parametric studies. Initial geometric imperfections were introduced at the first step of each nonlinear analysis. As mentioned earlier, the geometric imperfections were introduced in the form of the lowest buckling mode, which was estimated through an initial liner buckling analysis. The introduced magnitudes of the geometric imperfections were based on the comparison with the test data at the calibration process.

<table>
<tr><th colspan="3">Cross-sectional response (Chapters 4-6)</th></tr>
<tr><td>Stub columns</td><td>Members in 3-point and 4-point bending</td><td>Eccentrically loaded short columns</td></tr>
<tr><td colspan="3">cross-section slenderness c/tε (from stocky to slender)</td></tr>
<tr><td colspan="3">cross-section aspect ratio h/b</td></tr>
<tr><td>-</td><td>moment gradient</td><td>-</td></tr>
<tr><td>-</td><td>-</td><td>load eccentricity</td></tr>
</table>

Trusses (Chapter 7)
applied prestress load
truss configuration/shape
steel grade of the truss elements
curvature of the truss chords
cross-section sizes of the truss chords

Figure 3.14: Matrix of parametric studies.

A detailed description of the parametric studies is given in the relevant sections of Chapters 4-7. It is worth mentioning that for the execution of the parametric studies hereafter, python scripting was used, thus increasing significantly the efficiency of the required work. Moreover, all of the numerical analyses were realised at the supercomputer of the University of Birmingham named "Bluebear" that reduced substantially the computational time.

3.6. Analysis of the results and design recommendations

On the basis of the experimental and the numerical results, guidelines for the design of high strength steel hollow section members and structures were assessed. Particular emphasis was placed upon the applicability of current European specifications to HSS, whereas relevant design recommendations were made, where appropriate. Note that for all the comparisons, safety factors equal to unity were assumed.

CHAPTER 4: HIGH STRENGTH STEEL MEMBERS IN COMPRESSION

4.1. Introduction

The compressive behaviour of S460 and S690 hot-finished square and rectangular hollow sections is investigated in the present chapter. Finite element models were developed and calibrated against the experimental data of eleven concentrically compressed stub columns. In order to study the structural response of HSS hollow sections with varying cross-section slendernesses and aspect ratios, extensive parametric studies were subsequently performed. The obtained results were used to assess the applicability of the Eurocode Class 3 limit and the effective width equations to HSS sections. Plate element interaction effects were found significant for slender stub columns. Given that these effects are disregarded in BS EN 1993-1-1 (2014), an effective cross-section method making allowance of the interaction effects among the constituent plate elements in slender sections is developed and presented herein. Moreover, the continuous strength method is extended to stocky S460 sections, to capture the effect of strain-hardening and hence obtain more economic design.

4.2. Brief description of the test programme

A comprehensive experimental programme comprising eleven concentric stub columns was performed at the Structures Lab of Imperial College London in order to study the structural response of HSS hollow sections in compression. The dimensions of the tested specimens together with the measured initial geometric imperfections are presented in Table 4.1, where a photograph of the test set-up together with the definition of relevant symbols and the instrumentation are illustrated in Figure 4.1. According to relevant design guidelines (Galambos, 1998; Ziemian, 2010), an adequate representation of the residual stresses and the geometric imperfections, excluding the global buckling failure mode, can be achieved by setting the length of the specimens three times the largest cross-section dimension. This assumption has been adopted in Chapters 4-6.

Table 4.1: Measured dimensions of the concentric stub columns.

Cross-section	L (mm)	b (mm)	h (mm)	t (mm)	r_i (mm)	$\omega_0 (mm)$
S460 50×50×5	150.01	50.30	50.40	5.02	3.5	0.054
S460 50×50×4	150.01	50.30	50.33	3.82	3.38	0.043
S460 100×100×5	300.05	99.75	99.38	5.27	5.00	0.077
S460 90×90×3.6	269.83	90.42	90.78	3.77	5.00	0.083
S460 100×50×6.3	300.00	99.89	49.84	6.41	4.88	0.049
S460 100×50×4.5	299.95	99.70	49.79	4.71	5.00	0.070
S690 50×50×5	149.94	50.42	50.29	4.89	3.25	0.076
S690 100×100×5.6	300.05	100.73	100.39	5.74	4.88	0.081
S690 90×90×5.6	270.03	90.96	90.58	5.76	4.50	0.089
S690 100×50×6.3	300.00	100.24	50.08	6.44	5.00	0.106
S690 100×50×5.6	300.09	100.47	49.77	5.72	5.13	0.156

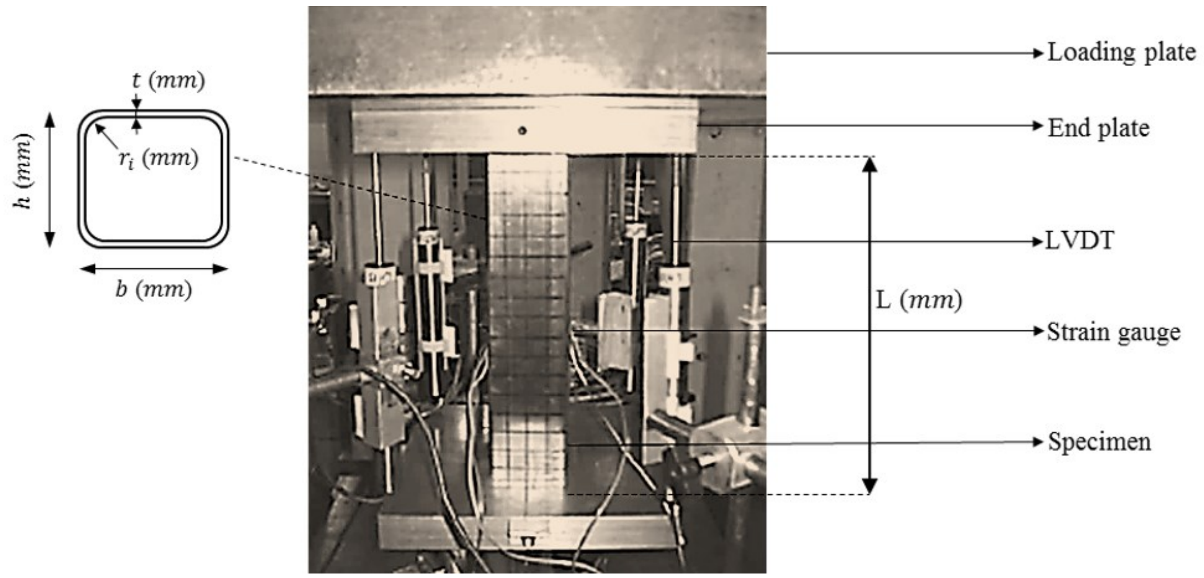

Figure 4.1: Photograph of the test set-up including symbols definition and instrumentation [adapted from HILONG (2016)].

An Instron 3500 kN hydraulic testing machine was used for the experiments. The test set-up was displacement controlled. The end-shortening of the stub columns between the end plates of the machine were measured with LVDTs, whilst axial strain readings were recorded by strain gauges. As anticipated, local buckling was the prevailing failure type. For certain stub columns in the stocky slenderness range and with small magnitude of initial geometric imperfections, the friction forces between the specimens and the plates of the machine led to the development of elephant foot failure mode. It is worth pointing out, though, that the ultimate load was bigger than the respective squash load in all specimens. A summary of the ultimate loads and the normalised compressive capacities is given in Table 4.2. Further details on the concentric stub column tests can be found in Wang et al. (2017).

Table 4.2: Summary of the concentric stub column tests.

Cross-section	$N_{u,Exp}\ (kN)$	$N_{u,Exp}/Af_y$
S460 50×50×5	645.16	1.59
S460 50×50×4	477.63	1.45
S460 100×100×5	1042.29	1.14
S460 90×90×3.6	628.34	1.05
S460 100×50×6.3	1188.45	1.47
S460 100×50×4.5	713.26	1.20
S690 50×50×5	804.04	1.27
S690 100×100×5.6	1673.94	1.05
S690 90×90×5.6	1511.56	1.07
S690 100×50×6.3	1409.59	1.08
S690 100×50×5.6	1212.21	1.05

4.3. Development of the finite element models

Following the modelling assumptions of Chapter 3, the finite element models were created with shell elements, whilst the loading and support conditions of the tests were accurately captured by the numerical models. A rigid body constraint was used at both ends of the stub column to apply both the axial compression and support reaction. All degrees of freedom apart from the translation along the column axis at the loaded end were restrained at both ends. Similarly to the experiments, the load was assigned in form of a forced incremental axial displacement. Figure 4.2 depicts a typical numerical model together with the considered boundary conditions.

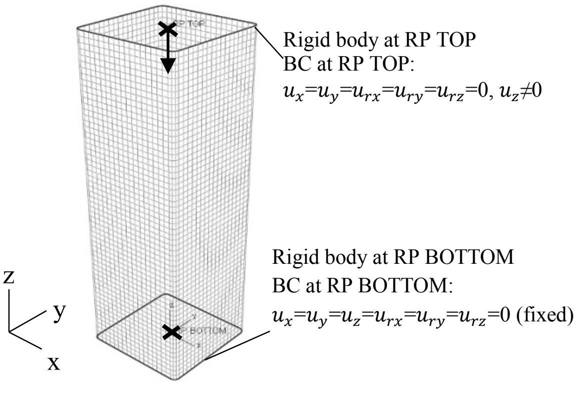

Rigid body at RP TOP
BC at RP TOP:
$u_x=u_y=u_{rx}=u_{ry}=u_{rz}=0$, $u_z \neq 0$

Rigid body at RP BOTTOM
BC at RP BOTTOM:
$u_x=u_y=u_z=u_{rx}=u_{ry}=u_{rz}=0$ (fixed)

Figure 4.2: Numerical stub column model.

In order to capture the observed failure modes, variations in the magnitude of the geometric imperfections of the sections had to be properly considered in the numerical models. The linear buckling mode shapes obtained from eigenvalue buckling analysis with different amplitudes were introduced at the initial step of the nonlinear static analysis to calibrate the initial geometric imperfections and were found capable of triggering local buckling and accurately capturing the experimental failure modes. The incremental load and the corresponding end-shortening throughout each numerical analysis were recorded, allowing the determination of the full load-deformation path.

4.4. Validation of the finite element models

In order to investigate the effect of initial geometric imperfections magnitude and assess the capability of the numerical models to capture the experimentally observed behaviour, six different imperfection magnitudes were considered and the comparison ratios are reported in Table 4.3. The ultimate loads of the FE models were considered as the maximum loads attained during the nonlinear static analysis. The experimentally obtained ultimate loads were generally well predicted in all cases by the numerical models. Even though best agreement was found for zero imperfection magnitudes, very good replication of the test performance was attained for initial geometric imperfections with a magnitude of $t/50$, achieving a mean value of $N_{u,FE}/N_{u,Exp}$ equal to 0.96 with COV of 0.04. The same amplitude gave the best agreement with the test results of Chapters 5 and 6, as will be seen later on. To maintain consistency, the magnitude $t/50$ has been adopted for all the parametric studies performed in Chapters 4-6.

In addition to the ultimate loads, representative load-end-shortening curves are depicted in Figure 4.3. As can be seen, the overall response is sufficiently predicted. The displacement at failure load appears rather dependent on the magnitude of the initial local geometric imperfections, whilst the ultimate load is only slightly affected by the variations in the imperfection amplitude. The accurate capture of the local buckling and the elephant foot failure modes by the numerical models are clearly shown in Figure 4.4.

Table 4.3: Comparison of FE and test data.

Cross-section	Imperfection amplitude					
	0	ω_0	$t/100$	$t/50$	$t/10$	ω_{DW}
	$N_{u,FE}/N_{u,Exp}$	$N_{u,FE}/N_{u,Exp}$	$N_{u,FE}/N_{u,Exp}$	$N_{u,FE}/N_{u,Exp}$	$N_{u,FE}/N_{u,Exp}$	$N_{u,FE}/N_{u,Exp}$
S460 50×50×5	0.95	0.93	0.95	0.93	0.95	0.95
S460 50×50×4	0.93	0.89	0.88	0.85	0.75	0.91
S460 100×100×5	1.05	0.96	0.96	0.96	0.94	0.96
S460 90×90×3.6	1.06	1.01	1.02	1.01	0.99	1.01
S460 100×50×6.3	0.99	1.02	1.01	0.95	0.86	1.01
S460 100×50×4.5	0.94	0.97	0.98	0.94	0.88	0.97
S690 50×50×5	0.90	0.90	0.90	0.90	0.83	0.90
S690 100×100×5.6	1.01	1.00	1.00	1.00	0.98	1.00
S690 90×90×5.6	1.00	0.99	1.00	0.99	0.96	1.00
S690 100×50×6.3	1.04	1.01	1.02	0.99	0.94	1.02
S690 100×50×5.6	1.01	0.99	1.03	1.00	0.97	1.00
MEAN	0.99	0.97	0.98	0.96	0.91	0.98
COV	0.05	0.05	0.05	0.05	0.08	0.04

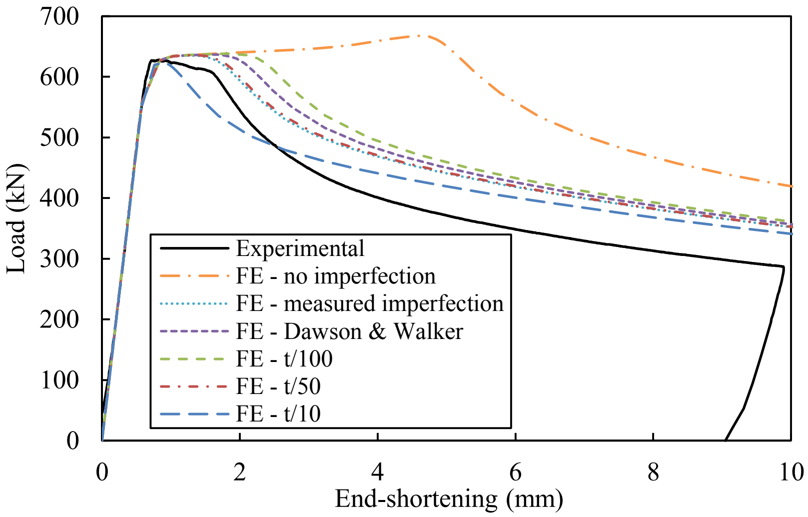

a) S460 90×90×3.6

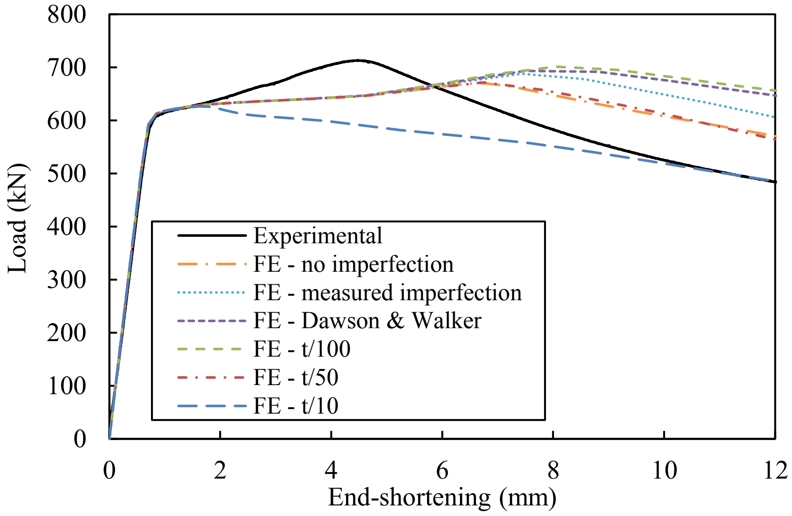

b) S460 100×50×4.5

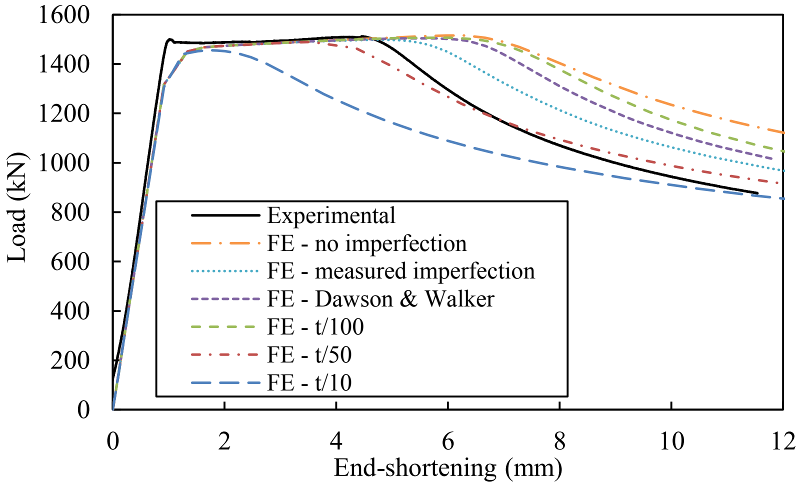

c) S690 90×90×5.6

Figure 4.3: Validation of FE models for concentric stub columns.

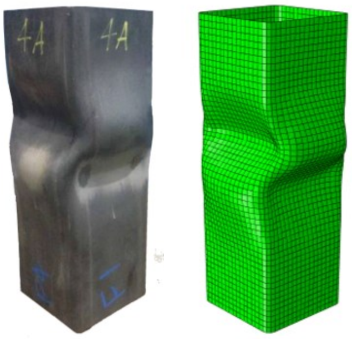

a) local buckling (S460 90×90×3.6)

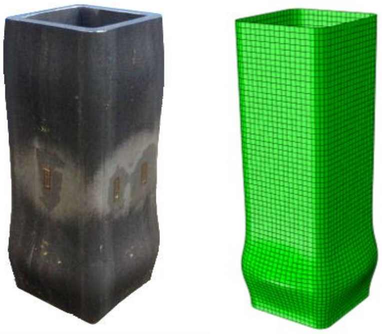

b) elephant foot (S690 50×50×5)

Figure 4.4: Typical experimental and numerical failure modes (Gkantou et al., accepted1).

4.5. Parametric studies

Upon calibration against the experimental behaviour, thorough parametric studies were carried out in order to investigate further the compressive response of HSS hollow sections. Aiming to examine the influence of the cross-section aspect ratio, the material strain-hardening properties and the cross-section slenderness on the overall cross-sectional performance, the following cases were studied for both S460 and S690 steel grades:

- Fifteen different sections with varying thickness to provide cross-section slenderness over the range $c/t\varepsilon$ = 10÷100.
- Six cross-section aspect ratios (h/b): 1.00, 1.25, 1.50, 2.00, 2.50 and 3.00.

Implementing previously mentioned principles (Ziemian, 2010; Galambos, 1998), the length of the specimens was set equal to three times the largest cross-section dimension. An initial geometric imperfection amplitude of $t/50$ was adopted for all the studied sections. The parametric studies comprised 180 additional analyses. Upon their completion, graphs like the one shown in Figure 4.5 were created in order to study the response of stub columns with the same cross-section aspect ratio and steel grade and increasing cross-section slenderness. The anticipated cross-sectional response with pronounced strain-hardening for stocky sections and failure at compressive strains within the elastic range for slender sections is evident. For each studied cross-section, both the lowest elastic critical buckling mode shapes and failure modes have been extracted, as illustrated for typical cases in Figure 4.6.

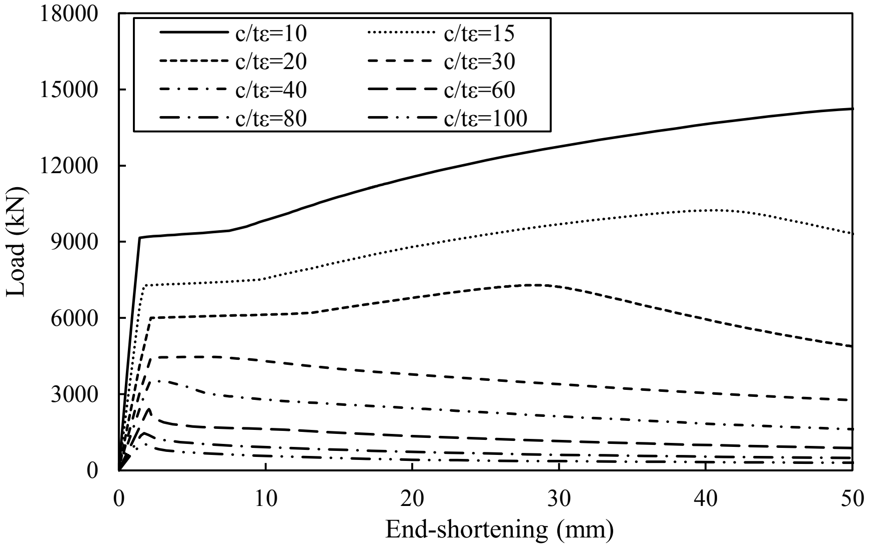

Figure 4.5: Typical load-end-shortening curves.

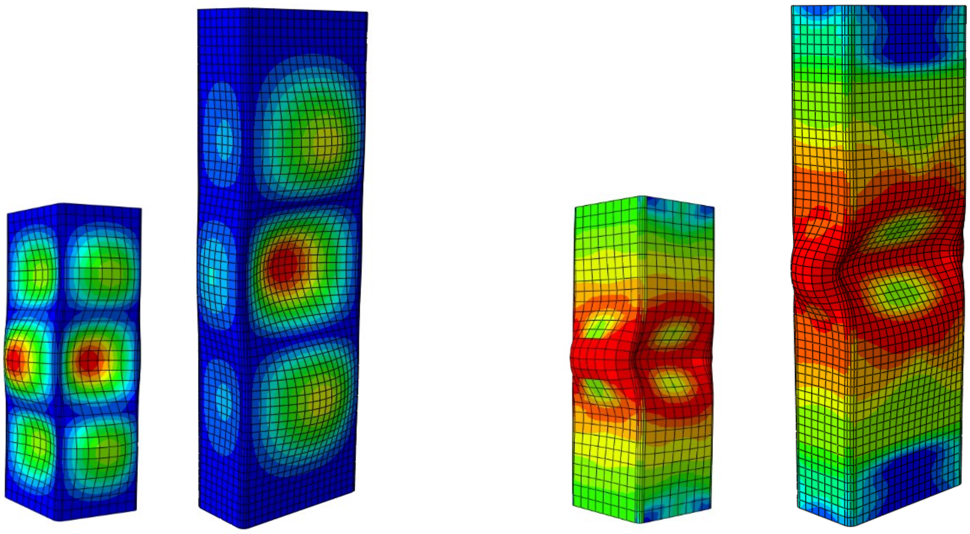

a) elastic buckling modes
SHS (left), RHS (right)
(displacement contour plot)

b) failure modes
SHS (left), RHS (right)
(stress contour plot)

Figure 4.6: Typical numerical elastic buckling mode shapes (left) and failure modes (right).

4.6. Analysis of the results and design recommendations

This section discusses the results on the stub column parametric studies and provides relevant design recommendations. The key parameters affecting the compressive strength of HSS stub columns are firstly discussed. The applicability of Eurocode specifications, namely the Class 3 limit for internal elements in compression and the effective width equations, to HSS sections is then assessed. On the basis of the results for slender sections, a new approach making allowance of the interaction effects among the constituent plate elements is proposed. For S460 sections in the stocky slenderness range, where pronounced strain-hardening has been observed, the suitability of the continuous strength method is investigated.

4.6.1. Influence of key parameters on the compressive response

The normalised ultimate compressive capacity obtained from the tests and the FE analyses is plotted against the cross-section slenderness $c/t\varepsilon$, thus enabling the influence of key parameters on the compressive behaviour to be visualised. The effect of the steel grade and the cross-section aspect ratio is shown in Figure 4.7(a) and Figure 4.7(b) respectively. As can be observed, the stocky S460 stub columns are able to reach higher normalised compressive capacities than their S690 counterparts, making evident the effect of the material strain-hardening characteristics on the performance of cross-sections in the stocky slenderness range. This effect appears minimal for slender sections, in which failure is triggered by local buckling at strains within or below the yield plateau. For sections, where failure occurs in the elastic range, the compressive behaviour is influenced by the cross-section aspect ratio. In particular, the normalised compressive performance improves for increasing aspect ratio. This can be associated with a delay in the onset of local buckling owing to the greater degree of restraints provided by the more stocky flanges of sections with increasing aspect ratio to the critical webs.

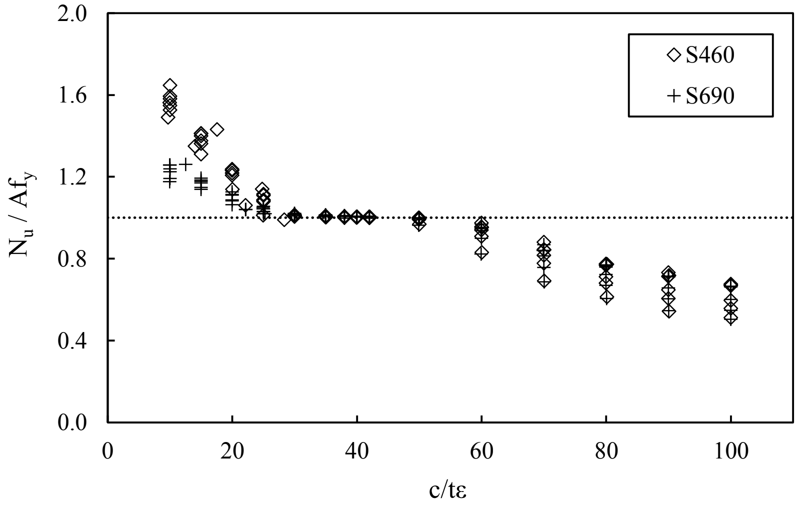

a) Steel grade

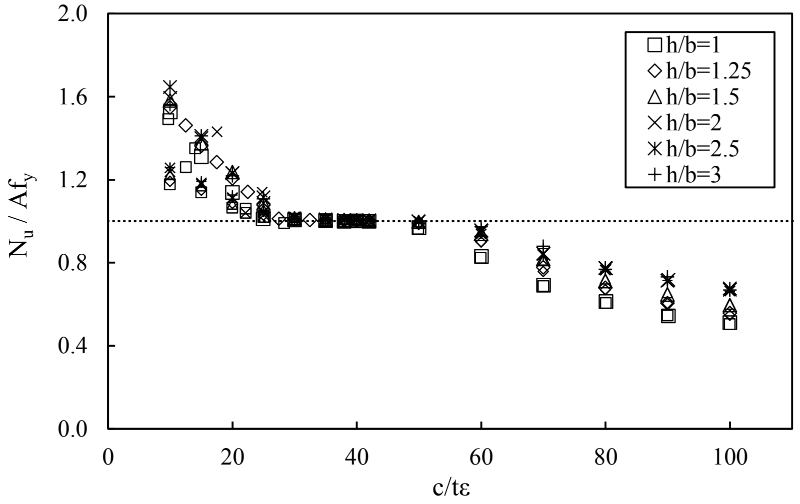

b) Cross-section aspect ratio

Figure 4.7: Influence of key parameters on the compressive response.

4.6.2. Assessment of the Eurocode Class 3 limit

In order to assess the suitability of the Eurocode Class 3 limit of 42 for internal elements in compression (BS EN 1993-1-1, 2014) for S460 and S690 hollow sections, the ultimate loads are normalised by their squash loads and plotted against the cross-section slenderness of the most slender constituent plate element. The results are presented in Figure 4.8. In order for the slenderness limit to be acceptable, the sections with cross-section slenderness lower than the specified limit should have a normalised load capacity higher than unity (i.e. ultimate load higher than the squash load). Since the sections within the cross-section slenderness range 30-42 have failed at strains within the yield plateau achieving a normalised axial capacity equal to unity, the limit of 42 could accurately predict the transition limit from a fully effective to a slender section.

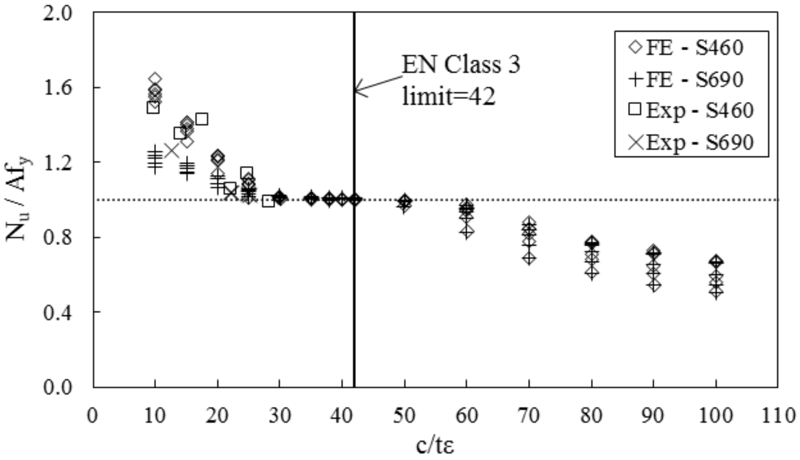

Figure 4.8: Assessment of the Eurocode Class 3 limit.

4.6.3. Assessment of the effective width equations

For the estimation of the axial capacity of Class 4 sections, the traditional method of effective width equations is adopted by EN 1993-1-5 (2006). As explained in Subsection 2.3.2, once determining the effective width of each constituent element as a function of the plate slenderness $\bar{\lambda}_p$ and the buckling coefficient k_c, then the total effective cross-sectional area can be found. Multiplying the effective cross-sectional area with the yield stress, the cross-sectional compressive resistance can be obtained.

In order to assess the applicability of the obtained results to Eurocode effective width equations, the actual reduction factor ρ_w of the FE results are plotted against the critical web slenderness λ_w in Figure 4.9, where the Eurocode design curve is also included. Given that focus is set on the plate interaction effects hereafter, the results are presented with respect to their cross-section aspect ratio.

For the calculation of the actual reduction factors ρ_w, Equations (4.1)-(4.2) have been developed for rectangular hollow sections with fully effective flanges (i.e. $c/t\varepsilon$ of the flange lower than Class 3 limit) and for square and rectangular hollow sections with critical both the flanges and the webs, respectively. Note that Equation (4.2) assumes that the ratio of the flange to the web reduction factor (ρ_f/ρ_w) is equal to the one specified in EN 1993-1-5 (2006).

$$\rho_w = \frac{N_{u,FE} - f_y A_c - 2 f_y b_f t}{2 f_y b_w t} \tag{4.1}$$

$$\rho_w = \frac{N_{u,FE} - f_y A_c}{2 f_y t (b_w + b_f \frac{\rho_f}{\rho_w})} \tag{4.2}$$

where $N_{u,FE}$ is the numerical failure load of the modelled stub column, A_c is the area of the corner region which is assumed to be fully effective, b_f is the width of the fully effective flanges and b_w the width of the slender webs (i.e. longer faces). In addition to Figure 4.9, Table 4.4 reports the achieved ratios of the Eurocode to the numerically attained reduction factors $\rho_{w,EC3}/\rho_{w,FE}$ for each studied cross-section aspect ratio. Ratios lower than unity correspond to safe predictions. Although Eurocode effective width equations are generally capable of predicting safe values, a trend of more conservative estimations for hollow sections with increasing aspect ratio is clearly apparent. Note that Eurocode recommends considering the buckling coefficient for internal elements in compression equal to 4, assuming simply-supported action on the edges, for both square and rectangular hollow sections. However, the performance of slender sections is affected by the cross-section aspect ratio. In particular, the delay on the commencement of local buckling of the slender webs occurring in sections with stockier flanges results in higher compressive capacities in sections with higher cross-section aspect ratio. The disregard of this phenomenon by Eurocode is the reason for the scattered estimations observed in rectangular hollow sections with different cross-section aspect ratios. In HSS structures that aim in reduced material use through the increased material strength, slender sections might often be encountered. Hence, a design approach providing consistently safe, yet economic strength predictions is needed.

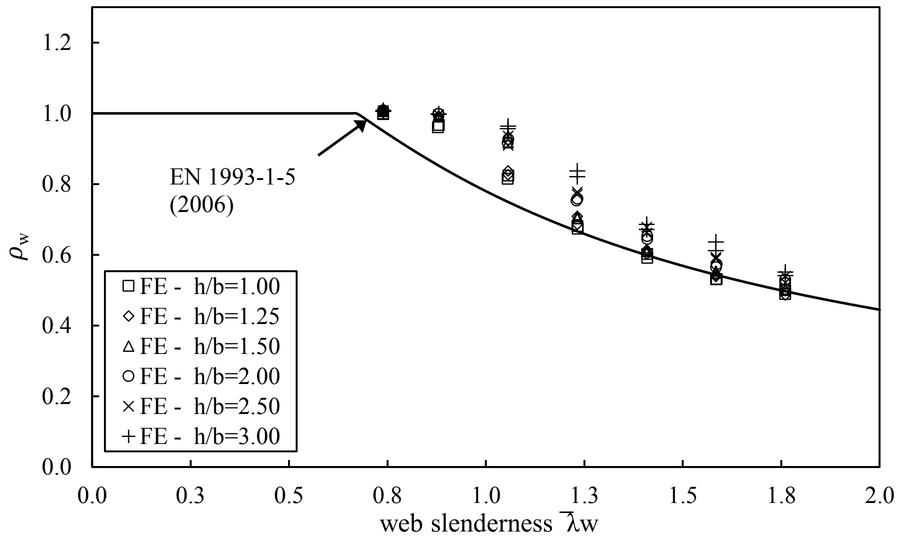

Figure 4.9: Assessment of the effective width equations.

Table 4.4: Assessment of the effective width equations.

Cross-section aspect ratio	h/b=1.00	h/b=1.25	h/b=1.50	h/b=2.00	h/b=2.50	h/b =3.00	MEAN	COV
$\rho_{w,EC3}/\rho_{w,FE}$	0.97	0.95	0.94	0.90	0.88	0.85	0.91	0.07

4.6.4. Effective cross-section method for slender sections

In this section, a method, named effective cross-section method hereafter, taking due account of the element interaction effects in slender sections is proposed. The design approach is based on a previously presented method for slender stainless steel sections (Zhou et al., 2013a; Bock and Real, 2015). Instead of determining a reduction factor for each constituent element, the new design approach recommends a reduction factor ρ_{cs}, expressed as a function of the plate slenderness $\bar{\lambda}_p$ and the cross-section aspect ratio h/b, applied to the whole gross cross-section area. The developed equations have been based on the numerical results of the validated finite element models and have been evolved in the following three steps.

As a first step, the normalised compressive capacities, excluding the contribution of the corner regions which are considered not to undergo local buckling, have been used for the determination of the cross-section reduction factor ρ_{cs}. The modified Winter curve of Equation (4.3), where the plate slenderness is in accordance with Eurocode, has been used in order to extract a relationship between the between the reduction factor ρ_{cs} and the cross-section slenderness $c/t\varepsilon$ of the most slender element.

$$\rho_{cs} = \frac{\bar{\lambda}_p - A}{\bar{\lambda}_p{}^B} = \frac{\frac{c}{28.4\sqrt{k_c}t\varepsilon} - A}{\left(\frac{c}{28.4\sqrt{k_c}t\varepsilon}\right)^B} = \frac{\frac{c}{56.8t\varepsilon} - A}{\left(\frac{c}{56.8t\varepsilon}\right)^B} \tag{4.3}$$

where the coefficients A and B have been determined with the execution of linear regression analysis for each of the considered cross-section aspect ratios. The extracted values plotted against the respective cross-section aspect ratios are shown in Figure 4.10.

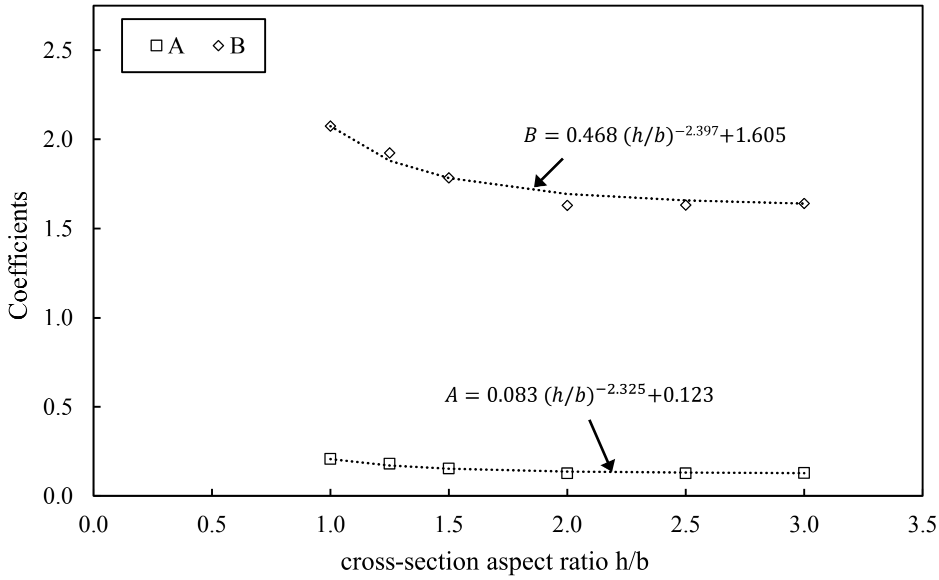

Figure 4.10: Determination of coefficients A and B.

At a second step, in order to relate the A and B coefficients to the aspect ratio h/b, best fit analysis has been applied to the data of Figure 4.10, leading to the empirical Equations (4.4)-(4.5).

$$\mathrm{A} = 0.083\ (h/b)^{-2.325} + 0.123 \tag{4.4}$$

$$\mathrm{B} = 0.468\ (h/b)^{-2.397} + 1.605 \tag{4.5}$$

The third step included the incorporation of Equations (4.4)-(4.5) to (4.3) that allowed the derivation of different design curves for each considered cross-section aspect ratio. The proposed curves together with results of the numerical study are depicted in Figure 4.11, whereas the attained $\rho_{\text{cs,Pred}}/\rho_{\text{cs,FE}}$ ratios are reported in Table 4.5. It is certainly evident that the new cross-section effective method is able to produce better predictions than the traditional method of effective width equations. It should also be noted that the strength calculation based on the effective width equations could be cumbersome for complex geometries, whilst the new design approach provides a reduced strength prediction as a function of the cross-section slenderness and the cross-section aspect ratio, without the need of compound calculations.

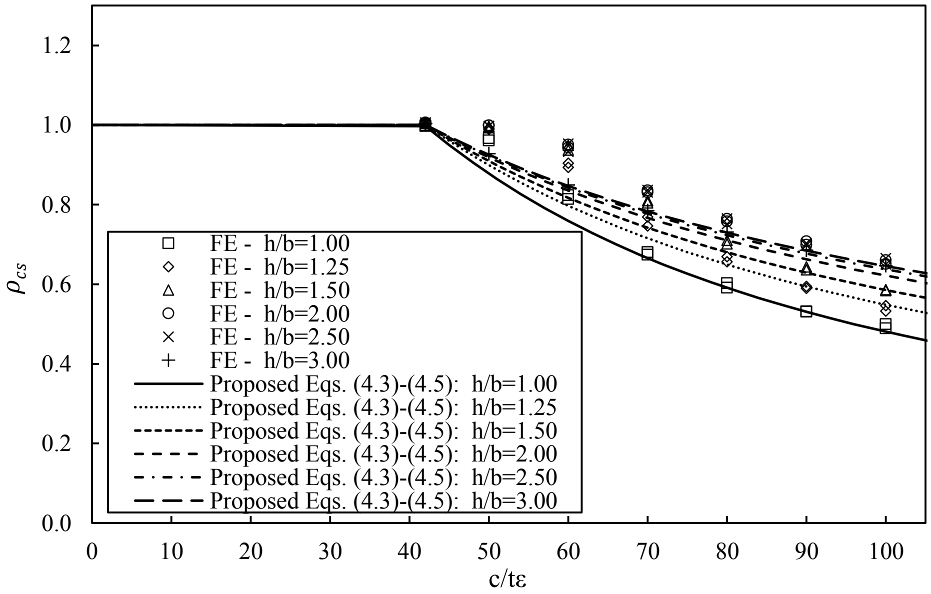

Figure 4.11: Proposed effective cross-section method for Class 4 HSS sections.

Table 4.5: Assessment of the proposed effective cross-section design method.

Aspect ratio	h/b =1.00	h/b =1.25	h/b =1.50	h/b =2.00	h/b =2.50	h/b =3.00	MEAN	COV
$\rho_{\text{cs,Pred}}$ $/\rho_{\text{cs,FE}}$	0.97	0.96	0.95	0.93	0.95	0.95	0.95	0.04

4.6.5. Continuous strength method for stocky sections

As earlier observed, the Eurocode strength predictions for S460 sections with $\bar{\lambda}_{cs} \leq 0.68$ were quite conservative owing to the pronounced material strain-hardening characteristics that are ignored by Eurocode, which considers an elastic-perfectly plastic material response. Improved estimations could be pursued through the application of the continuous strength method CSM that has been developed in order to allow for a balanced exploitation of the material strain-hardening properties.

CSM is based on a continuous relationship between the cross-section slenderness and the cross-section deformation capacity, the so-called base curve. In order to evaluate the applicability of CSM to S460 stocky sections, the $\varepsilon_u/\varepsilon_y$ ratio, where ε_u is the strain at failure load, defined as the end-shortening at ultimate load normalised by the initial stub column length and ε_y the strain at yield load, has been plotted against the cross-section slenderness $\bar{\lambda}_{cs}$ in Figure 4.12. The CSM base curve of Equation (2.14) is also plotted in the same figure for comparison purposes. As can be seen the obtained results do not match closely the CSM base curve. This might be attributed to the difference in the material characteristics between materials with a yield plateau (i.e. considered high strength steel grades) and Ramberg-Osgood material types (stainless steel, aluminium etc.), upon which CSM base curve was based. A least square regression analysis has been executed to obtain a new relationship applicable to the currently studied hot-finished sections and Equation (4.6) has been derived. It should be noted that the limit of $\varepsilon_{csm}/\varepsilon_y$ =15 set by CSM concerns ductility requirements and aims to prevent from ductile fracture in flexural members. This limit is related to the Eurocode material ductility requirements $(\varepsilon_u/\varepsilon_y)$ which is 15 for stainless and carbon steel (BS EN 1993-1-1, 2014), whilst has been reduced to 10 for higher steel grades (EN 1993-1-

12, 2007). Nevertheless, given that only compressive members, where tensile fracture cannot occur, are investigated in the current chapter, the aforementioned limit has not been adopted for the design of stub columns.

$$\frac{\varepsilon_{csm}}{\varepsilon_y} = \frac{0.027}{\bar{\lambda}_{cs}^{\,2.63+9.94\bar{\lambda}_{cs}}} \tag{4.6}$$

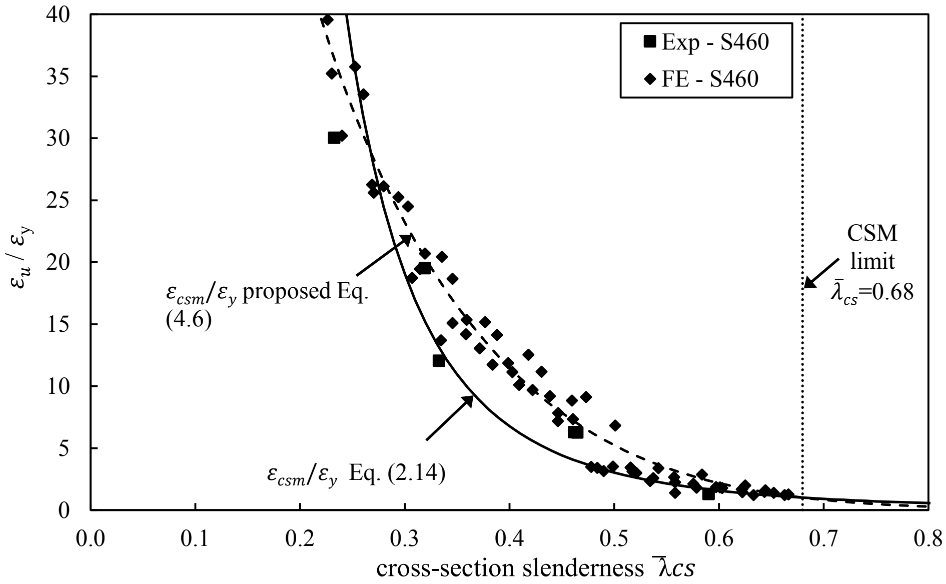

Figure 4.12: CSM base curve: $\varepsilon_u/\varepsilon_y$ against cross-section slenderness $\bar{\lambda}_{cs}$.

Once the base curve is established, focus is set on the assumed material response. The material model should be capable of sufficiently approximating the real material behaviour, whilst capturing the strain-hardening effect. Following the EN 1993-1-5 (2006) recommendation for a bilinear model with a modest strain-hardening modulus, equal to $E_{sh} = 1/100$, a very good representation of the S460 stress-strain response was achieved, as shown in Figure 4.13. Note that the evolution of more complicated trilinear models has been attempted, but was found to further complicate the design equations, without significantly improving the accuracy of the predicted capacities. This is due to the large scatter of the length of the yield plateau exhibited by steel.

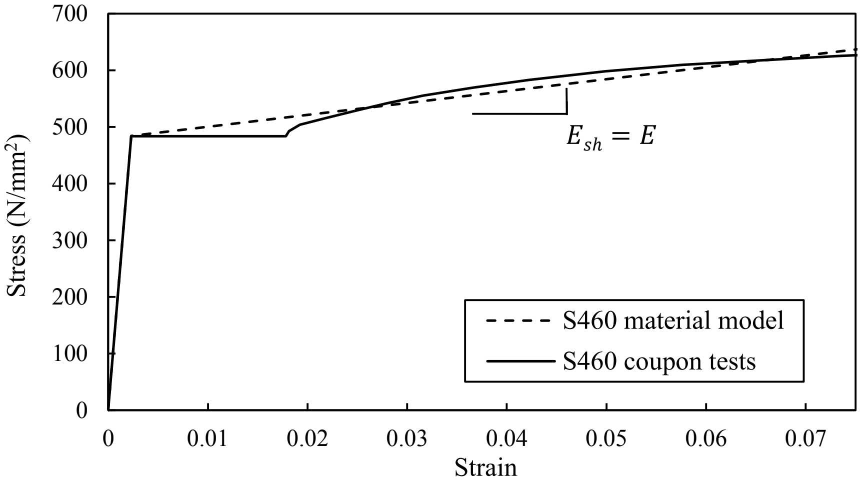

Figure 4.13: Assumed material model for the application of the CSM.

Having established the material model, the ultimate compressive capacities of the test and FE results are normalised by the CSM ones and plotted against the cross-section slenderness in Figure 4.14. For the calculation of the CSM strength, Equations (4.6) and (2.15) have been applied. As can be seen, an apparent improvement in the design estimations can be achieved by the application of the CSM. The same conclusion is drawn from Table 4.6, where the normalised Eurocode and CSM predictions are presented, showing more consistent and less conservative values for the CSM estimations.

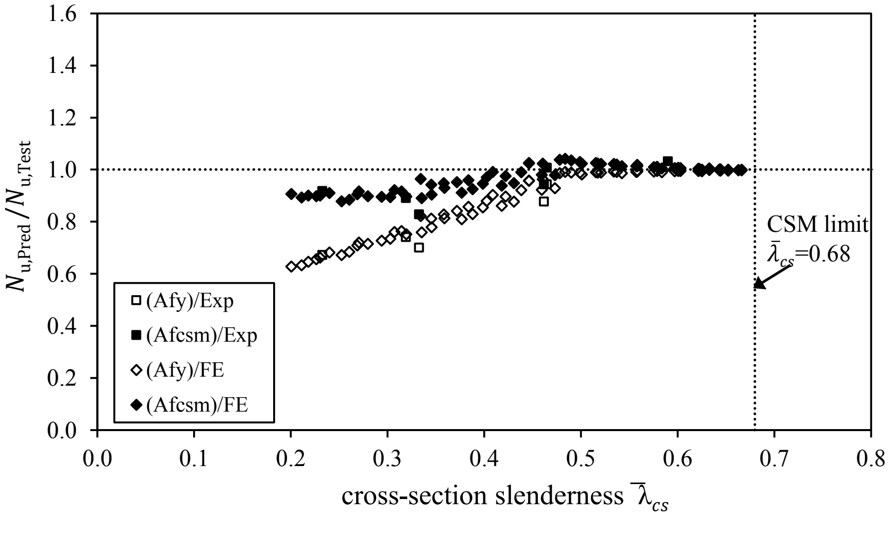

Figure 4.14: Assessment of the continuous strength method.

Table 4.6: Assessment of the continuous strength method.

	FE results (S460)		Experimental results (S460)	
	$N_{\mathrm{u,EC3}}/N_{\mathrm{u,FE}}$	$N_{\mathrm{u,CSM}}/N_{\mathrm{u,FE}}$	$N_{\mathrm{u,EC3}}/N_{\mathrm{u,Exp}}$	$N_{\mathrm{u,CSM}}/N_{\mathrm{u,Exp}}$
MEAN	0.82	0.97	0.88	0.94
COV	0.17	0.05	0.14	0.08

4.7. Concluding remarks

The current chapter investigated the compressive response of high strength steel square and rectangular hollow sections. The influence of the material characteristics and the cross-section aspect ratio were firstly discussed. On the basis of the results, the Eurocode Class 3 limit was assessed and it was concluded that the current limit seems acceptable for the results of the present study. The application of the Eurocode effective width equations led to conservative strength estimations for rectangular hollow sections with high aspect ratios. To overcome this issue, the effective cross-section method was presented. The new approach that suggests a reduction factor applied to the whole cross-sectional area, yields safe yet economic design estimations for hollow sections with different aspect ratios.

To improve the overly conservative Eurocode strength predictions for S460 stocky sections, the suitability of the continuous strength method was evaluated. In order to make the method applicable to the hot-finished sections investigated in the current chapter, a new relationship between the cross-section slenderness and the cross-section deformation capacity was introduced. The CSM, which is able to take into account the material strain-hardening characteristics, led to improved and more consistent strength predictions. Further research is necessary to evaluate the applicability of the proposed equations to other data of HSS grades, thus facilitating their inclusion in future versions of design specifications.

CHAPTER 5: HIGH STRENGTH STEEL MEMBERS IN BENDING

5.1. Introduction

This chapter presents an extensive study on the flexural response of HSS square and rectangular hollow sections. Numerical models were created and validated against the test data of twenty-two in-plane bending tests. Upon successful validation of the numerical models, the influence of the cross-section aspect ratio, the cross-section slenderness and the moment gradient on the structural performance of HSS sections was studied thorough parametric studies. The results were discussed and utilised for the assessment of current European specifications (BS EN 1993-1-1, 2014; EN 1993-1-12, 2007).

5.2. Brief description of the test programme

A schematic graph of the 3-point and the 4-point bending configuration test set-up at the Structures Lab of Imperial College London is shown in Figure 5.1(a) and Figure 5.1(b) respectively. The beams were simply-supported on steel rollers and loaded by a 2000 kN Instron hydraulic jack. In the 3-point bending tests, the load was applied at mid-span, whilst in the 4-point configuration a spreader beam was used to symmetrically distribute the load at two points at a distance $L/3$ from the end supports. Wooden blocks have been inserted in the hollow sections at the location of the supports and of the loading points in order to prevent local bearing failure. The test set-up was displacement controlled. In all cases, bending was about the cross-section major axis. Instrumentation including strain gauges, inclinometers and LVDTs, as shown in Figure 5.1 were used in order to measure the strains, the rotations and the vertical displacements during the tests. The recorded measurements allowed the capture of the moment-rotation and the moment-curvature response for the 3-point and the 4-point tests respectively, as well as the evaluation of the ultimate moment capacity M_u.

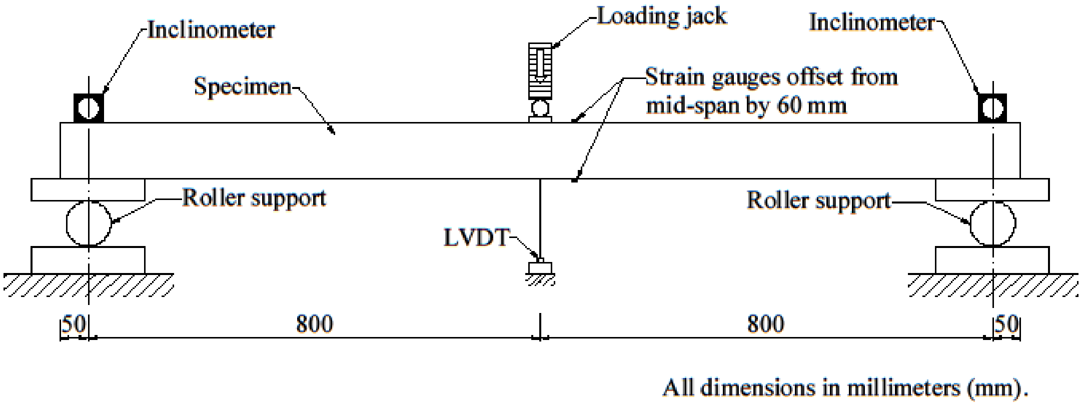

a) 3-point beam

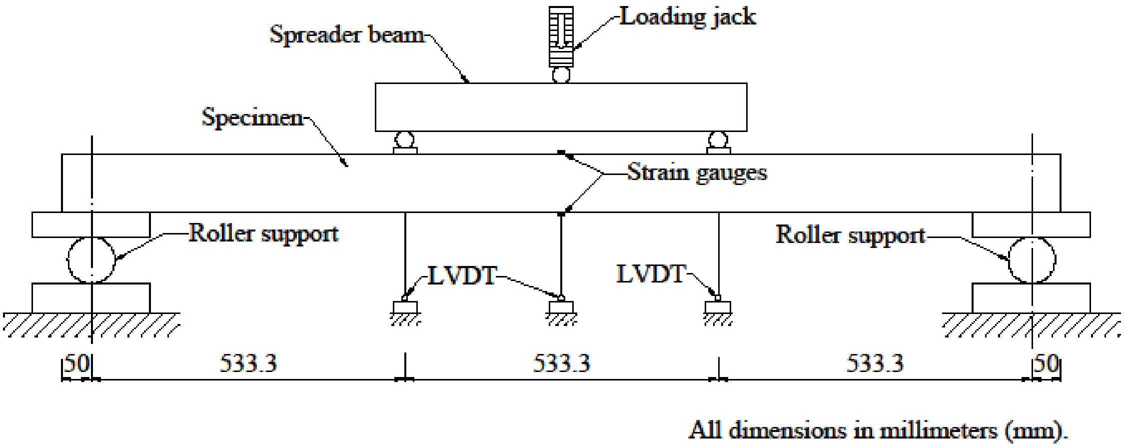

b) 4-point beam

Figure 5.1: Schematic diagram of the test set-up.

The average measured dimensions of the tested specimens together with the measured geometric imperfections are given in Table 5.1. All specimens were $1700\,mm$ long with $50\,mm$ overhang at each end, resulting in $1600\,mm$ clear span.

Table 5.1: Measured dimensions of the 3-point and 4-point beams.

Cross-section	Span (mm)	$h\ (mm)$	$b(mm)$	$t(mm)$	$r_i(mm)$	$\omega_0(mm)$
S460 SHS 50×50×5	1600	50.41	50.36	4.92	3.25	0.054
S460 SHS 50×50×4	1600	50.37	50.47	3.89	3.19	0.043
S460 SHS 100×100×5	1600	99.76	99.67	5.29	4.88	0.077
S460 SHS 90×90×3.6	1600	89.79	89.64	3.71	4.50	0.083
S460 RHS 100×50×6.3	1600	99.82	49.83	6.40	5.44	0.049
S460 RHS 100×50×4.5	1600	99.59	49.94	4.64	5.50	0.070
S690 SHS 50×50×5	1600	50.44	50.53	4.94	3.46	0.076
S690 SHS 100×100×5.6	1600	100.53	100.47	5.66	5.59	0.081
S690 SHS 90×90×5.6	1600	90.48	90.46	5.74	4.92	0.089
S690 RHS 100×50×6.3	1600	100.27	49.92	6.46	4.88	0.106
S690 RHS 100×50×5.6	1600	100.51	49.89	5.69	5.75	0.156

The two configurations allowed the comparison of the flexural response under both a moment gradient (3-point tests) and constant moment (4-point tests). Local buckling was the pronounced failure mode in all cases. Key results are reported in Table 5.2(a) and Table 5.2(b), whilst further details are provided in Wang et al. (2016). The calculation of the cross-section elastic M_{el} and plastic M_{pl} moment resistance was based on the measured geometry of the sections. The rotation capacity of the 3-point beams and the 4-point beams was calculated according to Equations (5.1) and (5.2) respectively, where θ_u (κ_u) is the rotation for 3-point bending (curvature for 4-point bending) at which the moment-rotation (moment-curvature) curve falls below M_{pl} on the descending branch, and θ_{pl} (κ_{pl}) is the elastic rotation (curvature) corresponding to M_{pl} on the ascending branch. For the determination of the curvature κ in the 4-point bending configuration, it was assumed that the deflected shape of the beam at the central region can be represented by a circular arc (of radius r) (Rasmussen and Hancock, 1993). Hence the curvature can be calculated according to Equation (5.3), where δ_M is the vertical displacement at mid-span and δ_L is the average vertical displacement at the two loading points, as shown in Figure 5.2. Note that in certain cases the tests needed to be stopped before the ultimate moment/rotation (or curvature) capacity was reached or before the bending moment fell below M_{pl}, due to reaching the maximum jack displacement. In these cases, the maximum recorded moment/rotation (or curvature) was used instead.

$$R = \frac{\theta_u}{\theta_{pl}} - 1, \text{ where } \theta_{pl} = M_{pl}L/(2EI) \tag{5.1}$$

$$R = \frac{\kappa_u}{\kappa_{pl}} - 1 \text{ where } \kappa_{pl} = M_{pl}/(2EI) \tag{5.2}$$

$$\kappa = \frac{1}{r} = \frac{8(\delta_M - \delta_L)}{L_2^2 + 4(\delta_M - \delta_L)^2} = \frac{8y}{L_2^2 + 4y^2} \tag{5.3}$$

Table 5.2: Summary of the beam tests.

a) 3-point beams

Cross-section	M_u (kNm)	M_{el} (kNm)	M_{pl} (kNm)	M_u/M_{el}	M_u/M_{pl}
S460 SHS 50×50×5	8.67	5.78	7.26	1.50	1.19
S460 SHS 50×50×4	7.17	5.01	6.14	1.43	1.17
S460 SHS 100×100×5	38.88	28.94	34.57	1.34	1.12
S460 SHS 90×90×3.6	20.73	16.51	19.47	1.26	1.06
S460 RHS 100×50×6.3	39.26	18.43	24.30	2.13	1.62
S460 RHS 100×50×4.5	23.68	14.57	18.78	1.63	1.26
S690 SHS 50×50×5	12.56	8.61	10.83	1.46	1.16
S690 SHS 100×100×5.6	58.25	47.11	56.55	1.24	1.03
S690 SHS 90×90×5.6	46.59	37.55	45.46	1.24	1.02
S690 RHS 100×50×6.3	46.44	30.57	40.26	1.52	1.15
S690 RHS 100×50×5.6	41.69	27.03	35.36	1.54	1.18

b) 4-point beams

Cross-section	M_u (kNm)	M_{el} (kNm)	M_{pl} (kNm)	M_u/M_{el}	M_u/M_{pl}
S460 SHS 50×50×5	7.03	5.61	7.04	1.25	1.00
S460 SHS 50×50×4	6.25	5.06	6.22	1.24	1.01
S460 SHS 100×100×5	38.61	28.79	34.42	1.34	1.12
S460 SHS 90×90×3.6	20.81	16.87	19.94	1.23	1.04
S460 RHS 100×50×6.3	32.46	18.94	24.91	1.71	1.30
S460 RHS 100×50×4.5	23.28	14.74	18.93	1.58	1.23
S690 SHS 50×50×5	11.59	8.55	10.74	1.36	1.08
S690 SHS 100×100×5.6	54.91	47.32	56.78	1.16	0.97
S690 SHS 90×90×5.6	42.88	37.37	45.14	1.15	0.95
S690 RHS 100×50×6.3	42.25	30.83	40.51	1.37	1.04
S690 RHS 100×50×5.6	37.87	26.93	35.13	1.41	1.08

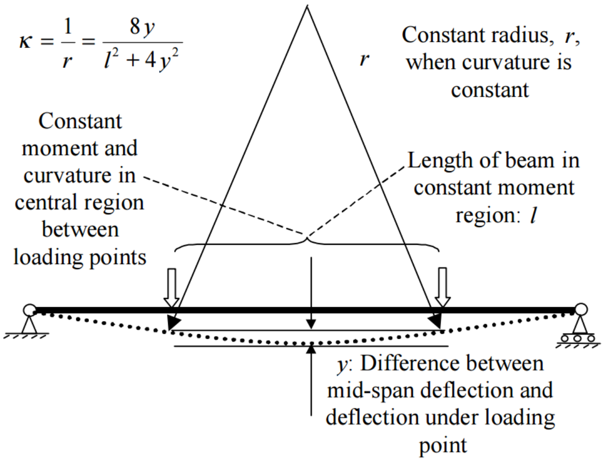

Figure 5.2: Determination of curvature from deflection (Wilkinson and Hancock, 1999).

5.3. Development of the finite element models

In line with the numerical modelling assumptions described in Chapter 3, S4R elements have been adopted for the development of the finite element models. Symmetry in geometry, loading, boundary conditions and observed failure modes of the test configuration was exploited in the finite element modelling of the beams. The modelled section together with the applied constraints and boundary conditions can be seen in Figure 5.3. The vertical and lateral displacements of the two supports were constrained at the bottom flange (RP LEFT/RIGHT), whilst kinematic coupling was employed at the support locations to ensure that the cross-sections remain undeformed. The longitudinal displacement along the axis of the beam was restrained at mid-span, whilst suitable symmetry boundary conditions were applied at the intersection of the section with assumed plane of symmetry. In order to prevent localised bearing failure at the point of load application, the load was assigned at the lower part of the web in the web-corner junction. This approach in line with similar studies (Theofanous and Gardner, 2010) was deemed able to capture the effect of the inserted wooden blocks, which local strengthened the loaded sections, on the observed structural response.

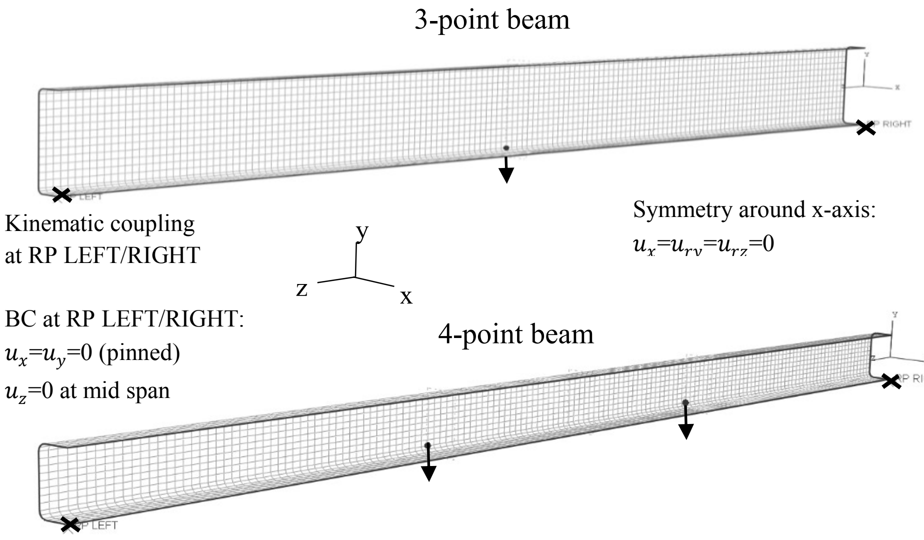

Figure 5.3: Numerical beam model.

Having developed the FE models, linear elastic buckling analysis was initially performed and the extracted mode shapes were introduced as initial geometric imperfections in the subsequent nonlinear static analysis. The incremental load, the mid-span vertical deflection, the end-rotation of the supports and the vertical displacement at the load location were recorded during the nonlinear analysis. Similarly to the experiments, the moment-rotation curves were created for the 3-point beams and the moment-curvature curves for the 4-point ones.

5.4. Validation of the finite element models

Upon the development of the numerical models, the flexural behaviour was investigated for six initial geometric imperfection amplitudes. The numerically obtained ultimate moment capacities were compared with the experimental ones. It should be noted that the ultimate moment capacity of the FE models was considered as the maximum moment achieved during the nonlinear static analysis. For some stocky beams that local buckling was not attained (see Figure 5.4(d)), it was assumed that the ultimate moment was the one corresponding to maximum tensile stress equal to the ultimate stress, since stress higher than that would lead to fracture. The comparisons are presented in Table 5.3. The best calibration against the test performance for both the 3-point and the 4-point bending configurations was obtained for the $t/50$ imperfection amplitude.

To further evaluate the accuracy of the numerical models, the full load-deformation paths were plotted together with test data for the purposes of model validation, as shown for typical cases in Figure 5.4(a)-Figure 5.4(d). As can be observed, the initial stiffness and the general form of the load-deformation response were accurately replicated. The ultimate moment capacity appeared to have small sensitivity to the imperfection amplitude, whereas the variation in the imperfection amplitude had more significant influence on the rotation at which the ultimate load was captured. Very good agreement between the finite element results and the tests was overall achieved. Finally, the numerical models were deemed capable of capturing the experimental failure modes, as illustrated for representative cases in Figure 5.5.

Table 5.3: Comparison of FE and test data.

a) 3-point beams

	Imperfection amplitude					
	0	ω_0	$t/100$	$t/50$	$t/10$	ω_{DW}
Specimen	$M_{u,FE}/M_{u,Exp}$	$M_{u,FE}/M_{u,Exp}$	$M_{u,FE}/M_{u,Exp}$	$M_{u,FE}/M_{u,Exp}$	$M_{u,FE}/M_{u,Exp}$	$M_{u,FE}/M_{u,Exp}$
S460 SHS 50×50×5	1.01	1.01	1.01	1.01	1.01	1.01
S460 SHS 50×50×4	1.05	1.04	1.04	1.03	0.99	1.04
S460 SHS 100×100×5	0.98	0.95	0.96	0.95	0.9	0.96
S460 SHS 90×90×3.6	0.98	0.96	0.98	0.97	0.92	0.97
S460 RHS 100×50×6.3	1.01	1.01	1.01	1.00	0.98	1.01
S460 RHS 100×50×4.5	1.06	1.06	1.06	1.06	1.02	1.06
S690 SHS 50×50×5	0.99	0.99	0.99	0.99	0.97	0.99
S690 SHS 100×100×5.6	1.01	1.00	1.00	1.00	0.97	1.00
S690 SHS 90×90×5.6	1.02	1.02	1.02	1.02	0.99	1.02
S690 RHS 100×50×6.3	1.00	1.00	1.00	1.00	0.98	1.00
S690 RHS 100×50×5.6	0.98	0.98	0.98	0.98	0.96	0.98
MEAN	1.01	1.00	1.01	1.01	0.97	1.01
COV	0.03	0.03	0.03	0.03	0.04	0.03

b) 4-point beams

	Imperfection amplitude					
	0	ω_0	$t/100$	$t/50$	$t/10$	ω_{DW}
Specimen	$M_{u,FE}/M_{u,Exp}$	$M_{u,FE}/M_{u,Exp}$	$M_{u,FE}/M_{u,Exp}$	$M_{u,FE}/M_{u,Exp}$	$M_{u,FE}/M_{u,Exp}$	$M_{u,FE}/M_{u,Exp}$
S460 SHS 50×50×5	1.04	1.04	1.04	1.04	1.03	1.04
S460 SHS 50×50×4	0.96	0.96	0.95	0.95	0.95	0.95
S460 SHS 100×100×5	0.96	0.95	0.96	0.94	0.86	0.95
S460 SHS 90×90×3.6	1.01	0.93	0.96	0.94	0.92	0.95
S460 RHS 100×50×6.3	0.97	0.97	0.97	0.97	0.97	0.97
S460 RHS 100×50×4.5	0.96	0.96	0.96	0.96	0.95	0.96
S690 SHS 50×50×5	1.00	1.00	1.00	1.00	1.00	1.00
S690 SHS 100×100×5.6	1.01	1.01	1.01	1.01	1.00	1.01
S690 SHS 90×90×5.6	1.04	1.04	1.04	1.04	1.03	1.04
S690 RHS 100×50×6.3	1.01	1.01	1.01	1.01	1.01	1.01
S690 RHS 100×50×5.6	0.98	0.98	0.98	0.98	0.98	0.98
MEAN	0.99	0.99	0.99	0.99	0.97	0.99
COV	0.03	0.03	0.03	0.04	0.05	0.03

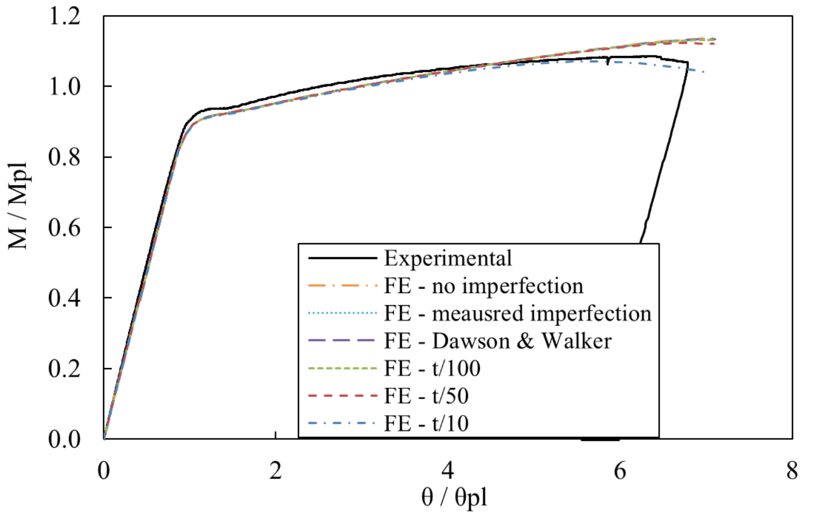

a) 3-point beam - SHS S460 50×50×4

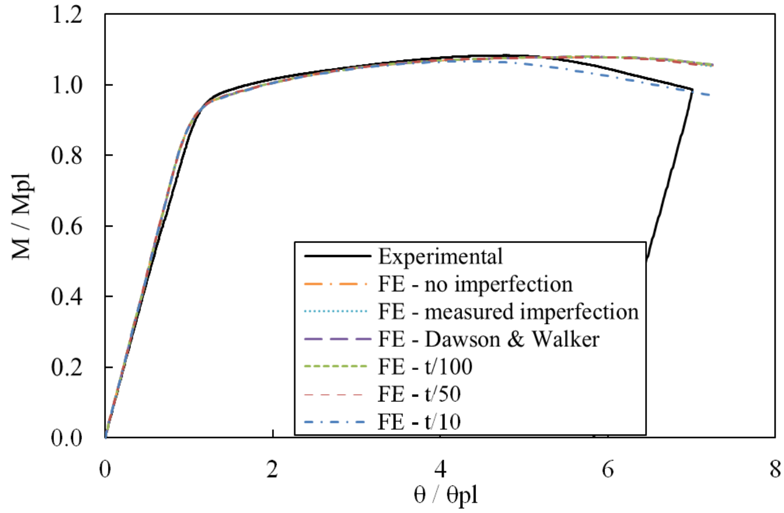

b) 3-point beam - RHS S690 100×50×6.3

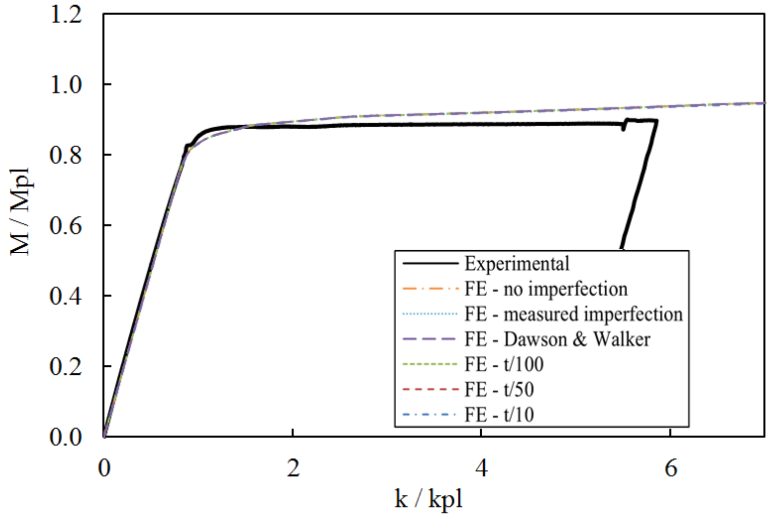

c) 4-point beam - SHS S460 50×50×5

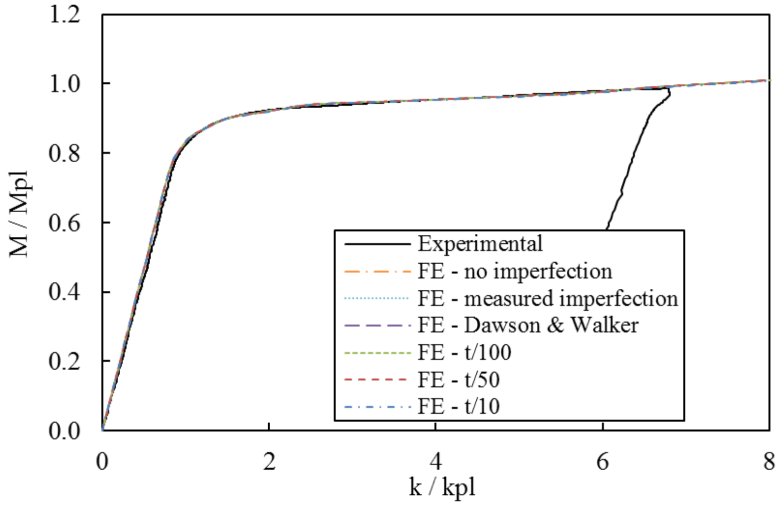

d) 4-point beam - RHS S690 90×90×5.6

Figure 5.4: Validation of FE models for 3-point and 4-point beams.

a) 3-point beam - S460 RHS 100×50×4.5

b) 4-point beam - S690 SHS 50×50×5

Figure 5.5: Typical experimental and numerical failure modes (Wang et al., 2016).

5.5. Parametric studies

Following the successful validation of the finite element models, comprehensive parametric studies were performed in order to generate additional data. Focus was set on the influence of the cross-section slenderness, the cross-section aspect ratio (i.e. the plate-element interaction), the moment gradient and the material strain-hardening characteristics on the structural behaviour of tubular sections under bending. Therefore, the following cases were considered for both S460 and S690 steel grades:

- Twelve different sections with varying thickness to provide cross-section slenderness $c/t\varepsilon$ = 10÷90.
- Three cross-section aspect ratios (h/b): 1.00, 2.00 and 2.44.

- Three testing configurations: 3-point with L/h=10, 3-point with L/h=20, 4-point with L/h=20.

In total, 216 additional 3-point and 4-point bending tests were performed using the validated finite element models. The material properties adopted in the parametric studies were based on the averaged flat coupon stress-strain curves (Figure 3.8). An initial elastic linear buckling analysis was executed and a geometric imperfection amplitude of $t/50$ which was the one that gave the best calibration against the test results was adopted in the parametric studies. Typical elastic buckling and failure modes are shown in Figure 5.6, whereas the full moment-rotation histories for some representative cases are plotted in Figure 5.7.

It is worth pointing out that based on the equation of the non-dimensional plate slenderness $\lambda_p = \sqrt{\frac{f_y}{f_{cr}}}$, as defined in EN 1993-1-5 (2006), and on the different stress distribution of the flange and the web through the Eurocode values for the buckling coefficient k_σ ($k_\sigma = 4$ for internal simply supported elements under compression, hence the flange, and $k_\sigma = 23.9$ internal simply supported elements under bending, hence the web), 2.44 is the limit in aspect ratio value that leads to equal slenderness for the compression flange and the web of a hollow section subjected to bending. Therefore, 2.44 is the most unfavorable aspect ratio value, as both the flange and the web are equally slender and hence prone to local buckling and no support offered from the stockier to the more slender elements.

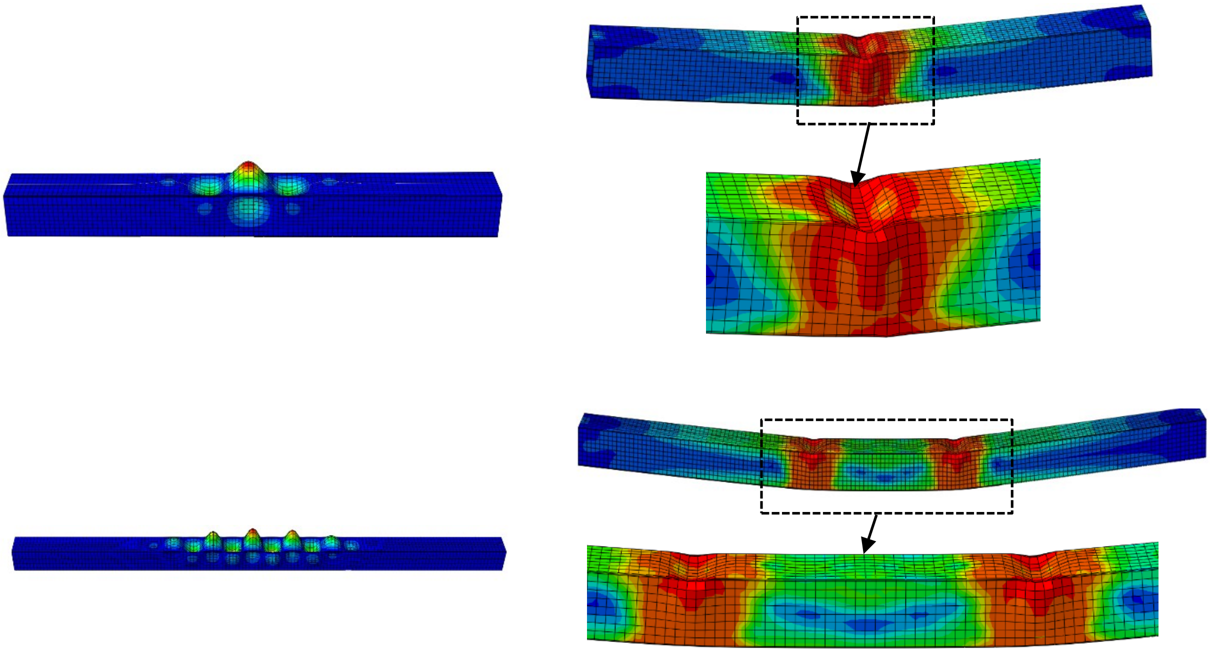

a) elastic buckling modes
3-point (top), 4-point (bottom)
(displacement contour plot)

b) failure modes
3-point (top), 4-point (bottom)
(stress contour plot)

Figure 5.6: Typical numerical elastic buckling mode shapes (left) and failure modes (right).

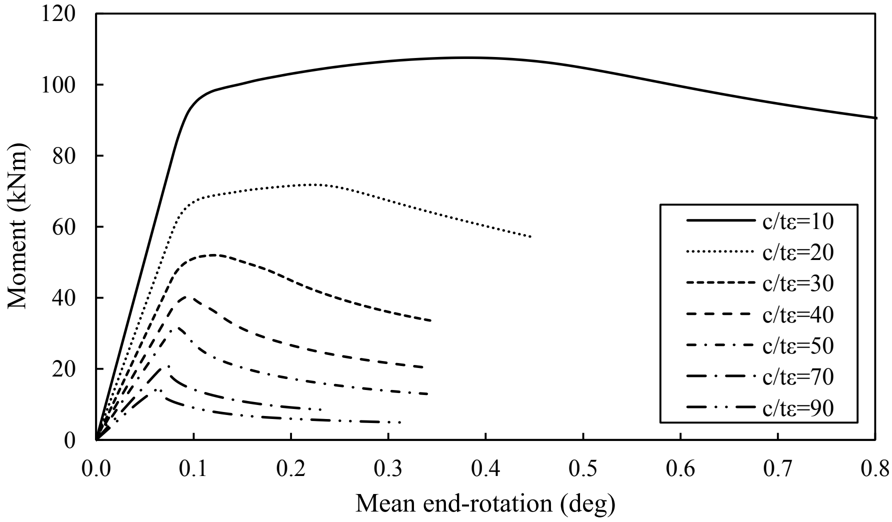

Figure 5.7: Typical moment-end-rotation curves.

5.6. Analysis of the results and design recommendations

The experimental and numerical results of high strength steel hollow section beams are discussed in this section. The normalised ultimate moment capacity and the rotation capacity obtained from the tests and the FE analyses are plotted against the cross-section slenderness $c/t\varepsilon$, thus allowing the effect of key parameters on the bending behaviour to be evaluated. The obtained results are used for the assessment of current European provisions. In particular, the applicability of the existing cross-section classification limits provided in EN 1993-1-1 (2014) for internal elements in compression and for internal elements in bending and of the Eurocode effective width equations to high strength steel hollow sections is assessed.

5.6.1. Influence of key parameters on the flexural response

The influence of the material strain-hardening characteristics and the cross-section aspect ratio can be seen in Figure 5.8, which presents the experimental and numerical results for the three considered cross-sections under the same moment gradient (i.e. L/h=20). In line with the conclusion drawn in Chapter 4, the stocky S460 beams are able to reach higher normalised moment capacities, up to 50% beyond their plastic moment capacity, and higher rotation capacity values, of up to 30, than their S690 counterparts, making evident the effect of the material strain-hardening characteristics on the performance of cross-sections in the stocky slenderness range. This effect reduces for slender sections, where failure occurs in the elastic range and the bending behaviour appears dependent on the cross-section aspect ratio, exhibiting improved normalised flexural performance for decreasing aspect ratio. This can be related with restraints provided by the less slender webs of sections with decreasing aspect ratio to the critical compression flanges that delays local buckling. Even though the effect of plate element interaction on the flexural performance decreases for stocky sections, the rotation capacity is still affected by the cross-section ratio, indicating higher rotation capacity values for sections with decreasing aspect ratio.

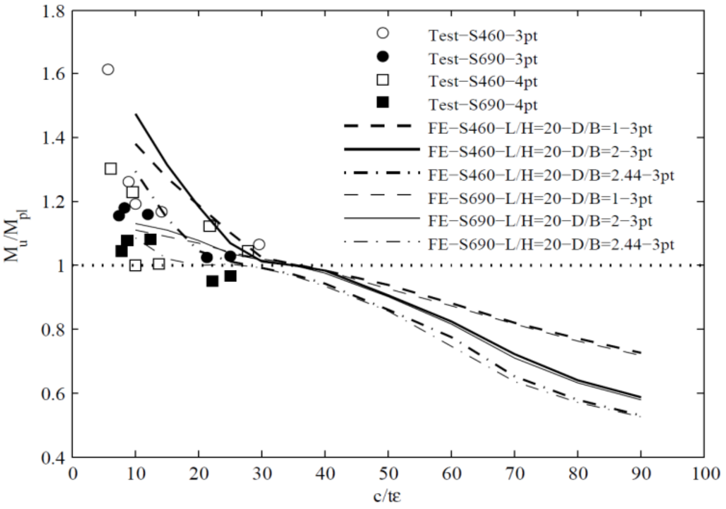

a) on the normalised moment capacity

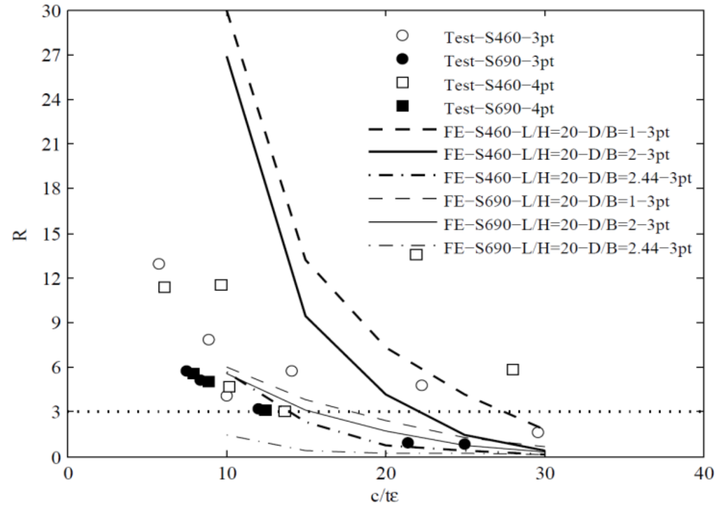

b) on the rotation capacity of SHS and RHS sections

Figure 5.8: The effect of strain-hardening and cross-section aspect ratio.

In order to study the effect of the moment gradient on the flexural response of HSS beams, the results corresponding to a fixed aspect ratio 2.00 are shown in Figure 5.9. As can be observed, the moment gradient has a fairly minimal influence on the normalised flexural behavior, but affects the rotation capacity, which exhibits higher achieved values for beams with L/h=10 than their corresponding with L/h=20. Note that for 4-point bending tests, the calculation of the rotation capacity is based on curvatures, rather than rotations and hence the results are not directly comparable. Similar conclusions regarding the effect of the material stress-strain characteristics, the moment gradient and the interaction of web and compression flange slenderness on the rotation capacity of steel beams were also found by other researchers (Lay and Galambos, 1967; Kuhlmann, 1989; Ricles et al., 1998).

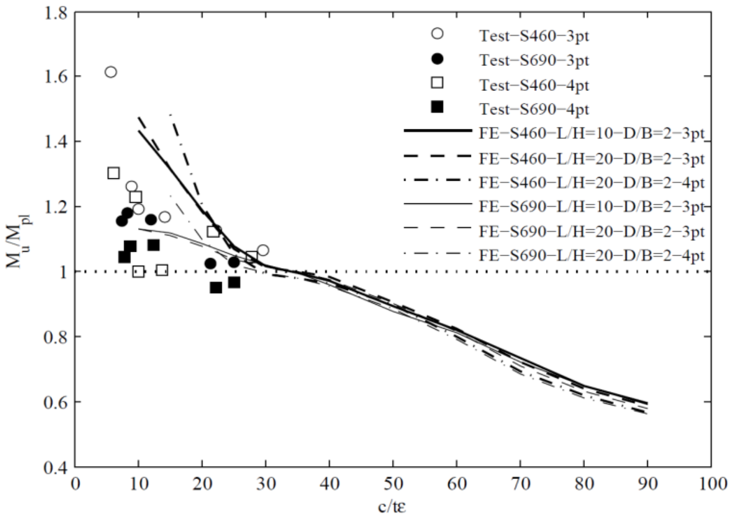

a) on the normalised moment capacity

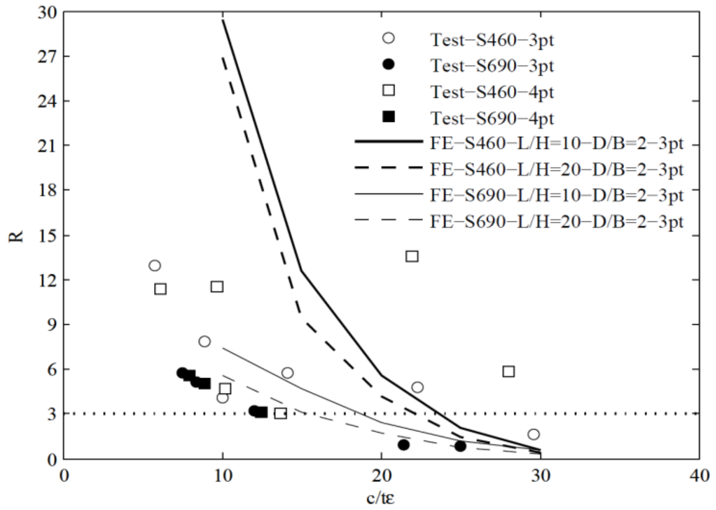

b) on the rotation capacity of RHS sections

Figure 5.9: The effect of moment gradient.

5.6.2. Assessment of the Eurocode slenderness limits for internal elements in compression

In order to assess the applicability of the Eurocode Class 1, Class 2 and Class 3 limits for internal elements in compression to HSS, the experimental and numerical results of HSS beams are presented in Figure 5.10(a), Figure 5.10(b) and Figure 5.10(c) respectively. Data on ordinary strength steel collated from literature (Gardner et al., 2010; Zhao and Hancock, 1991; Wilkinson and Hancock, 1998) have also been included in the same graphs.

Even though plastic design is not permitted by EN 1993-1-12 (2007) for high strength steels, the results on HSS hollow section beams have been used for the assessment of Class 1 limit, considering deformation capacity requirement R=3 proposed by Sedlacek and Feldmann (1995) and slenderness limit of 33, which are applied for normal strength steel in BS EN 1993-1-1 (2014). As can be observed in Figure 5.10(a), the current limit of 33, recommended for mild steel, appears questionable not only for HSS sections but also for ordinary carbon steel sections. Even though the previously proposed limit of 28 (Taras et al., 2013; Wang et al., 2017) seems more appropriate, some results still remain below the rotation capacity requirement. Note that details on the research leading to the design proposals of Taras et al. (2013) are reported on Greiner et al. (2008, 2011). The Class 1 limit of 15, shown in Figure 5.10(a), would allow for safe predictions for all of the S460 and S690 sections studied herein, The proposal of the aforementioned limit is hence supported by this study.

The applicability of Class 2 limit of 38 is assessed in Figure 5.10(b), where the ultimate moment is normalised by the plastic moment capacity and plotted against the $c/t\varepsilon$ slenderness of the compressive flange. The Eurocode Class 2 limit may be seen to be unconservative for high strength steel hollow sections, especially for sections with higher aspect ratio, whilst the lower proposed limit of 34 follows closer the tests and FE results.

The Class 3 limit of 42 is assessed in Figure 5.10(c), where the ultimate moment capacity M_u obtained by test and numerical results is normalised by the elastic moment M_{el} and plotted against the $c/t\varepsilon$ flange slenderness. The results show that the current slenderness limit for fully effective sections is applicable to high strength steel square and rectangular hollow sections.

In addition, the high normalised moment capacity ratios observed in Figure 5.10(c) reveals an uneconomic design. Following the proposal for amended Eurocode rules regarding the semi-compact design that suggests linear strength transition between Class 2 and Class 4 sections (Taras et al., 2013), as illustrated in Figure 5.11, the average value of ultimate normalised moment capacity for Class 3 sections falls from 1.17 to 1.06, leading to a more economic but safe design and therefore demonstrating the suitability of this particular amendment.

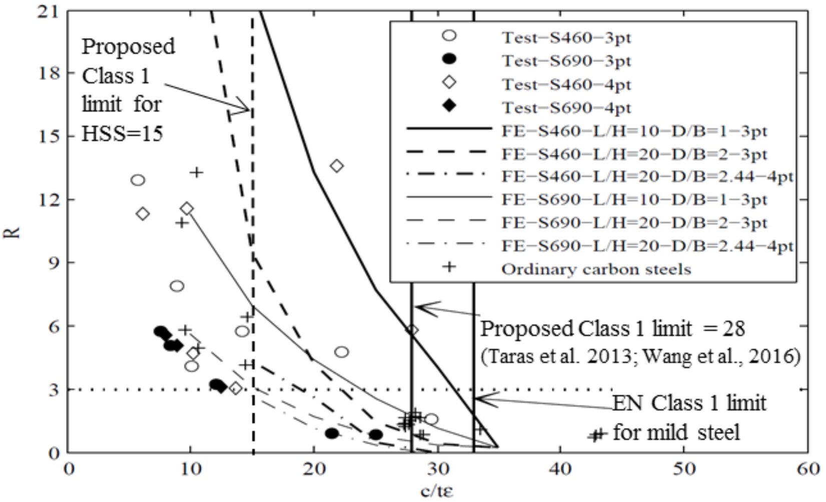

a) Class 1 limit

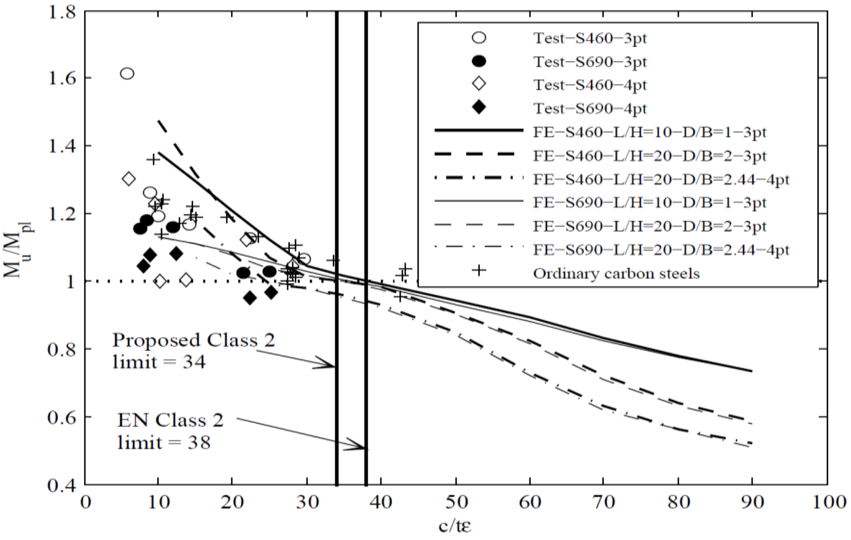

b) Class 2 limit

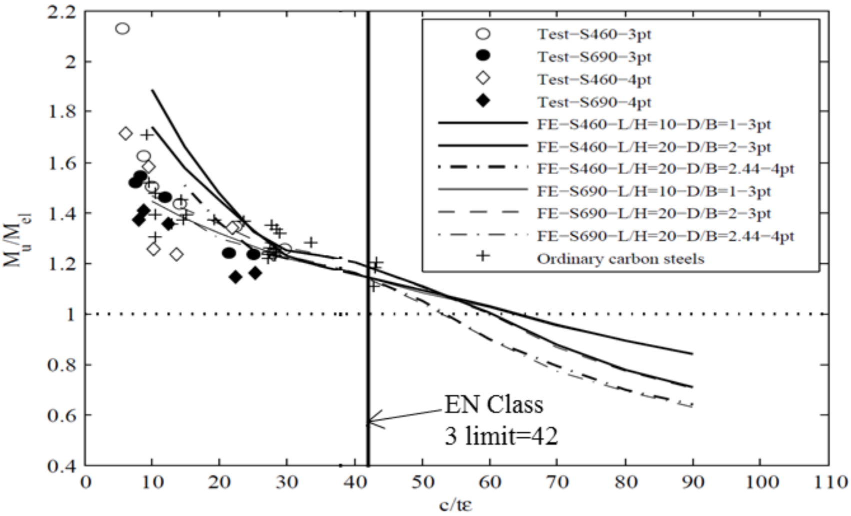

c) Class 3 limit

Figure 5.10: Assessment of the Eurocode slenderness limits.

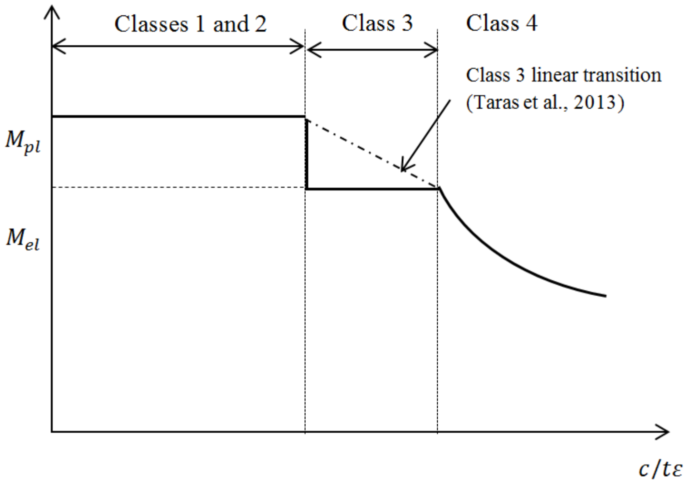

Figure 5.11: Bending resistances for different cross-section classes, including depiction of linear transition for Class 3 cross-sections proposed by Taras et al. (2013).

5.6.3. Assessment of the Eurocode slenderness limits for internal elements in bending

The results of the numerical parametric studies for cross-sections with aspect ratio value h/b=2.44 can be employed to assess the applicability of the Eurocode slenderness limits for internal plate elements in bending. The $c/t\varepsilon$ limits given in BS EN 1993-1-1 (2014) for internal elements in bending are 72, 83 and 124 for Class 1, Class 2 and Class 3 elements, respectively. Figure 5.12(a), Figure 5.12 (b) and Figure 5.12 (c) show the relevant response characteristics (R, M_u/M_{pl} and M_u/M_{el}) plotted against the slenderness parameter $c/t\varepsilon$ of the web element in bending. It can be observed that the current Eurocode Class 2 and Class 3 limits appear adequate for the studied HSS sections. However, the rotation capacity requirement of $R = 3$ for mild steel is not met for HSS internal elements in bending. It is worth observing that the required rotation capacity requirement is met for S460 sections, when considering a stricter Class 1 limit of 42, whose incorporation is supported by the present thesis. For the currently studied S690 sections though, Class 1 sections could not fulfill the rotation capacity requirements even for the stricter proposed limit.

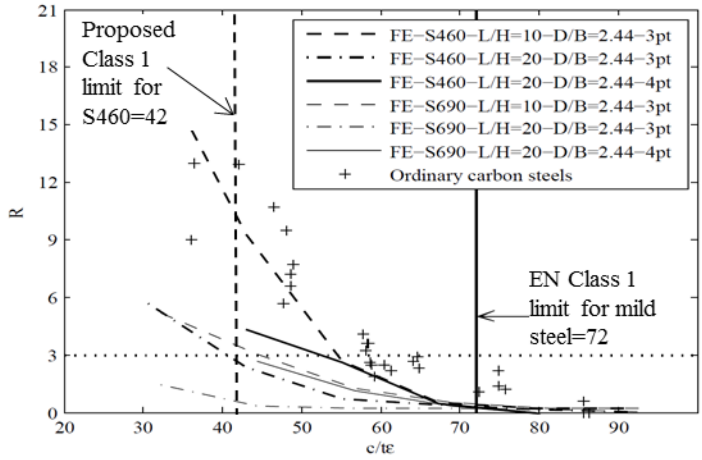

a) Class 1 limit

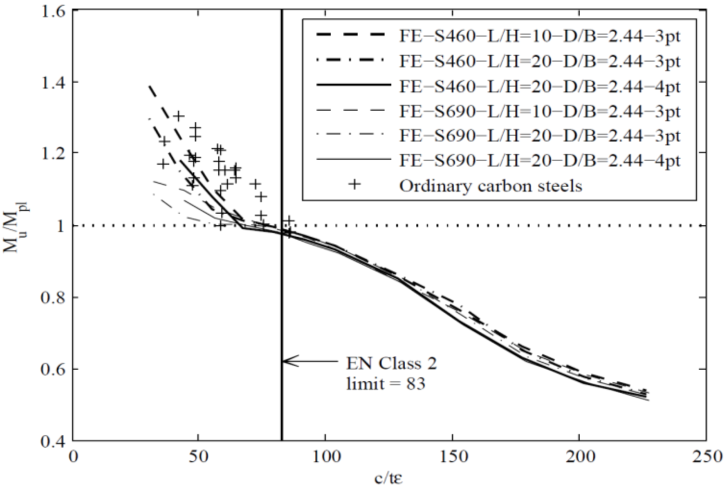

b) Class 2 limit

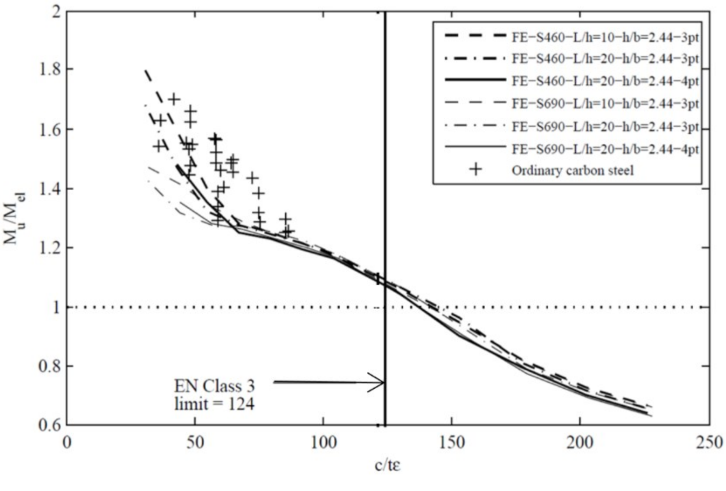

c) Class 3 limit

Figure 5.12: Assessment of Class 1, 2 and 3 limits for internal elements in bending.

5.6.4. Assessment of the effective width equations

Based on the numerical results of effective sections, the suitability of the European provisions to predict the moment resistance of slender S460 and S690 sections can also be evaluated. Upon calculating the effective section modulus (W_{eff}), the normalised moment capacities $M_u/(W_{eff}f_y)$ are plotted against the cross-section slenderness in Figure 5.13. As can be seen, safe estimations are obtained through the application of the Eurocode effective width equations, whilst the effect of the aspect ratio, though apparent is not significant enough to warrant an elaboration of the current codified approach.

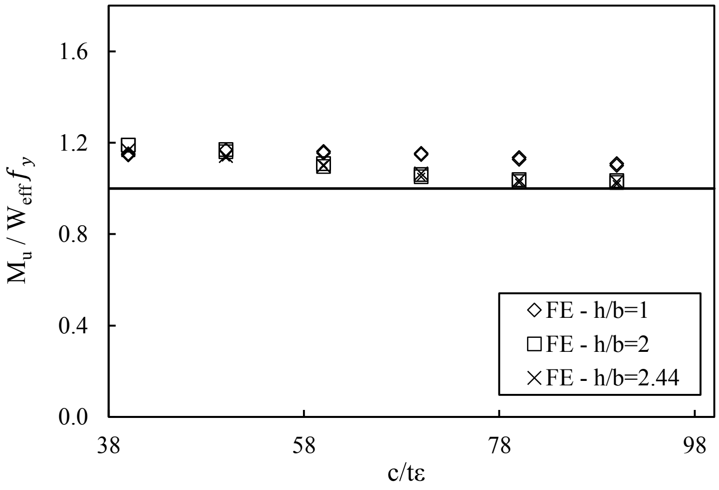

Figure 5.13: Assessment of the effective width equations.

5.7. Concluding remarks

A series of 3-point and 4-point high strength steel beams have been studied in the current chapter. For the square and rectangular hollow sections, key factors influencing the flexural performance are the material strain-hardening characteristics in the stocky slenderness range and the cross-section aspect ratio in the slender range. The moment gradient has little effect on the obtained normalised moment resistance of cross-sections, but affects the attained rotation capacity.

Eurocode slenderness limits have been assessed based on both experimental and numerical results. Additionally, ordinary carbon steel results have been collected for the purpose of comparison. For Class 1 sections, the limit of 15 that appeared suitable for the currently studied HSS sections, has been proposed, whereas further research is necessary to investigate the possibility of applying plastic design for high strength steel structures. The applicability of the current Eurocode Class 2 limit to the studied HSS sections appears problematic, whilst the proposed limit of 34 is able to provide overall safe predictions. The Class 3 slenderness limit of 42 has been shown adequate for the presently considered sections. Furthermore, a linear strength transition between Class 2 and 4 sections is capable of producing more economic yet safe strength estimations for Class 3 sections. The slenderness limits for internal elements in bending have been assessed on the basis of the results with $h/b = 2.44$, showing that the Class 2 and Class 3 limits yield overall safe predictions for HSS sections. For S460 internal elements in bending, the value of 42 has been proposed for Class 1 limit, as the value of 72 recommended for mild steel, was found largely unsafe. Finally, the effective width equations provided by Eurocode appear applicable to slender HSS square and rectangular hollow sections.

CHAPTER 6: HIGH STRENGTH STEEL MEMBERS IN COMBINED BENDING AND COMPRESSION

6.1. Introduction

Having studied the response of high strength steel members under pure compression (Chapter 4) and under pure bending (Chapter 5), the present chapter focuses on the structural behaviour of S460 and S690 square and rectangular hollow sections under combined bending and compression. The generated numerical models were validated against test data on twelve stub columns under eccentric compression. Two series of extensive parametric studies were subsequently performed for cross-sections with different thicknesses, aspect ratios and combinations of axial load to bending moment ratios. The first one encompassed studies on cross-sections under uniaxial bending and compression, whilst at the second one, the studies were extended to cross-sections under combined biaxial bending and compression loading. On the basis of the results, the Eurocode interaction surfaces were assessed. The applicability of Taras et al. (2013) proposal for Class 3 sections was assessed. For cross-sections with $\bar{\lambda}_{cs}>0.68$, the ability of the recently proposed CSM equations for slender sections (Anwar-us-saadat et al., 2016) to predict the cross-section resistance was assessed.

6.2. Brief description of the test programme

A series of twelve tests on eccentrically compressed stub columns was executed at the Structures Lab of Imperial College London in order to study the response of high strength steel hot-finished cross-sections under combined compression and bending. One square hollow section 50×50×5 in grade S460 and two square hollow sections, SHS 50×50×5 and SHS 90×90×5.6, in grade S690 were tested under various loading eccentricities.

The specimens were loaded with a SATEC 2000 kN hydraulic loading machine under displacement control. The ends of the specimens were welded at a predetermined distance from the centre of the end plates, which were bolted to two loading plates loaded with knife edges, thus allowing the inclusion of loading eccentricities. The knife edges provided pin-ended supports about the bending axis and fix-ended boundary conditions about the other axis, thus subjecting the specimens to combined compression and uniaxial bending. Similar to the previous series of tests, instrumentation including LVDTs at the mid-height of the specimens, strain-gauges on both the convex and the concave faces of the specimens and inclinometers at the end plates were used in order to measure the lateral displacements, the longitudinal strains and the end-rotations respectively. The schematic diagram of the test set-up together with a photograph of the testing machine are depicted in Figure 6.1. A detailed description of the experimental procedure are given in Gkantou et al. (accepted2).

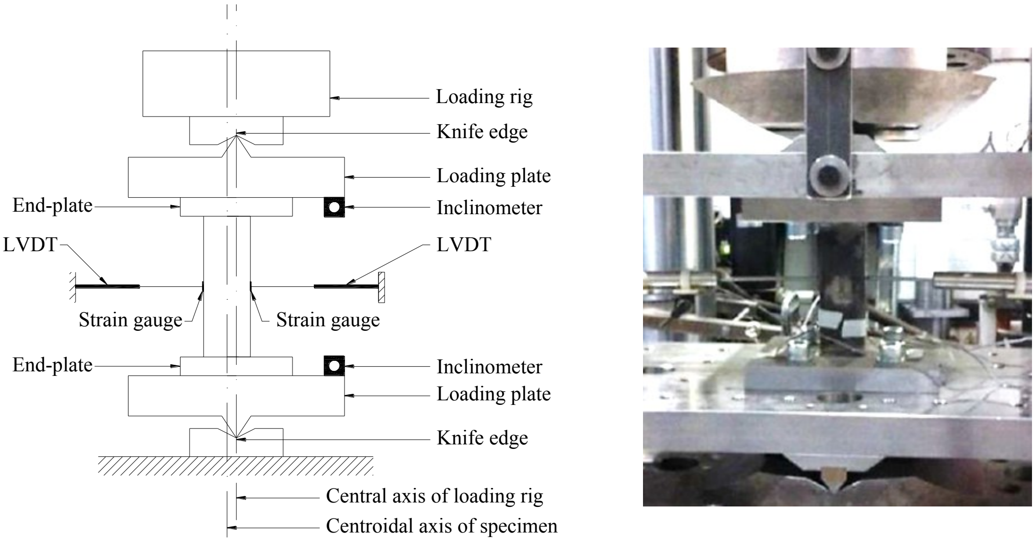

a) Schematic diagram of test set-up b) Photograph of test set-up

Figure 6.1: Experimental set-up including instrumentation (Gkantou et al., accepted2).

The dimensions of the specimens are reported in Table 6.1, where $e_{0,n}$ the nominal initial loading eccentricity and the rest as previously defined. In order to exclude global buckling, the length in all cases was three times the largest cross-sectional dimension.

Table 6.1: Measured dimensions of the eccentric stub columns.

Cross-section	$e_{0,n}$ (mm)	L (mm)	h (mm)	b (mm)	t (mm)	r_i (mm)	ω_0 (mm)
S460 SHS 50×50×5	5	149.98	50.03	49.86	4.94	3.00	0.054
	10	150.01	49.86	50.16	4.98	3.00	0.054
	20	149.95	50.32	50.11	4.90	3.00	0.054
	30	149.97	50.07	50.36	4.95	3.00	0.054
S690 SHS 50×50×5	5	149.91	50.24	50.60	5.03	3.00	0.076
	10	149.96	50.27	50.39	4.94	3.00	0.076
	15	149.84	50.45	50.52	4.96	3.00	0.076
	20	149.98	50.16	50.36	4.97	3.00	0.076
S690 SHS 90×90×5.6	5	269.07	89.56	89.81	5.68	4.50	0.089
	10	269.00	89.84	90.10	5.65	4.63	0.089
	25	268.96	90.21	90.65	5.72	4.88	0.089
	30	269.02	90.57	90.08	5.59	4.63	0.089

The longitudinal strain measurements together with the measured values of the lateral displacements at mid-height enabled the determination of the actual initial loading eccentricities. At the initial stages of the experiment, when the specimen is loaded in the elastic range, Equations (6.1) and (6.2) were applied for the evaluation of the bending moment and the compressive force corresponding to the recorded strain values.

$$M = \frac{EI(\varepsilon_{convex} - \varepsilon_{concave})}{h} \tag{6.1}$$

$$N = \frac{EA(\varepsilon_{convex} + \varepsilon_{concave})}{2} \tag{6.2}$$

where ε_{convex} and $\varepsilon_{concave}$ are the strains on the convex side and concave side of the cross-section at mid-span, respectively.

The measured values of the lateral displacements at mid-height were used for the calculation of the second-order bending moments (i.e. additional bending moment due to deviation of the centroid form the line of loading) through Equation (6.3) that defines the relationship between the moment M and the axial force N applied to a cross-section as a function of the initial eccentricity e_0 and the eccentricity generated due to the 2nd-order effect e'.

$$M = N(e_0 + e') \tag{6.3}$$

Substituting Equations (6.1) and (6.2) to (6.3), Equation (6.4) is derived, where ψ is the ratio $\varepsilon_{concave}/\varepsilon_{convex}$. This was used to evaluate the actual initial eccentricities.

$$e_0 = \frac{2I\ \times (1-\psi)}{Ah\ \times (1+\psi)} - e' \tag{6.4}$$

The key results of the eccentric stub column tests are reported in Table 6.2, where N_u is the failure load, e_0 is the calculated initial loading eccentricity based on the strain gauge readings using Equation (6.4), $e_u{}'$ is the recorded lateral deflection at failure load, referred to as the 2nd-order eccentricity, M_u is the failure moment given by $M_u = N_u(e_0 + \ e_u{}')$ and φ_u is the mean end-rotation at failure load.

All specimens employing SHS 90×90×5.6 and the S690 SHS 50×50×5 specimen under initial nominal eccentricity 5 mm exhibited clear signs of local buckling. The remaining specimens which were stockier failed without visible signs of local buckling deformations.

Table 6.2: Summary of the eccentric stub column tests.

Cross-section	e_0 (mm)	N_u (kN)	$e_u{}'$ (mm)	M_u (kNm)	φ_u (deg)
S460 SHS 50×50×5	4.83	333.8	8.70	4.5	6.98
	9.70	297.3	9.28	5.7	7.62
	20.22	226.6	8.72	6.6	7.19
	33.02	181.4	10.32	7.9	8.39
S690 SHS 50×50×5	5.58	530.8	1.12	3.6	1.02
	10.26	459.5	0.98	5.3	1.80
	13.65	398.7	1.67	6.0	2.25
	19.32	338.2	6.34	8.7	5.20
S690 SHS 90×90×5.6	5.37	1289.5	0.61	7.6	0.46
	10.25	1195.3	0.55	12.9	0.62
	25.49	864.0	3.12	24.9	2.04
	29.80	819.6	2.12	26.2	4.85

6.3. Development of the finite element models

In line with the modelling assumptions stated in Chapter 3, numerical models were developed for all stub columns tested under eccentric compression at Imperial College London. In order to maximise efficiency, appropriate boundary conditions replicating those provided from the test set-up were introduced in the numerical models. In the experiments, the edges of the specimens were welded to the end-plates, thus preventing any deformation at the cross-section ends. In order to model this condition, rigid body constraints were introduced at both edges and all degrees of freedom of the end cross-sections were restrained to the motion of a reference point RP, located at a plane perpendicular to the specimen axis and at a distance equal to the knife's edge thickness (i.e. $103\ mm$). The rotational degree of freedom of the RP relating to the flexure about the axis of bending and the translational degree of freedom along the specimen's axis were free, whilst all remaining degrees of freedom of the RP were restrained. The existence of knife edges in the tests increased the actual buckling length of the specimens, influencing the overall performance. Note that for the subsequent parametric studies the RP was moved within the plane of the end-sections, as shown in Figure 6.2.

Similarly to the experiments, a prescribed displacement was assigned to the reference point at the top of the specimen. The full load-deformation path of each modelled specimen was traced. The load, end-shortening, end-rotations as well as the lateral displacement at the mid-point height that allowed the calculation of the additional 2nd-order moment generated due to the deformation of the specimens, were reported for every increment of the nonlinear static analysis.

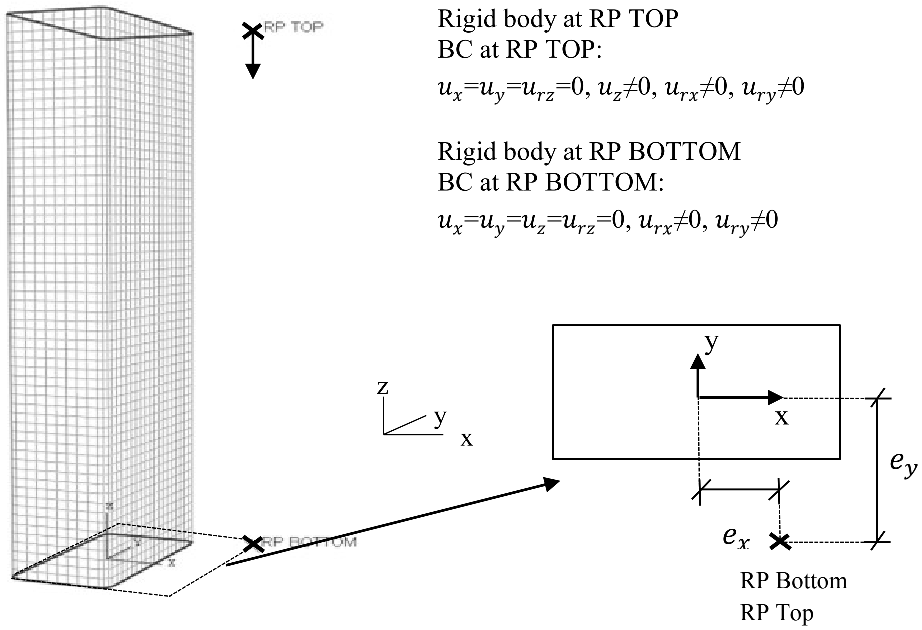

Figure 6.2: Numerical eccentric stub column model.

6.4. Validation of the finite element models

The numerically generated ultimate loads $N_{u,FE}$ and moments $M_{u,FE}$ for six imperfection magnitudes are compared with the respective experimental ones in Table 6.3. Note that $N_{u,FE}$ was the maximum recorded load during the FE analysis, while $M_{u,FE}$ was the corresponding moment, evaluated according to Equation (6.3). As can be seen, the failure loads and moments are overall well-predicted, with the FE results being slightly more conservative than the respective experimental ones. Most accurate calibration has been achieved for the measured and the $t/50$ imperfection magnitude with a mean value of $N_{u,FE}/N_{u,exp}$ equal to 0.92 with COV 0.03 and a mean value of $M_{u,FE}/M_{u,exp}$ equal to 0.98 with higher but still acceptable COV equal to 0.10, has been achieved.

Table 6.3: Comparison of FE and test data.

Cross-section	$e_{0,n}$ (mm)	Imperfection amplitude											
		0		ω_0		$t/100$		$t/50$		$t/10$		ω_{DW}	
		$\frac{N_{u,FE}}{N_{u,Exp}}$	$\frac{M_{u,FE}}{M_{u,Exp}}$	$\frac{N_{u,FE}}{N_{u,Exp}}$	$\frac{M_{u,FE}}{M_{u,Exp}}$	$\frac{N_{u,FE}}{N_{u,Exp}}$	$\frac{M_{u,FE}}{M_{u,Exp}}$	$\frac{N_{u,FE}}{N_{u,Exp}}$	$\frac{M_{u,FE}}{M_{u,Exp}}$	$\frac{N_{u,FE}}{N_{u,Exp}}$	$\frac{M_{u,FE}}{M_{u,Exp}}$	$\frac{N_{u,FE}}{N_{u,Exp}}$	$\frac{M_{u,FE}}{M_{u,Exp}}$
S460 SHS 50×50×5	5	0.92	0.93	0.92	0.93	0.92	0.93	0.93	0.94	0.94	0.96	0.92	0.93
	10	0.91	0.93	0.91	0.93	0.91	0.93	0.91	0.93	0.9	0.53	0.91	0.92
	20	0.92	0.95	0.92	0.95	0.92	0.95	0.91	0.95	0.91	0.92	0.92	0.95
	30	0.87	0.86	0.87	0.86	0.87	0.86	0.87	0.86	0.86	0.85	0.87	0.86
S690 SHS 50×50×5	5	0.94	0.95	0.94	0.95	0.94	0.95	0.94	0.95	0.95	0.95	0.94	0.95
	10	0.89	0.97	0.89	0.97	0.89	0.97	0.89	0.97	0.89	0.96	0.89	0.97
	15	0.93	1.01	0.93	1.01	0.93	1.01	0.93	1.01	0.93	1.01	0.93	1.01
	20	0.94	0.84	0.94	0.84	0.94	0.84	0.94	0.84	0.94	0.84	0.94	0.84
S690 SHS 90×90×5.6	5	0.93	1.01	0.93	1.01	0.93	1.01	0.93	1.01	0.92	0.97	0.93	1.01
	10	0.89	1.00	0.89	1.00	0.89	1.00	0.89	1.00	0.89	0.97	0.89	1.00
	25	0.96	1.09	0.96	1.09	0.96	1.12	0.96	1.09	0.95	0.94	0.96	1.12
	30	0.94	1.21	0.94	1.21	0.94	1.23	0.94	1.21	0.93	1.06	0.94	1.23
MEAN		0.92	0.98	0.92	0.98	0.92	0.98	0.92	0.98	0.92	0.91	0.92	0.98
COV		0.03	0.10	0.03	0.10	0.03	0.11	0.03	0.10	0.03	0.15	0.03	0.11

The numerically obtained structural response has been plotted together with the respective experimental one, as shown for typical specimens in Figure 6.3, where overall very good agreement can be seen. It is worth noting that for the specimen SHS 90×90×5.6 where failure was evidently triggered by local buckling, the variation in the geometric imperfection amplitudes yields a corresponding variation in the post-buckling path. An accurate capture of the failure modes for typical cases is illustrated in Figure 6.4.

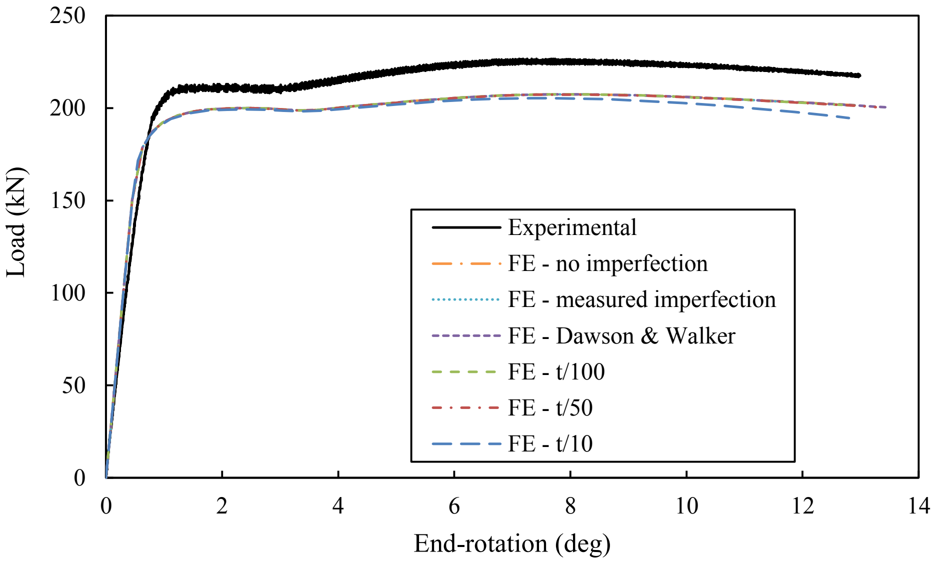

a) S460 SHS 50×50×5 (e_0=20.22mm)

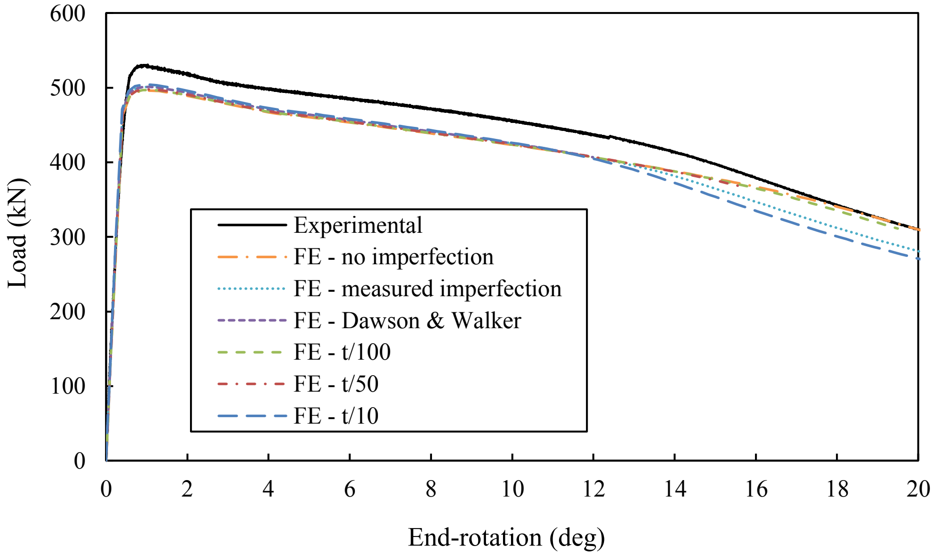

b) S690 SHS 50×50×5 (e_0=5.58mm)

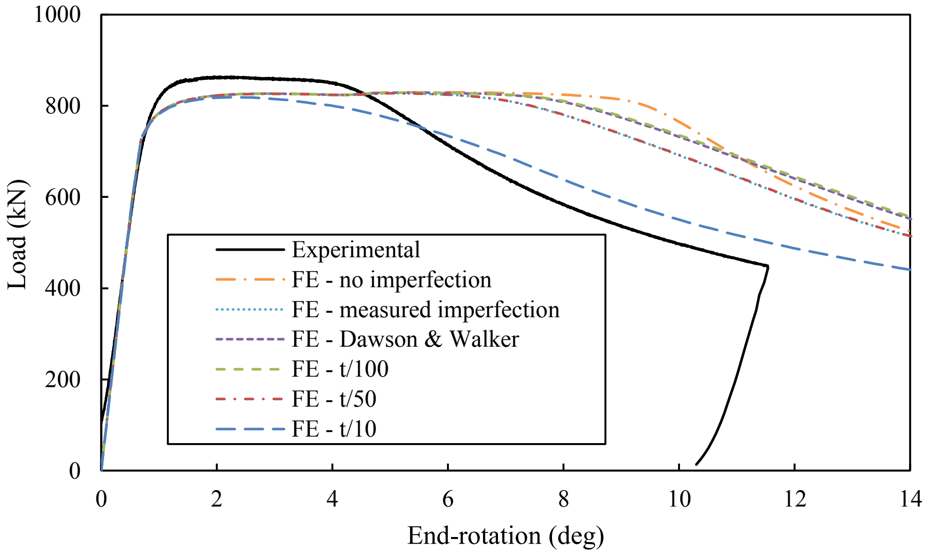

c) S690 SHS 90×90×5.6 (e_0=25.49mm)

Figure 6.3: Validation of FE models for eccentric stub columns.

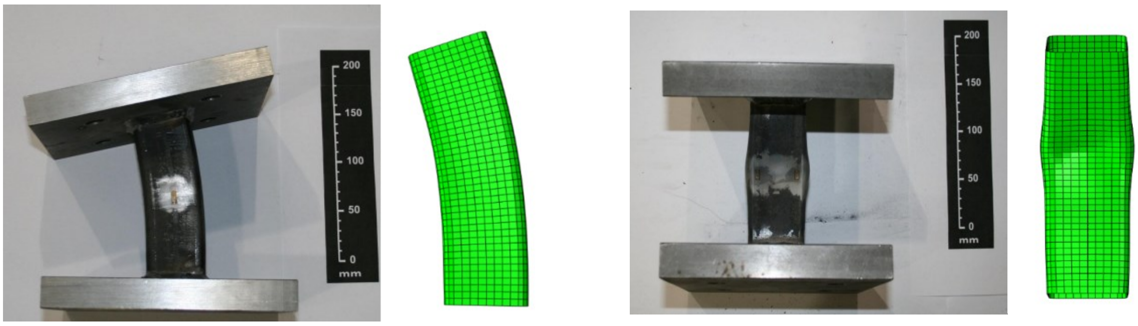

a) S460 SHS 50×50×5 (e_0=20.22 mm)

b) S690 SHS 50×50×5 (e_0=5.58 mm)

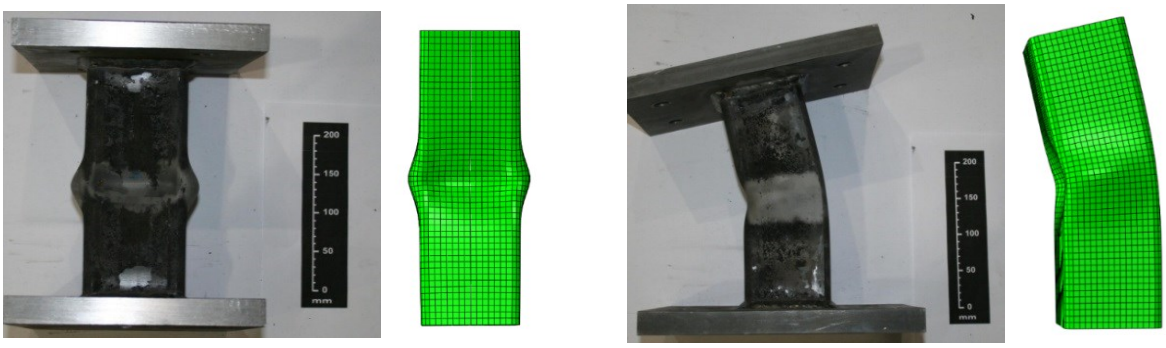

c) S690 SHS 90×90×5.6 (e_0=5.37 mm)

Figure 6.4: Typical experimental and numerical failure modes (Gkantou et al., accepted2).

6.5. Parametric studies

With the aim to thoroughly investigate the response of eccentrically loaded stub columns, two series of comprehensive parametric studies were performed. The first series focused on sections under combined uniaxial bending and compression, while the second one focused on stub columns subject to combined biaxial bending and compression. In order to study the effect of various loading eccentricities, ψ, defined as the ratio of the strain of the concave side (or most heavily compressed) to that of the convex (or less heavily compressed side), was used. The cases of pure compression ψ = 1.00, pure uniaxial bending about the major axis ψ_y = -1.00 and pure uniaxial bending about the minor axis ψ_z = -1.00 were also included as the limiting cases of the response. The subscripts y and z denote the major and minor axis, respectively.

Initial local geometric imperfections with an amplitude $t/50$ were incorporated at the initial step of each analysis. The average material properties derived from tensile flat coupon tests (Figure 3.8) were adopted. The internal radius of the sections was set equal to half the cross-sectional thickness, while the stub column length was set to be three times the biggest cross-sectional dimension.

6.5.1. Uniaxial bending and compression

The first series of parametric studies considered the following parameters for both S460 and S690 steel grades:

- Eight sections with varying thickness to provide cross-section slenderness $c/t\varepsilon$ = 10÷60.
- Three cross-section aspect ratios (h/b): 1.00, 2.00, 2.44.

- Nine loading eccentricities - bending about the major axis (ψ_y= -1.00÷1.00 with step 0.25).
- Nine loading eccentricities - bending about the minor axis (ψ_z= -1.00÷1.00 with step 0.25).

For each of the additional 720 analyses, the ultimate load bearing capacity N_u and the corresponding moment at mid-height accounting for second order effects M_u were determined. The results were plotted in such a way to allow the comparison of the structural behaviour of sections with the same cross-section slenderness and varying loading eccentricity and vice versa, as depicted for typical cases in Figure 6.5. Typical examples of elastic critical buckling and failure modes are shown in Figure 6.6.

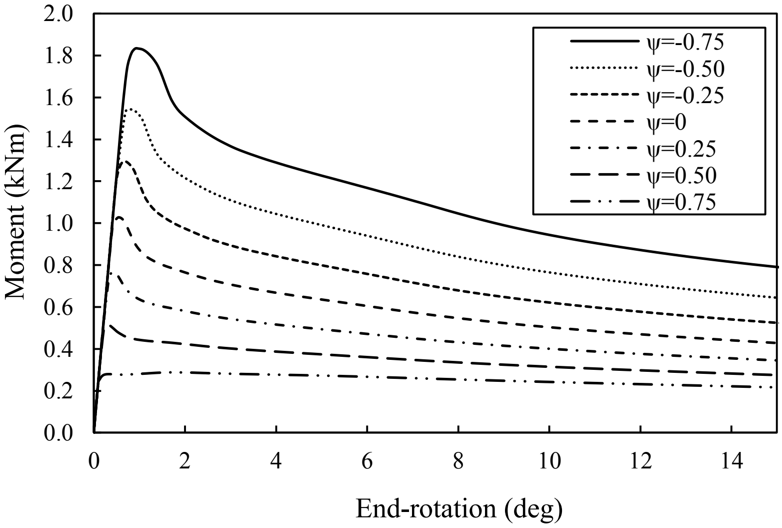

a) S460 SHS, $c/t\varepsilon$=50

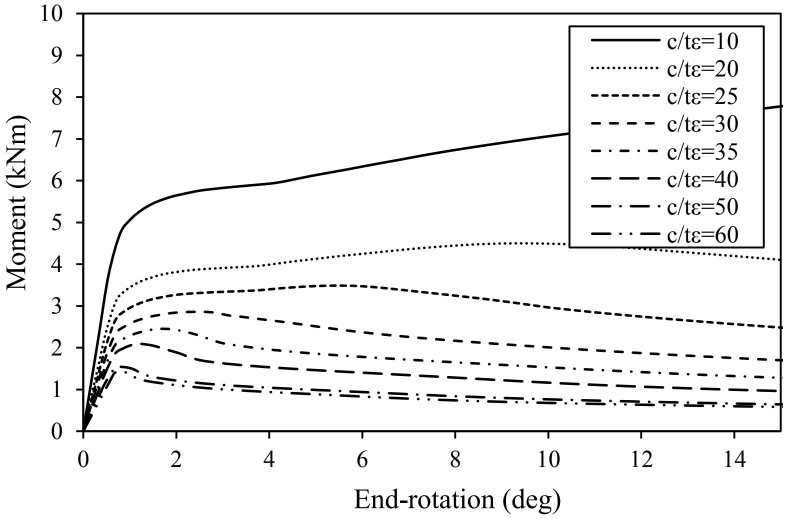

b) S460 SHS, ψ= -0.50

Figure 6.5: Typical numerical moment-end-rotation curves.

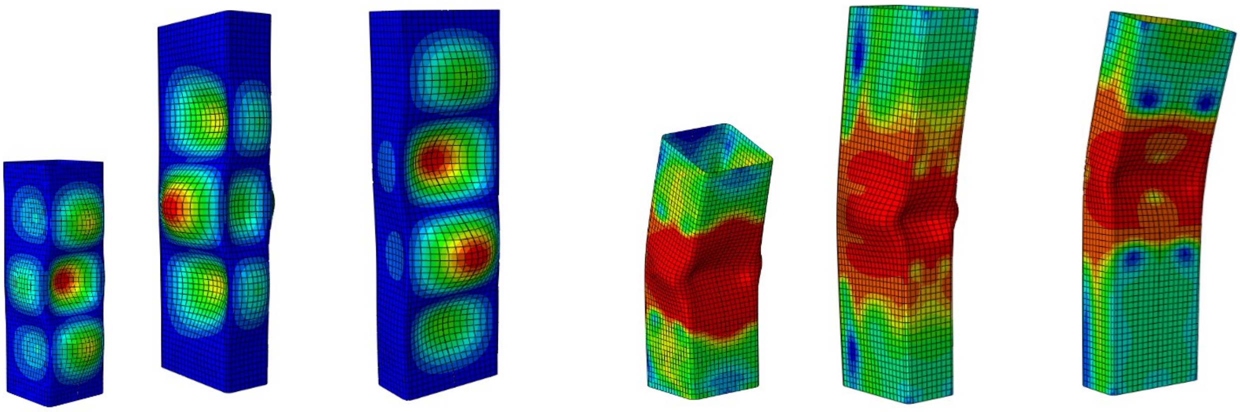

a) Elastic buckling modes (SHS, RHS major, RHS minor) (displacement contour plot)

b) Failure modes (SHS, RHS major, RHS minor) (stress contour plot)

Figure 6.6: Typical numerical elastic buckling mode shapes (left) and failure modes (right).

6.5.2. Biaxial bending and compression

The second series of parametric studies investigated the following parameters for both S460 and S690 steel grades:

- Eight sections with varying thickness to provide cross-section slenderness $c/t\varepsilon$ = 10÷60.
- Two cross-section aspect ratios (h/b): 1.00, 2.00.

- Forty-three loading eccentricities - bending about both axes (ψ_y= -1.00÷1.00 with step 0.33 and ψ_z= -1.00÷1.00 with step 0.33).

For each of the 1376 analyses that were performed, the load-deformation histories were extracted. Figure 6.7 presents the structural performance of a rectangular cross-section under five representative combinations of initial stress ratios ψ_y and ψ_z. Both load-end-shortening and moment-mid-span displacement curves are displayed. As anticipated, the highest moment and the lowest load bearing capacity is observed for sections predominantly under bending moment, whereas the highest load and the lowest moment resistance is attained for sections loaded primarily in compression.

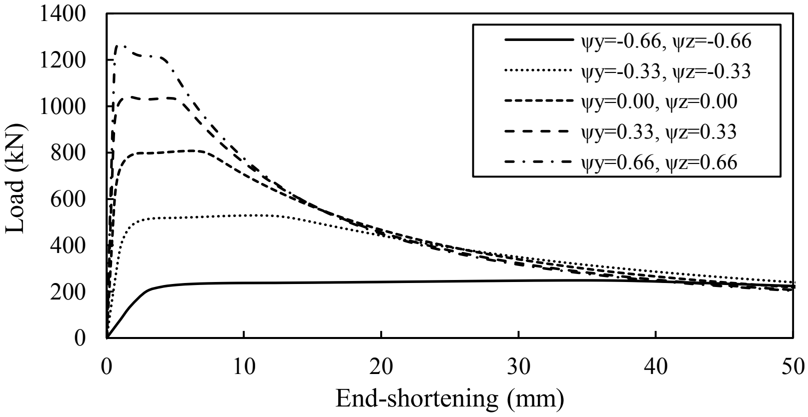

a) Load-end-shortening curve

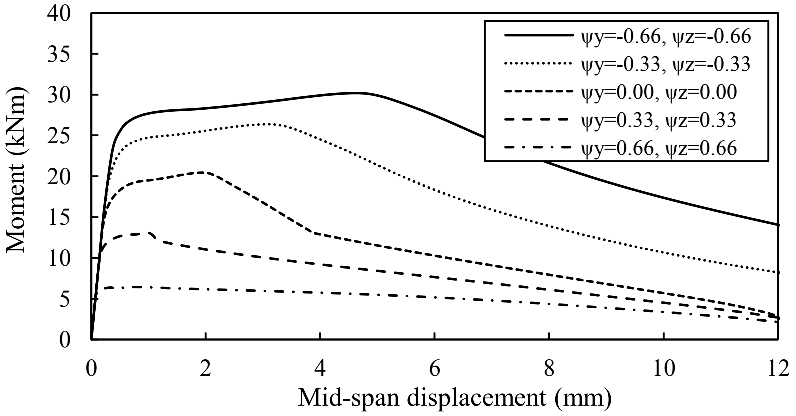

b) Moment-mid-span displacement curve

Figure 6.7: Typical numerically obtained curves.

Normalising the ultimate load and moment capacity with the respective Eurocode resistances, Figure 6.8 illustrates a typical interaction failure surface. Similar surfaces were generated for each of the 32 studied cross-sections (see Appendix B). The three planes, corresponding to the case of uniaxial bending (either major or minor) and compression and the case of biaxial bending without compression, together with representative failure modes, are depicted. The three extreme cases of pure compression, pure uniaxial bending about the major axis and pure uniaxial bending about the minor axis, corresponding to the three vertices of the failure surface are also indicated.

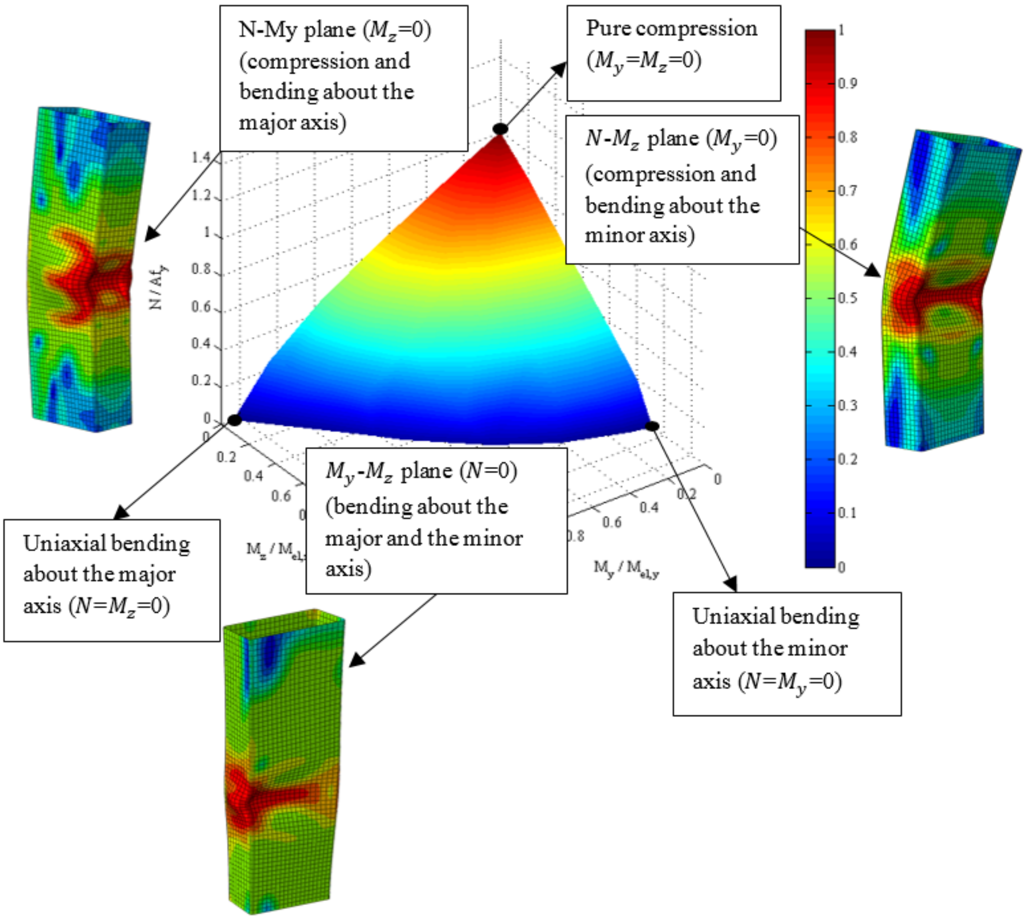

Figure 6.8: Typical numerically obtained interaction surface.

6.6. Analysis of the results and design recommendations

Upon completion of the parametric studies, the experimental and numerical results were used for the assessment of current design specifications. Particular focus was placed on the evaluation of Eurocode's interaction curves and surfaces. The axial compressive and second-order bending moment resistance were normalised by the respective resistances according to the cross-section class. The suitability of the proposal by Taras et al. (2013) for semi-compact cross-sections was also assessed. For sections with $\bar{\lambda}_{cs}$>0.68, the suitability of a new design approach, recently proposed by Anwar-us-saadat et al. (2016), was evaluated.

6.6.1. Definition of utilisation ratio

In order to compare the obtained results with the Eurocode provisions, the utilisation ratio of the test or FE to the predicted capacity (R_{Exp}/R_{pred} or R_{FE}/R_{pred}) has been used. A graphical definition of the aforementioned ratio for sections under uniaxial bending and compression and for sections under biaxial bending and compression is illustrated in Figure 6.9 and Figure 6.10 respectively. Note that points outside the boundary of the design curve (or surface) correspond to capacities higher than the predicted one (i.e. utilisation ratio higher than unity) and lead to safe predictions. The opposite applies for points inside the boundary. The same utilisation ratio is applied in order to evaluate the design recommendations proposed by Taras et al. (2013).

The comparisons are presented separately for Classes 1 and 2, Class 3 and Class 4 cross-sections and for each studied steel grade in Table 6.4 and Table 6.5. For sections with uniaxial bending and compression, the bending axis and the considered aspect ratio is also indicated. The attained results are thoroughly described in the following sections.

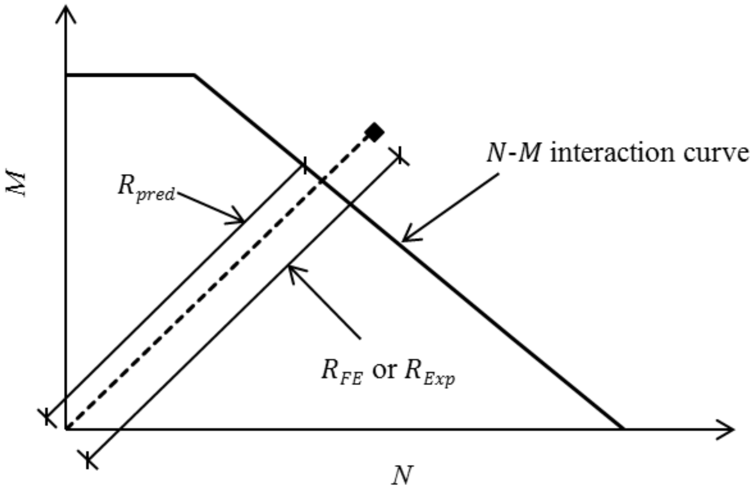

Figure 6.9: Definition of utilisation ratio for sections under uniaxial bending and compression.

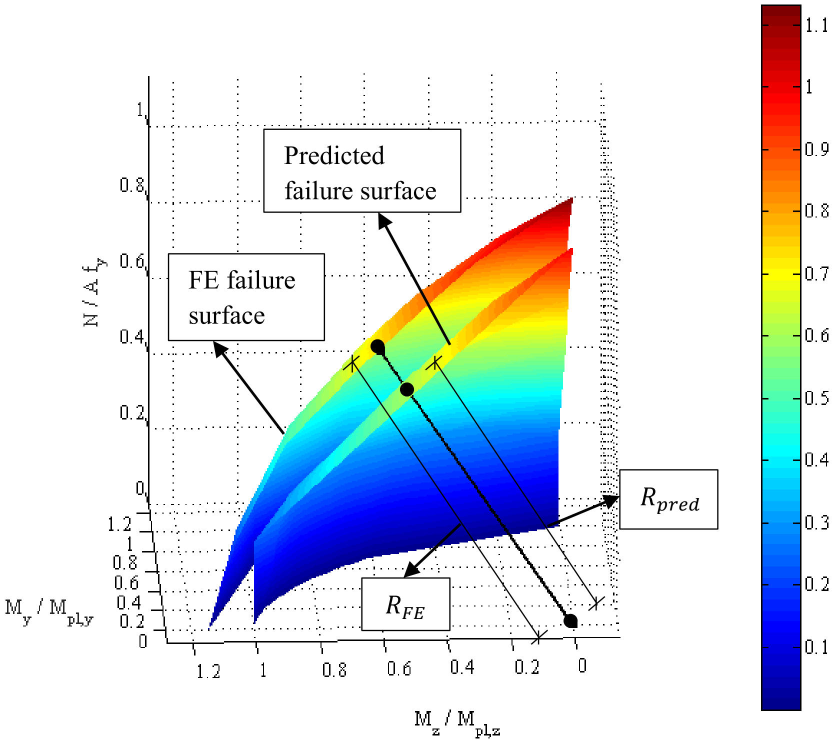

Figure 6.10: Definition of utilisation ratio for sections under biaxial bending and compression.

Table 6.4: Assessment of the Eurocode design predictions based on utilisation ratios of the test or FE to the predicted capacities for sections under uniaxial bending and compression.

				R_{Exp}/R_{pred} or R_{FE}/R_{pred}			
Cross-section	Aspect ratio	Bending axis	No. of test or FE results	Classes 1 and 2	Class 3	Class 3 (linear transition)	Class 4
S460 - test	1.00	N/A	4	1.29	N/A	N/A	N/A
S690 - test	1.00	N/A	8	1.07	N/A	N/A	N/A
S460 - FE	1.00	N/A	72	1.11	1.11	1.07	1.11
S690 - FE	1.00	N/A	72	1.05	1.11	1.07	1.10
S460 - FE	2.00	major	72	1.16	1.19	1.13	1.10
S690 - FE	2.00	major	72	1.07	1.19	1.12	1.08
S460 - FE	2.00	minor	72	1.05	1.08	1.05	1.12
S690 - FE	2.00	minor	72	1.02	1.08	1.05	1.11
S460 - FE	2.44	major	72	1.10	1.23	1.13	1.10
S690 - FE	2.44	major	72	1.03	1.23	1.13	1.09
S460 - FE	2.44	minor	72	1.03	1.09	1.05	1.16
S690 - FE	2.44	minor	72	1.02	1.09	1.05	1.13
MEAN				1.05	1.15	1.09	1.10
COV				0.09	0.07	0.05	0.04

Table 6.5: Assessment of Eurocode design predictions based on utilisation ratios of the test or FE to the predicted capacities for sections under biaxial bending and compression.

	R_{Exp}/R_{pred} or R_{FE}/R_{pred}						
	Classes 1 and 2		Class 3			Class 4	
Cross-section	No. of test or FE results	EC3	No. of test or FE results	EC3	(linear transition)	No. of test or FE results	EC3
S460 - test	4	1.29	-	N/A	N/A	-	N/A
S690 - test	8	1.27	-	N/A	N/A	-	N/A
S460 - FE	430	1.08	86	1.37	1.14	172	1.23
S690 - FE	430	1.04	86	1.37	1.14	172	1.23
MEAN		1.06		1.37	1.14		1.23
COV		0.10		0.12	0.07		0.11

6.6.2. Assessment of the Eurocode provisions for Classes 1 and 2 cross-sections

The Eurocode interaction curves are assessed in Figure 6.11 for sections under uniaxial bending and compression and in Figure 6.12 for sections under biaxial bending and compression. In particular, Figure 6.11(a) shows the results for square and rectangular hollow sections in compression and major axis bending, while Figure 6.11(b) presents the results for rectangular hollow sections in compression and minor axis bending. Figure 6.12(a) provides a typical numerically interaction surface corresponding to a Class 1 cross-section together with the Eurocode design surface, whereas Figure 6.12(b) presents all the results for the case of biaxial bending in the absence of compression (i.e. horizontal plane with z=0 of the interaction surface).

From the figures, it can be seen that the obtained results generally follow sufficiently the shape of the Eurocode predictions for Classes 1 and 2 sections. The same conclusion is drawn from the comparison tables, where a mean value of utilisation ratio equal to 1.05 and to 1.06 has been achieved for the two series of parametric studies. As anticipated, some stocky S460 sections have achieved normalised capacities much beyond unity. This owes to material strain-hardening properties and is more evident in sections with high deformation capacity. The apparent overstrength is significantly lower for S690 sections, which display inferior material strain-hardening properties. Furthermore, an apparent change in the response of stockier S460 RHS specimens under compression and minor axis bending at the higher axial load levels is evident. This could be attributed to the sensitivity of the second-order ultimate moment to where the peak load occurs on the rather flat load-lateral displacement curves.

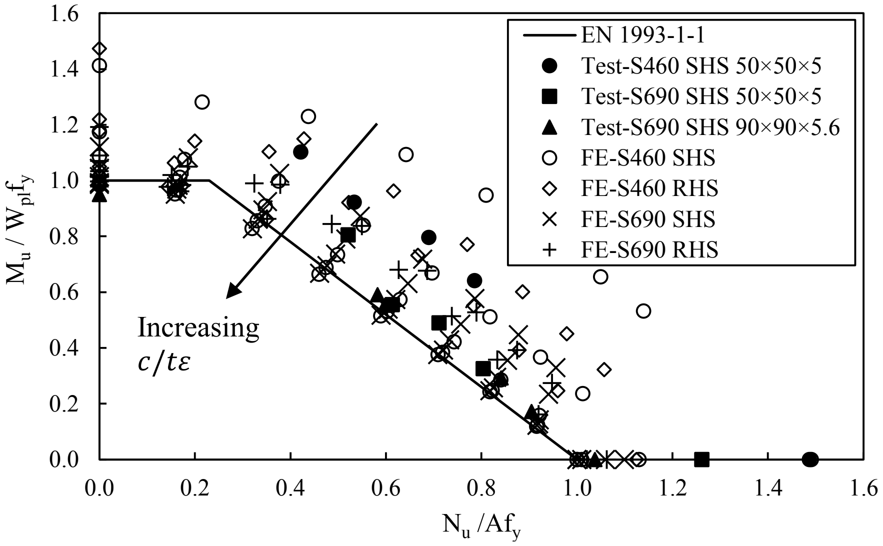

a) SHS and RHS bending about the major axis

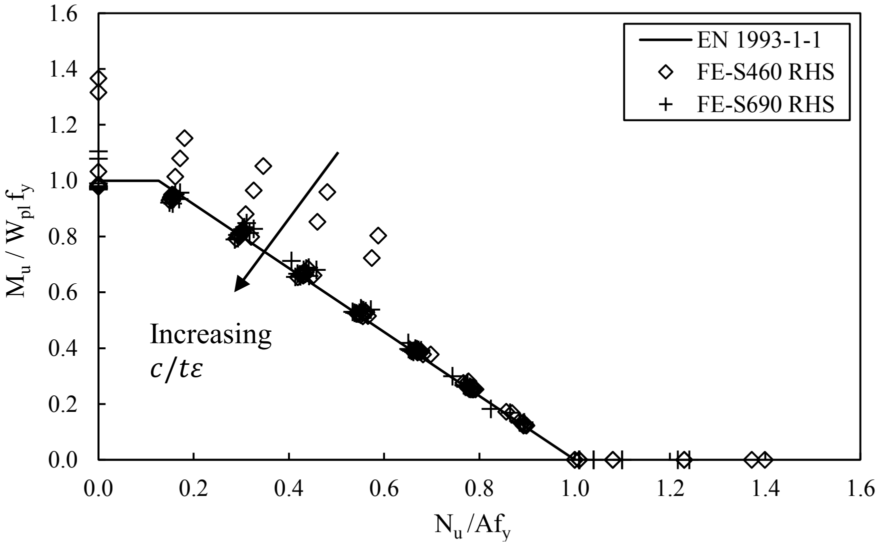

b) RHS bending about the minor axis

Figure 6.11: Assessment of the N-M interaction curves for Classes 1 and 2 cross-sections under uniaxial bending and compression.

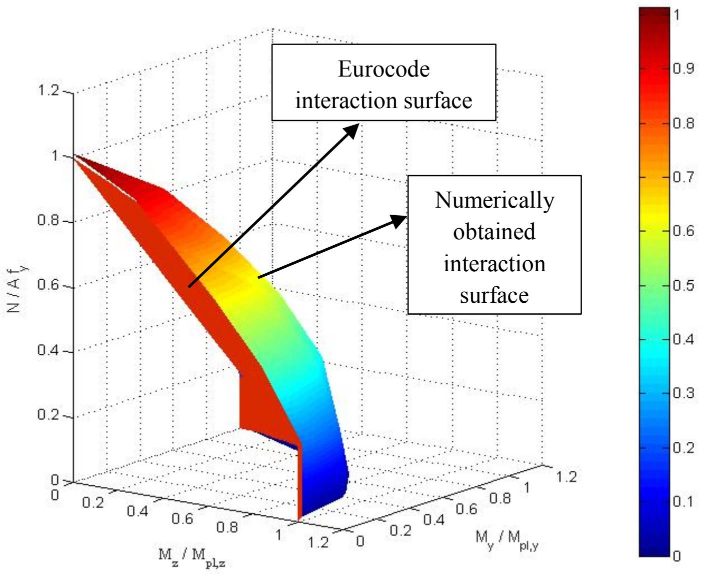

a) Typical interaction surface for Class 1 section

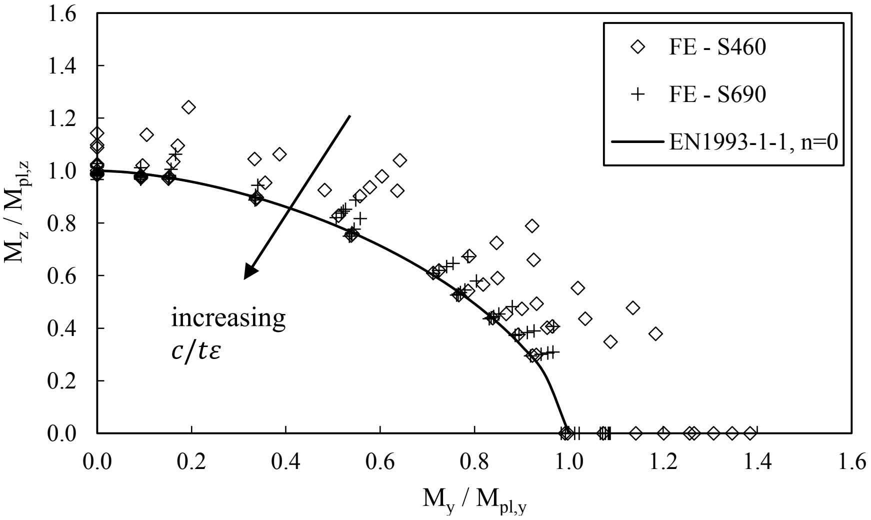

b) Biaxial bending

Figure 6.12: Assessment of the N-M interaction curves for Class 1 and 2 cross-sections under biaxial bending and compression.

6.6.3. Assessment of the Eurocode Class 2 limit for internal elements in compression

Overall the current Eurocode interaction curves and surfaces are applicable to high strength steel hollow sections. However, as can be observed in Figure 6.11, some results with high bending moment fall below the design estimation. To further elaborate on this, the utilisation ratios for each of the studied cross-sections are reported in Table 6.6. An utilisation ratio slightly lower than unity (i.e. unsafe design) is obtained for the cross-sections with $c/t\varepsilon$=35. Note that in accordance with the current Eurocode specifications that define the Class 2 limit for internal elements in compression equal to 38, the cross-sections with flange slenderness 35 are classified as Class 2 sections. Even though the utilisation ratio only falls short of unity, it is recommended the incorporation of the previously proposed stricter limit of 34 that would make the referred cross-sections fall to Class 3, thereby leading to safe predictions for all the studied cross-sections. The adoption of a stricter Class 2 limit is therefore supported also from the results of the current chapter.

Table 6.6: Assessment of the Eurocode Class 2 limit for internal elements in compression on the basis of the results on eccentrically loaded stub columns.

R_{exp}/R_{pred} or R_{FE}/R_{pred}				
Cross-section slenderness $c/t\varepsilon$	S460		S690	
	No. of test or FE results	EC3	No. of test or FE results	EC3
10	5 Exp	1.29	5 Exp	
	86 FE	1.36	86 FE	1.17
20	86	1.16	5 Exp	
			86 FE	1.07
25	86	1.07	86	1.03
30	86	1.02	86	1.01
35	86	0.99	86	0.98
MEAN		1.08		1.06
COV		0.12		0.10

6.6.4. Assessment of the Eurocode provisions for Class 3 cross-sections

Eurocode recommends a linear interaction between moment and compression for Class 3 cross-sections. The results of the first series of parametric studies are shown in Figure 6.13, where safe predictions can be seen for all the cases considered.

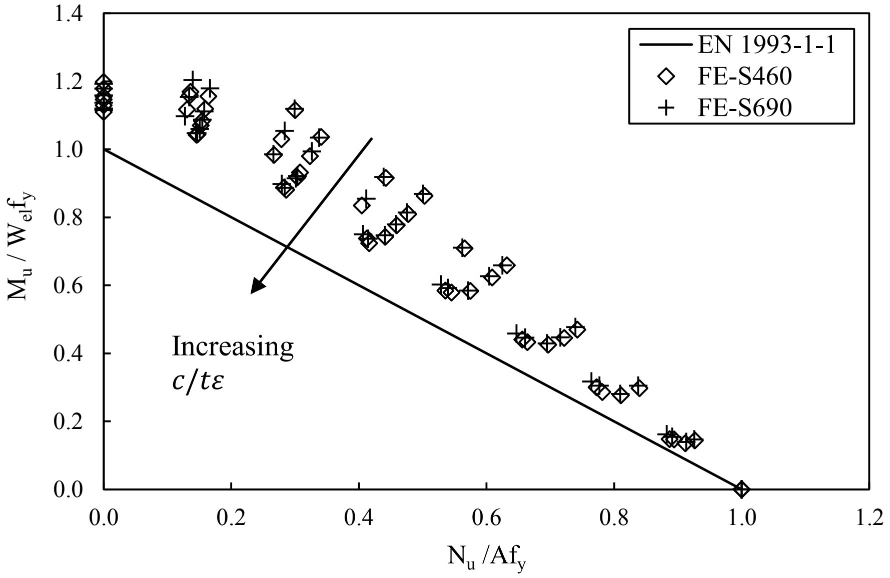

Figure 6.13: Assessment of the N-M interaction curve for Class 3 cross-sections under uniaxial bending and compression.

In addition, the utilisation ratios of Table 6.4 and Table 6.5 on the safe side, but with rather conservative estimations for the sections under biaxial bending and compression. This owes largely to the fact that Eurocode assumes a step transition in the moment resistance of Class 3 sections, whereas in reality the transition from the plastic to elastic resistance is gradual and hence the moment resistance of Class 3 sections is higher than the respective elastic moment resistance, particularly for cross-sections with $c/t\varepsilon$ closer to the Class 2 limit.

Aiming to improve the conservative estimations, Taras et al. (2013) recommended the use of a linear transition between the M_{el} and M_{pl}, as previously shown in Figure 5.11. Incorporating this proposal in the first series of results, better estimations and reduced scattered were obtained (from R_{FE}/R_{pred}=1.15 to R_{FE}/R_{pred}=1.09).

In order to apply the linear transition proposed by Taras et al. (2013) to the case of hollow sections under combined biaxial bending and compression, the following three steps are followed:

i) The strength for pure bending $M_{ep,y/z}$ is determined on the basis of Figure 5.11 which corresponds to a linear interpolation from the Eurocode strength at the Class 2 to 3 and 3 to 4 transition, as defined in Equation (6.5). It should be noted that Equations (6.6)-(6.7) are based on the current slenderness limits and are different from those provided by Taras et al. (2013) that were in line with their proposed slenderness limits, which have not been adopted by the Eurocode yet.

$$M_{ep,y/z} = M_{pl,y/z} - \left(M_{pl,\frac{y}{z},Rd} - M_{el,\frac{y}{z},Rd}\right) c/t_{ref,y/z} \tag{6.5}$$

$$c/t_{ref,y} = \max\left[\frac{\frac{c}{t_f} - 38\varepsilon}{4\varepsilon}; \frac{\frac{c}{t_w} - 83\varepsilon}{41\varepsilon}; 0\right] \leq 1 \tag{6.6}$$

$$c/t_{ref,z} = \max\left[\frac{\frac{c}{t_w} - 38\varepsilon}{4\varepsilon}; 0\right] \leq 1 \tag{6.7}$$

ii) In line with Eurocode, in order to account for the effect of axial forces, the pure bending capacity $M_{N,ep,y/z}$ is linearly reduced, according to Equation (6.8).

$$M_{N,ep,y/z} = M_{ep,y/z}\,(1 - n) \tag{6.8}$$

iii) Having considered the influence of the axial force, a nonlinear interaction formula of Equation (6.9) is used to account for the effect of biaxial bending. Exponents α and β are given from Equations (6.10)-(6.11) and are different from those recommended by Eurocode for Classes 1 and 2 sections.

$$\left(\frac{M_{y,Ed}}{M_{N,ep,y}}\right)^{\alpha} + \left(\frac{M_{z,Ed}}{M_{N,ep,z}}\right)^{\beta} \leq 1 \tag{6.9}$$

$$\alpha = \beta = \frac{1.66}{1 - 1.13n^2} \leq 2 + 4\,[(1 - \max(c/t_{ref,y/z}))]^4 \tag{6.10}$$

$$n = N_{Ed}/N_{pl,Rd} \tag{6.11}$$

Figure 6.14(a) presents both the Eurocode interaction surface together with the Taras et al. (2013) interaction surface for a typical square hollow section with $c/t\varepsilon$=40, for the purposes of comparison. Moreover, the predicted curves together with the obtained numerical envelopes are depicted in Figure 6.14(b), showing that the proposed equations by Taras et al. (2013) follow more closely the FE results, whereas the linear interaction curves specified in the Eurocode appear rather conservative. The same conclusion concerning the improved capacities with the application of the linear transition between the elastic and plastic moment resistance for Class 3 sections is drawn from Table 6.5, where the mean R_{FE}/R_{pred}=1.37 ratio is seen to decrease to 1.14. It is worth noting that the scatter of the design estimations is also significantly reduced through the application of Equations (6.5)-(6.11). Hence, their adoption is recommended herein.

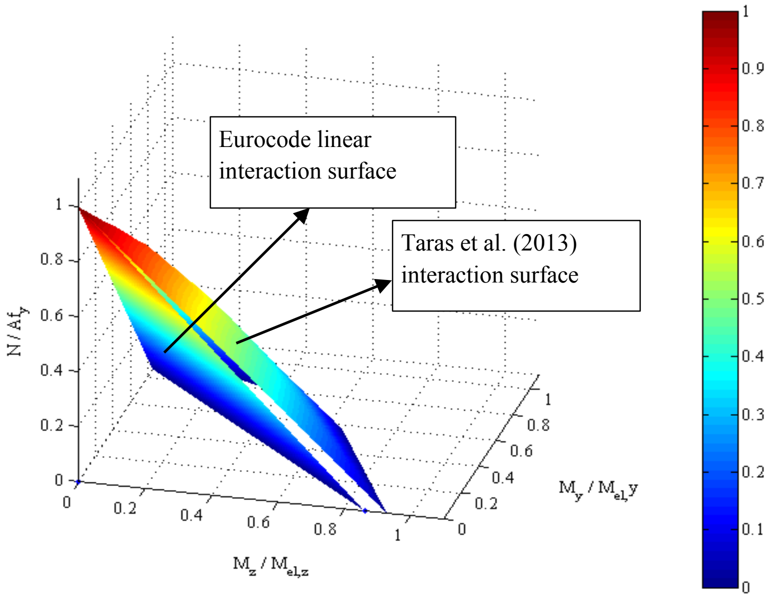

a) Design interaction surface of Eurocode and of Taras et al. (2013)

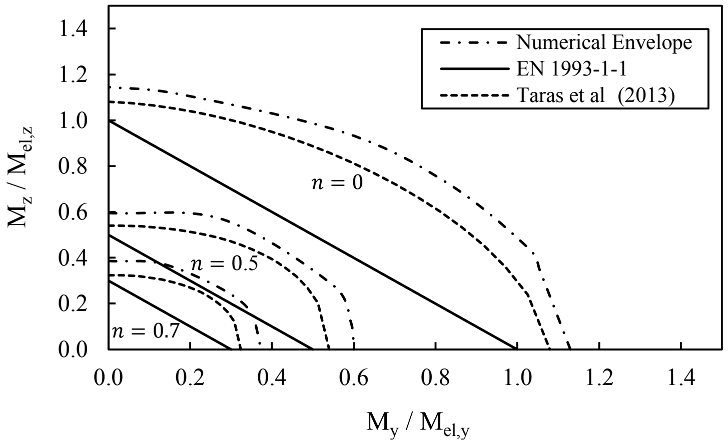

b) Numerical envelope and predicted interaction curves of typical square hollow section

Figure 6.14: Assessment of the design recommendations proposed by Taras et al. (2013) for Class 3 sections under biaxial bending and compression.

6.6.5. Assessment of the Eurocode provisions for Class 4 cross-sections

The current section assesses the Eurocode provisions for Class 4 sections. After calculating the effective cross-sectional area and the effective section modulus, the normalised axial and bending moment capacities of the studied cross-sections were evaluated. An utilisation ratio equal to R_{FE}/R_{pred}=1.10 was found for the case of combined uniaxial bending and compression. For the case of biaxial bending and compression more conservative design estimations with R_{FE}/R_{pred}=1.23 were found. This owes to the fact that sections with a Class 4 flange and Class 1-2 webs achieved higher normalised bending moment resistances, due to the interaction between flange and web local buckling, which is not accounted for in Eurocode. The results in the N-M plane are shown in Figure 6.15. The effective width equations are overall deemed applicable to high strength steel hollow sections.

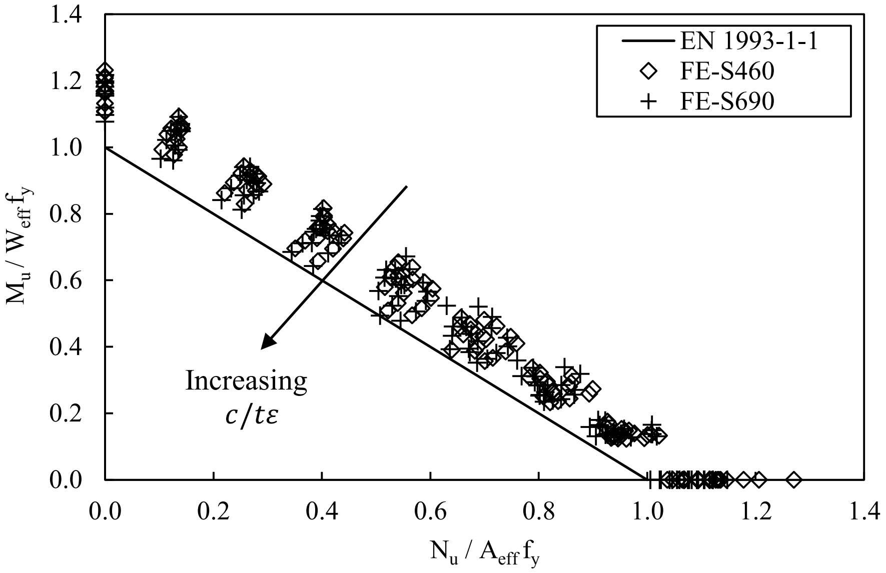

Figure 6.15: Assessment of the effective section properties and interaction curves for Class 4 cross-sections.

6.6.6. Assessment of the continuous strength method for slender sections

A modified continuous strength method applicable to sections with cross-section slenderness $\bar{\lambda}_{cs}$>0.68 has been recently proposed by Anwar-us-saadat et al. (2016). Similarly to the CSM for stocky sections, the method is based on the strain ε_{csm}, which is a function of the cross-section slenderness $\bar{\lambda}_{cs}$ and the yield stress ε_y. In order to take into account the reduced strength in slender cross-sections, a coefficient C, expressed as a function of two coefficients, A and B, and the cross-section slenderness $\bar{\lambda}_{cs}$, is introduced. Coefficients A and B for square and rectangular hollow sections under compression, major axis bending and minor axis bending were calibrated to the values shown in Table 6.7 (Anwar-us-saadat et al., 2016). The stress for slender sections $f_{csm,slender}$ is evaluated from Equation (6.12), where the coefficient C is given by Equation (6.13), whilst the load bearing and the bending moment capacity are calculated as the product of $f_{csm,slender}$ with the cross-sectional area A in Equation (6.14) and the elastic section modulus in the respective axis $W_{el,y/z}$ in Equation (6.15), respectively. The interaction of biaxial bending is considered through the application of Equation (6.16), in which the exponents are in function of the axial force, as given in Equations (6.17) and (6.18).

Table 6.7: Calibrated coefficients A and B.

	compression		major axis		minor axis	
	A	B	A	B	A	B
SHS	3.00	2.75	3.75	2.95	-	-
RHS	3.18	2.90	3.52	2.65	3.69	3.10

$$f_{csm,slender} = E\ C\ \varepsilon_{csm} \tag{6.12}$$

$$C = A\,\bar{\lambda}_{cs}{}^{B} \tag{6.13}$$

$$N_{csm} = A f_{csm,slender} \tag{6.14}$$

$$M_{csm,y/z} = f_{csm,slender}\ W_{el,y/z} \tag{6.15}$$

$$\left(\frac{M_{y,Ed}}{M_{csm,y}}\right)^{\alpha} + \left(\frac{M_{z,Ed}}{M_{cms,z}}\right)^{\beta} \leq 1 \tag{6.16}$$

$$\alpha = \beta = 20/(5n + 13) \tag{6.17}$$

$$n = N_{Ed}/N_{pl,Rd} \tag{6.18}$$

Initially, the applicability of Coefficients A and B to the currently studied sections is assessed. The numerical results of Chapters 4-5 were utilised. Note that the experiments included sections in the stocky slenderness range only, whereas the validated numerical models were applied for the production of results over a wide cross-section slenderness range. For the evaluation of the cross-section slenderness $\bar{\lambda}_{cs}$, Equations (2.16)-(2.18) were used. As can be seen in Figure 6.16, the results match closely the C curves.

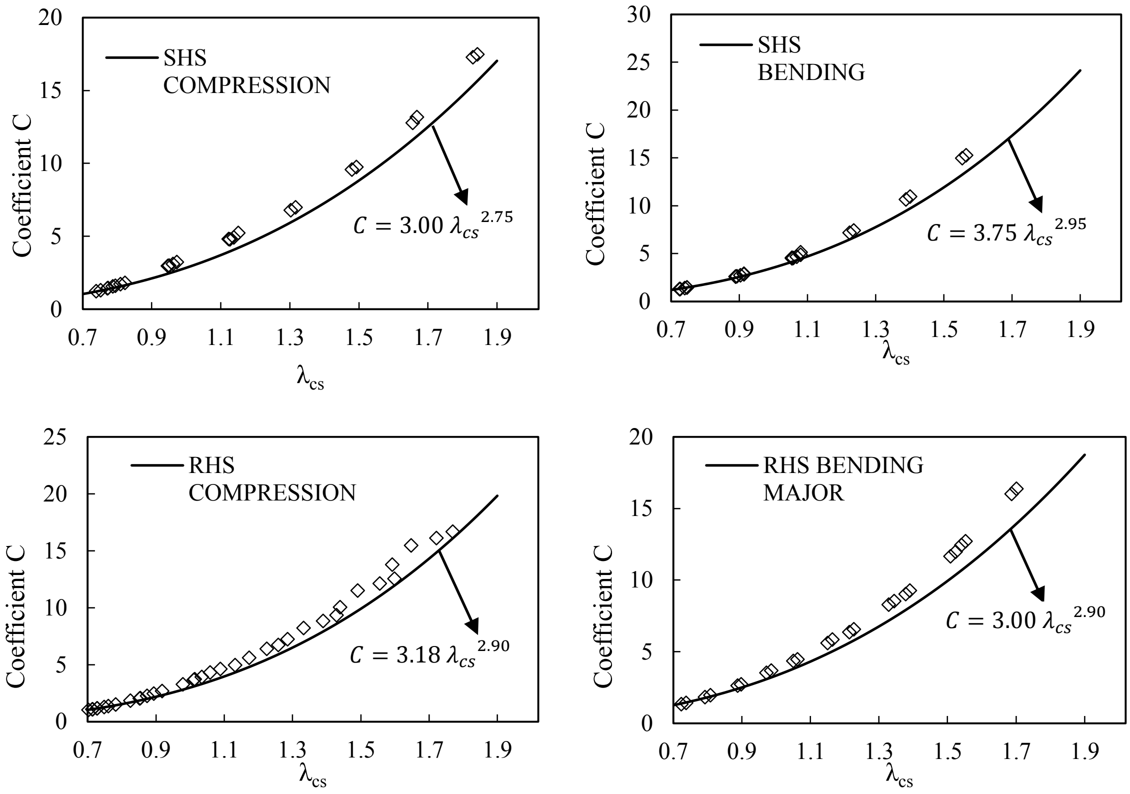

Figure 6.16: Coefficient C based on the results of Chapters 4-5.

Having checked the suitability of C curves, the applicability of Equations (6.12)-(6.18) to S460 and S690 hollow sections under biaxial bending and compression was assessed. It is worth pointing out that for some rectangular hollow sections under biaxial bending and compression, the cross-section slenderness $\bar{\lambda}_{cs}$ was higher than 0.68 for the case of minor axis bending and compression, but less than 0.68 for the case of major axis bending and compression. To allow for the evaluation of the method even for these sections, the coefficient C was considered equal to unity for the latter case. The obtained utilisation ratios are shown in Table 6.8. The modified continuous strength method for slender sections appears applicable to hot-finished hollow sections, achieving improved and more consistent predictions when compared to Eurocode estimations. Further research for a wide range of cross-sections and steel grades is recommended.

Table 6.8: Assessment of modified continuous strength method for sections with $\bar{\lambda}_{cs}$>0.68.

	S460		S690	
	No. of test or FE results: 258 FE		No. of test or FE results: 258 FE	
	R_{FE}/R_{EC3}	R_{FE}/R_{CSM}	R_{FE}/R_{EC3}	R_{FE}/R_{CSM}
MEAN	1.28	1.20	1.28	1.20
COV	0.12	0.09	0.13	0.08

6.7. Concluding remarks

The current chapter presented a detailed investigation of the structural behaviour of S460 and S690 short columns under combined bending and compression. Finite element models were validated against the test data of twelve eccentrically loaded stub columns. Aiming to expand the results over a wide range of axial load over bending moment ratios, two series of parametric studies, comprising 720 and 1376 additional analyses were executed. The results of the parametric studies on the cross-sections subjected to biaxial bending and compression facilitated the formation of interaction failure surfaces. On the basis of both the experimental and the numerical results, Eurocode specifications were assessed. The comparison was based on the R_{FE}/R_{pred} utilisation ratio.

For Classes 1 and 2 sections, Eurocode provisions were found to accurately predict the combined compressive and bending moment resistance of high strength steel hollow cross-sections, achieving an average utilisation ratio close to unity and a relatively small coefficient of variation. Only for some very stocky S460 sections that exhibited noticeable strain-hardening, Eurocode underestimates the predicted ultimate load and moment capacity. Nevertheless, Eurocode specifications for Classes 1 and 2 sections under eccentric compression are deemed overall acceptable.

Keeping in mind that the current Eurocode Class 2 limit is 38, the studied sections with cross-section slenderness $c/t\varepsilon$=35 were classified as Class 2 sections. For these sections an utilisation ratio lower than unity was found. In previous chapters, a stricter Class 2 limit of 34 was proposed for internal elements in compression. This limit would move the $c/t\varepsilon$=35 sections from Class 2 to Class 3, thereby providing safe predictions and supporting further the conclusion of Chapter 5 for a revised stricter slenderness limit for Class 2.

Comparing the results of Class 3 sections with Eurocode provisions, rather conservative design estimations were achieved. The predicted capacities could be considerably improved, both in terms of achieved mean value but also of consistency, through the implementation of the design recommendations proposed by Taras et al. (2013), which recommends a linear transition from M_{pl} to M_{el} for Class 3 sections. The current study strongly supports the adoption of this design recommendation for HSS Class 3 SHS and RHS.

For Class 4 sections, the load and bending moment capacities were firstly normalised with the respective ones determined according to the effective width method and then compared with the linear interaction Eurocode provisions. The comparison displays generally sufficiently accurate predictions.

For sections with $\bar{\lambda}_{cs}$>0.68 (i.e. Class 3 and Class 4 sections of the current chapter), the applicability of modified CSM for slender sections, recently proposed by Anwar-us-saadat et al. (2016), was assessed. In order to evaluate the suitability of the previously proposed coefficient C to the slender hot-fished cross-sections, the numerical results of Chapters 4-5 were utilised. The method was found to be applicable to the presently studied sections, providing better design predictions than Eurocode.

CHAPTER 7: HIGH STRENGTH STEEL PRESTRESSED TRUSSES

7.1. Introduction

In previous chapters, studies concerning the ultimate strength of high strength steel individual members were carried out. When designing a long span structure, the serviceability limit state is likely to govern the design. In HSS structures, the material strength f_y is higher than that of ordinary steel structures but the Young's modulus E remains the same. Hence, stiffness rather than strength is more likely to control the design of structures with higher steel grades. This becomes increasingly important for long span structures.

In order to justify the aforementioned statement, the results of the HSS beams of Chapter 5 have been utilised. Making the assumption that the deflection limit δ_{SLS} for simply-supported beams of length L is $L/200$ (Gardner and Nethercot, 2011), the corresponding load F_{SLS} has been derived from each numerical analysis. Note that in most cases, the extracted force F_{SLS} was found in strains within the elastic range, leading to a value very close to that found from the application of the simplified formula for the evaluation of the mid-span deflection of pinned beams with one concentrated load at the mid-point: $F_{SLS} = \delta_{SLS} 48EI/L^3$, where I the section moment of area of the beam. In order to evaluate which limit state is more critical for design, the F_{SLS} for each studied cross-section was divided by the corresponding ultimate strength F_{ULS}. Based on the obtained results and assuming different values for the G_{ULS}/G_{SLS} ratio (i.e. the ratio of design load combinations of the ULS to the SLS limit state, including the partial safety factors γ, as defined in Eurocode (EN 1990, 2002)), the tables of Figure 7.1 have been developed.

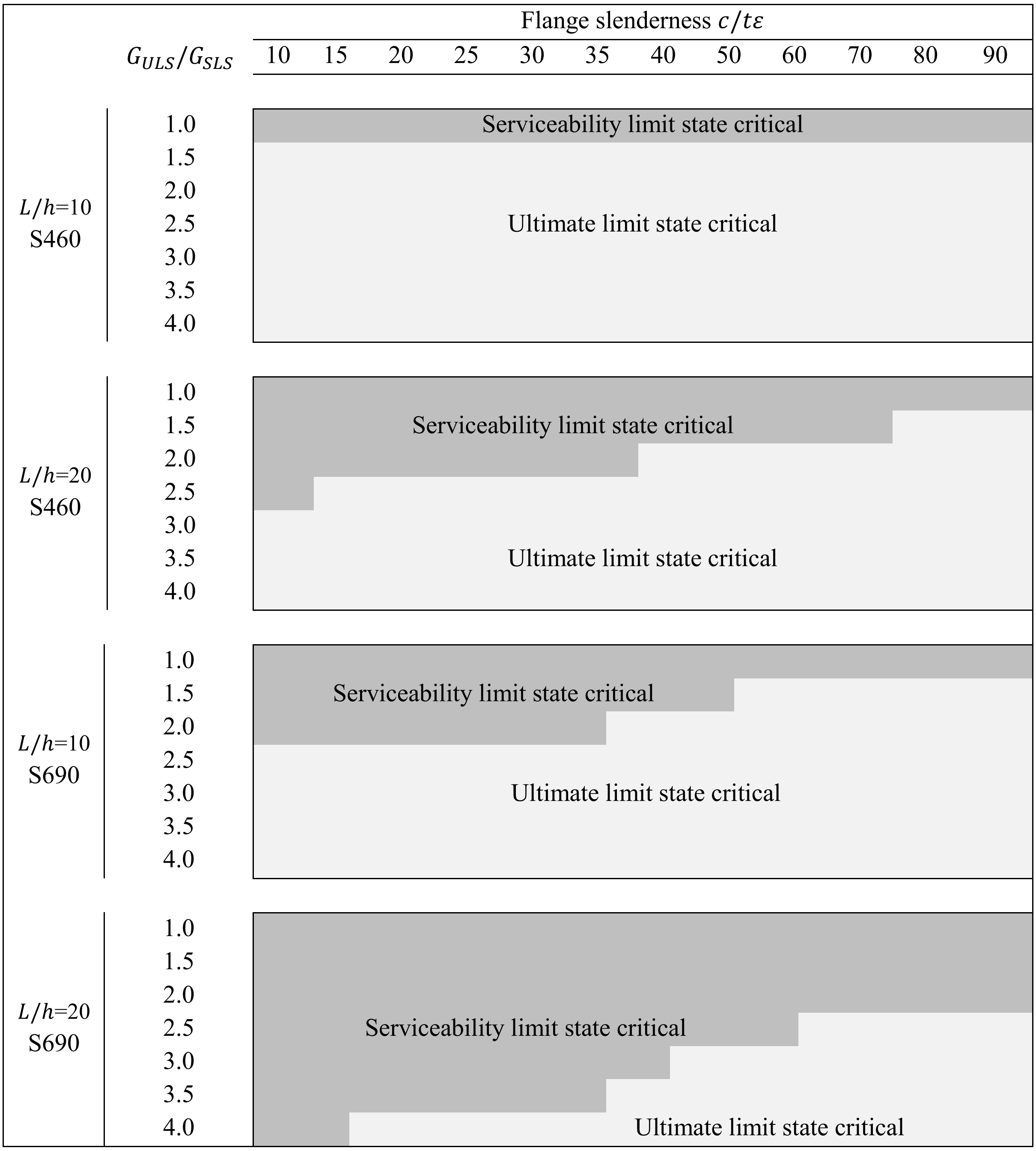

Figure 7.1: Critical limit state based on the results of HSS beams.

As can be observed, for some cases, the ultimate limit state can be critical, adding extra value to the research performed in the previous chapters. However, as anticipated for increasing steel grade (S690 compared to S460) and for increasing span (L/h=20 compared to L/h=10), the design is expected to be governed by serviceability limit state verifications. Hence, it is essential to find a way to mitigate excessive deflections, thus preventing from limited exploitation of the increased material strength in HSS structures.

Based on a concept, which originated several years ago in Australia (Clarke and Hancock, 1995, 1994) and implemented by S-Squared company (S-Squared, 2017), the possibility of utilising prestess in order to control the deflections in high strength steel structures is examined. Aiming to investigate the concept of storing energy under increasing preload, thus allowing minimum material consumption, the current chapter reports an extensive study on high strength steel prestressed trusses comprising tubular members, in which prestress is introduced via pretensioning of a cable inserted in the bottom chord, prior to application of service loads. Besides controlling the vertical deflections, the cables contribute to enhancing the lateral stability and reducing further the material usage. Comprehensive finite element models have been developed and validated against test results. Thereafter, parametric studies were performed and relevant design recommendations were provided. Even though the studied trusses employed square hollow sections, the results are expected to be applicable for any type of tubular members.

7.2. Brief description of the test programme

Four high strength steel trusses have been tested to failure at the structures Lab of Imperial College London. The trusses spanned over a length of 11 m and comprised S460 hot-finished square hollow section members. The top and bottom chord elements employed SHS 70×70×6.3 and SHS 50×50×5 respectively, whilst the vertical and diagonal elements employed SHS 40×40×2.9, apart from those at the end supports, which were SHS 50×50×5. All adopted high strength steel tubular elements were Class 1 sections to avoid premature failure by local buckling. All joints were fabricated with full penetration butt welds. The overall configuration and a photo of the set-up are shown in Figure 7.2(a) and Figure 7.2(b). Each of the trusses was fabricated in three pieces and was assembled in the Structures Laboratory at Imperial College London by bolting together the construction joints.

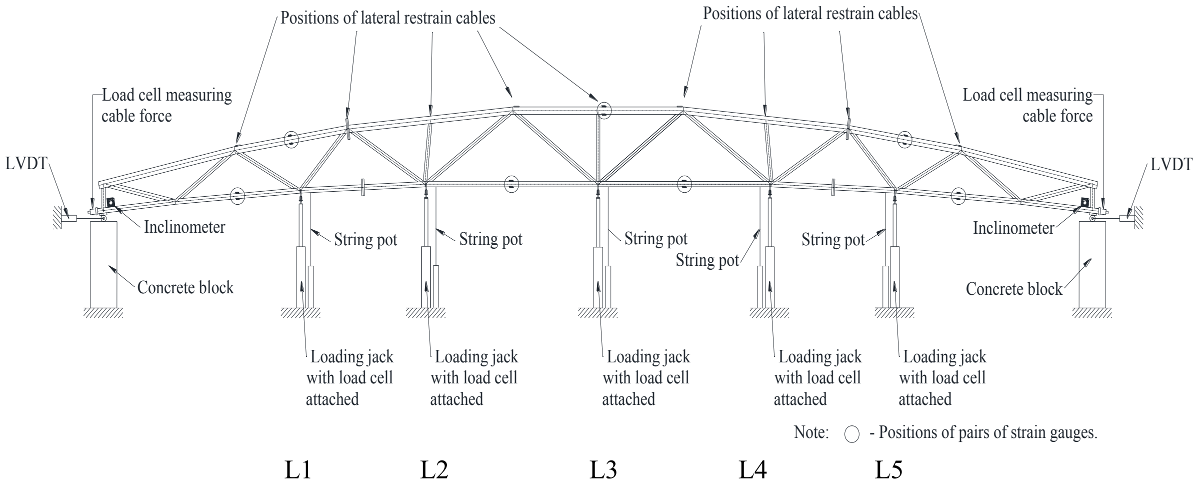

a) Schematic diagram

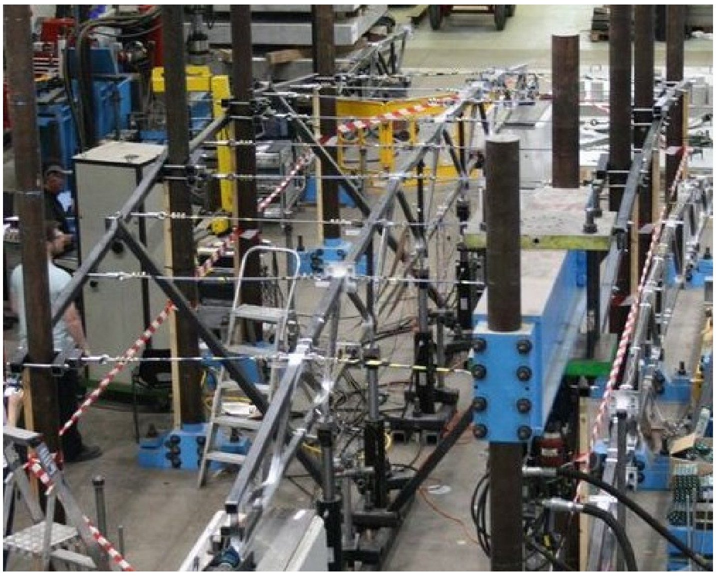

b) Test set-up

Figure 7.2: Truss test rig set-up.

One truss had no prestressing cable and was used as a control specimen (Truss 1), whilst the remaining three trusses had a 7-wire strand prestressing cable, with tensile strength of 1860 N/mm^2, inserted within their bottom chord. In order to study the effect of the prestress level to the overall response, varying initial loads have been assigned to the cable. In particular, Truss 2, Truss 3 and Truss 4 were prestressed to P_{nom}, 0.5 P_{opt} and P_{opt} respectively. P_{nom} is the nominal prestress to remove slack, whilst the optimal prestress value P_{opt} is the prestress that causes the cable and the surrounding steel tube to yield simultaneously when subjected to tension and is given by Equation (7.1) (Gosaye et al., 2014).

$$P_{opt} = \left(\frac{A_c A_t}{A_t E_t + A_c E_c}\right)\left(f_{cy} E_t - f_{ty} E_c\right) \;\; but \; P_{opt} \leq A_t f_{yt} \;\; and \;\; A_c f_{yc} \tag{7.1}$$

where A, E and f_y are the cross-sectional area, Young's modulus and yield strength, whilst the subscripts c and t refer to the cable and surrounding steel tube respectively.

The average measured geometry of the truss is shown in Table 7.1, where h is the section depth, b is the section width, t is the section thickness and r_i is the internal corner radius.

Table 7.1 Measured dimensions of the truss elements.

Cross-section	h (mm)	b (mm)	t (mm)	r_i (mm)
SHS 70×70×6.3	69.95	70.02	6.21	3.79
SHS 50×50×5	50.48	50.44	4.95	3.50
SHS 40×40×2.9	40.16	40.20	2.87	1.27

Instrumentation including string potentiometers, inclinometers, LVDTs and strain gauges were used in order to capture in detail the structural performance, which was recorded with the aid of data acquisition system DATASCAN and logged using the DSLOG computer package. In Trusses 2-4, prestressing was employed to the specimens by a stressing jack. The nominal and applied prestress loads are shown in Table 7.2.

Table 7.2: Nominal and measured prestress loads.

Specimen	Nominal prestress (kN)	Measured prestress (kN)
Truss 1	0	0
Truss 2	5.0 (P_{nom})	5.9 (P_{nom})
Truss 3	94.5 $(0.50P_{opt})$	80.8 $(0.43P_{opt})$
Truss 4	189.0 (P_{opt})	149.9 $(0.79P_{opt})$

Five hydraulic jacks were used for the application of vertical downward loading through five point loads on the bottom chord. Steel plates welded onto the bottom chord of the trusses at the specified loading locations were utilised to connect the loading jacks to the truss. Steel rollers were applied for the introduction of simply supported conditions at the truss ends. In order to simulate the lateral restrain provided by the purlins to the compression chord of a real structure, a series of lateral restraints through cables tied to pillars were provided to the top chord of the truss at the joint locations. The ultimate loads and the corresponding failure modes are reported in Table 7.3. A thorough description of the experiments is given in Wang et al. (in preparation). The experimental load-deformation together with the respective numerically obtained behaviours are discussed in the following sections.

Table 7.3: Summary of the truss tests.

Specimen	Failure mode	Ultimate load (kN)
Truss 1	In-plane buckling of top chord element	185.4
Truss 2	In-plane buckling of top chord element	258.0
Truss 3	Out-of-plane buckling of top chord	243.2
Truss 4	In-plane buckling of top chord element	269.2

7.3. Development of the finite element models

In order to produce finite element models, able to accurately predict the test response, extensive numerical modelling, considering various influential parameters, was performed.

In order to investigate the influence of the selected element type on the response of the whole structure, two numerical truss models were developed. A model with beam elements (B31) for the truss members and truss elements (T3D2) for the cable (denoted as model B) and a model with shell elements (S4R) for the truss members and solid elements (C3D8R) for the cable (denoted as model S) have been examined. The main difference between the two studied models is that model B cannot precisely capture the localised deformations at the joints which can be achieved by model S. Note that model B is much simpler and requires less computational time than model S. In order to ensure an adequately refined mesh size able to provide accurate results within reasonable computational time, a mesh convergence study was initially performed. Appropriate boundary conditions and constraints were introduced in order to replicate the test conditions. In particular, simply-supported conditions were employed at the truss ends, whereas the top chord joints were restrained laterally at the place of the restraint cables. Five vertical concentrated loads were applied at the bottom chords at the location of the loading jacks, whilst in model S, the loads were assigned at the lower part of the web at the web-corner junction, in line with the validated model of Chapter 5. For Trusses 2-4, the cable was tied to the bottom chord.

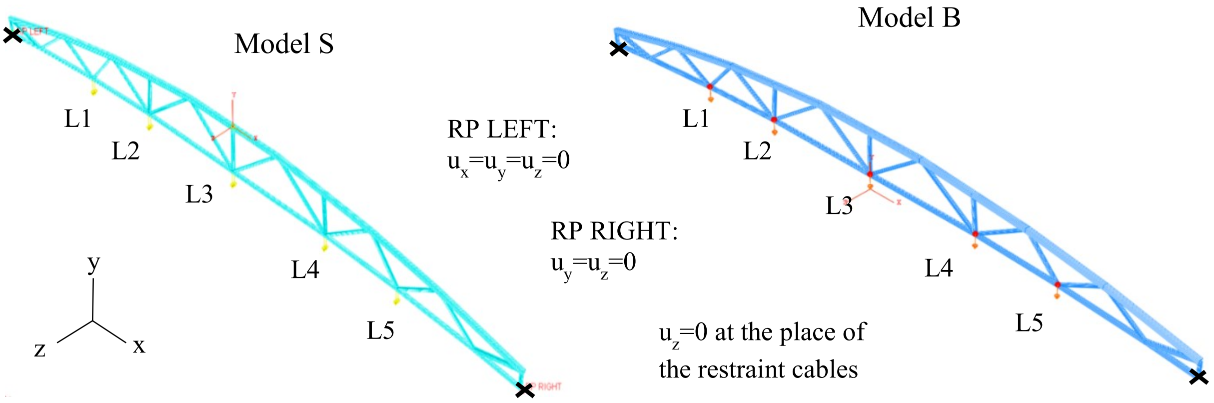

Figure 7.3: Numerical truss model.

The average material properties derived from S460 tensile flat coupon tests were incorporated for the truss members. As presented in Figure 3.9, apparent discrepancies were noticed in the stress-strain response for cables of varying lengths. Hence, it was deemed important to study the effect of the cable's apparent material properties on the structural behaviour of the truss within the FE investigation. To this end, models incorporating cables with Young's modulus 90000 N/mm^2, 130000 N/mm^2 and 215000 N/mm^2 denoted as Ec90, Ec130 and Ec215 hereafter have been examined. An elastic-plastic material model with a Von Mises yield criterion and isotropic hardening was employed for both the truss members and the cable. The engineering material properties have been appropriately converted to true stresses and logarithmic plastic strains before their input into the software.

The mode shapes extracted from a linear eigenvalue buckling analysis were introduced at the truss models before the execution of the nonlinear static analysis. The selected in-plane and out-of-plane mode shapes, which were found to correspond accurately to the observed experimental failure modes, are illustrated in Figure 7.4. In order to account for geometric and material nonlinearities, the Riks algorithm was used. Additionally, prior to Riks analysis, a predefined stress state together with an initial general static step to achieve equilibrium, were executed in order to account for the initial prestressing applied to the trusses. Similarly to the previous chapters, the residual stresses which were found to be of very low magnitude were not explicitly modelled.

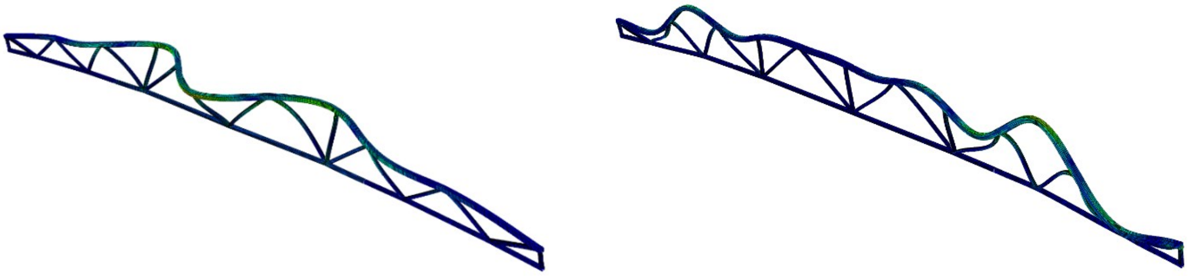
a) out-of-plane buckling

b) in-plane buckling

Figure 7.4: Numerical elastic buckling mode shapes.

As mentioned in Section 7.2, each truss comprised two assembly bolted connections on the bottom and the top chord, to facilitate its erection in the lab. When the truss is subjected to vertical loading, the bottom chord is under tension and hence it was decided to investigate the effect of the bottom connections' flexibility on the stiffness of the whole structure. In order to allow for a simplified calculation of the contribution of the connections' stiffness to the bottom chord's stiffness, a numerical model of the connection was developed, as shown in Figure 7.5. 3D solid elements, eight-noded for the plate elements and the stiffeners and ten-noded for the bolts were used, whilst five elements were employed through the thickness of the plates. Given that the initial stiffness of the connection was of interest, only the elastic material properties of the steel components were employed. The connection was loaded under tensile static load and the deformed shape is shown in Figure 7.5. The connection stiffness k was obtained by plotting the incremental load (N) against the gap opening in the middle of the plates (mm) and was found equal to 590000 N/mm.

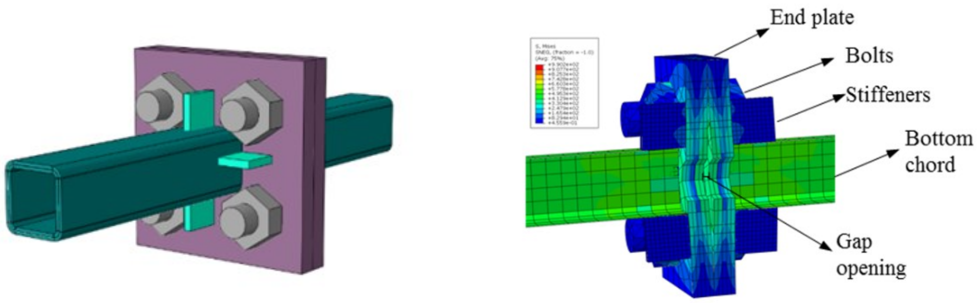

a) solid model b) deformed shape illustrating the gap opening

Figure 7.5: Connection of the bottom chord.

Assuming the bottom chord as a straight member with two springs of stiffness k=590000 N/mm, its axial stiffness for elastic response can be approximated by Equations (7.2) and (7.3).

$$\delta_{bottom\,chord} = \frac{PL}{EA} = \frac{1000 \times 11000}{210000 \times 858} = 0.061\,mm \tag{7.2}$$

$$\delta_{connection} = \left(\frac{1}{k}\right)P = \left(\frac{1}{590000}\right)1000 = 0.00169\,mm \tag{7.3}$$

where δ is the axial deformation of the subscript, P is the unit axial load (set equal to 1000 N), E the Young's modulus of the truss members, A the cross-sectional area of the bottom chord and k the stiffness of the connection, as previously evaluated. Equations (7.4) and (7.5) show that by ignoring the effect of the connections of the bottom chord, an overestimated stiffness by 5% should be anticipated by the numerical model.

$$\delta_{total} = 2\,\delta_{connection} + \delta_{bottom\,chord} = 0.0644\,mm \tag{7.4}$$

$$(2\delta_{connection})/\,\delta_{total} = 5.24\% \tag{7.5}$$

Hence, a model where the connections were modelled with springs of axial stiffness 590000 N/mm (denoted as spr590) and a model where the connections were ignored (denoted as sprNO) were studied, in order to examine the effect of the connections' stiffness on the overall response.

7.4. Validation of the finite element models

The numerically generated load-deformation response is compared with the experimental one in Figure 7.6-Figure 7.9 for Truss 1-4 respectively. In each truss, the introduced imperfection magnitude has led to an accurate capture of the respective failure mode. The effect of the employed FE element type on the overall structural response has been studied for all trusses. For Truss 1, focus was also placed upon the flexibility of the bottom chord's connections. The effect of cable's material characteristics on the overall structural response has been examined for Trusses 2, 3 and 4.

As can be observed in Figure 7.6-Figure 7.9, model B overpredicts the stiffness of the system in all cases. Model S, which is able to account accurately for the actual stiffness of the joints, results in a more flexible response, closer to the experimental observations. In addition, Figure 7.6 reveals that through the incorporation of the bottom chord connections, as springs of axial stiffness 590000 N/mm in model S, the initial numerical stiffness matches precisely the experimental one. This assumption was also incorporated for the prestressed trusses of

Figure 7.7-Figure 7.9, in which FE results achieve better agreement with the experimental ones when the lowest Young's modulus value is employed. It is worth noting that the effect of the apparent Young's modulus of the cable on the overall structural behaviour is more evident in Truss 2 than in Truss 3 and 4. This might be related to the effect of sagging of the cable within the bottom chord tube due to its lower effective stiffness. For a very low prestress level (i.e. in Truss 2), which will not commonly be the case in the real practice, this effect appears more pronounced. For increasing prestress level (i.e. in Trusses 3 and 4) the sagging of the cable is considerably decreased and so does the discrepancies in the response of trusses employing cables with different Young's modulus. Finally, as anticipated, the applied prestress in Truss 3 and Truss 4 led overall to a stiffer structural response compared to the response of Truss 2.

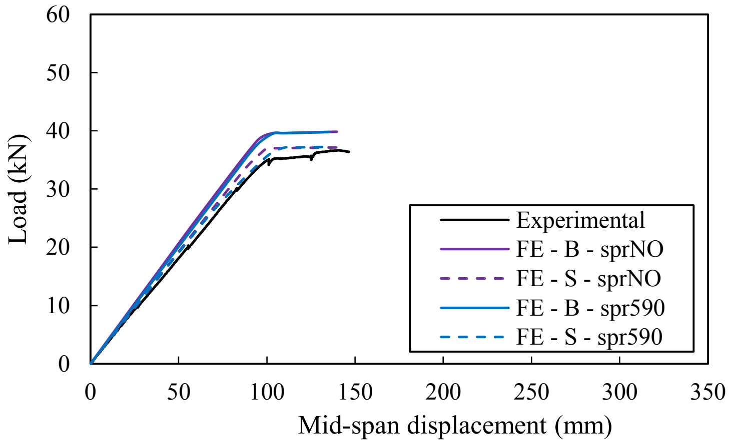

Figure 7.6: Truss 1 - Validation of Truss 1.

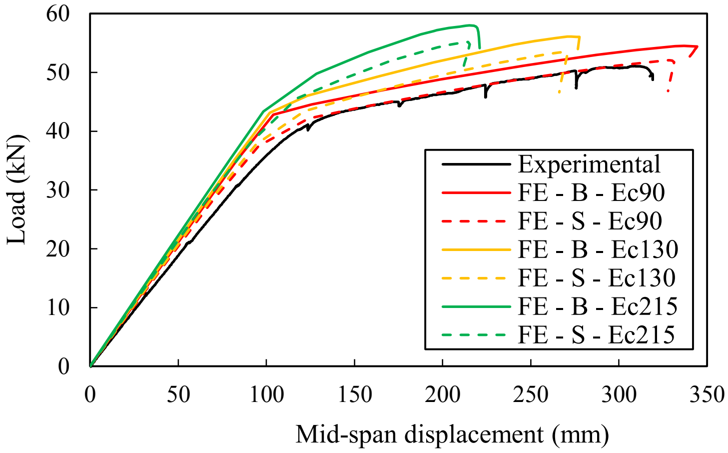

Figure 7.7: Truss 2 - Validation of Truss 2.

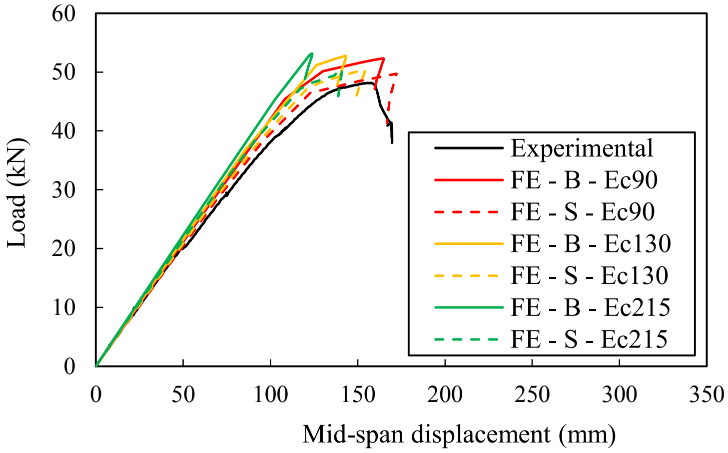

Figure 7.8: Truss 3 - Validation of Truss 3.

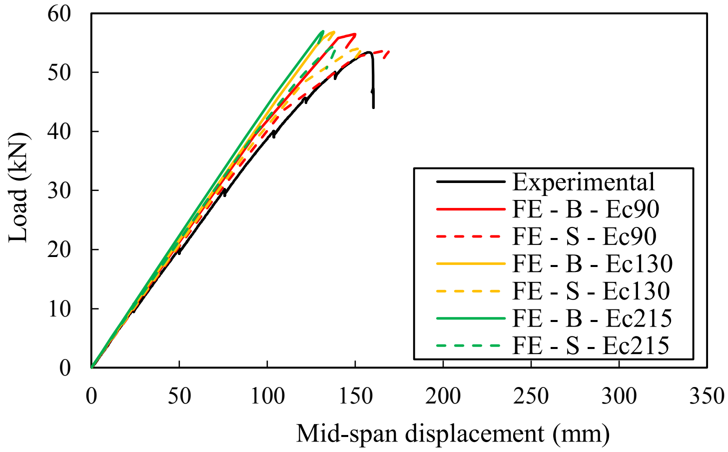

Figure 7.9: Truss 4 - Validation of Truss 4.

Overall, the model with shell elements for the truss members, with an axial spring in place of the connections of the bottom chord and a cable with lowest Young's modulus led to an excellent agreement with the test results. For this model, the total load-vertical displacement curves for load points L3, L1/L5 and L2/L4 are illustrated in Figure 7.10. Note that for the FE models, the displacements reported at L1 and L2 were equal to those reported at L5 and L4 respectively. The accurately captured both in-plane and out-of-plane failure modes are depicted in Figure 7.11.

On the basis of the both the experimental and the numerical results, it is evident that the addition of a non-prestressed cable in Truss 2 leads to a small increase in the overall stiffness and a significant increase (i.e. 45%) of the maximum load achieved by the bare truss (Truss 1), owing to the increased capacity of the bottom chord. However, due to the cable having much higher yield strength than the surrounding tube, the maximum load of Truss 2 is attainable only at high inelastic deformations i.e. long after the bottom chord has yielded. In Trusses 3 and 4, it is apparent the effect of prestress in delaying the yielding of the bottom chord and hence extending the elastic range of the system response. In these cases, the maximum loads are close to those of Truss 2, but are attained at much lower and almost elastic deformations. In particular, the ultimate load in Truss 4 was achieved at 49% smaller mid-span displacement than in Truss 2. It can be stated that the addition of an optimally prestressed cable significantly increases the overall capacity of the truss, provided, though, that buckling of the top chord does not occur prematurely.

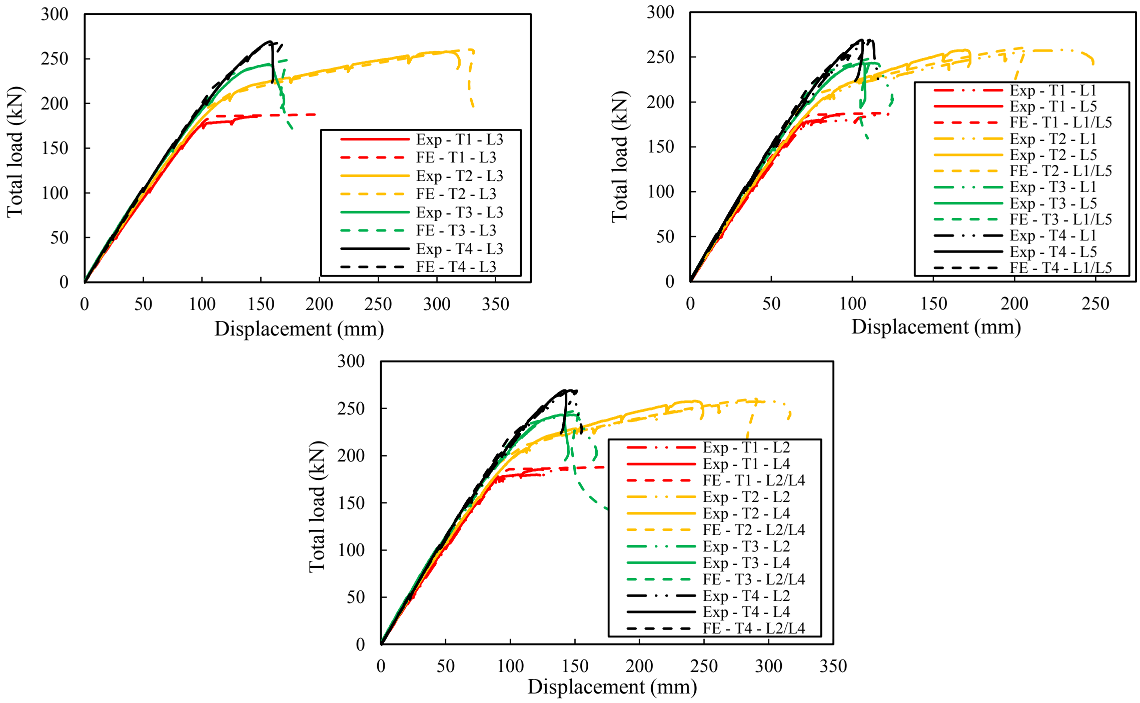

Figure 7.10: Validation of FE models for trusses.

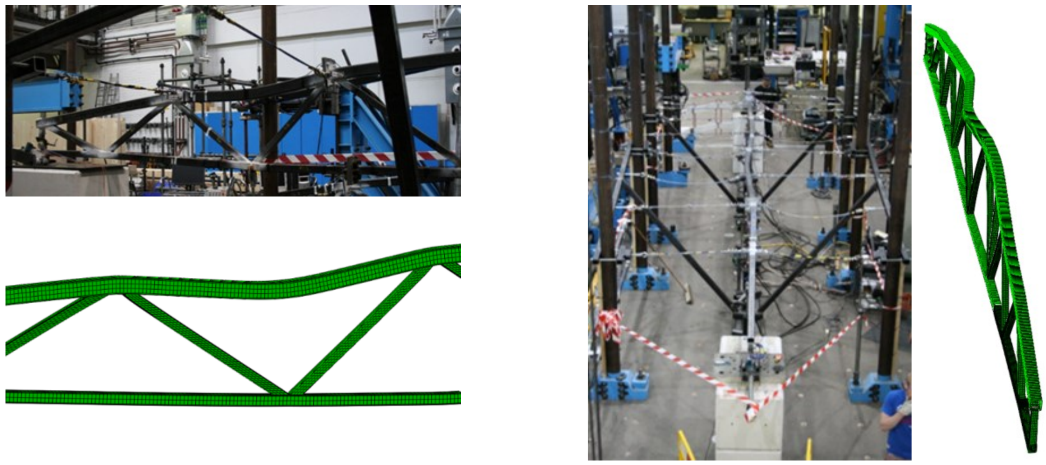

a) in-plane buckling of the compressive top chord

b) out-of-plane buckling of the top chord

Figure 7.11: Typical experimental and numerical failure modes (Gkantou et al., 2016).

Upon establishment of the FE models, ten combinations of varying in-plane and out-of-plane geometric imperfection magnitudes, expressed in function of the length L of the buckled member, have been examined. For all considered imperfection magnitudes, the full load-displacement response was tracked, while the numerical to experimental ratios of the initial stiffness ($k_{\text{initial,FE}}/k_{\text{initial,Exp}}$), the maximum recorded load during the analysis/test, named as ultimate or failure load, ($F_{\text{u,FE}}/F_{\text{u,Exp}}$) and the displacement at failure load ($\delta_{\text{u,FE}}/\delta_{\text{u,Exp}}$) were reported. After estimating the comparison ratios for all five loading points of each truss, the average values for the four trusses (T1, T2, T3, T4), with F_u being averaged from all load points of each truss and k_{initial} and δ_{u} based on the mid-span deflections only, were evaluated, as shown in Table 7.4. The ultimate load and the initial stiffness were generally very well predicted, whereas the mid-span displacement at failure load appeared to be more sensitive to the magnitude of the initial geometric imperfections. As can be observed, less conservative results were attained for in-plane imperfections higher than the out-of-plane ones. Overall, the models with out-of-plane imperfection amplitude of $L/750$ and in-plane imperfection magnitude $L/1500$ led to excellent agreement with the test results, achieving values of $F_{\text{u,FE}}/F_{\text{u,Exp}}$ and $k_{\text{initial,FE}}/k_{\text{initial,Exp}}$ equal to 0.98 and 1.02 respectively. The aforementioned magnitudes will be employed in the subsequent parametric studies. It should be noted that assuming $L/1000$ and 0 for the out-of-plane and the in-plane imperfection magnitude respectively, good capture of the test behaviour was achieved, but this combination was not preferred, as it does not consider any initial in-plane geometric imperfections and hence is not a realistic scenario.

Table 7.4: Comparison of FE and test data - Summary for all trusses.

Imperfection magnitude		$F_{\text{u,FE}}/F_{\text{u,Exp}}$		$\delta_{\text{u,FE}}/\delta_{\text{u,Exp}}$ (only for L3)		$k_{\text{initial,FE}}/k_{\text{initial,Exp}}$ (only for L3)	
Out-of-plane	In-plane	MEAN	COV	MEAN	COV	MEAN	COV
L/1000	L/1000	0.99	0.041	1.02	0.176	1.02	0.043
L/2000	L/1000	1.01	0.041	1.15	0.180	1.02	0.043
L/1000	L/2000	1.00	0.053	1.03	0.175	1.02	0.043
L/1500	L/750	1.01	0.040	1.10	0.174	1.02	0.043
L/750	**L/1500**	**0.98**	**0.042**	**0.96**	**0.178**	**1.02**	**0.043**
L/1000	0	0.99	0.041	1.03	0.175	1.02	0.043
0	L/1000	1.04	0.047	1.32	0.236	1.02	0.043
L/2000	L/2000	1.02	0.041	1.15	0.181	1.02	0.043
L/750	L/750	0.98	0.044	0.96	0.185	1.02	0.043
L/1500	L/1500	1.01	0.041	1.10	0.176	1.02	0.043

7.5. Parametric studies

Upon successful validation of the FE models, parametric studies were performed in order to investigate the influence of key parameters, on the gains in strength and the reduction of the mid-span displacement at failure load, that emerge from the use of the prestress.

7.5.1. Simplified models

The accurately validated model that employed shell and solid elements involved overly demanding computational analyses. Aiming to improve the computational efficiency and ensure reasonable computational times that would allow the execution of comprehensive parametric studies, a simplified model was developed and compared with the validated FE model. The simplified model employed beam elements for the truss members and truss elements for the cable, without considering any springs for the modelling of the connections, which is what is also happening in design practice. Note that attempts to precisely model only the members, at which failure was anticipated, combining shell and beam elements were also made. However, the explicit incorporation of only certain members further complicated the models without significantly affecting the observed response. Focus was therefore placed upon models comprising only beam and truss elements.

The previously validated model is denoted as model V hereafter, whilst the new simplified model that is aimed for use in the subsequent parametric studies is denoted as model P. In order to ensure that the anticipated benefits associated with the use of prestress are accurately captured by both models, the gains in strength and the reduction of the mid-span displacement at failure load due to prestress were the basis of the comparison. The gains in strength were evaluated by normalising the ultimate load of a prestressed truss (Truss 2, 3 or 4) with the corresponding load of the bare truss (Truss 1) (F_{uV}/F_{uV1} and F_{uP}/F_{uP1} for model V and model P respectively). Similarly, the reduction of the mid-span displacement at failure load was evaluated by normalising the mid-span deflection of the models with $0.5P_{opt}$ or P_{opt} prestress (Truss 3 or 4) with the respective deflection of the models with P_{nom} prestress (δ_{uV}/δ_{uV2} and δ_{uP}/δ_{uP2}). Upon completion of the nonlinear static analyses on the new simplified models, the load deformation response of model P and model V has been compared, as shown in Figure 7.12. The respective comparison ratios are reported in Table 7.5. An can be seen, both models yield similar results concerning the beneficial effects owing to prestress, with a mean value of the compared gains in strength equal to 1.01 and of the compared reduction of the mid-span displacement at failure load equal to 1.07. Hence, it can be concluded that explicitly incorporating the connection stiffness and the joint flexibility (i.e. through the shell element idealisation of the joints) eventually affects the results of the model and the response to the control model used for normalisation. This shows that although the simplified model overestimates the overall structural stiffness, it is able to safely estimate the gains in strength and the reduction of the mid-span displacement at failure load arising from the application of prestress in trusses. Using the simplified models for further study led to significant computational cost savings.

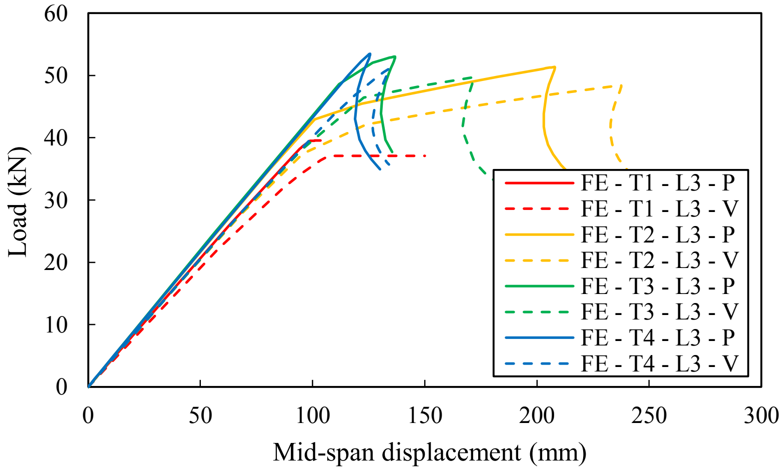

Figure 7.12: Comparison between simplified (model P) and validated (model V) model.

Table 7.5: Gains in strength and reduction of the mid-span displacement at failure load.

Specimen	Simplified model (model P) Beam elements & no springs				Validated model (model V) Shell elements & springs				Simplified / Validated model P / model V	
	F_{uP}	δ_{uP}	F_{uP} $/F_{uP1}$	δ_{uP} $/\delta_{uP2}$	F_{uV}	δ_{uV}	F_{uV} $/F_{uV1}$	δ_{uV} $/\delta_{uV2}$	(F_{uP}/F_{uP1}) $/(F_{uV}/F_{uV1})$	$(\delta_{uP}/\delta_{uP2})$ $/(\delta_{uV}/\delta_{uV2})$
Truss 1	195.21	97.21	-	-	185.56	108.17	-	-	-	-
Truss 2	256.82	207.87	1.32	-	242.07	237.39	1.30	-	1.01	-
Truss 3	265.23	162.07	1.36	0.78	248.58	172.18	1.34	0.73	1.01	1.07
Truss 4	267.42	125.61	1.37	0.60	255.61	134.35	1.38	0.57	0.99	1.07
								MEAN	1.01	1.07
								COV	0.01	0.05

7.5.2. Parametric studies

Comprehensive parametric studies have been executed in order to study the effect of key parameters on the structural behaviour of prestressed steel trusses for a wide range of structural configurations likely to occur in practice. Emphasis was placed upon: i) the level of the applied prestress, ii) the effect of the curvature of the truss chords, iii) the steel grade of the truss elements, iv) the employed cross-section sizes for the truss-chords and v) the truss shape.

Increasing prestress levels have been investigated for the arched truss considered earlier, as shown in Figure 7.13, where the total vertical load of all the studied cases has been normalised with the bare truss failure load (i.e. the truss without any cable) and plotted against the mid-span displacement. As anticipated, the ultimate load gets higher for increasing prestress level, whereas the displacement at failure load decreases respectively. For prestress force higher than the P_{opt} value (and lower than the yield load of the cable), no further benefit, in terms of gains in strength or of reduction of the mid-span displacement at failure load, appears.

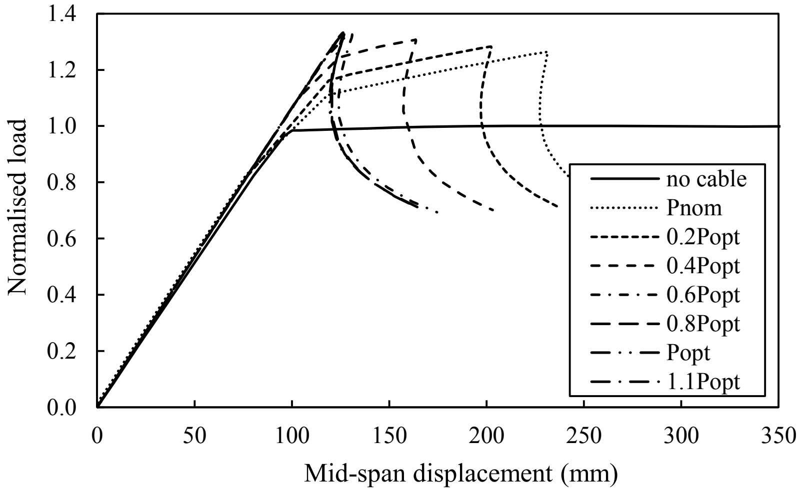

Figure 7.13: Load-mid-span displacement curves for various levels of applied prestress.

In order to consider the effect of the curvature of the truss chords on the gains related with the use of prestress, trusses with varying span-to-depth ratios (where span is the horizontal distance between the truss supports and depth is the vertical distance between the mid-span of the arched bottom chord and the mid-span of an assumed straight bottom chord) have been studied. In addition to $L/44$ (=11000/250) which corresponds to the span-to-depth ratio of the truss examined earlier, three additional values for the span-to-depth ratios: 0 (i.e. straight bottom chord), $L/90$ and $L/30$, have been examined for four prestress levels (i.e. no cable, P_{nom}, $0.5P_{opt}$, P_{opt}). For the truss elements, the same section sizes and steel grade with the validated model have been employed.

Table 7.6 presents the achieved gains in strength and the reduction of the mid-span displacement at failure load. As can be seen, the application of prestress appears advantageous in all cases. For the considered truss configurations, no clear trend among varying span-to-depth ratios has been observed.

Table 7.6: Effect of curvature of the truss chords on the response of prestressed trusses.

span-to-depth: 0	F_u/F_{u1}	δ_u/δ_{u2}	span-to-depth: $L/90$	F_u/F_{u1}	δ_u/δ_{u2}
no cable	-	-	no cable	-	-
P_{nom}	28%	-	P_{nom}	23%	-
$0.5P_{opt}$	33%	39%	$0.5P_{opt}$	28%	38%
P_{opt}	35%	50%	P_{opt}	29%	46%
span-to-depth: $L/44$	F_u/F_{u1}	δ_u/δ_{u2}	span-to-depth: $L/30$	F_u/F_{u1}	δ_u/δ_{u2}
no cable	-	-	no cable	-	-
P_{nom}	21%	-	P_{nom}	23%	-
$0.5P_{opt}$	26%	38%	$0.5P_{opt}$	29%	39%
P_{opt}	28%	46%	P_{opt}	30%	47%

The effect of the applied steel grade on the structural response of prestressed trusses is illustrated in Figure 7.14. Five trusses comprising elements in commonly applied steel grades (S235, S275, S355, S460, S690) have been examined, assuming elastic-perfectly plastic material behaviour. The same truss configuration and cross-section sizes with the validated model have been employed to the truss elements in the considered steel grade. As expected, the introduction of prestress in trusses of various steel grades increases the normalised (with the respective bare truss load) ultimate load and reduces the corresponding mid-span displacement in all cases.

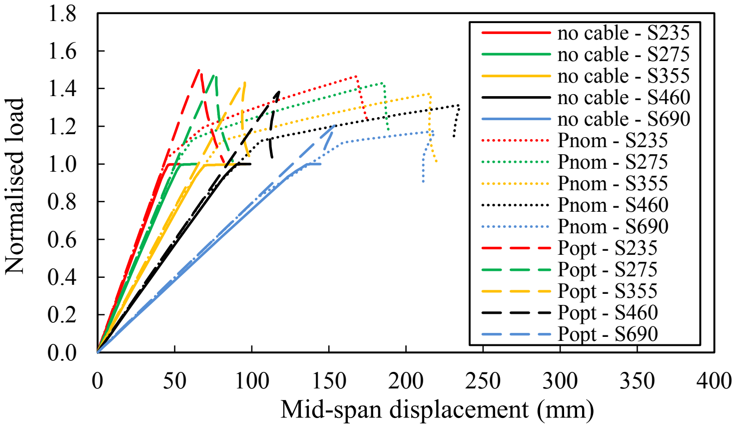

Figure 7.14: Load-mid-span displacement curves for various steel grades.

In order to assess the effect of the employed cross-section sizes for the top (A_{top}) and the bottom chord (A_{bottom}), five ratios of A_{top}/A_{bottom} were assessed. Four prestress levels (i.e. no cable, P_{nom}, $0.5P_{opt}$, P_{opt}) have been studied for the following five cases:

- Top chord 70×70×7, bottom chord 40×40×4, A_{top}/A_{bottom} =2.80 - case (a)
- Top chord 80×80×8, bottom chord 50×50×5, A_{top}/A_{bottom} =2.56 - case (b)
- Top chord 70×70×7, bottom chord 50×50×5, A_{top}/A_{bottom} =1.79 - case (c)
- Top chord 60×60×6, bottom chord 50×50×5, A_{top}/A_{bottom} =1.44 - case (d)
- Top chord 70×70×7, bottom chord 60×60×6, A_{top}/A_{bottom} =1.25 - case (e)

Note that case (c) corresponds to the test specimens studied earlier in this chapter, whilst two representative cases of higher (cases (a) and (b)) and lower (cases (d) and (e)) ratios have been selected for further study. Table 7.7 presents the gains in strength and the reduction of the mid-span displacement at failure load, together with the corresponding failure modes. As can be observed, in both cases (a) and (b), the introduction of prestress increases the ultimate load. In case (b), no significant strength gains appeared for varying prestress levels, whereas the large section of the top chord delayed buckling and the truss finally failed due to yielding of the tensile bottom chord, leading to more prominent stiffness gains for optimal prestress level compared to those at case (a). Case (c) with an intermediate A_{top}/A_{bottom} ratio presented increasing gains (both in strength and in reduction of the mid-span displacement at failure load) for increasing prestress level. In cases (d) and (e) with the lowest A_{top}/A_{bottom} ratios, the truss failed at small strains, due to out-of-plane buckling of the top chord, preventing the benefits of prestress to emerge. This shows that the truss design can affect significantly the achieved gains by the use of prestresss. Failure due to yielding of the tension chord should occur prior to buckling of the compression chord, thus ensuring a ductile failure mode and increasing the beneficial effect of prestressing.

Table 7.7: Effect of employed chord section ratio (A_{top}/A_{bottom}) on the response of prestressed trusses.

Prestress level	Gains – Strength (F_u/F_{u1})	Gains – Mid-span Displacement (δ_u/δ_{u2})	Failure Mode
Top chord 70×70×7, Bottom chord 40×40×4, A_{top}/A_{bottom} =2.80 (case (a))			
no cable	-	-	Y
P_{nom}	67%	-	Y & OUT
$0.5P_{opt}$	73%	22%	Y & OUT
P_{opt}	76%	46%	Y & OUT
Top chord 80×80×8, Bottom chord 50×50×5, A_{top}/A_{bottom} =2.56 (case (b))			
no cable	-	-	Y
P_{nom}	47%	-	Y & OUT
$0.5P_{opt}$	47%	15%	Y & OUT
P_{opt}	49%	70%	Y & OUT
Top chord 70×70×7, Bottom chord 50×50×5, A_{top}/A_{bottom} =1.79 (case (c))			
no cable	-	-	Y
P_{nom}	21%	-	Y & OUT
$0.5P_{opt}$	26%	38%	Y & OUT
P_{opt}	28%	46%	Y & OUT
Top chord 60×60×6, Bottom chord 50×50×5, A_{top}/A_{bottom} =1.44 (case (d))			
no cable	-	-	OUT
P_{nom}	2%	-	OUT
$0.5P_{opt}$	2%	0%	OUT
P_{opt}	2%	0%	OUT
Top chord 70×70×7, Bottom chord 60×60×6, A_{top}/A_{bottom}=1.25 (case (e))			
no cable	-	-	OUT
P_{nom}	0%	-	OUT
$0.5P_{opt}$	0%	0%	OUT
P_{opt}	0%	0%	OUT

Y=Yielding of the tensile bottom chord
OUT= Out-of-plane buckling of the compressive top chord

In order to examine the effect of the truss shape on the structural behaviour of the truss, two additional truss types have been considered. Schematic graphs of the studied trusses (truss configurations 1-3) together with the achieved gains are shown in Table 7.8. Truss configuration 1 is the truss studied earlier. For truss configurations 2 and 3, steel grade S460 and the same section sizes with the validated model have been employed to the truss members. It can be stated again, that in all cases, prestress improves significantly the truss performance, whilst no clear trend with regard to the truss configuration has been observed for the considered trusses.

Table 7.8: Effect of truss shape on the response of prestressed trusses.

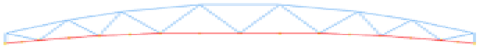

truss configuration 1

	F_u/F_{u1}	δ_u/δ_{u2}
no cable	-	-
P_{nom}	21%	-
$0.5P_{opt}$	26%	38%
P_{opt}	28%	46%

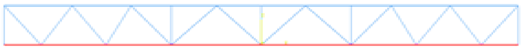

truss configuration 2

	F_u/F_{u1}	δ_u/δ_{u2}
no cable	-	-
P_{nom}	27%	-
$0.5P_{opt}$	31%	31%
P_{opt}	33%	45%

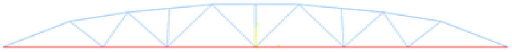

truss configuration 3

	F_u/F_{u1}	δ_u/δ_{u2}
no cable	-	-
P_{nom}	16%	-
$0.5P_{opt}$	20%	39%
P_{opt}	20%	48%

7.6. Design recommendations

Having examined thoroughly the structural behaviour of prestressed trusses, this section provides design recommendations, in form of simplified design checks for long span trusses employing tubular members. Focus is set on the three following cases: i) trusses without any cable inserted in the bottom chord, ii) trusses with nominally prestressed cable and iii) trusses with optimally prestressed cable.

As a first step, the designer needs to decide the geometry of the truss (i.e. span, depth, configuration of diagonals, number of girders and curvature of the bottom and top chord), which usually comes after a number or iterations and is a compromise between aesthetics, economy, weight, fabrication cost and so on.

Once the geometry is set, the cross-section sizes of the truss members according to the identified ultimate limit state should be determined. The process begins with the design of the bottom chords, which depends on whether a cable is to be inserted. Assuming that the truss behaves macroscopically like a simply supported beam, subjected to uniform gravity (or uplift) loading q_{Ed}, the design bending moment at mid-span at ULS can be found by the formula $q_{Ed}L^2/8$, where L is the span of the truss. Hence, the design tensile (or compressive) load in the bottom chord, $N_{Ed,bottom,t}$ (or $N_{Ed,bottom,c}$), equals the maximum gravity (or uplift) bending moment, $M_{Ed,gravity}$ (or $M_{Ed,uplift}$), divided with the lever arm (i.e. the depth of the truss at mid-span).

When no cable is to be inserted in the bottom chord, the cross-section of the bottom chord ($A_{t,bottom}$) in the considered steel grade (f_{yt}) can be evaluated from Equations (7.6) and (7.7), being checked against the tensile and compressive design loads, respectively.

$$N_{Ed,bottom,t} \leq N_{pl,Rd,bottom} = (A_{t,bottom} \times f_{yt})/\gamma_{M0} \tag{7.6}$$

$$N_{Ed,bottom,c} \leq N_{b,Rd,bottom} \tag{7.7}$$

where $N_{pl,Rd,bottom}$ is the design plastic resistance, γ_{M0} the partial factor for resistance of cross-sections with a recommended value of 1.0 and $N_{b,Rd,bottom}$ the design buckling resistance of the bottom chord member, evaluated according to the design method specified in BS EN 1993-1-1 (2014).

When a P_{nom} prestressed cable is to be inserted in the bottom chord, the contribution of P_{nom} prestress force and the cross-sectional area of the cable (A_c) and the tube ($A_{t,bottom}$) can be calculated, assuming that the bottom chord will fail when the tube yields, as shown in Equations (7.8) and (7.9) for tensile and compressive design loads respectively.

$$N_{Ed,bottom,t} \leq N_{pl,Rd,bottom} = A_{t,bottom} f_{yt} (1 + A_c E_c / A_{t,bottom} E_{t,bottom}) / \gamma_{M0} \tag{7.8}$$

$$N_{Ed,bottom,c} \leq N_{b,Rd,bottom} \tag{7.9}$$

where f_{yt} is the yield stress of the tube, and $N_{b,Rd,bottom}$ the tube buckling strength, without taking into consideration the presence of the cable due to the negligible magnitude of the prestress level.

When a P_{opt} cable is to be inserted, the cross-sectional area of the tube and the cable can be determined according to Equation (7.10), whereas the P_{opt} force can be evaluated from Equation (7.11). The design compressive load, $N_{Ed,bottom,c}$, should not exceed the buckling resistance of the bottom chord, as stated in Equation (7.12), where $N_{b,Rd,bottom,p}$ is the design buckling resistance of the bottom chord, taking due account of the prestress force.

$$N_{Ed,bottom,t} \leq N_{pl,Rd,bottom} = (A_{t,bottom} f_{yt} + A_c f_{cy}) / \gamma_{M0} \tag{7.10}$$

$$P_{opt} = A_{t,bottom} A_c (f_{cy} E_{t,bottom} - f_{ty,bottom} E_c) / (A_{t,bottom} E_{t,bottom} + A_c E_c) \tag{7.11}$$

$$N_{Ed,bottom,c} \leq N_{b,Rd,bottom,p} \tag{7.12}$$

$N_{b,Rd,bottom,p}$ may be determined using the modified Perry-Robertson approach, proposed by Gosaye et al. (2016). The aforementioned approach was based on the method proposed by Ayrton and Perry (1886) and was derived in conjunction with the codified column buckling curves in BS EN 1993-1-1 (2014). Employing the same framework with Eurocode, the method is able to account for the effect of the prestressing cables, through Equations (7.13)-(7.18), where the symbols are consistent with those used in BS EN 1993-1-1 (2014). In order to account for member instability, the compressive resistance of the system is expressed as the plastic cross-sectional resistance multiplied by a reduction factor χ_p.

$$N_{b,Rd,p} = \chi_p N_{pl} \,/\, \gamma_{M1} \tag{7.13}$$

where χ_p depends on the member slenderness through Equation (7.15)-(7.16).

$$N_{pl} = A_t f_{ty} \tag{7.14}$$

$$\chi_p = \frac{(1 - P_i/N_{pl})}{\alpha_k\left[\phi_p + \sqrt{{\phi_p}^2 - \frac{(1 - P_i/N_{pl})}{\alpha_k}\bar{\lambda}^2}\right]} \tag{7.15}$$

$$\phi_p = \frac{(1 - P_i/N_{pl})\bar{\lambda}^2 + \left[\alpha_k + \alpha(\bar{\lambda} - 0.2)\right]}{2\alpha_k} \tag{7.16}$$

$\bar{\lambda}$ is the member slenderness given Equation (7.17), α_k is defined in Equation (7.18) and α is the imperfection factor, selected from Table 6.2 of BS EN 1993-1-1 (2014), but on the basis of an effective yield strength of the tube, defined as $f_{ty,eff} = f_{ty} - P_i/A_{bottom,t}$. Note that a buckling curve a with α=0.21 is proposed for hot-finished hollow sections with $f_{ty,eff}$<460 N/mm^2, whilst buckling curve a_0 with α=0.13 should be used for $f_{ty,eff}$ ≥460 N/mm^2. It should be born in mind that prestressing leads to a reduced yield strength for members under compression, thus rendering the sensitivity to geometric imperfections and effect of the residual stresses (expressed as a proportion of the yield strength) considerable for the member buckling resistance.

$$\bar{\lambda} = \sqrt{\frac{N_{pl}}{N_{cr}}} \tag{7.17}$$

$$\alpha_k = \frac{K_t}{K_c + K_t} \tag{7.18}$$

where K_c and K_t are the axial stiffness of the cable and the tube ($A_c E_c/L$ and $A_t E_t/L$), respectively.

Once the bottom chord is designed, the top chord can be designed as well. The maximum tensile and compressive design loads ($N_{Ed,top,t}$ and $N_{Ed,top,c}$), which correspond to the uplift and gravity ULS, respectively, should be carried by the top chord. The tensile and compressive design criteria are shown in Equation (7.19) and (7.20) respectively. Note that in order to have a ductile failure mode under gravity loading, buckling of the compressive top chord (both in-plane and out-of-plane) should occur after the yielding of the tensile bottom chord.

$$N_{Ed,top,t} \leq N_{Rd,top} = (A_{top} \times f_{yt})/\gamma_{M0} \tag{7.19}$$

$$N_{Ed,top,c} < N_{b,Rd,top} \tag{7.20}$$

where A_{top} is the cross-sectional area of the top chord member, and $N_{b,Rd,top}$ is the design buckling resistance of the top chord.

A simple static analysis can be executed in order to calculate the design force in the diagonals ($N_{Ed,diagonals,t}$ and $N_{Ed,diagonals,c}$) and the cross-sectional area of the diagonals $A_{diagonals}$ can be found applying Equations (7.21) and (7.22).

$$N_{Ed,diagonals,t} \leq N_{Rd,diagonals} = (A_{diagonals} \times f_{yt})/\gamma_{M0} \tag{7.21}$$

$$N_{Ed,diagonals,c} \leq N_{b,Rd,diagonals} \tag{7.22}$$

where $N_{b,Rd,diagonals}$ is the buckling resistance of the diagonal members under compression, as defined in BS EN 1993-1-1 (2014). A summary of the design checks for long span tubular truss (with or without prestress) is given in Figure 7.15.

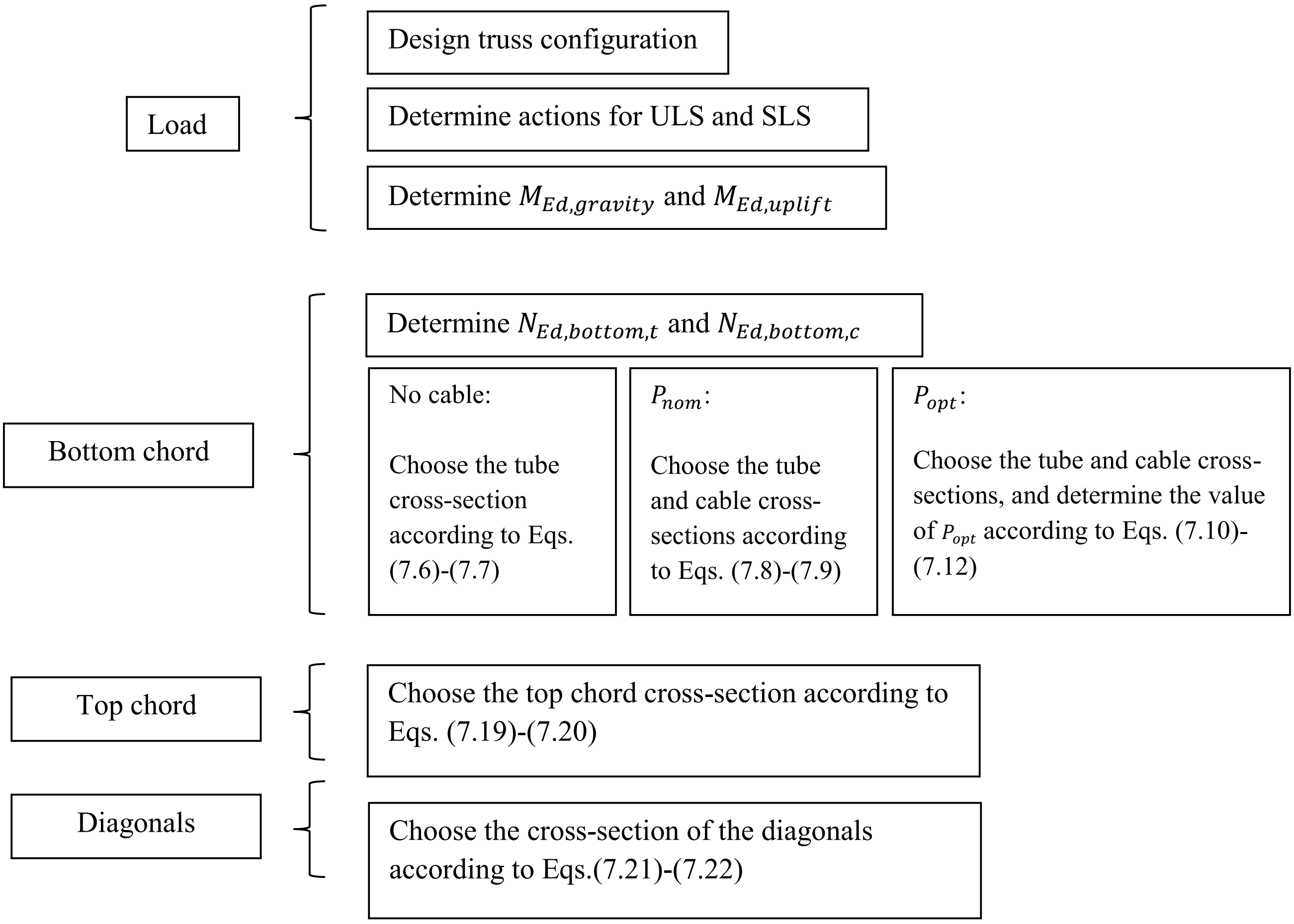

Figure 7.15: Summary of checks for long span tubular truss (with or without prestress).

Applying the recommended design checks, a worked example of a 80 m span Warren truss, comprising members in S460 square hollow sections is presented hereafter. Three prestress cases (no cable, P_{nom}, P_{opt}) were considered. Elastic-perfectly plastic material response was assumed for both the steel members and the cable. Seven-wire strands with yield strength 1700 N/mm^2, were considered for the cable. A scheme of the studied truss, along with its main geometry characteristics, are given in Figure 7.16. A span-to-depth ratio equal to 15 which is considered to be an economic solution (ESDEP Course, 2017) and which was also similar to that of the trusses investigated earlier, was selected.

Geometry	
Truss span (m)	80
Depth (m)	5.30
Distance between joints on top chord (m)	5.71
Length of diagonals (m)	6.02
Angle of diagonals to the bottom chord (°)	61.67
Number of joints on top chord	14

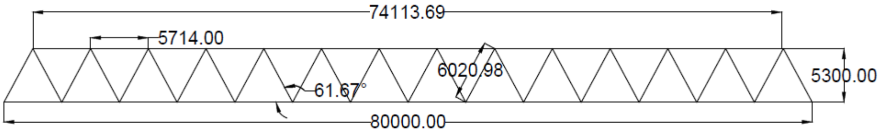

Figure 7.16: Worked example for 80 m span truss.

The ULS loading was based on Brettle and Brown (2009), considering the distance between two typical trusses across the length of the building equal to 6 m. Wind loading was not considered. It is worth mentioning that according to guidelines for top chord truss design, the out-of-plane buckling length L_{cr} is considered to be $0.90L$, where L is the distance between the points of lateral support for the chord, and the in-plane buckling length equal to $0.90L$, where L is the distance between the chord panel points. For the diagonals, the buckling length in both planes is $0.75L$, where L is the length of the member (Packer et al., 2009).

Implementing the checks, the design for a truss employing S460 steel grade for the truss members is given in Table 7.9. Note that for the case with P_{opt} prestressed cable, the cross-section of the bottom chord is reduced from 120×120×10 to 120×120×5, compared to the case with no/P_{nom} cable.

Table 7.9: Design of 80 m S460 span truss.

LOADS		
ULS (kN/m): 12.14	$maxM_{Ed}$ (kNm) = 9714.60	
SLS (kN/m): 3.6	$maxN_{Ed}(kN)$ = $(M_{Ed,gravity}/h)$ =1821.49	
BOTTOM CHORD		
i) no cable	TUBE (SHS): 120×120×10	
	$N_{Rd}(kN)$= 1973.40	N_{Ed}/N_{Rd}=0.92
ii) P_{nom}	TUBE (SHS): 120×120 ×10	CABLE (7-wire strand, No. of strands × diameter in mm): 4 ×12.7
	$N_{Rd,total}$ (kN): 2117.69	$N_{Ed}/N_{Rd,total}$: 0.86
iii) P_{opt}	TUBE (SHS): 120 × 120 × 5	CABLE (7-wire strand, No. of strands × diameter in mm): 4 ×12.7
	$N_{Rd,total}$ (kN): 1905.60	$N_{Ed}/N_{Rd,total}$: 0.96
	σ_{opt} (N/mm^2): 1243.42	P_{opt}/P_{yc}: 0.73
	P_{opt} (kN): 630.05	$\varepsilon_{yt} = \varepsilon_{yc}$: 0.003512
TOP CHORD	TUBE (SHS): 200×200×10	
	$N_{b,Rd}$ (kN): 2520.82	$N_{Ed}/N_{b,Rd}$: 0.72
DIAGONALS	TUBE (SHS): 120×120×8	
	$N_{b,Rd}$ (kN): 654.51	$N_{Ed}/N_{b,Rd}$: 0.84

In order to evaluate the proposed procedure, FE models, adopting the modelling assumptions presented earlier in this chapter, have been developed. Nonlinear static analysis has been performed and the results are depicted in Figure 7.17. As can be seen, the trusses have achieved ultimate loads slightly higher than the designed ones. The case of a truss employing same cross-sections with the P_{opt} truss, but considering no cable -labelled as no cable(2)- and a cable in P_{nom} -labelled as $P_{nom}(2)$- have also been included for comparison purposes. It can be seen that the addition of a cable almost doubles the ultimate load. Prestressing the cable to the optimal level reduces significantly the mid-span displacement at ultimate load compared to the case, in which the cable is prestressed to P_{nom}.

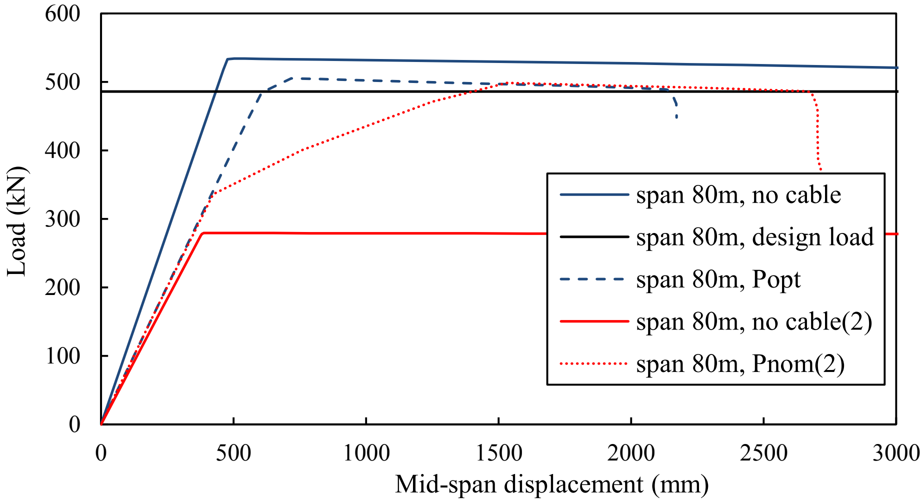

Figure 7.17: Load-mid-span displacement curves for 80 m span truss.

Having verified the design checks, the worked example of 80 m truss has also been examined, considering conventional structural steel grades (S235, S275, S355) for the truss members. The total weight of the structural steel has been evaluated and the results are shown in Figure 7.18, where significant structural weight reductions, with an average value of 35%, can be seen when the adopted steel grade changes from S235 to S460, thus demonstrating the considerable material savings that can arise from the use of high strength structural steel. As anticipated, the structural weight savings are less significant (approximately 8%), but still existing, when comparing S460 with S355. This value increases, could even be doubled, when moving from S460 to S690 and thus when comparing S690 with S355. It should be born in mind that the aforementioned savings concern only the truss configurations of Figure 7.16. Different structural configurations, or even combination of lower with higher steel grades, with the latter employed only in members subjected to tension, are expected to further enhance the gains due to the use of HSS.

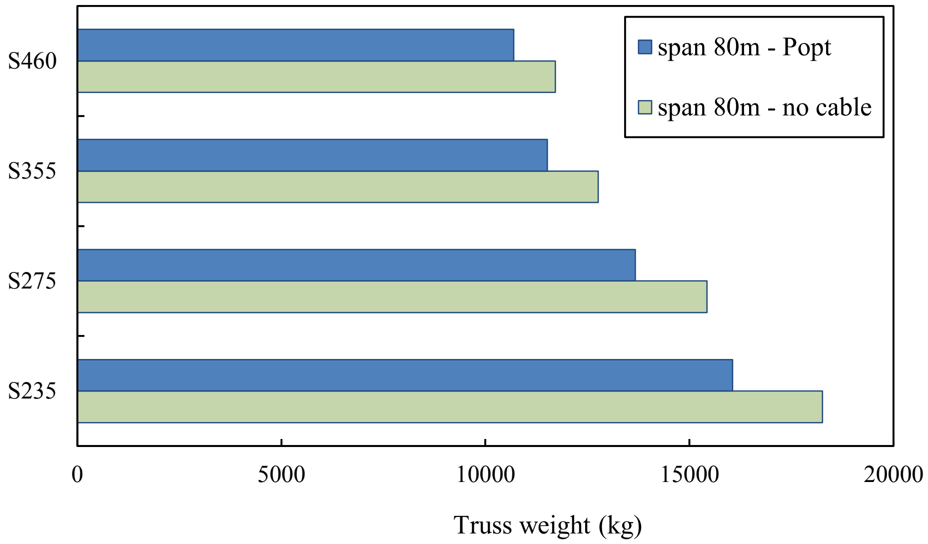

Figure 7.18: Truss weight for trusses in various steel grades.

7.7. Concluding remarks

The structural response of high strength steel prestressed trusses has been examined in the current chapter. Finite element models were developed and validated against the test data of four trusses comprising hot-finished square hollow sections in S460 grade and spanning over 11 m length. Different parameters that can affect the overall response, namely the selection of FE element type, the cable's effective material properties and the effect of the bottom connection on the overall response, were considered in the numerical analysis.

An excellent calibration against the experimental load-deformation response, failure loads and observed failure modes, was achieved by the numerical models. In order to improve the computational efficiency, simplified FE models capable of capturing accurately the gains emerging by the use of prestress were utilised for the execution of the subsequent parametric studies.

On the basis of both the experimental and the numerical results, it was shown that prestressing could be beneficial in extending the elastic range and increasing the strength of long span structures. In particular, it was found that Truss 4 which was prestressed at the optimal prestress level achieved 45% higher ultimate load than Truss 1 (control specimen), whilst presented 49% decreased mid-span displacement at failure load, compared to Truss 2, in which the cable was not prestressed. The parametric studies showed that the application of prestress can be beneficial in trusses of various structural configurations, as long as the truss members have been designed in order to allow the maximum prestress utilisation.

Finally, a series of simplified design checks for prestressed steel trusses have been proposed and verified with FE analysis. Applying the aforementioned checks in Warren type trusses, it was found that a significant reduction in weight, with an average value of 35%, can be achieved through the application of grade S460 instead of S235.

Combining HSS material with prestressing technology, the overall structural performance can considerably improve, SLS limitations can be overcome, while the structural weight is kept to minimum, allowing for even lighter and potentially more elegant structures.

CHAPTER 8: CONCLUSIONS AND FUTURE RESEARCH

8.1. Conclusions

The present research study investigated the structural response of high strength steel members and structures. Focus was placed upon hot-finished square and rectangular hollow sections in S460 and S690 steel grades.

Chapters 4 and 5 studied the compressive and flexural response respectively. In Chapter 6, the structural behaviour under combined loading, including both the case of uniaxial bending and compression and the case of biaxial bending and compression was examined. Moving from individual components to more complex structures, the performance of HSS trusses was studied in Chapter 7.

In order to establish the accuracy of the numerical results, the developed finite element models were validated against test data. Overall the experimental results of 11 stub column tests (Chapter 4), 22 beams (Chapter 5), 12 stub columns under eccentric compression (Chapter 6) and 4 tubular trusses under different prestress levels (Chapter 7) have been used for the calibration of the numerical models presented herein. Initial geometric imperfections were introduced in the form of the elastic buckling mode shapes corresponding to the relevant failure modes. For the models of Chapters 4-6, it was found that initial local geometric imperfections with an amplitude of $t/50$, where t the section's thickness, led to excellent agreement with the experimental results. After the execution of rigorous finite element modelling in Chapter 7, it was concluded that the magnitudes $L/750$ and $L/1500$ for the out-of-plane and in-plane initial geometric imperfections respectively, where L the buckled member's length, resulted in accurate calibration against the overall test response. The validated models were utilised for the generation of additional structural performance data. Within the scope of the present research study, 2850 additional nonlinear static analyses were performed in order to obtain the response of S460 and S690 members and structures.

The parametric studies provided structural performance data for a large number of cross-sections, various aspect-ratios, loading and structural configurations, well beyond those determined from the experiments. The large number of results contributed to an increase in the pool of data of HSS structures employing hot-finished hollow sections, while enabled the evaluation of the effect of key parameters on the structural behaviour, as detailed in Subsections 4.6.1, 5.6.1, 6.6.2 and 7.5.2. The comments and conclusions drawn in the aforementioned subsections can be used by designers and researchers. An additional significant impact related to the data generated from the parametric studies is the assessment of the current design provisions as well as the proposal of new design approaches, upon execution of best fit data analysis. The design recommendations provided in line with the observed response in Chapters 4-7 are summarised hereafter.

The Eurocode slenderness limits for internal elements in compression and bending were assessed. Even though design specifications of HSS do not provide guidance for plastic design, the applicability of the Class 1 limits of 33 and 72 for internal elements in compression and bending respectively, together with the deformation capacity requirement R=3, provided for carbon steel, to HSS sections was evaluated. The limits were found unsafe, while the limits of 15 and 42 have been proposed for HSS internal elements in compression and for S460 internal elements in bending respectively. Further research is key to determine the possibility of applying plastic design in HSS structures. The current Class 2 limit of 38 for internal elements in compression led to unconservative estimations and the adoption of a stricter limit of 34 was recommended. The results of the present study seemed to justify the application of the Class 3 limit of 42. However, it worth noting that the application of a lower limit was deemed necessary by recent studies (Taras et al., 2013; Wang et al., 2017) and its approval should be further explored. The Class 2 and Class 3 limits for internal elements in bending were found suitable for HSS cross-sections.

For stocky cross-sections, Eurocode provisions were overall capable of adequately predicting the capacity under compression, bending moment and combined loading. However, the obtained results were conservative, particularly for S460 sections, as the effect of the material strain-hardening characteristics on the ultimate cross-sectional performance are not reflected in the codified design provisions. To overcome this issue, the suitability of the continuous strength method, which rationally accounts for strain-hardening, has been investigated and relevant recommendations were proposed in order to make the method applicable to HSS hot-finished sections subjected to compression.

For semi-compact cross-sections, overall conservative design predictions were attained for all loading configurations, whilst the proposal by Taras et al. (2013) that suggests a linear transition from M_{pl} to M_{el} led to more accurate and consistent moment resistance predictions.

For slender sections, the application of the traditional method of effective width equations safely predicted the capacity of cross-sections under compression, bending moment and combined loading. As expected, the effect of interaction between the constituent plate elements on the structural response was more pronounced for these sections. In particular, for compressive cross-sections, the normalised performance improves for increasing aspect ratio, owing to the delay in the onset of local buckling as a result of the greater degree of restraints provided by the more stocky flanges of sections with increasing aspect ratio to the critical compression webs. For cross-sections subjected to bending about the major axis, the normalised flexural resistance increases with decreasing aspect ratio. This relates to the more effective restraint provided by the less slender webs of sections with a small aspect ratio to the critical compression flanges thus delaying local buckling. Given that Eurocode does not consider the plate element interaction effects, a new method, accommodating a reduction factor for the whole cross-sectional area and able to provide safe yet economic design estimations for compressive hollow sections with different aspect ratios, has been presented.

For semi-compact and slender cross-sections under combined loading, the modified CSM method resulted in better design estimations compared to those of Eurocode.

Having assessed the applicability of several design methods to HSS square and rectangular hot-finished hollow sections, the structural performance of trusses comprising HSS tubular members was studied. The experimental response was meticulously captured by finite element models. Overall the application of prestress to the trusses led to an extension of the elastic response of the bottom chord, thus increasing the overall strength of the trusses. Combining HSS material with prestressing technology significantly enhanced the overall structural performance, allowing for minimum material consumption and deflection control. A series of simplified verifications for prestressed steel truss design have been presented to facilitate their application in modern practice.

8.2. Suggestions for future research

In order to allow an optimised design of HSS members and thus encourage a wider application of HSS in the construction industry, design methods that are both simple to use and efficient, yet safe, are needed. To this end, the effective cross-section method for compressive cross-sections and the modified CSM for slender sections under combined loading have been presented, whereas the applicability of the CSM to HSS compressive stocky sections and the proposal for a linear transition between the elastic and plastic moment resistance of HSS semi-compact cross-sections was evaluated. Further research is needed to assess the suitability of the proposed design equations for additional cross-sectional shapes and material grades, thus facilitating their inclusion in future versions of design specifications.

Additionally, research on the flexural buckling of long columns and unrestrained beams comprising HSS sections is suggested to verify the applicability of relevant design methods and optimise the design equations based on the obtained experimental and numerical results.

Furthermore, as concluded in Chapter 5, non-negligible deformation capacity has been found for stocky S460 cross-sections. Given the current exclusion of high strength steel structures from plastic design, an interesting research area concerns the feasibility of plastic design for high strength steel structures. A series of experimental and numerical work on high strength steel continuous beams and frames would be required.

The reduced material ductility of HSS is expected to affect the deformation capacity of HSS structures. The execution of experimental and numerical investigations on different types of HSS connections together with the study of the robustness of HSS structures is hence recommended.

Similar to the research on the HSS prestressed trusses presented herein, the optimisation of the structural performance through the combination of the increased material strength with advanced technologies could also be pursued for other structural configurations. Arches, domes or spatial trusses could be examined. Further to the load-deformation path and the obtained ultimate capacity under downward loading, the failure load under upward loading is recommended to be explored for the aforementioned structures. The latter that has not examined in this thesis, presents a situation likely to occur in practice and its consideration is suggested for future work.

Based on the conclusions of Chapter 7, different parameters can affect the benefits that can emerge from prestress usage in HSS structures. An optimisation algorithm, maximising the structural efficiency, while minimising the structural weight and material cost, could be executed for the prestressed spatial structures. Moreover, the possibility of efficiently combining high strength and mild steel members together with the prestress application, could be investigated for a series of structural configurations.

Finally, in order to quantify the sustainability gains related to the use of HSS and prestress in steel structures, life cycle analysis can be performed. Comparisons with counterpart mild steel structures are suggested in order to visualise the potential environmental benefits through the application of HSS in structural engineering. The latter could add significant value to the research on the structural performance of HSS.

The recommendations for future work are summarised in Table 8.1.

Table 8.1: Recommendations for future work.

	Future work	Scope
1.	Additional tests/numerical studies on HSS cross-sections employing different cross-sectional shapes and material grades.	Verify the proposed Equations (4.3), (4.4)-(4.6), (6.5)-(6.8), the proposed slenderness limits, the linear transition for Class 3 sections.
2.	Tests/numerical studies on long columns and unrestrained beams.	Verify current design methods and provide recommendations in line with the observed response.
3.	Tests/numerical studies on HSS continuous beams and frames.	Explore the possibility for plastic design in HSS.
4.	Tests/numerical studies on different types of HSS connections. Examine the robustness of HSS structures.	Examine the influence of reduced material ductility on the structural performance.
5.	Tests/numerical studies on the structural performance of different HSS prestressed structures including other spatial trusses, arches or domes. Study the ultimate performance considering the cases of both downward and upward loading.	Combine the increased material strength of HSS with the benefits owing to prestress for different structural configurations. Establish the structural response for different loading scenarios likely to occur in practice.
6.	For the structures of future work recommendations (5), optimise the structural configurations.	Investigate the configuration that would optimise the structural performance, minimising structural weight and cost.
7.	Tests/numerical studies on prestressed steel structures that combine efficiently high strength with mild steel members.	Study the potential benefits through the combination of high strength steel, mild steel and prestress.
8.	Perform Life Cycle Analysis for HSS and mild steel (prestressed/no prestressed) structures.	Quantify the environmental impacts of HSS structures and compare with their mild steel counterparts.

APPENDIX A

Sedlacek, G. and Feldmann, M. (1995) Background document 5.09 for chapter 5 of Eurocode 3 Part 1.1: the b/t ratios controlling the applicability of analysis models in Eurocode 3 Part 1.1. Technical report. Aachen

Rotation Capacity Requirement: 3

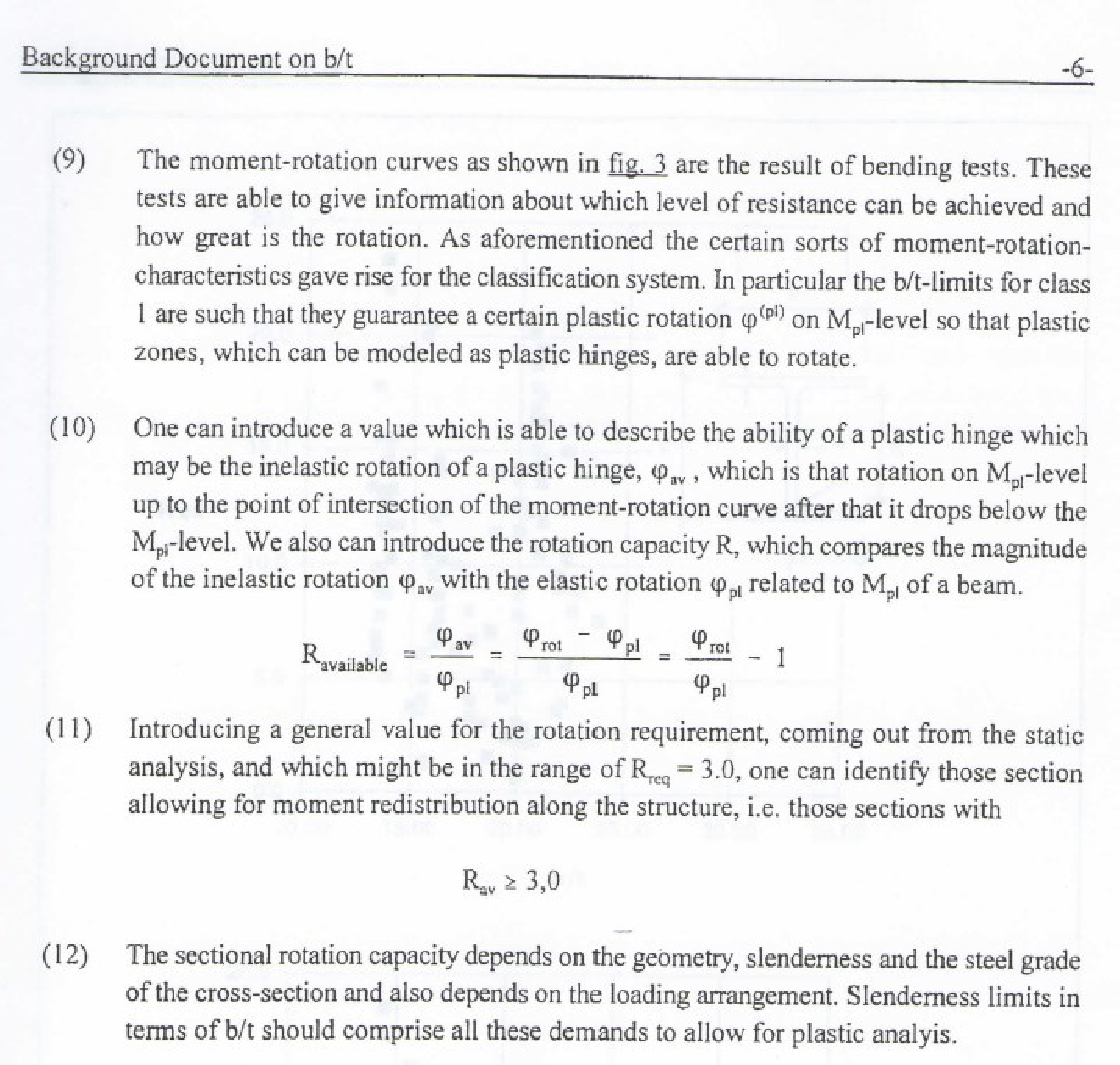

(9) The moment-rotation curves as shown in fig. 3 are the result of bending tests. These tests are able to give information about which level of resistance can be achieved and how great is the rotation. As aforementioned the certain sorts of moment-rotation-characteristics gave rise for the classification system. In particular the b/t-limits for class 1 are such that they guarantee a certain plastic rotation $\varphi^{(pl)}$ on M_{pl}-level so that plastic zones, which can be modeled as plastic hinges, are able to rotate.

(10) One can introduce a value which is able to describe the ability of a plastic hinge which may be the inelastic rotation of a plastic hinge, φ_{av}, which is that rotation on M_{pl}-level up to the point of intersection of the moment-rotation curve after that it drops below the M_{pl}-level. We also can introduce the rotation capacity R, which compares the magnitude of the inelastic rotation φ_{av} with the elastic rotation φ_{pl} related to M_{pl} of a beam.

$$R_{available} = \frac{\varphi_{av}}{\varphi_{pl}} = \frac{\varphi_{rot} - \varphi_{pl}}{\varphi_{pl}} = \frac{\varphi_{rot}}{\varphi_{pl}} - 1$$

(11) Introducing a general value for the rotation requirement, coming out from the static analysis, and which might be in the range of $R_{req} = 3.0$, one can identify those section allowing for moment redistribution along the structure, i.e. those sections with

$$R_{av} \geq 3,0$$

(12) The sectional rotation capacity depends on the geometry, slenderness and the steel grade of the cross-section and also depends on the loading arrangement. Slenderness limits in terms of b/t should comprise all these demands to allow for plastic analyis.

APPENDIX B

Results of parametric studies on high strength steel members in combined biaxial bending and compression – interaction failure surfaces.

Class 1 cross-sections – c/tε=10 – S460 (left), S690 (right) – SHS (top), RHS (bottom)

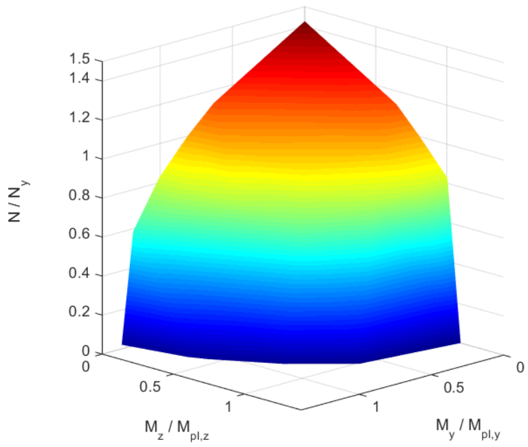

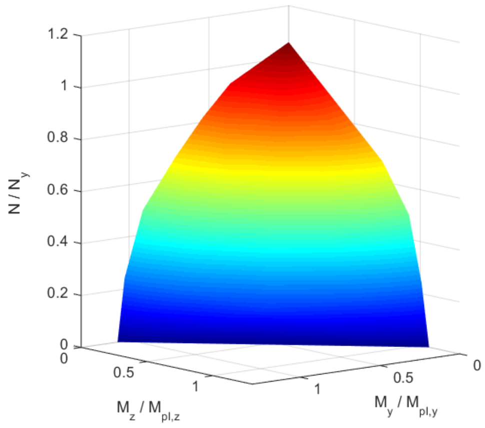

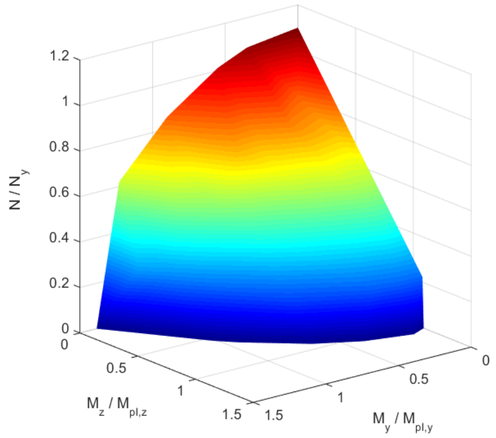

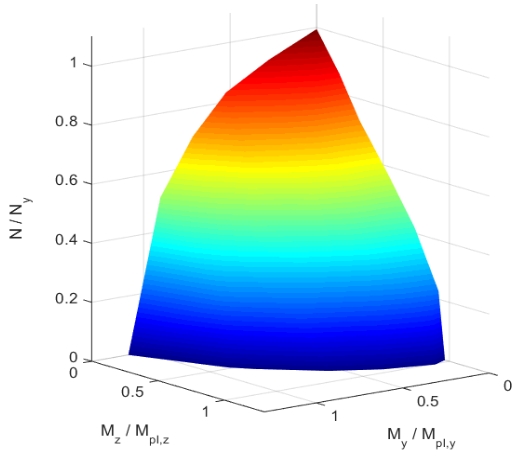

Class 1 cross-sections – c/tε=20 – S460 (left), S690 (right) – SHS (top), RHS (bottom)

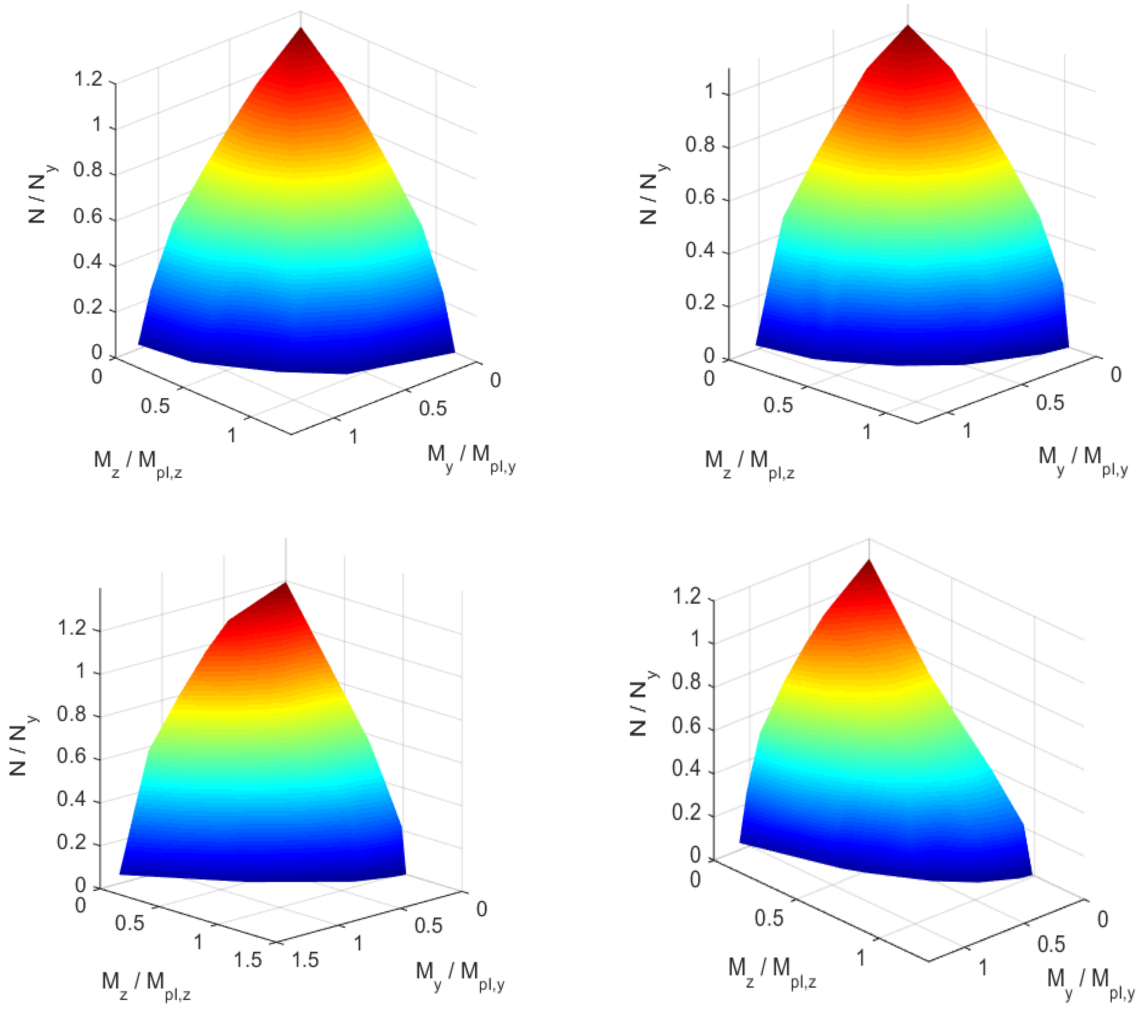

Class 1 cross-sections – c/tε=25 – S460 (left), S690 (right) – SHS (top), RHS (bottom)

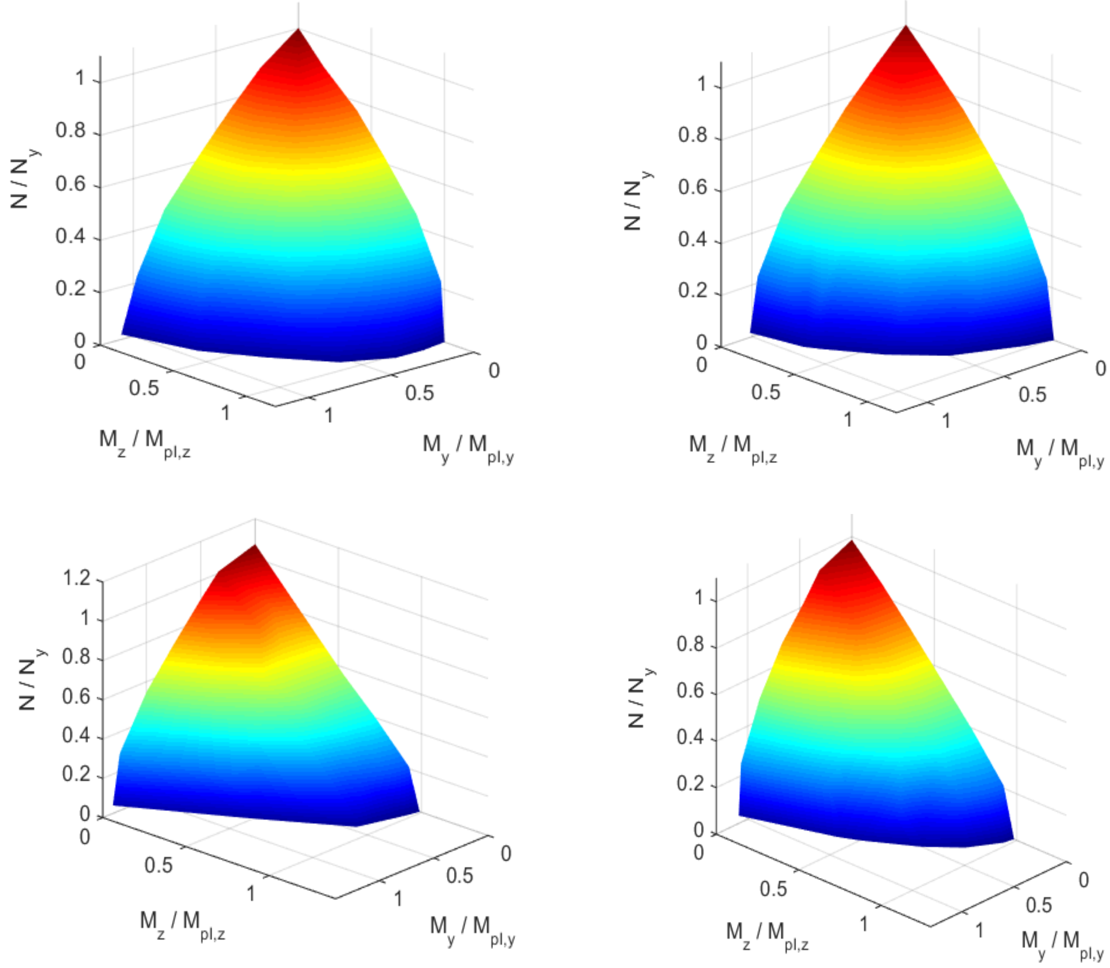

Class 1 cross-sections – c/tε=30 – S460 (left), S690 (right) – SHS (top), RHS (bottom)

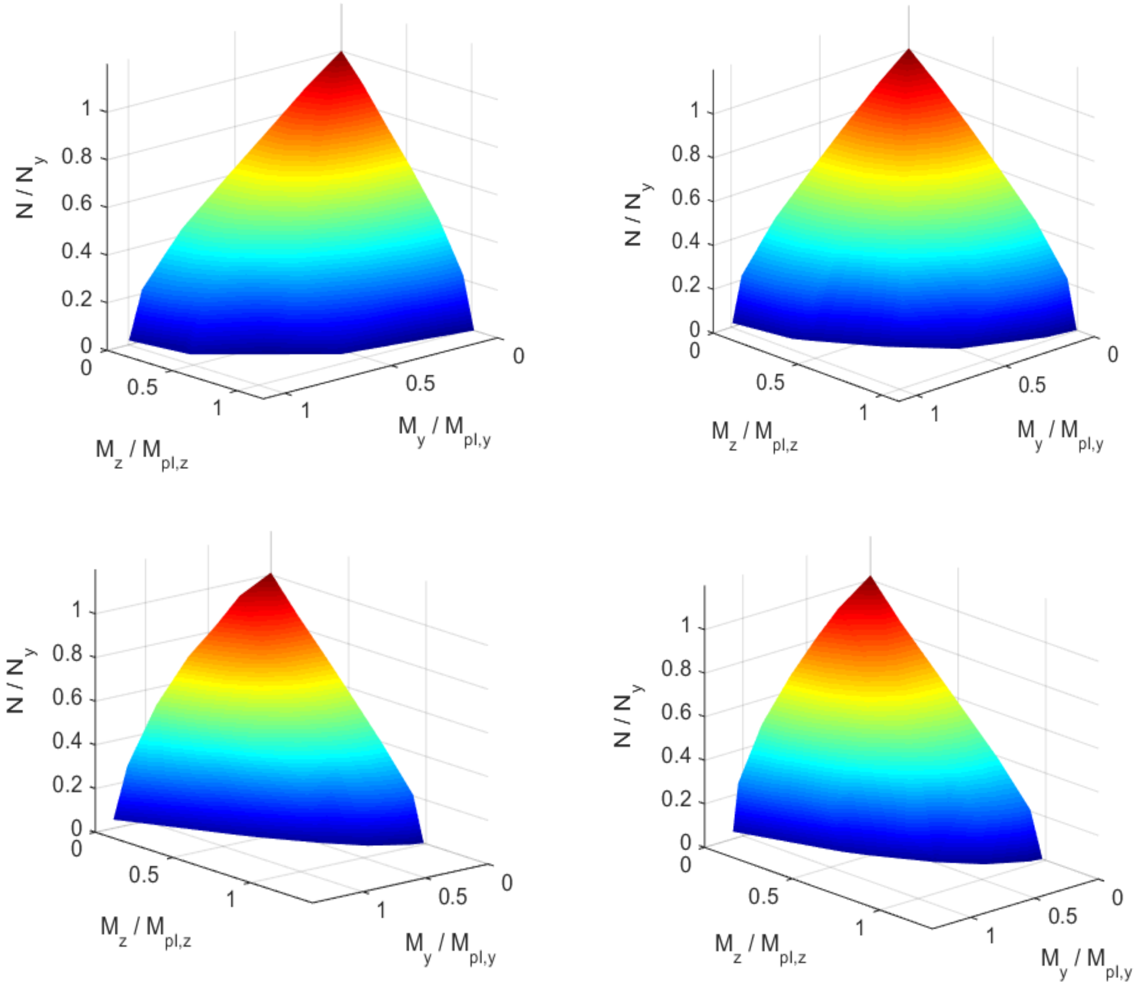

Class 2 cross-sections – c/tε=35 – S460 (left), S690 (right) – SHS (top), RHS (bottom)

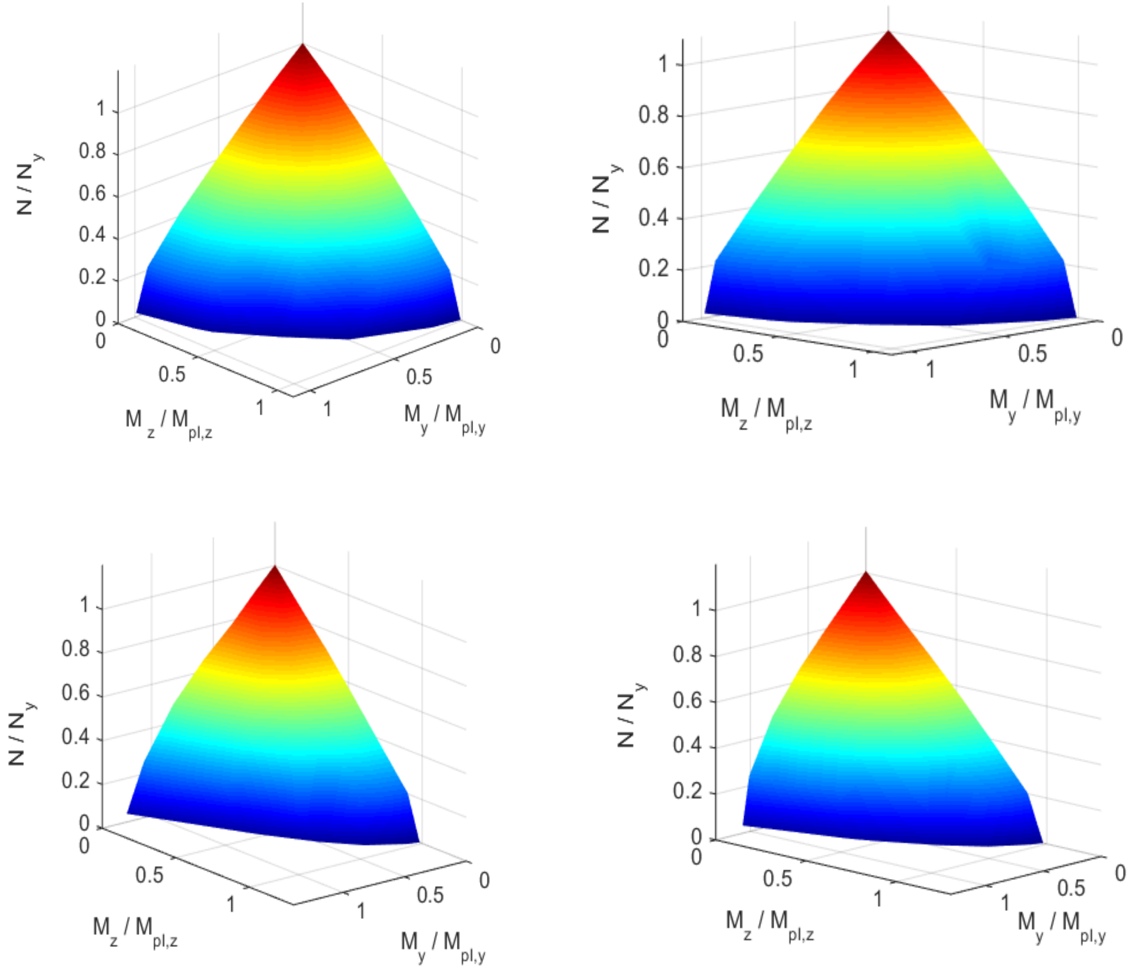

Class 3 cross-sections – c/tε=40 – S460 (left), S690 (right) – SHS (top), RHS (bottom)

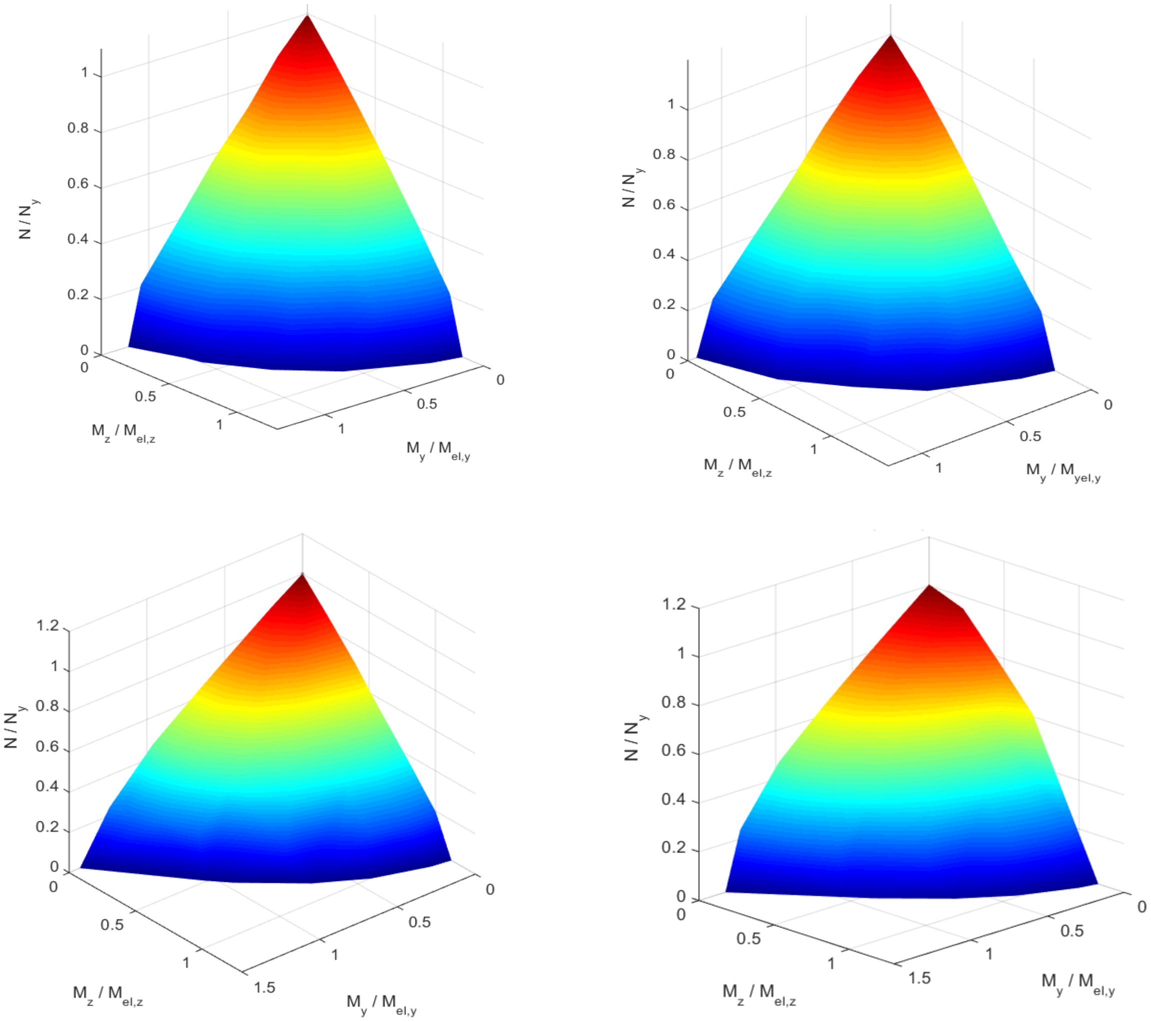

Class 4 cross-sections – c/tε=50 – S460 (left), S690 (right) – SHS (top), RHS (bottom)

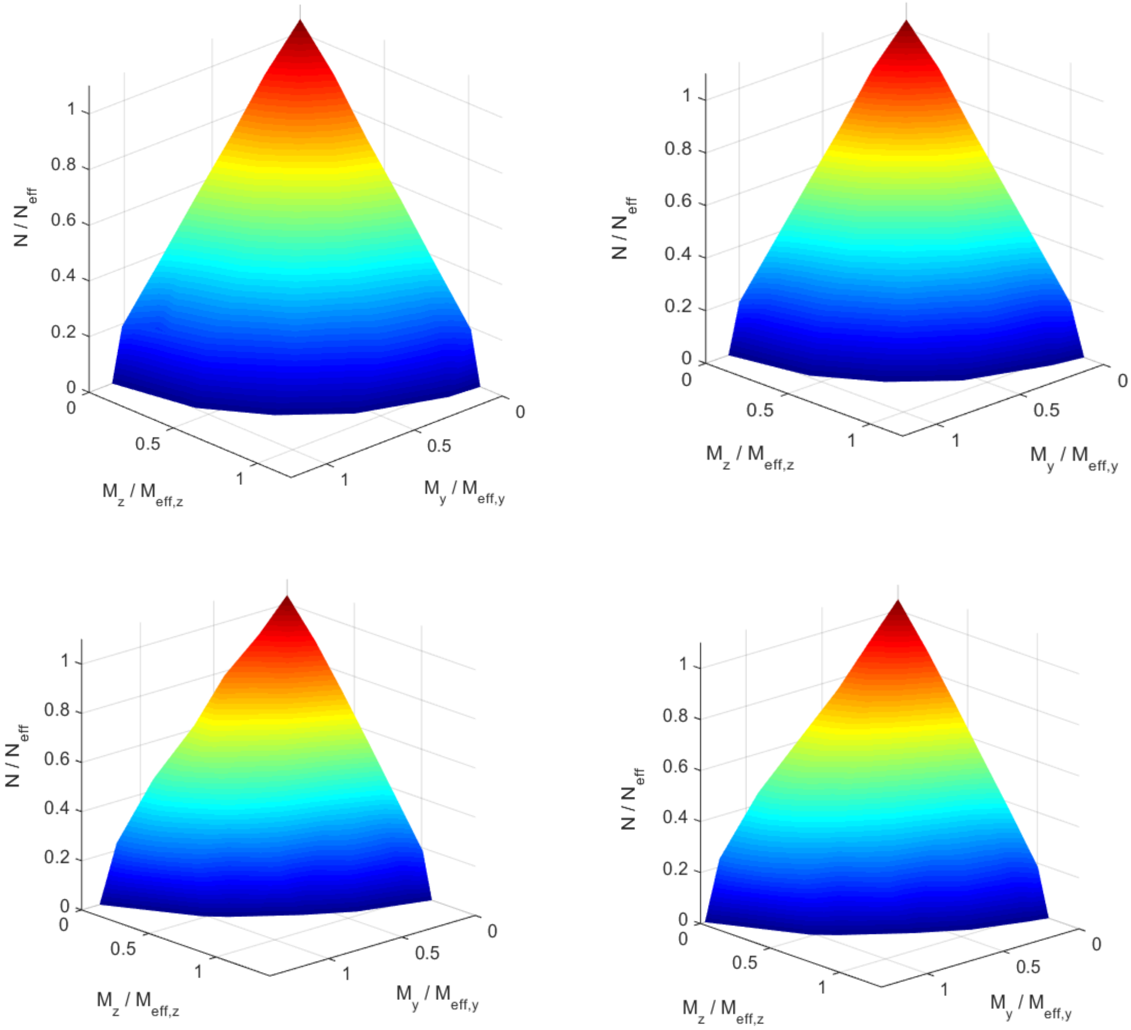

Class 4 cross-sections – c/tε=60 – S460 (left), S690 (right) – SHS (top), RHS (bottom)

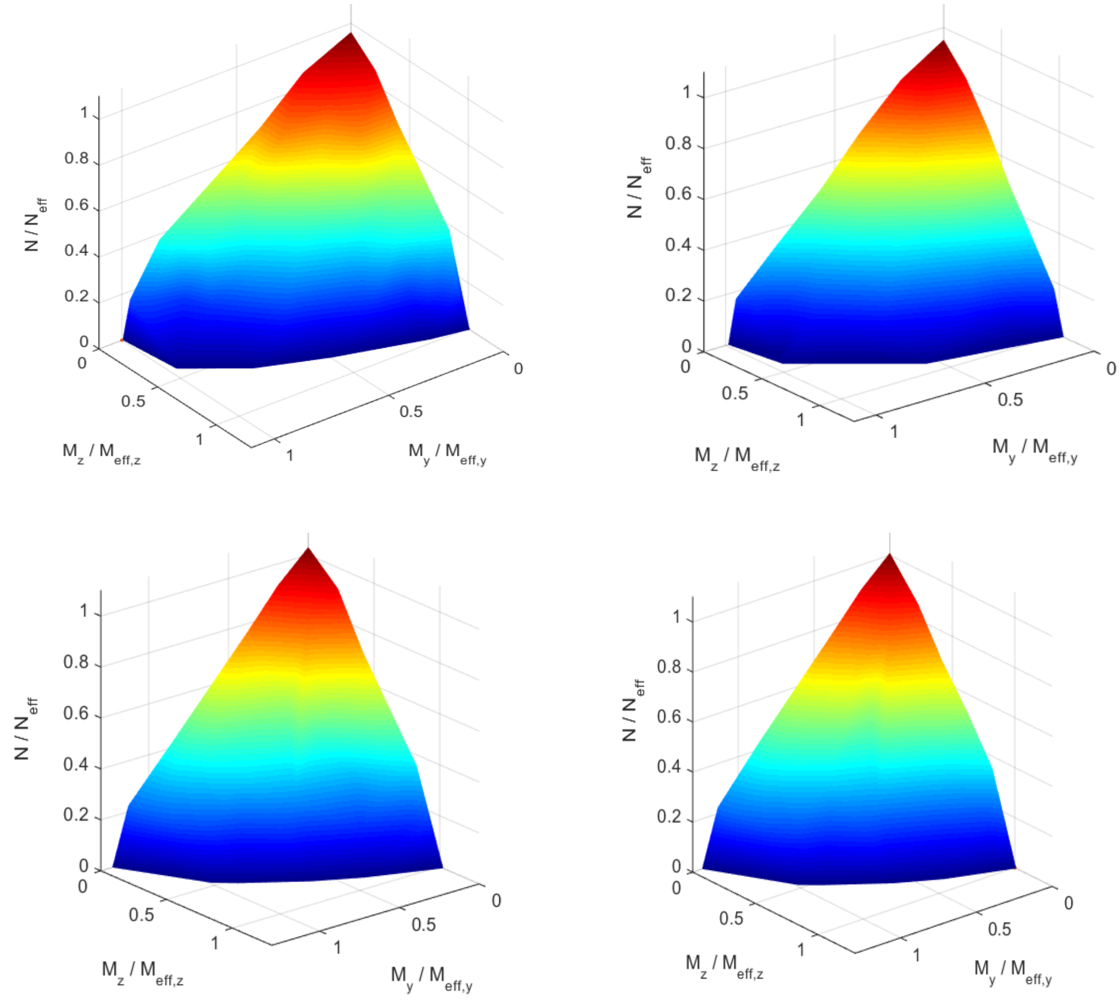

REFERENCES

ANSI/AISC 360-10 (2010) **Specification for Structural Steel Buildings**. Chicago, USA: American National Standard, American Institute of Steel Construction

Anwar-us-saadat, M., Ashraf, M. and Ahmed, S. (2016) Behaviour and design of stainless steel slender cross-sections subjected to combined loading. **Thin Walled Structures**, 104: 225–237

ArcelorMittal (2017) **The One World Trade Center** [online]. Available from: http://corporate.arcelormittal.com/ [Accessed 7 January 2017]

AS-4100-A1 (2012) **Amendment No.1 to AS 4100-1998 Steel Structures**. Sydney, Australia: Australian Standard

Aslam, H. (2017) **Strongest Bridge and Tallest Bridge in the World 2016** [online]. Available from: http://www.strongestinworld.com/top-10-strongest-bridge [Accessed 7 January 2017]

Ayrton, W. and Perry, J. (1886) On struts. **The Engineer (London)**, 62: 464–465

Ayyub, B.M. and Ibrahim, A. (1990) Posttenioned Trusses: Reliability and and redundancy. **Journal of Structural Engineering**, 116 (6): 1507–1521

Ban, H., Shi, G., Shi, Y. and Bradford, M.A. (2013) Experimental investigation of the overall buckling behaviour of 960MPa high strength steel columns. **Journal of Constructional Steel Research**, 88: 256–266

Ban, H., Shi, G., Shi, Y. and Wang, Y. (2012) Overall buckling behavior of 460MPa high strength steel columns: Experimental investigation and design method. **Journal of Constructional Steel Research**, 74: 140–150

Bathe, K.J. (1982) Finite Element Procedures for Solids and Structures - Linear Analysis. **Finite Element Procedures**, pp. 148–214

Bathe, K.J. and Wilson, E.L. (1973) Solution methods for eigenvalue problems in structural mechanics. **International Journal for Numerical Methods in Engineering**, 6 (2): 213–226

Beg, D. and Hladnik, L. (1996) Slenderness limit of class 3 I cross-sections made of high strength steel. **Journal of Constructional Steel Research**, 38 (3): 201–217

Belenya, E.I. (1977) **Prestressing load-bearing metal structures**. Moscow: Mir Publishers

Belletti, B. and Gasperi, A. (2010) Behavior of prestressed steel beams. **Journal of Structural Engineering**, 136: 1131–1139

Biliouri, M. (2016) **Friends Arena Stadium**. photograph, viewed 03 July 2016: Solna, Stockholm, Sweden

Bjorhovde, R. (2004) Development and use of high performance steel. **Journal of Constructional Steel Research**, 60: 393–400

Bock, M. and Real, E. (2015) Effective width equations accounting for element interaction for cold-formed stainless steel square and rectangular hollow sections. **Structures**, 2: 81–90

Bradford, M.A. (1991) Buckling of prestressed steel girders. **Engineering journal, AISC**, 28 (3): 98–101

Brettle, M.E. and Brown, D.G. (2009) **Steel Building Design: Worked examples for students, In accordance with Eurocodes and the UK National Annexes**. Steel Construction Institute, UK

BS EN 1993-1-1 (2014) **BS EN 1993-1-1: 2005+A1:2014, Eurocode 3 : design of steel structures, Part 1-1: general rules and rules for buildings**. London: BSI

Buro Happold Engineering (2012) **High Strength Steel Long Span Structures**. Presentation for HILONG meeting. Sweco Structures AB, Sweden

Buro Happold Engineering (2014) **Experiences with Olympic Stadium Transformation**. Presentation for HILONG meeting. Lulea, Sweden

Clarke, M.J. and Hancock, G.J. (1991) Finite-element nonlinear analysis of stressed-arch frames. **Journal of Structural Engineering**, 117: 2819–2837

Clarke, M.J. and Hancock, G.J. (1994) Simple design procedure for the cold-formed tubular top chord of stressed-arch frames. **Engineering Structures**, 16 (5): 377–385

Clarke, M.J. and Hancock, G.J. (1995) Tests and nonlinear analyses of small-scale stressed-arch frames. **Journal of Structural engineering**, 121: 187–200

Collin, P. and Johansson, B. (2006) “Bridges in high strength steel.” In **IABSE Symposium Report. International Association for Bridge and Structural Engineering. 2006**

Dahl, W., Hesse, W. and Krabiell, A. (1983) Zur Verfestigung von Stahl und dessen Einflub auf die Kennwerte des Zugversuchs. **Stahl und Eisen**, 103: 87–90

Dawson, R.G. and Walker, A.C. (1972) Post-buckling of geometrically imperfect plates. **Journal of the Structural Division, ASCE**, 98: 75–94

Dubina, D. (2008) “Performance and Benefits of Using High Strength Steels.” In **ECCS Annual Meeting Aalesund**. **2008**

Dubina, D., Stratan, A., Vulcu, C. and Ciutina, A. (2014) “High strength steel for seismic resistant building frames.” In **Eurosteel. Naples, Italy**. **2014**

Ellen, M.E., Gosaye, J., Gardner, L. and Wadee, M.A. (2012) “Design and construction of long-span post-tensioned tubular steel structures.” In **Tubular Structures XIV**. **2012**. pp. 687–693

Ellen, P.E. (1987) **Post-tensioned steel structure (Patent US 4,676,045)**.

Ellobody, E., Ran Feng, A. and Young, B. (2013) **Finite element analysis and design of metal structures.** Elsevier

EN 10025 (2004) **Hot rolled products of structural steels**. Brussels: European Committee for Standardization (CEN)

EN 1990 (2002) **Eurocode 0: Basis of structural design**. Brussels: European Committee for Standardization (CEN)

EN 1993-1-12 (2007) **Eurocode 3: Design of steel structures, Part 1-12: Additional rules for the extension of EN 1993 up to steel grades S 700**. Brussels: European Committee for Standardization (CEN)

EN 1993-1-5 (2006) **Eurocode 3: Design of steel structures - Part 1-5: Plated structural elements**. Brussels: European Committee for Standardization (CEN)

ESDEP Course (2017) **WG 15B, Elements, Lecture 15B.5: Truss Bridges** [online]. Available from: http://fgg-web.fgg.uni-lj.si/~/pmoze/ESDEP/master/toc.htm [Accessed 7 January 2017]

Ferrario, F., Iori, F., Pucinotti, R. and Zandonini, R. (2016) Seismic performance assessment of concentrically braced steel frame buildings with high strength tubular steel columns. **Journal of Constructional Steel Research**, 121: 427–440

Foster, A.S.J., Gardner, L. and Wang, Y. (2015) Practical strain-hardening material properties for use in deformation-based structural steel design. **Thin-Walled Structures**, 92: 115–129

Full, R.J. (2002) Quantifying Dynamic Stability and Maneuverability in Legged Locomotion. **Integrative and Comparative Biology**, 42 (1): 149–157

Galambos, T. V. (1998) **Guide to stability design criteria for metal structures**. John Wiley & Sons

Gardner, L. (2002) **A new approach to stainless steel structural design**. Department of Civil and Environmental Engineering, Imperial College London

Gardner, L. and Ashraf, M. (2006) Structural design for non-linear metallic materials. **Engineering Structures**, 28 (6): 926–934

Gardner, L. and Nethercot, D.A. (2004a) Experiments on stainless steel hollow sections-Part 1: Material and cross-sectional behaviour. **Journal of Constructional Steel Research**, 60 (9): 1291–1318

Gardner, L. and Nethercot, D.A. (2004b) Numerical modeling of stainless steel structural components-A consistent approach. **Journal of Structural Engineering**, 130: 1586–1601

Gardner, L. and Nethercot, D.A. (2011) **Designers' Guide to Eurocode 3: Design of Steel Buildings Second edition**. ICE publishing

Gardner, L., Saari, N. and Wang, F. (2010) Comparative experimental study of hot-rolled and cold-formed rectangular hollow sections. **Thin-Walled Structures**, 48 (7): 495–507

GB 50017-2003 (2006) **Code for design of Steel Structures**. Beijing: China Architecture and Building Press [in Chinese]

Gkantou, M., Theofanous, M., Antoniou, N. and Baniotopoulos, C. (accepted1) Compressive behaviour of high strength steel cross-sections. **Proceedings of the Institution of Civil Engineers**

Gkantou, M., Theofanous, M. and Baniotopoulos, C. (2016) "On the structural response of high strength steel prestressed trusses. A numerical approach." In **11th HSTAM International Congress on Mechanics**. **Athens, Greece. 2016**

Gkantou, M., Theofanous, M., Wang, J., Baniotopoulos, C. and Gardner, L. (accepted2) Behaviour and design of high strength steel cross-sections under combined loading. **Proceedings of the Institution of Civil Engineers**

Gosaye, J., Gardner, L., Ahmer Wadee, M. and Ellen, M.E. (2014) Tensile performance of prestressed steel elements. **Engineering Structures**, 79: 234–243

Gosaye, J., Gardner, L., Wadee, M.A. and Ellen, M.E. (2016) Compressive behaviour and design of prestressed steel elements. **Structures**, 5: 76–87

Green, P.S., Sause, R. and Ricles, J.M. (2002) Strength and ductility of HPS flexural members. **Journal of Constructional Steel Research**, 58 (5–8): 907–941

Greiner, R., Kettler, M., Lechner, A., Jaspart, J.P., Boissonade, N., Bortolotti, E., Weynand, K., Ziller, C. and Örder, R. (2008) **Plastic Member Capacity of Semi-Compact Steel Sections–a more Economic Design (SEMI-COMP)**. Research Fund for Coal and Steel, European Commission.

Greiner, R., Lechner, A., Kettler, M., Jaspart, J.P., Weynand, K., Oerder, R. and Dehan, V. (2011) **Valorisation action of plastic member capacity of semi-compact steel sections — a more economic design (SEMI-COMP+)**. Research Fund for Coal and Steel, European Commission.

Griffis, L.G., Axmann, G., Patel, V.B., Waggoner, M.C. and Vinson, J. (2003) "High-Strength Steel in the Long-Span Retractable Roof of Reliant Stadium." In **NASCC, Baltimore, USA**. **2003**

Han, K.B. and Park, S.K. (2005) Parametric study of truss bridges by the post-tensioning method. **Canadian Journal of Civil Engineering**, 32 (2): 420–429

Hancock, G.J., Key, P.W. and Olsen, C.J. (1988) "Structural behaviour of a stressed arch structural system." In **Ninth International Specialty Conference on Cold-Formed Structures. St Luis, Missouri, USA**. **1988**

Hanus, F., Schröter, F. and Schütz, W. (2005) "State of art in the production and use of high-strength heavy plates for hydropower applications." In **High Strength Steel for Hydropower Plants. Graz, Austria**. **2005**

Hibbitt, Karlsson & Sorensen and Inc (2012) **ABAQUS. ABAQUS/Standard User's Manual Volumes I–III and ABAQUS CAE Manual**. Pawtucket, USA: Dassault Systèmes

HILONG (2016) **High Strength Long Span Structures (HILONG). Reserach programme for the reserach fund for coal and steel. Technical Group: TGS8.** Final Report

Institute of Steel Development and Growth (2017) **Introduction in the plate buckling** [online]. Available from: http://www.steel-insdag.org/ [Accessed 7 January 2017]

Jernkontoret (2017) **Environmental benefits of high strength steel in the Friends Arena** [online]. Available from: http://www.jernkontoret.se/sv/forskning--utbildning/ [Accessed 7 January 2017]

de Jesus, A.M.P., Matos, R., Fontoura, B.F.C., Rebelo, C., Da Silva, L.S. and Veljkovic, M. (2012) A comparison of the fatigue behavior between S355 and S690 steel grades. **Journal of Constructional Steel Research**, 79: 140–150

Johansson, B. and Collin, P. (2005) "Eurocode for high strength steel and applications in construction." In **Super-High Strength Steels: 1st international conference. Rome, Italy**. **Rome, Italy**. **2005**

Kato, B. (1989) Rotation capacity of H-section members as determined by local buckling. **Journal of Constructional Steel Research**, 13 (2–3): 95–109

Kato, B. (1990) Role of Strain-hardening of Steel in Structural Performance. **ISIJ International**, 30: 1003–1009

Kato, B. and Kuwamura, H. (1989) "Inelastic behavior of high strength steel members with low yield ratio." In **Pacific Structural Steel Conference. Gold Coast, Queensland, Australia**. **1989**

Kemp, A.R. (1986) Factors affecting the rotation capacity of plastically designed members. **Structural Engineer**, Part B (64): 28–35

Kim, D.K., Lee, C.H., Han, K.H., Kim, J.H., Lee, S.E. and Sim, H.B. (2014) Strength and residual stress evaluation of stub columns fabricated from 800MPa high-strength steel. **Journal of Constructional Steel Research**, 102: 111–120

Kuhlmann, U. (1989) Definition of flange slenderness limits on the basis of rotation capacity values. **Journal of Constructional Steel Research**, 14 (1): 21–40

Lay, M.G. and Galambos, T.V. (1967) Inelastic Beams under moment gradient. **Journal of the Structural Division, ASCE**, 93 (ST1): 381–399

Lee, C., Han, K. and Uang, C. (2012) Flexural Strength and Rotation Capacity of I-Shaped Beams Fabricated from 800-MPa Steel. **Journal of Structural Engineering**, 139 (6): 1043–1058

Liew, A. and Gardner, L. (2015) Ultimate capacity of structural steel cross-sections under compression, bending and combined loading. **Structures**, 1: 2–11

Long, H. Van, Jean-François, D., Lam, L.D.P. and Barbara, R. (2011) Field of application of high strength steel circular tubes for steel and composite columns from an economic point of view. **Journal of Constructional Steel Research**, 67 (6): 1001–1021

Ma, J.-L., Chan, T.-M. and Young, B. (2015) Material properties and residual stresses of cold-formed high strength steel hollow sections. **Journal of Constructional Steel Research**, 109: 152–165

Magnel, G. (1950) Prestressed Steel Structures. **The Structural Engineer**, 28: 285–295

McDermott, J.F. (1969) Plastic bending of A514 steel beams. **Journal of Structural Division, ASCE**, 95: 1851–1871

Miki, C., Homma, K. and Tominaga, T. (2002) High strength and high performance steels and their use in bridge structures. **Journal of Constructional Steel Research**, 58: 3–20

von Mises (1913) Mechanik der festen Körper in plastisch-deformablen Zustand. **Nachr. Ges. Wiss. Gottingen**, pp. 582–592

Muzeau, J.P. (2014) “Recent steel constructions in France.” In **Eurosteel. Naples, Italy**. **2014**

Nishino, F., Ueda, Y. and Tall, Y. (1966) **Experimental investigation of the buckling of plates with residual stress**. Fritz Engineering Laboratory Report No. 290.3, Lehigh University, Bethlehem, Pennsylvania, USA

Nunziata, V. (2003) “Prestressed steel structures design: a new frontier for structural engineering.” In **2nd International Conference on Structural Engineering and Construction. Rome, Italy**. **2003**

Osofero, A.I., Wadee, M.A. and Gardner, L. (2012) Experimental study of critical and post-buckling behaviour of prestressed stayed columns. **Journal of Constructional Steel Research**, 79: 226–241

Packer, J.A., Wardenier, J., Zhao, X.L., van der Vegte, G.J. and Kurobane, Y. (2009) **Design guide for rectangular hollow section (RHS) joints under predominatly static loading**. 2nd ed. CONSTRUCTION WITH HOLLOW STEEL SECTIONS (CIDECT)

Pijpers, R.J.M. (2011) **Fatigue strength of welded connections made of very high strength cast and rolled steels**. TU Delft, Delft University of Technology.

Pijpers, R.J.M. and Kolstein, M.H. (2010) “Fatigue strength of truss girders made of Very High Strength Steel.” In **Tubular Structures XIII**. **2010**. pp. 499–505

prEN 10138-3 (2000) **Prestressing steels - Part 3 : Strand**. Brussels: European Committee for Standardization (CEN)

Rasmussen, K.J.R. and Hancock, G.J. (1992) Plate slenderness limits for high strength steel sections. **Journal of Constructional Steel Research**, 23: 73–96

Rasmussen, K.J.R. and Hancock, G.J. (1993) Design of cold-formed stainless steel tubular members, II: Beams. **Journal of Structural Engineering**, 119 (8): 2368–2386

Rasmussen, K.J.R. and Hancock, G.J. (1995) Tests of high strength steel columns. **Journal of Constructional Steel Research**, 34: 27–52

Ricles, J.M., Sause, R. and Green, P.S. (1998) High-strength steel: implications of material and geometric characteristics on inelastic flexural behavior. **Engineering Structures**, 20: 323–335

Russell, P. and Dowell, G. (1933) **Competitive Design of Steel Structures**. London : Chapman & Hall, ltd.

Saito, D. and Wadee, M.A. (2009) Numerical studies of interactive buckling in prestressed steel stayed columns. **Engineering Structures**, 31: 432–443

Samuelsson, A. and Schröter, F. (2005) "Production Processes, Mechanical and Chemical Properties, Fabrication Properties." In **Use and Application of High-Performance Steels for Steel Structures (SED 8)**. IABSE. pp. 99–109

Sause, R. and Fahnestock, L. (2001) Strength and ductility of HPS-100W I-girders in negative flexure. **Journal of Bridge Engineering**, (October): 316–323

Sawant, J. and Vijapur, V. (2013) Analysis and Design of Tubular and Angular Steel Trusses By Post-Tensioning Method. **Journal of Engineering Computers & Applied Sciences**, 2 (8): 30–44

Schafer, B.. and Peköz, T. (1998) Computational modeling of cold-formed steel: characterizing geometric imperfections and residual stresses. **Journal of Constructional Steel Research**, 47 (3): 193–210

Schafer, B.W., Li, Z. and Moen, C.D. (2010) Computational modeling of cold-formed steel. **Thin-Walled Structures**, 48 (10–11): 752–762

Schillo, N. and Feldmann, M. (2016) The rotational capacity of beams made of high-strength steel. **Proceedings of the Institution of Civil Engineers - Structures and Buildings**, pp. 1–12

Schmidt, L.C. and Li, H. (1998) Studies on post-tensioned and shaped space-truss domes. **Journal of Structural Engineering**, 6: 693–710

Schröter, F. (2006) "Trends of using high-strength steel for heavy steel structures." In **Progress in Steel, Composite and Aluminium Structures. Zielona Góra, Poland**. **2006**

Sedlacek, G. and Feldmann, M. (1995) **Background document 5.09 for chapter 5 of Eurocode 3 Part 1.1: the b/t ratios controlling the applicability of analysis models in Eurocode 3 Part 1.1. Technical report.** Aachen

Seif, M. and Schafer, B.W. (2010) Local buckling of structural steel shapes. **Journal of Constructional Steel Research**, 66 (10): 1232–1247

Shi, G., Ban, H. and Bijlaard, F.S.K. (2012) Tests and numerical study of ultra-high strength steel columns with end restraints. **Journal of Constructional Steel Research**, 70: 236–247

Shi, G., Hu, F. and Shi, Y. (2014a) Recent research advances of high strength steel structures and codification of design specification in China. **International Journal of Steel Structures**, 14 (4): 873–887

Shi, G., Xu, K., Ban, H. and Lin, C. (2016) Local buckling behavior of welded stub columns with normal and high strength steels. **Journal of Constructional Steel Research**, 119: 144–153

Shi, G., Zhou, W., Bai, Y. and Lin, C. (2014b) Local buckling of 460MPa high strength steel welded section stub columns under axial compression. **Journal of Constructional Steel Research**, 100: 60–70

da Silva, L.S., Marques, L. and Serra, M. (2014) **Special structural solutions for exploiting benefits of HSS**. Presentation for HILONG meeting. Lulea, Sweden

S-Squared (2017) **Creators of super powerful structures** [online]. Available from: http://www.s-squared.com.au/home.aspx [Accessed 7 January 2017]

Steel Construction Institute (2014) **HSS in different sectors**. Personal Communication

Stroetmann, R. (2011) "High strength steel for improvement of sustainability." In **Eurosteel. Budapest, Hungary**. **2011**

Su, M.N., Young, B. and Gardner, L. (2014) Deformation-based design of aluminium alloy beams. **Engineering Structures**, 80: 339–349

Subcommittee 3 on Prestressed Steel of Joint ASCE-AASHO Committee on Steel Flexural (1968) Development and use of prestressed steel flexural members. **Journal of Structural Division, ASCE**, (94 (9)): 2033–2060

Taras, A., Greiner, R. and Unterweger, H. (2013) **Proposal for amended rules for member buckling and semi-compact cross-section design.** Technical report, Consolidated version of documents of the same title submitted to the SC3 Evolution Group 1993-1-1

Theofanous, M., Chan, T.M. and Gardner, L. (2009) Structural response of stainless steel oval hollow section compression members. **Engineering Structures**, 31 (4): 922–934

Theofanous, M. and Gardner, L. (2010) Experimental and numerical studies of lean duplex stainless steel beams. **Journal of Constructional Steel Research**, 66 (6): 816–825

Timoshenko, S.P. and Gere, J.M. (1961) **Theory of Elastic Stability**. New York: McGraw-Hill, 2nd edition

Tran, A.T., Veljkovic, M., Rebelo, C. and da Silva, L.S. (2016a) Resistance of cold-formed high strength steel circular and polygonal sections - Part 1: Experimental investigations. **Journal of Constructional Steel Research**, 120: 245–257

Tran, A.T., Veljkovic, M., Rebelo, C. and da Silva, L.S. (2016b) Resistance of cold-formed high strength steel circular and polygonal sections - Part 2: Numerical investigations. **Journal of Constructional Steel Research**, 125: 227–238

Troitsky, M.S. (1990) **Prestressed steel bridges: Theory and Design**. NewYork, USA: Van Nostrand Reinhold

Usami, T. and Fukomoto, Y. (1982) Local and Overall Buckling of Welded Box Columns. **Journal of the Structural Division**, 108 (3): 525–542

Wadee, M.A., Gardner, L. and Osofero, A.I. (2013) Design of prestressed stayed columns. **Journal of Constructional Steel Research**, 80: 287–298

Wang, J., Afshan, S., Gkantou, M., Theofanous, M., Baniotopoulos, C. and Gardner, L. (2016) Flexural behaviour of hot-finished high strength steel square and rectangular hollow sections. **Journal of Constructional Steel Research**, 121: 97–109

Wang, J., Afshan, S., Gkantou, M., Theofanous, M., Baniotopoulos, C. and Gardner, L. (in preparation) **Structural behaviour and design of prestressed steel arched trusses**.

Wang, J., Afshan, S., Schillo, N., Theofanous, M., Feldmann, M. and Gardner, L. (2017) Material properties and compressive local buckling response of high strength steel square and rectangular hollow sections. **Engineering Structures**, 130: 297–315

Wang, Y.B., Li, G.Q. and Chen, S.W. (2012a) Residual stresses in welded flame-cut high strength steel H-sections. **Journal of Constructional Steel Research**, 79: 159–165

Wang, Y.B., Li, G.Q. and Chen, S.W. (2012b) The assessment of residual stresses in welded high strength steel box sections. **Journal of Constructional Steel Research**, 76: 93–99

Wang, Y.B., Li, G.Q., Chen, S.W. and Sun, F.F. (2012c) Experimental and numerical study on the behavior of axially compressed high strength steel columns with H-section. **Engineering Structures**, 43: 149–159

Wang, Y.B., Li, G.Q., Chen, S.W. and Sun, F.F. (2014) Experimental and numerical study on the behavior of axially compressed high strength steel box-columns. **Engineering Structures**, 58: 79–91

Wikipedia (2017) **Akashi Bridge.JPG** [online]. Available from: https://commons.wikimedia.org/wiki/File:Akashi_Bridge.JPG [Accessed 7 January 2017]

Wilkinson, T. and Hancock, G.J. (1998) Tests to examine compact web slenderness of cold-formed RHS. **Journal of Structural Engineering**, 124 (10): 1166–1174

Wilkinson, T. and Hancock, G.J. (1999) **Finite Element Analysis of Plastic Bending of Cold-Formed Rectangular Hollow Section Beams**. Research Report No R792. The University of Sydney

Willms, R. (2009) “High strength steel for steel constructions.” In **Nordic Steel Construction Conference. Malmo, Sweden**. **2009**. pp. 597–604

Winter, G. (1947) Strength of thin steel compression flanges. **Transactions of the American Society of Civil Engineers**, 112 (1): 527–554

Withers, P.J. and Bhadeshia, H.K.D.H. (2001) Residual stress. Part 1–measurement techniques. **Materials science and Technology**, 17 (4): 355–365

World Steel Association (WSA) (2017) **Sustainable Steel: at the core of a green economy** [online]. Available from: http://www.worldsteel.org/ [Accessed 7 January 2017]

Yang, D. and Hancock, G.J. (2004) Compression Tests of Cold-Reduced High Strength Steel Sections. I : Stub Columns. **Journal of Structural Engineering**, 130 (11): 1772–1781

Yang, D., Hancock, G.J. and Rasmussen, K.J.R. (2002) “Compression Tests of Cold-Reduced High Strength Steel Long Columns.” In **Sixteenth International Specialty Conference on Cold-Formed Steel Structures**. **2002**. pp. 285–304

Yoo, J.H., Kim, J.W., Yang, J.G., Kang, J.W. and Lee, M.J. (2013) Local buckling in the stub columns fabricated with HSA800 of high performance steel. **International Journal of Steel Structures**, 13 (3): 445–458

Yuan, B. (1997) **Local Buckling of High Strength Steel W-Shaped Sections**. McMaster University, Hamilton, Ontario, Canada

Zhao, X.L. and Hancock, G.J. (1991) Tests to determine plate slenderness limits for cold-formed rectangular hollow sections of grade C450. **Journal of The Australian Steel Institute**, 25 (4): 1–16

Zhou, F., Chen, Y. and Young, B. (2013a) Cold-formed high strength stainless steel cross-sections in compression considering interaction effects of constituent plate elements. **Journal of Constructional Steel Research**, 80: 32–41

Zhou, F., Tong, L. and Chen, Y. (2013b) Experimental and numerical investigations of high strength steel welded H-section columns. **International Journal of Steel Structures**, 13: 209–218

Ziemian, R. (Ed) (2010) **Guide to stability design criteria for metal structures**. 6th ed. John Wiley & Sons